

UNIVERSITY OF BIRMINGHAM

Microstructure and Oxidation Behaviour of Inconel 625 Manufactured by Laser Powder Bed Fusion

EMILY ROSE LEWIS

Supervised by:

Prof. Moataz M. Attallah (University of Birmingham)

Dr Sam Cruchley (University of Birmingham)

Dr Amanda C. Cruchley (Manufacturing Technology Centre, MTC)

Dr Nick Cruchley (Reaction Engines Ltd., formerly MTC)

Date: November 11, 2024

Word count: 49921

School of Metallurgy and Materials

College of Engineering and Physical Sciences

The University of Birmingham

UNIVERSITY OF
BIRMINGHAM

University of Birmingham Research Archive

e-theses repository

This unpublished thesis/dissertation is copyright of the author and/or third parties. The intellectual property rights of the author or third parties in respect of this work are as defined by The Copyright Designs and Patents Act 1988 or as modified by any successor legislation.

Any use made of information contained in this thesis/dissertation must be in accordance with that legislation and must be properly acknowledged. Further distribution or reproduction in any format is prohibited without the permission of the copyright holder.

Contents

Contents i

List of Figures iv

List of Tables xii

Acknowledgments xiv

Publications xv

Nomenclature xvii

1 Abstract 1

2 Introduction 2

2.1 Ni-based superalloys for extreme environments, Inconel 625 2

2.2 Additive Manufacturing of Ni-based superalloys, Inconel 625 4

2.3 Thesis outline 6

3 Aims and Objectives 8

4 Literature Review 9

4.1 Inconel 625, High temperature materials and their application 9

4.2 Metallurgy of Ni-based superalloys, Inconel 625 13

4.3 Laser Powder Bed Fusion of Inconel 625, Fundamentals and trends 18

4.4 High temperature oxidation of Ni-based superalloys in air, Thermodynamics and kinetics 38

4.5 Oxidation of Inconel 625, A comparison of wrought and AM alloy 51

4.6 Corrosion of Ni-based superalloys in nuclear applications 66

4.7 Grain boundary engineering and oxidation, control of microstructure and texture 75

4.8 Summary 81

5 Experimental procedure and theory 83

5.1 Materials, Laser Powder Bed Fused and Wrought Inconel 625 83

5.2 Post-processing: Surface finishes and heat treatments 85

5.3 Characterisation of as-received materials 88

5.4 High temperature isothermal oxidation in air 91

5.5 Oxide sample preparation post-exposure . . . 92
5.6 Characterisation of oxidation products . . . 94
5.7 Corrosion testing, Simulating a Pressurized Water Reactor (PWR) . . . 100
5.8 Characterisation of corrosion products . . . 101

6 Microstructure and surface finish effects, Oxidation 104
6.1 Abstract . . . 104
6.2 Highlights . . . 104
6.3 Introduction . . . 105
6.4 Material and Methods . . . 107
6.5 Results . . . 111
6.6 Discussion . . . 121
6.7 Conclusions . . . 132
6.8 Acknowledgements . . . 132
6.9 Funding . . . 133
6.10 Data availability . . . 133
6.11 CRediT authorship contribution statement . . . 133
6.12 Declaration of interests . . . 133

7 Grain boundary character and internal oxidation 134
7.1 Abstract . . . 134
7.2 Highlights . . . 135
7.3 Introduction . . . 135
7.4 Materials and Methods . . . 137
7.5 Results . . . 139
7.6 Discussion . . . 152
7.7 Conclusion . . . 155
7.8 Acknowledgments . . . 156
7.9 Funding . . . 156
7.10 Data availability . . . 156
7.11 CRediT authorship contribution statement . . . 156
7.12 Declaration of Interests . . . 156

8 PWR hydrogenated water corrosion 157
8.1 Abstract . . . 157
8.2 Highlights . . . 158
8.3 Introduction . . . 158
8.4 Experimental procedure . . . 160
8.5 Results . . . 163
8.6 Discussion . . . 182
8.7 Conclusion . . . 186
8.8 Acknowledgments . . . 186

8.9 Funding 186
8.10 Data availability 187
8.11 CRediT authorship contribution statement 187
8.12 Declaration of Interests 187

9 Conclusions and Future Works **188**
9.1 Conclusions 188
9.2 Future work 190

References **193**

Appendix **226**

List of Figures

2.1 Schematic of components inside a Pressurized Water Reactor (PWR). Taken from Staehle *et al.* via Zinkle and Busby (2009). 3
2.2 Schematic of the Laser Powder Bed Fusion processing route. Taken and adapted from Criales *et al.* (2017). 4

4.1 Overview of thermal capability of high temperature superalloys since their emergence. Taken from Reed (2006). 11
4.2 BSE-SEM micrographs showing the microstructure of AM and wrought IN625. Taken from Marchese *et al.* (2020) and Arnold *et al.* (2017). 18
4.3 Compositional profiles in γ-matrix of L-PBF IN625, as predicted using DICTRA, taken and adapted from Lindwall *et al.* (2019). 20
4.4 Summary of EBSD IPF maps showing the microstructures obtained following standard heat treatment, L-PBF IN625. Taken and adapted from Marchese *et al.* (2020). 23
4.5 Simulation of the phases (wt.%) in IN625 as a function of temperature. Taken from Mariano de Sousa Malafaia *et al.* (2020). 24
4.6 Time-Temperature-Transformation (TTT) diagram for L-PBF IN625. Taken from Lindwall *et al.* (2019). 25
4.7 BSE-SEM micrographs showing the enhanced precipitation of δ-phase in L-PBF IN625 following stress relieving at 870°C. Taken from Zhang *et al.* (2018). 26
4.8 SE-SEM micrograph, and EDS map of as-built IN625. Taken from Zhang *et al.* (2017) 27
4.9 TC-PRISMA volume phase fraction of δ-phase at stress relief temperatures T = 870°C. Taken from Lindwall *et al.*, (2019). 28
4.10 HAADF-STEM micrograph and corresponding EDS maps showing a MN precipitate in as-built IN625, manufactured using powders with high Fe content (4 wt.%). Taken from Zuback *et al.* (2019) 29
4.11 SE-SEM micrographs showing the surface profiles of L-PBF IN625 fabricated with varying laser power. Taken and adapted from Balbaa *et al.* (2019) 31
4.12 SE=SEM and confocal microscope surface profiles of L-PBF IN625 following electropolishing. Taken from Ali *et al.* (2020). 32

4.13 SE-SEM micrographs, KAM (Kernal Average Misorientation) maps, and band contrast images of as-built and shot peened L-PBF IN625, taken and adapted from Balbaa *et al.* (2022). 34
4.14 A schematic showing the cutting, smoothing and polishing steps involved in Centrifugal High Energy Finishing (CHEF) 36
4.15 Simplified model for diffusion-controlled oxidation in metals. Taken from Birks *et al.* (2005). 39
4.16 Standard Ellingham-Richardson diagram. diagram. Taken from Birks *et al.* (2006) 41
4.17 BSE-SEM micrograph showing the external chromia scale formed upon wrought IN625 following isothermal oxidation for 1000 h at T = 900˚C in air. Taken from Arnold *et al.* (2018). 42
4.18 Schematic showing the elemental depletion of A and B in the near oxide region of a selectively oxidised metal alloy, AB. Taken from Young (2016). . . . 43
4.19 Graph showing the depletion of Chromium from the bulk to the scale for Fe-32Cr, measured using Electron Probe Microanalysis (EPMA) after exposures of T = 977˚C. Reprinted from G. L. Wulf *et al.* (1969). Taken from Young (2016). 44
4.20 Schematic showing the stress-failure response of an oxide when placed under compressive stress, (a) Buckling, (b) Wedging. Adapted from Evans (1997). . 49
4.21 Arrhenius plot, comparing the oxidation performance of AM IN625 to wrought IN625 and chromia forming Ni-based superalloys from literature. 52
4.22 BSE-SEM micrograph showing the oxide film cross-section through wrought IN625, 900˚C, 1000 h. Taken and adapted from Chyrkin *et al.* (2011). 54
4.23 BSE-SEM micrograph showing an oxide cross-section through L-PBF IN625 following isothermal oxidation at 900˚C, for 168 h. Taken and adapted from Chyrkin *et al.* (2022). 56
4.24 BSE-SEM micrographs showing the oxide cross-section through wrought IN625 following isothermal oxidation at 900˚C, for periods up to 1000 h. Taken and adapted from Arnold *et al.* (2018). 57
4.25 Cr depletion in wrought IN625, 900˚C, t = 100 − 1000 h. Taken from Chyrkin *et al.* (2011). 58
4.26 Wrought IN625, chemical potential against Cr mass fraction, at 900˚C. Taken from Chyrkin *et al. (2011).* 59
4.27 SEM-BSE micrographs showing the two morphologies of Kirkendall voids observed in L-PBF IN625 exposed to 900˚C, for 168 h. (a) Ridge voids, and (b) Spherical voids. Taken and adapted from Chyrkin *et al.* (2022). 59

4.28 SEM-BSE micrographs showing the oxides formed upon ODS IN625 manufactured using SPS after 215 h – 1000 h exposure to 900˚C in air. Taken and adapted from Arnold *et al.* (2018). 61
4.29 SE-SEM micrographs showing the relationship between scan speed and the relative measured densities for L-PBF IN625. (a) Depicts a line graph of the relative density (%) recorded for increasing scan speed, (b) 600 mm/s, (c) 750 mm/s, (d) 900 mm/s, (e) 1050 mm/s and (f) 1200 mm/s. Taken and adapted from Huang *et al.* (2022). 62
4.30 A selection of SEM-BSE micrographs showing the external oxide formed after 100 h of isothermal oxidation at 900˚C for L-PBF IN625 samples manufactured with a VED of (a) 167 J/mm^3, (b) 104 J/mm^3, and (c) 76 J/mm^3. (a1), (b1) and (c1) displays the 3D surface topographies of the aforementioned samples prior to oxidation, respectively. Taken and adapted from Sun *et al.* (2020) 64
4.31 BSE-SEM image and corresponding EDS micrographs showing the distribution of elements in the cross-sectioned oxide scale formed upon electron beam melted IN718 exposed to 850˚C for 1000 h. Taken and adapted from Sanviemongska *et al.* (2018). 64
4.32 A summary of SE-SEM micrographs showing the external oxides formed upon wrought IN625 following exposure to PWR hydrogenated water, held at 260˚C for 1000 – 10,000 h. Taken and adapted from Ziemniak *et al.* (2003). 69
4.33 A schematic showing the duplex oxide films formed upon IN625 when exposed to sub-to-supercritical primary water. Taken and adapted from Rodriguez *et al.* (2017). 71
4.34 SE-SEM micrographs (a) and (b) with their corresponding EDS maps, showing the elements present in and around pits formed upon the surface of wrought IN625 following exposure to SCW held at 800˚C for a period of 12 h. Taken from Behnamian *et al.* (2016). 72
4.35 The proportion of CSL grain boundaries in conventional and GBE IN600 showing the effects upon the corrosion rate. Taken from Lin *et al.* (1995). 77
4.36 Wrought IN718 following oxidation at 850˚C in static air. SEM-BSE micrograph showing presence of internal oxide upon randomly orientated grain boundaries. Taken and adapted from Krupp *et al.* (2013). 78

4.37 Graph showing the TGA oxidation kinetics taken for a set of IN718 samples with differing CSL fractions following oxidation at 850˚C in air. Taken from Krupp *et al.* (2013). 79
4.38 (a) EBSD IPF map showing the external oxide formed on Haynes 230 alloy, with corresponding (b,c) AFM maps and surface roughness line scan (d), correlating the effects of surface grain orientation upon oxidation. Taken and adapted from Schuh *et al.* (2003). 80
4.39 Flowchart of key research topics outlined for the PhD project. 82

5.1 A schematic showing the two L-PBF builds carried out for the duration of the PhD project. Build 2 included bar support struts. BD indicates the building direction. 83
5.2 L-PBF IN625 oxide samples, pre-oxidation 93
5.3 A BSE-SEM micrograph depicting summary of oxide scale measurements . . 95
5.4 A plot showing the peak shift experienced by chromia grown upon an as-built token of L-PBF IN625, exposed to 950˚C for 100 h in air. 97
5.5 A diagram showing the co-ordinate system used to calculate the strain and stress in the surface of an oxide. Taken from the Measurement Good Practice Guide No. 52, National Physical Laboratory, NPL. 98
5.6 An example of an interplanar spacing, d, vs $sin^2\psi$ graph (116) plane of Cr_2O_3. 99

6.1 A schematic showing the orientations of L-PBF IN625 samples fabricated in Build 1 and 2. Build 2 tokens including bar-supports. *BD indicates the building direction. 107
6.2 SEM-BSE micrographs and EBSD IPF maps showing the microstructure of L-PBF IN625 in the as-built and solution heat-treated conditions. 111
6.3 Confocal images showing the height variation observed across the (a) CHEF (ST) surface, and (b) as-received additive (ST) surface L-PBF IN625 samples in the XY orientation. 112
6.4 Mean mass gained/area vs time for each condition of L-PBF IN625, oxidised at 950˚C for up to 1000 h compared to wrought IN625 114
6.5 Oxide cross-section obtained for L-PBF IN625 exposed to 950˚C in laboratory air and pressure for 24 - 1000 h. 115
6.6 BSE-SEM micrograph showing the oxide cross-section through as-built L-PBF IN625 exposed to 950˚C in laboratory air and pressure for 1000 h, with the corresponding EDS maps (Cr, Mn, Al, Nb). 115
6.7 XRD patterns obtained for L-PBF IN625 exposed to 950˚C for 1000 h 116

6.8 Spallation in the Ground (ST) L-PBF IN625 samples, exposed for 1000 h. (a) BSE-SEM oxide cross-section showing perfectly adhered chromia, (b) BSE-SEM oxide cross-section showing a spalled area of oxide, (c) external oxide SE-SEM showing spalled oxide, (d) EDS maps showing enrichment in Ni, Nb, Mo, indicating oxide delamination from the near-continuous δ-phase, (e) a bar chart showing growth of the Ni_3Nb δ-phase as percentage coverage at the scale-alloy interface for all conditions of L-PBF IN625. 117
6.9 BSE-SEM micrograph and corresponding EDS maps showing oxide cross-sections for additive (ST) tokens of L-PBF IN625, oxidised for 500 h. 118
6.10 (a) SE-SEM micrograph showing an oxide cross-section through Ground (AB) L-PBF IN625 oxidised for 100 h at T = 950°C, indicating the region of a FIB lift-out. (b) Shows the trenching of the FIB lift-out sample during the thinning stages. (c) A High-Angle Annular Dark Field (HAADF) micrograph showing a ridge void formed in Ground (AB) sub-scale after 100 h, with the corresponding STEM-EDS maps (d) showing the elemental distribution of Ni, O, Al, and Ti. 119
6.11 Chromium depletion profiles generated for all conditions of L-PBF IN625 after oxidation at 950°C for 1000 h. Profiles generated from EDS line scan measurements averaged and fitted to Fick's second law of diffusion 120
6.12 A bar chart showing the compressive stresses measured using the XRD $sin^2(\psi)$ method, for surface oxides formed for all conditions of L-PBF IN625, exposed to 950°C for 1000 h. 121
6.13 Curves showing the critical temperature change (ΔT_c) required to initiate spallation for increasing oxide thickness, for chromia growing on L-PBF IN625, chromia growing on Ni_3Nb δ-phase, and Ni_3Nb δ-phase growing on IN625. . 129
6.14 Arrhenius graph, showing the temperature dependence of the parabolic K_P rate constants for the oxidation of L-PBF and wrought IN625 taken from literature and this study. 131

7.1 A summary of BSE-SEM micrographs, and Inverse Pole Figures (IPF) maps showing the microstructure of as-built and solution-treated L-PBF IN625. Imaged perpendicular to the build direction. 140
7.2 Mean mass gain/area vs time for as-built and solution-treated L-PBF IN625, exposed to 950°C for up to 1000 h, compared to wrought IN625, taken from Chyrkin *et al.* (2022) [1]. Data fit to Wagner's classical equation for oxidation. 141

7.3 A summary of optical micrographs, and Inverse Pole Figures (IPFs) showing the external oxide of as-built and solution-treated L-PBF IN625 from t = 0.5 h – 100 h. Imaged perpendicular to the build direction. 142
7.4 A summary of 3D profilometry maps of the surface of samples of as-built and solution-treated L-PBF IN625 held at 950˚C for 0.5 – 100 h. 143
7.5 A summary of 2D profilometry maps of the surface of samples of as-built and solution-treated L-PBF IN625 held at 950˚C for 0.5 – 100 h. Note the elevated topography along scan tracks and grain boundaries at early periods of oxidation, t<2 h. 144
7.6 (a) EBSD phase map showing a fully indexed cross-section through as-built L-PBF IN625 exposed to 950˚C for 1000 h. (b) EBSD band contrast map showing grain boundary character, with special boundaries highlighted in colour. . . 146
7.7 SEM-SE micrograph of a cross-section through as-built L-PBF IN625 exposed at 950˚C for 1000 h. Note internal oxide growing primarily along random oriented boundaries only. 147
7.8 EBSD IPF maps and their corresponding band contrast maps with grain boundary character overlaid, for (a) as-built L-PBF IN625 before, and (b) after 1 h of isothermal oxidation at 950˚C. 149
7.9 EBSD IPF maps and their corresponding band contrast maps with grain boundary character overlaid, for as-built L-PBF IN625 before (a), and after 100 h (b) of isothermal oxidation at 950˚C. (c) Shows a magnified band contrast image, highlighted in (b) 150
7.10 Phase map of the site shown in Figure 7.9, showing the elemental distribution across the sample surface following partial oxide removal via vibropolishing. 151
7.11 (a) BSE-SEM micrograph showing the location of the FIB lift-out performed for solution-treated L-PBF IN625 following exposure at 950˚C for 100 h. (b) HAADF micrograph produced showing the sub-scale microstructure, and corresponding STEM-EDS maps (c – h) showing the elemental distribution of Ni, Cr, O, Al, Nb and Ti. 152

8.1 Mass gain change experienced by different conditions of L-PBF IN625 in hydrogenated PWR primary water held at 300˚C for 500 h and 1500 h. (a) Microstructure study, (b) surface finish study. 165

8.2 X-ray diffraction patterns from the surfaces of the corrosion tokens of different conditions of L-PBF IN625 following exposure to hydrogenated PWR primary water held at 300˚C for 1500 h. 166
8.3 Raman spectra recorded from the surfaces of the corrosion tokens of different conditions of L-PBF IN625 following exposure to hydrogenated PWR primary water held at 300˚C for 1500 h. (a) Microstructure study, (b) surface finish study. 167
8.4 BSE-SEM micrographs of the external oxide formed upon corrosion tokens of different heat-treated conditions of L-PBF and wrought IN625 following exposure to hydrogenated PWR primary water held at 300˚C for 1500 h. . . . 169
8.5 BSE-SEM micrograph and the corresponding EDS elemental maps showing the oxide crystallites formed upon (a) as-built, (b) solution-treated and (c) wrought IN625 following exposure to hydrogenated PWR primary water held at 300˚C for 1500 h. Note the texture enhanced oxidation. 170
8.6 SE-SEM micrographs of selected regions of solution-treated L-PBF IN625 corrosion tokens and their corresponding EBSD IPF maps following oxide removal after 1500 h exposure to hydrogenated PWR primary water. 171
8.7 BSE-SEM micrographs of the external oxide formed upon corrosion tokens of different surface finish conditions of L-PBF IN625 following exposure to hydrogenated PWR primary water held at 300˚C for 1500 h. 173
8.8 BSE-SEM micrograph and the corresponding EDS elemental maps showing the oxide crystallites formed upon additive surface L-PBF IN625 following exposure to hydrogenated PWR primary water held at 300˚C for 1500 h. . . . 175
8.9 Higher magnification BSE-SEM micrograph and the corresponding EDS elemental maps showing the oxide crystallites formed upon additive surface L-PBF IN625 following exposure to hydrogenated PWR primary water . . . 176
8.10 BSE-SEM micrographs and the corresponding Nb EDS elemental maps showing the evolution of the (Nb,Mo)-rich precipitate following solution heat-treatment and prolonged exposure to hydrogenated PWR primary water held at 300˚C for 500 and 1500 h. 177
8.11 BSE-SEM micrographs showing FIB cross-sections of the oxides formed upon corrosion tokens of different heat-treated and surface finished conditions of L-PBF and wrought IN625 following exposure to hydrogenated PWR primary water held at 300˚C for 1500 h. 178

8.12 HAADF, BF and DF micrographs and corresponding STEM-EDS elemental maps showing the FIB cross-section through oxide scales formed upon additive surface L-PBF IN625 following exposure to hydrogenated PWR primary water held at 300°C for 1500 h. Note the duplex scale, with Fe-rich outer scale and Cr-rich inner scale. 179
8.13 HAADF, BF and DF micrographs and corresponding STEM-EDS elemental maps showing the FIB cross-section through oxide scales formed upon additive surface L-PBF IN625 following exposure to hydrogenated PWR primary water held at 300°C for 1500 h. Note the (Nb,Mo)-rich needle-like precipitate. 180
8.14 TEM-EDS elemental map and corresponding labelled STEM-EDS line scan (see white dotted line) through: (a) oxide scales, (b) Nb-rich precipitate, (c) Al-rich precipitate formed in the sub-scale region of the additive surface L-PBF IN625 following exposure to hydrogenated PWR primary water held at 300°C for 1500 h 181

1 Appendix Figure 1: Laser Powder Bed Fusion (L-PBF) manufactured IN625 upon build plate, containing a total of 72 cylindrical rod samples, and 8 cuboid samples. The samples consist of cylindrical shapes with diameters of 14 mm and heights of 120 mm, and cuboids of 10 mm height, by 10mm width, by 10 mm depth. The build plate showcases a variety of sample geometries, strategically arranged for optimal space utilization and heat management during the manufacturing process. 228
2 Appendix Figure 2: Laser Powder Bed Fusion (L-PBF) manufactured IN625 samples upon build plate, containing a total of 420 circular tokens on support struts. The samples dimensions were set to produce tokens of diameter of 14 mm and thickness of 2 mm. Four test cuboid samples were also placed in each corner (of 10 mm height, by 10 mm width, by 10 mm depth) to test for possible variations in microstructure across the build plate. The build plate showcases a variety of sample geometries, strategically arranged for optimal space utilization and heat management during the manufacturing process. . 228

List of Tables

4.1 Standard heat treatments for IN625 - AMS2774E. 11
4.2 Nominal chemical composition of IN625 for L-PBF, ASTM F3056-14e1. 13
4.3 Summary of phases and precipitates in IN625 taken and adapted from Reed (2006), Donachie (2002), Floreen (1994), and Lewis (2020). 15
4.4 Comprehensive summary of heat treatments for L-PBF IN625 in the literature. 22
4.5 Selected heat treatments for L-PBF IN625 from literature. 23
4.6 An overview of the surface roughness values obtained with standard surface finishing techniques for AM Ni-based superalloys from literature. 37
4.7 Summary of key isothermal oxidation studies investigating AM IN625, and the oxides observed from literature. 53

5.1 Set chemical compositions of conventional and L-PBF IN625. 84
5.2 Powder composition for L-PBF IN625 used in the present study. 84
5.3 Wrought and L-PBF IN625 sample chemical composition 85
5.4 Standard heat treatments for IN625 - AMS2774E. 86
5.5 Chemical agents applied during CHEF, ActOn Finishing Ltd. 87
5.6 Table showing a summary of the conditions of the material investigated. . . 88
5.7 Oxidation matrix, T = 950˚C, t = 0.5 − 1000 h. 92
5.8 Corrosion matrix, T = 300˚C, P = 10.8 MPa, t = 500 h, 1500 h. 101

6.1 Powder composition for L-PBF IN625 used in the study 107
6.2 Overview of materials, heat treatments and surface finishes investigated. Roughness values taken using Alicona confocal microscope. 108
6.3 Values of the exponent, n, parabolic, K_P, and cubic, K_C, rate constants for the oxide growth at 950˚C, 1000 h, for L-PBF IN625. 113
6.4 Values for the chromium depletion depth and calculated chromium diffusion coefficients in IN625 measured for all sample conditions of L-PBF IN625. . . 120
6.5 Elastic constants and fracture energies taken from literature for Cr_2O_3, Ni_3Nb and IN625 126

7.1 Powder composition for L-PBF IN625 used in the present study. 137
7.2 Exponent, n, and K_P, rate constant for oxide growth at 950˚C for t = 0.5 − 1000 h. 141
7.3 Σ3 boundaries (%) in as-built and solution-treated L-PBF IN625 before and after oxidation at T = 950˚C for T = 100, 1000 h, related to internal oxide penetration depth. 148

8.1 Measured composition for L-PBF IN625 metallic powders, and consolidated tokens used in the corrosion study. 160
8.2 Overview of materials, microstructures and surface finishes investigated. . . 162
8.3 Summary of oxidation data collected for L-PBF IN625 held at 300˚C for 1500 h. 164

1 Appendix Table 1: Summary of the oxidation performance of wrought Ni-based superalloys in literature, following isothermal oxidation testing in laboratory air and pressure [1–11]. 226
2 Appendix Table 2: Summary of the oxidation performance of L-PBF manufactured IN625 in literature, following isothermal oxidation testing in laboratory air and pressure [1, 9, 10, 12–17]. 227

Acknowledgments

I am deeply grateful to my supervisors Dr Sam Cruchley, Professor Moataz M. Attallah, Dr Amanda C. Cruchley, and Dr Nick Cruchley. Their knowledge, encouragement, and guidance over the past four years have been invaluable.

My heartfelt thanks to my collaborators in this work: Amanda, for her mentorship, and for contributions in the printing of samples at the Manufacturing Technology Centre (MTC); Dr David Stewart at Rolls Royce; Dr Fabio Scenini and Dr Jonathan Duff at the University of Manchester, for their vital expertise in corrosion testing at the Henry Royce Institute; and Dr Bonnie Attard and the DMME team at the University of Malta, who graciously hosted me for a month, allowing me to investigate the effects of grain boundary misorientation on internal oxidation. I am also thankful to Dr Mary Taylor for introducing me to the fascinating field of oxidation during my Masters studies.

A huge thank you to the AMPLab team for first welcoming me into the group during my undergraduate internship in 2018. Special thanks to Alessandro Sergi for sharing his knowledge of Hot Isostatic Pressing IN625 and for contributing materials to this project.

To my close friends and collaborators, Jóhan Pauli Magnussen, Alex Dickinson Lomas, Una O'Hara, Liam Hughes, and Miles Fan, your friendship and our coffee breaks kept me smiling. To Bonnie, your unwavering support and guidance have been a source of inspiration throughout this PhD journey. Our trips to Malta were some of the highlights of my PhD.

I am profoundly grateful to my family and friends; Lizzie Miers, Lucy Scott and Charlotte Kerr, for their understanding, love and support. Mum, you inspire me most of all and taught me to never give up. Finbarr O'Rafferty, meeting you at the Birmingham Theatre School gave me the strength to finish this work.

This work would not have been possible without the support of the funding via the MTC and valuable contributions from Rolls-Royce, Parker Aerospace, and travel grants; the IOM3 Grants to Support Knowledge Exchange, the Mohan S. Devgun fund, and the Turing Scheme.

Publications

The following peer-reviewed papers were produced during this project:

1. **E. R. Lewis**, M. P. Taylor, B. Attard, N. Cruchley, A. P. C. Morrison, M. M. Attallah, S. Cruchley, *Microstructural Characterisation and High Temperature Oxidation Performance of Additively Manufactured Inconel 625*, *Materials Letters*, 2022, Volume 311.

This work incorporates the following chapters written in preparation for publication as papers:

1. *Chapter 6*: **E. R. Lewis**, B. Attard, Z. Gao, N. Cruchley, A. C. Cruchley, M. M. Attallah, S. Cruchley, *The effect of microstructure and surface finish on the high temperature oxidation of Laser Powder Bed Fused IN625.* (In submission).
2. *Chapter 7*: **E. R. Lewis**, B. Attard, Z. Gao, J. P. Magnussen, Y. L. Chui, N. Cruchley, A. C. Cruchley, M. M. Attallah, S. Cruchley, *The effect of grain boundary character on the internal oxidation behaviour of Laser Powder Bed Fused IN625.*
3. *Chapter 8*: **E. R. Lewis**, N. Cruchley, J. P. Magnussen, A. Dickinson-Lomas, J. Duff, A. C. Cruchley, Y. L. Chui, F. Scenini, S. Cruchley, M. M. Attallah *Corrosion behaviour of Laser Powder Bed Fused IN625 in hydrogenated high temperature water.*

The following conference talks/posters have resulted from this work:

1. **E. R. Lewis**, N. Cruchley, M. M. Attallah, S. Cruchley, *Microstructure and Oxidation of Laser Powder Bed Fused IN625.* Oral Presentation. ESPRC & SFI International Student Conference in Advanced Metallic Systems. Symposium: Advanced Processing and Characterisation (University of Sheffield, UK, July 2021).
2. **E. R. Lewis**, N. Cruchley, M. M. Attallah, S. Cruchley, *Microstructural Characterisation and Oxidation of Laser Powder Bed Fusion Processed IN625.* Poster Presentation. International Conference on Microscopy of Oxidation (Cranfield University, UK, September 2022).

3. **E. R. Lewis**, N. Cruchley, M. M. Attallah, S. Cruchley, *Microstructural Characterisation and Oxidation of Laser Powder Bed Fusion Processed IN625.* Oral Presentation. Materials Science and Technology (MS&T). Symposium: Additive Manufacturing: Mechanisms and Mitigation of Aqueous Corrosion and High-Temperature Oxidation - Corrosion Behaviour (Pittsburgh, Pennsylvania, USA, October 2022).
4. **E. R. Lewis**, A. C. Cruchley, N. Cruchley, A. Dickinson-Lomas, J. Duff, F. Scenini, Y. L. Chui, S. Cruchley, M. M. Attallah *Corrosion Behaviour of Laser Powder Bed Fused Inconel 625 in Hydrogenated High Temperature Water.* Oral Presentation. TMS 153rd Annual Meeting and Exhibition. Symposium: Materials Corrosion Behaviour in Advanced Nuclear Reactor Environments (Orlando, Florida, USA, March 2024).

The following undergraduate Master's Projects have resulted from this work at the School of Metallurgy and Materials, University of Birmingham:

1. A. S. Butt, N. Cruchley, **E. R. Lewis**, M. P. Taylor, S. Cruchley, *Oxidation of Additively Manufactured Inconel 625*, Materials Eningeering with Industrial Experience MEng, 2021.
2. B. S. Karbaron, **E. R. Lewis**, N. Cruchley, S. Cruchley, *High Temperature Oxidation of Additively Manufactured IN625*, Materials Eningeering with Industrial Experience BEng, 2023.
3. E. Aston, **E. R. Lewis**, N. Cruchley, S. Cruchley, *High Temperature Oxidation of Additively Manufactured IN625*, Nuclear Engineering MEng, 2024.

Nomenclature

Item	Description
AB	As-Built
AES	Auger Electron Spectroscopy
AFM	Atomic Force Microscopy
AM	Additive Manufacturing
APT	Atom Probe Tomography
ASTM	American Society for Testing Materials
BCT	Body Centred Tetragonal
BD	Building Direction
BF	Bright-Field
BSE	Backscattered Electron
CAD	Computer Assisted Design
CERT	Constant Extension Rate Tensile Testing
CFB	Carbide Free Bainitic
CHEF	Centrifugal High Energy Finishing
CSL	Coincident Site Lattice
CTE	Coefficient of Thermal Expansion
DF	Dark-Field
DICTRA	Thermo-Calc Diffusion Module
DIGM	Diffusion Induced Grain Boundary Migration
DSC	Displacement Shift Complete
EBSD	Electron Backscattered Diffraction
EBM	Electron Beam Melted
EDM	Electrical Discharge Machining
EDS	Energy Dispersive Spectroscopy
EECG	Environmentally Assisted Crack Growth
EPMA	Electron Probe Micro-Analyser
FCC	Face Centred Cubic
GBE	Grain Boundary Engineering
GCP	Geometrically Close Packed
GDOES	Glow Discharge Optical Emission Spectroscopy
GND	Geometrically Necessary Dislocations
HAADF	High-Angle Annular Dark-Field Imaging
HAGB	High Angle Grain Boundary
HAZ	Heat Affected Zone
HCP	Hexagonal Close Packed
HIP	Hot Isostatically Pressed
ICP-MS	Inductively Coupled Plasma Mass Spectrometry
IPF	Inverse Pole Figure
KAM	Kernel Average Misorientation
LAGB	Low Angle Grain Boundary

Item	Description
LBM	Laser Beam Melted
LMD	Laser Metal Deposition
L-PBF	Laser Powder Bed Fusion
LWR	Light Water Reactor
MTC	Manufacturing Technology Centre
ODS	Oxide Dispersion Strengthened
PBR	Pilling-Bedworth Ratio
PIO	Preferential Intergranular Oxide
PWR	Pressurised Water Reactor
PWSCC	Primary Water Stress Corrosion Cracking
SAED	Selected Area Electron Diffraction
SCC	Stress Corrosion Cracking
SCWR	Super Critical Water Reactor
SE	Secondary Electron
SEM	Scanning Electron Microscopy
SFB	Semi-Friable Bainitic
SIMS	Secondary Ion Mass Spectrometry
SPS	Spark Plasma Sintering
SR	Stress Relief
SSRT	Slow Strain Rate Testing
ST	Solution Heat Treated
TEM	Transmission Electron Microscopy
TGB	Twin Grain Boundary
TTT	Time-Temperature-Transformation
VED	Volumetric Energy Density
XPS	X-ray Photoelectron Spectroscopy
XRD	X-ray Diffraction
XRF	X-Ray Fluorescence

Chapter 1

Abstract

The high temperature oxidation of L-PBF IN625 was investigated following heat-treatment and surface finishing. Sub-parabolic oxidation behaviour was shown, demonstrating similar growth rates to wrought IN625. Regardless of surface morphology and stress-state, chromia (Cr_2O_3) scale was formed alongside a near-continuous δ-phase layer (Ni_3Nb) at the scale/alloy interface. The continuity of the δ-phase layer was influenced by surface finishing via changes to the oxide morphology. Less δ-phase at the scale/alloy interface was correlated to increased spallation. This was related to modeled values for the temperature change required for spallation (ΔT_c), alongside physical measurements of stress (XRD $\sin^2(\psi)$) within the scale. It was concluded that surface finish is key in the maintenance of a continuous δ-phase layer to ensure relaxation of Cr_2O_3 upon cooling.

Internal oxide (Al_2O_3) was detected at grain boundaries in the sub-scale. Significant fractions of Coincident Site Lattice (CSL) boundaries formed in L-PBF IN625 following heat-treatment and oxidation (up to 70%). Nucleation of internal oxide was strongly influenced by grain boundary character, forming preferentially along random orientation grain boundaries. Higher fractions of CSL boundaries in the substrate corresponded to a shallower depth of internal oxidative attack.

Corrosion of L-PBF IN625 was investigated following heat-treatment and surface finishing in simulated Pressurised Water Reactor (PWR) hydrogenated water. Oxidation was not influenced significantly by L-PBF microstructure, but by changes to surface finish. Rougher and/or stressed surfaces led to scale spallation at early exposures. Mass gain was observed after 1500 hours (h), with similar oxide crystallite size and morphology to wrought IN625. No pitting corrosion was observed. A duplex layered oxide formed, comprised of an Fe-rich outer scale ($Ni(Fe,Cr)_2O_4$), on a Cr-rich dense inner scale. Grain orientation directly influenced oxidation. EBSD revealed the following grain orientation-oxidation relationship, in order of increasing oxidation rate: [100] < [101] < [111]. Overall, electropolished surfaces were deemed most suitable for PWR environments.

Chapter 2

Introduction

This chapter outlines the significance of Ni-based superalloy Inconel 625 (IN625) in high termperature environments, providing a background on its applications in industry, and how Additive Manufacturing (AM) techniques such as Laser Powder Bed Fusion (L-PBF) can be applied to address issues encountered with standard processing routes. This is followed by the aims and objectives set for the body of this project.

2.1 Ni-based superalloys for extreme environments, Inconel 625

The high temperature oxidation resistance of an alloy plays an important role in determining the lifetimes of components used in extreme high temperature and aqueous environments. Inconel 625 (IN625, UNS N06625) is a Ni-based superalloy with a Face Centred Cubic (FCC) crystal structure, maintaining excellent corrosion resistance, high fatigue cycle and creep resistance at elevated temperatures owing to its high Cr content, and solid solution strengthening via additions of Nb and Mo [18–21]. The combination of high temperature mechanical properties and oxidation resistance in harsh environments makes IN625 a versatile alloy suited to multiple applications across the nuclear, aerospace, marine and automotive industries. This is particularly demonstrated by its application in Pressurized Water Reactors (PWRs), where it is used in the manufacture of steam generator tubing and heat exchangers, where pitting corrosion mechanisms can limit lifetime. This is non-specific to IN625 and similar Ni based superalloys, and can occur by local galvanic coupling effects between dissimilar metals, sensitisation to specific elements (e.g. Sulphur), structural defects such as grain boundaries and localised stress concentrations, and increased temperatures of exposure [20, 22–28].

Despite optimisation in terms of composition and microstructure, environmental degra-

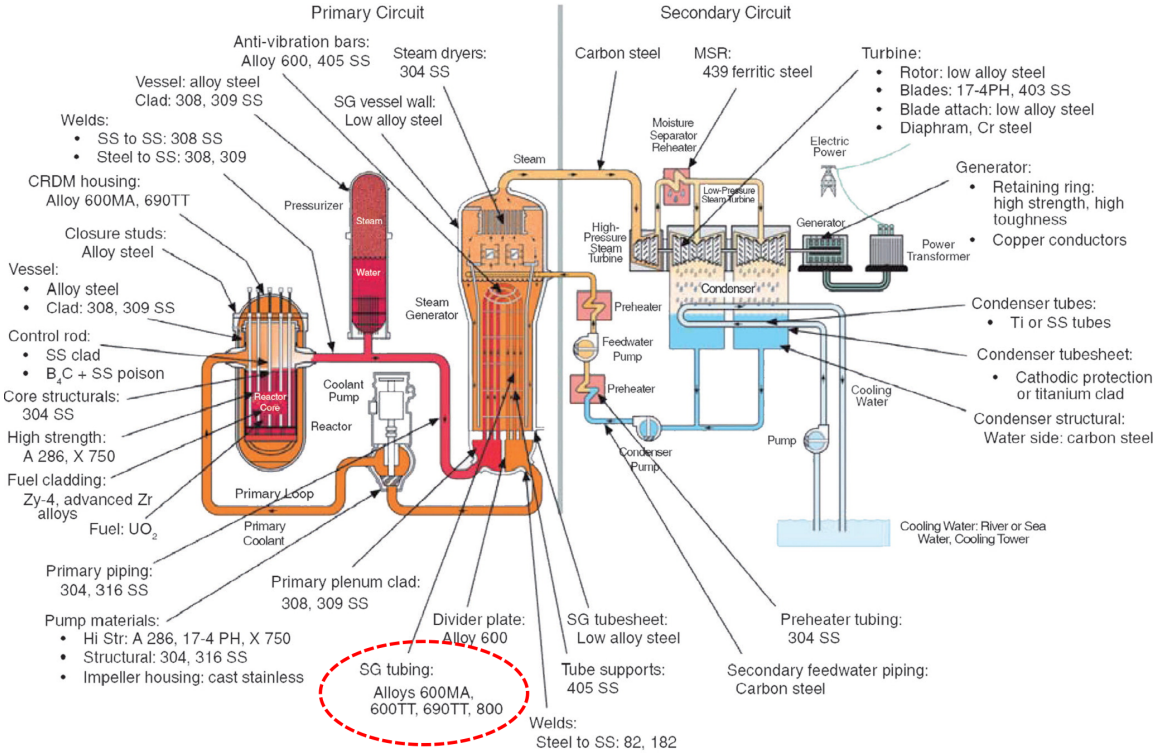


Figure 2.1: Schematic of components inside a PWR. See the steam generator tubing using IN600 and IN690 as structural materials circled in red. Taken and adapted from Staehle via Zinkle and Busby (2009) [31].

dation remains a life-limiting factor. This provides an additional challenge when designing for increased fuel efficiency and reduced CO_2 emissions [19]. Generation IV Super Critical Water Reactors (SCWRs) provide simplified designs and higher thermal efficiencies (45% compared to 33% in Light water Reactors (LWRs)) following an increase in operation pressure and temperature [22–24, 29–31]. The aforementioned operational conditions produce low density water/steam dependent on the reactor design. Supercritical coal-fired plants use supercritical water at P = 25 MPa, and steam temperatures of T = 500 – 600˚C to increase operational efficiency. Low density water/steam readily dissolves gases like oxygen, but has low solubility of ionic species. This alters the oxidation kinetics of the alloy, often leading to the promotion of Stress Corrosion Cracking (SCC) [22, 25, 29, 32]. IN625 is a prime candidate for the design of PWR and Generation IV components, therefore it is clear that a strong understanding of the microstructure and oxidation kinetics is needed in sustaining IN625's performance in future high temperature applications [20, 31, 33].

A significant downside to the use of IN625 is its poor machinability due to the alloy's high hardness and high strength at high temperatures, and its affinity to react with tool

materials, making the manufacturing of complex geometries difficult [34–37]. Standard manufacturing routes such as casting, forging and machining have been observed to lead to high amounts of tool wear, the generation of heat, and subsequently thermal damage and dimensional warping of the final component.

2.2 Additive Manufacturing of Ni-based superalloys, Inconel 625

Additive Manufacturing (AM) techniques pose a clear solution to this, with the ability to produce highly complex near-netshape components without need of machining, preventing complications due to IN625's high work hardening rates [33, 38, 39]. IN625 lends itself well to Laser Powder Bed Fusion (L-PBF) due to its high weldability and slow precipitate formation, allowing for the manufacturing of near-fully dense (>95%), unique geometry components previously unobtainable using more conventional subtractive methods (see Figure 2.2) [39–41]. This can introduce capabilities for the manufacturing of complex internal structures such as cooling channels to increase the efficiency of the component. Despite high costs associated with high quality pre-alloyed powder manufacturing (e.g. powder atomisation and spheroidisation), an AM approach can lead to reduced costs, lead times, and reduced materials wastage [42]. AM also circumvents the requirement to fabricate multiple modular parts which would previously have needed to be assembled in an additional manufacturing step [39, 43].

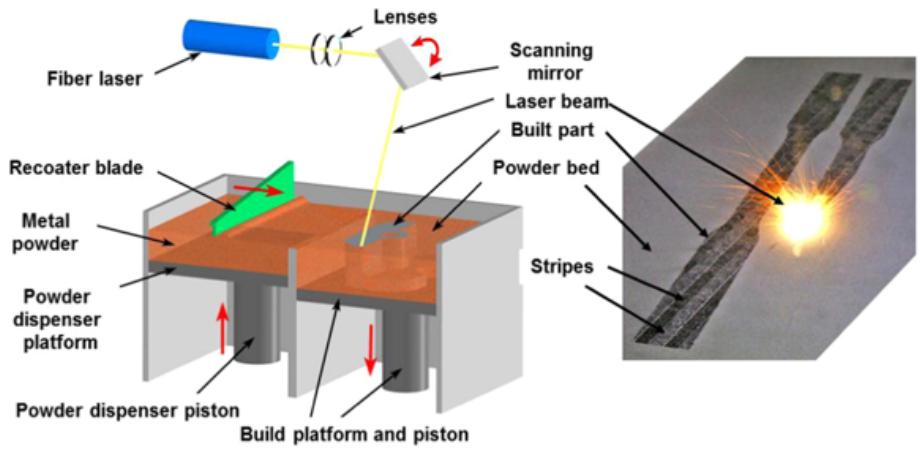


Figure 2.2: Schematic of the Laser Powder Bed Fusion processing route, showing the manufacturing of a standard tensile bar geometry. Taken and adapted from Criales *et al.* (2017) [40].

However, new complications have been observed to arise due to the unique heating, cooling rates, and thermal gradients experienced during the incremental melting of powder with a high energy laser. AM processing introduces a wide range of directional microstructural and compositional features. Fast solidification rates common to L-PBF (up to 10^6 K/s) produce highly anisotropic microstructures and mechanical properties, as well as producing strong textural effects in the component [33–35, 38, 44–46]. The application of heat treatments is crucial to remove any of the aforementioned anisotropy in the build prior to the components use in-service, where currently the standard ASTM heat treatments designed for standard fabrication routes for the alloy are used. From the literature, it is yet unclear as to whether these produce the same effects in the highly anisotropic as-built L-PBF microstructure, where microsegregation of heavy elements can lead to the enhanced formation of deleterious phases and precipitates such as the brittle δ-phase (Ni_3Nb) [38, 47–49].

Flexibility of the laser size, shape and scanning parameters has made it possible to modify the microstructure and surface texture of a component during melting (e.g. advanced graded microstructure turbine blades for application in aerospace) [45, 50]. This may have interesting applications in the tailoring of microstructure to specifically design for enhanced oxidation resistance. This could be achieved by taking a Grain Boundary Engineering (GBE) approach to control the oxidation kinetics of the alloy via grain boundaries and grain texture [29, 46, 50]. However, limitations remain where the surface roughness of as-built components is significantly coarser and uneven compared to those encountered with traditional machining techniques. This can lead to accelerated oxidation rates and spallation of the protective oxide film [16, 29].

In a time where there is an increased demand for complex high temperature resistance parts, and a drive to improve efficiency, it is of the utmost importance that the microstructural and chemical differences encountered with AM processing are fully understood to allow for the maintenance of desirable properties such as oxidation resistance and creep resistance when exposed to high temperatures to prevent critical failure [33]. The key concern of this research is to further the understanding of the post-processing of L-PBF IN625 in terms of the application of heat treatment and surface finishing. This work contributes to the development of novel surface finishes more applicable to complex geometry components common to IN625s uses in industry, and the enhanced understanding

of how heat treatment and surface finish combine to influence the oxidation and corrosion resistance of the alloy in both high temperature air and Pressurised Water Reactor (PWR) primary water conditions.

2.3 Thesis outline

This PhD research project investigates the high temperature oxidation resistance of L-PBF IN625 in both air and Pressurized Water Reactor primary water conditions, evaluating the influence of post-processing heat treatment and surface finishing.

Chapter 4 outlines a literature review on the metallurgy of IN625 together with a description of the common applications and standard strengthening mechanisms. The fundamentals of AM-L-PBF are laid out, as well as standard post-process heat treating and surface finishing of typical AM alloys. The standard thermodynamics and kinetics of the oxidation of Ni-based superalloys are discussed and summarised. Literature covering the oxidation resistance of both standard wrought IN625 and AM IN625 and similar Ni-based superalloys and high Cr alloy is then critically compared, contrasted and reviewed, with a focus on the effect of microstructure and surface finish upon the high temperature oxidation performance. From this, unexplored gaps in the research were identified and outlined, including the following topics: the effects of special grain boundaries, AM texture, and AM IN625 application in PWR corrosive environments.

Chapter 5 outlines the experimental procedures and theory followed throughout the thesis, with a data presented for all materials investigated. Specific standards adhered to have been referenced.

Chapter 6 outlines a paper drafted for the journal of Corrosion Science (Elsevier), and investigates the effect of on the post-processing upon the isothermal oxidation resistance of IN625. This is namely through the application of heat treatment and a variety of surface finishing processes including: additive surfaces, electropolished, and Centrifugal High Energy Finishing (CHEF). Solution heat treatment was applied to selected tokens to obtain an equiaxed microstructure comparable to wrought annealed IN625, and to reduce the effects of microsegregation. The oxides and growth rates obtained for both the heat treatment and surface finish approaches are compared to the performance of standard

wrought annealed IN625 and similar Ni-based superalloys exposed to high temperature air. The oxidation growth kinetics were calculated for each, to investigate the influence of microstructure, surface roughness and surface topography on the oxidation mechanism and spallation. Sub-scale surface damage and phase growth in each condition was examined to inform mechanisms, related directly to theoretical calculations of the critical temperature drop for spallation, and physical stress state measurements of the resultant oxide scale.

Chapter 7 presents a study investigating the effect of grain boundary character on the internal oxidation of L-PBF IN625, with a focus on the application of heat treatment and its effect upon the formation of Coincident Site Lattice (CSL) grain boundaries to theoretically enhance oxidation resistance. Correlation between microstructures before and after exposure to elevated temperatures inform the microstructural evolution occurring during oxidation of the alloy, revealing a relationship between grain boundaries and the formation of internal oxide at the scale/alloy interface. This paper was drafted for eventual submission to the journal Acta Materialia (Elsevier).

Chapter 8 expands the investigation of L-PBF IN625 to Pressurised Water Reactor (PWR) simulated hydrogenated primary water, namely investigating the effect of additive microstructure, and surface finishing upon the corrosion resistance of the L-PBF alloy. Direct comparisons are made to standard wrought and annealed Ni-based superalloy in Generation III – IV build nuclear reactors in primary water to evaluate L-PBF IN625 corrosion performance, via qualitative (SEM with EDS), and quantitative analysis (specific weight change, FIB cross-sectioning, TEM, STEM EDS) of the external oxides formed, their cross-sections and morphology, and sub-scale surface damage. The effect of grain texture is highlighted, where a relationship between grain texture and oxide growth is established. This paper was drafted for submission to the Journal of Nuclear Materials (Elsevier).

Chapter 9 outlines the main conclusions drawn from this work, summarising the impact of the findings and future work needed to further establish standardised post-processing routes for the alloy and enhanced oxidation resistance.

Chapter 3

Aims and Objectives

The present work aims to investigate the effects of heat-treatment and surface modifications on the oxidation behaviour of Laser Powder Bed Fused Inconel 625, with the aim of furthering the development of post-processing of additively manufactured Ni-based superalloy for enhanced oxidation resistance in high temperature air and aqueous environments.

The objectives for this PhD project were set as follows:

- To characterise the oxidation behaviour of L-PBF IN625, exposed at 950˚C for prolonged periods of time (~1000 h).
- To investigate the effects of heat treatment and surface modifications applicable to AM complex geometries upon the oxidation resistance of L-PBF IN625.
- To characterise the mechanisms of oxidation and the extent of sub-surface elemental depletion with respect to time.
- Evaluate the influence Coincident Site Lattice (CSL) grain boundaries and grain texture on the oxidation behaviour of L-PBF IN625 in high temperature air.
- To characterise the corrosion behaviour of L-PBF IN625 exposed to simulated PWR primary hydrogenated water conditions for prolonged periods of time (~1500 h).

Chapter 4

Literature Review

The following chapter outlines the physical metallurgy of Ni-based superalloy IN625, discussing current manufacturing routes and the drawbacks of each. Additive Manufacturing (AM), particularly Laser Powder Bed Fusion (L-PBF) of IN625, is critically discussed, with a focus on literature exploring the effectiveness of standard ASM heat treatment upon as-built microstructure, as well as existing surface finishing technologies applicable to complex AM IN625 and Ni-based superalloy components. Studies investigating the effect of microstructure and surface finishing upon the isothermal oxidation and corrosion of L-PBF IN625 are critically examined in multiple environments, for comparison to standard wrought annealed IN625 and similar Cr containing Ni-based superalloys.

4.1 Inconel 625, High temperature materials and their application

Materials with the ability to maintain a combination of desirable chemical or mechanical properties at elevated temperatures are defined as high temperature materials. Often tolerant for a wide range of operational temperatures, pressures and mechanical load regimes, high temperature materials are applicable to a large number of industries with extreme environments as in aerospace, nuclear, marine and automotive applications. To remain versatile, such materials commonly exhibit a blend of several of the following characteristics [19, 42]:

- The ability to withstand mechanical loads at service temperatures close to the alloy melting temperature T_m;
- Resist the degradation of mechanical properties over long periods of time at elevated temperatures;
- The ability to resist and tolerate extreme operating conditions.

The Ni-based superalloy (e.g. Hastelloy, Inconel and Nimonic) family of alloys are a prime example high temperature materials, providing significant resistance to high temperature creep (used in the range of T = 540 − 1000˚C), fatigue, oxidation and stress corrosion cracking (SCC), see Figure 4.1 [19, 33, 42].

IN625 UNS N06625 is a chromia (Cr_2O_3) forming Ni-based superalloy, widely used in a variety of applications common to the coal, natural gas, aerospace, marine, petroleum and automotive industries for over the last 60 years, first introduced to meet demands for high strength steam line piping materials [21]. This versatility is by virtue of its combination of high temperature mechanical properties such as its high tensile strength (> 414 MPa, Grade 1), elongation (> 30%), fracture toughness, and excellent oxidation resistance for T ≤ 982˚C [18–21, 42, 51, 52]. As such, IN625 is the alloy of choice for manufacturing components in a diverse number of oxidising and reducing media, as well as mixed acid solutions including: sea-water, fuel exhausts, turbine environments (S, Na), and molten salts, making it a key alloy for the fabrication of heat exchangers, ammonium cracker tubes, and exhaust manifolds [2, 20, 22–28, 51, 53, 54]. More recently, IN625 has also been considered for the fabrication of solar receivers in concentrated solar power plants operating at high temperatures up to 1400 K (1126.85˚C), replacing the likes of stainless-steels due to their superior creep resistance, high solar absorptivity and total emissivity [6].

4.1.1 Inconel 625, Role in the nuclear industry

In particular, IN625 has an established history in the nuclear industry, where a number of high temperature aqueous environments with thermal cycling are commonplace. IN625 has been selected for the manufacturing of steam generator tubing, heat exchangers, among several other reactor-core and control-rod components in nuclear water reactors [29]. The superior pitting corrosion resistance of IN625 at the range of 260 − 316˚C, makes the alloy a perfect candidate alloy to resist the operational conditions of current generation Pressurised Water Reactors (PWRs), typically exposed to 300˚C hydrogenated alkaline primary water (pH = 7.1 − 10.2) at pressures of 15 − 20 MPa [55, 56].

It is a testament to the adaptability of IN625, that the alloy is also being considered for newer Generation IV advanced nuclear reactor concepts, including the likes of supercritical water-cooled reactors (SCWR). Where there is a drive for an increase in efficiency and

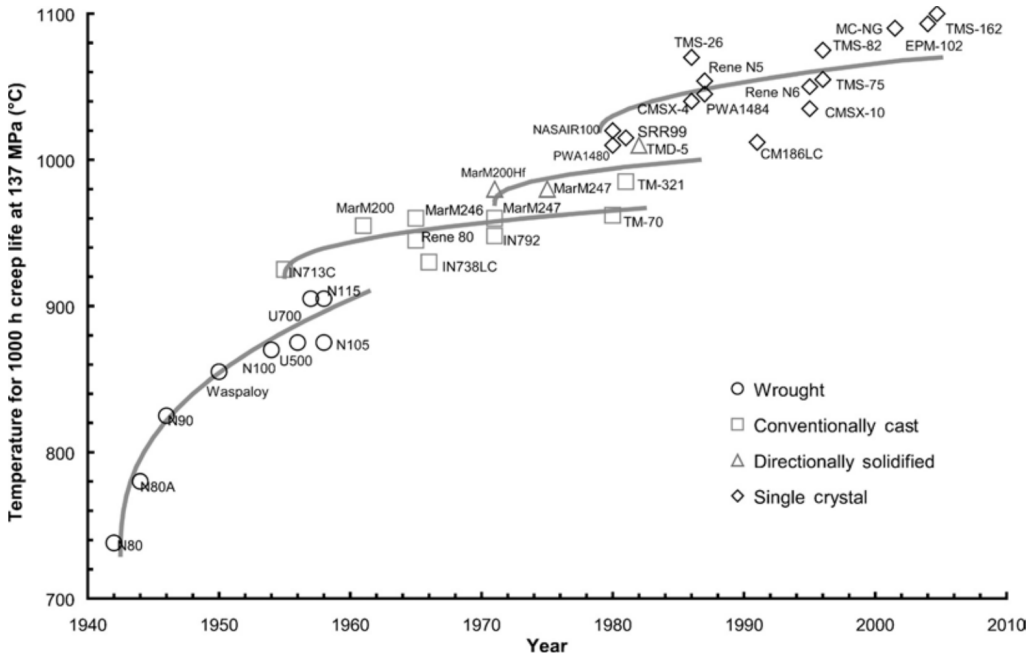


Figure 4.1: Overview of thermal capability of high temperature superalloys since their emergence. Taken from Reed (2006) [19].

TABLE 4.1
STANDARD HEAT TREATMENTS FOR IN625 - AMS2774E [61].

Heat Treatment	**Temperature (◦C)**	**Holding Time**
Stress Relieving	870 ˚C	1hr hold
Annealing	980˚C	1hr hold
Solution Treating	1150˚C	2hr hold

*Water quench applied to all immediately following removal from furnace.

plant simplification, higher operational temperatures are demanded, exposing core and cladding materials to super-heated steam and high CO_2 gases at T = 280 - 800˚C and P = 22.1 - 25.0 MPa, where previous ferritic-martensitic steels and austenitic stainless-steels fall short on their mechanical and corrosion resistance compared to Ni superalloys like IN625, IN617 and alloy 800 [23, 29, 57, 58]. This is also the case for other common advanced coal and gas supercritical designs with increased thermal operation temperatures for reduced emissions [59].

IN625 is also a key candidate in the design of vacuum systems required in the nuclear fusion industry. IN625's high temperature strength and creep resistance in hydrogen plasma environments is a key criteria for the design of toroidal reactors such as the COMPASS Tokamak, where temperatures vary between the range of 600 – 1600 K [60]

4.1.2 Traditional routes for manufacturing

In terms of its manufacturing, IN625 is a standard wrought alloy used commonly in its polycrystalline form, following the application of heat treatment, outlined in AMS2774 for wrought Nickel alloy and Cobalt alloy parts, see Table 4.1. The alloy is available in two ASTM grades: Grade I and II. Grade I describes wrought annealed material (annealed from T = 871 - 1038˚C), for lower in-service temperatures of 593˚C in aqueous and corrosive environments. Fine grain structures are therefore maintained in Grade I IN625 to provide high tensile strength via Hall-Petch Strengthening [42]. Grade II however, is applied in more severe operational environments (common to emerging Gen IV nuclear advanced reactor designs) where high temperature creep and corrosion resistance is a key requirement. To achieve this, Grade II is solution annealed at higher temperatures from T = 1093 - 1172˚C, providing a coarsening effect upon grains to limit thermal creep of the alloy [51, 61].

Due to the high temperature heat treatments applied to IN625, the chemical homogeneity found in wrought IN625 is an additional attractive property. Segregation effects of heavy elements such as Nb and Mo to interdendritic regions encountered with previous methods such as casting can be avoided completely [62]. In addition, compared to their cast alloy counterparts, wrought IN625 allows for greater control over the grain size, providing improved grain refinement for strengthening. Wrought alloys also tend to form smaller amounts (in size and density) of carbide and intermetallic precipitates compared to cast alloys [62].

Another key draw for the use of IN625 is its high weldability, due to the alloys high Ni content, where high alloying additions lead to an decrease in the ductility of the alloy [62]. Typically welded in its annealed form and degreased state, preheating is often not required and is only applied in the cases where material contains high residual stresses following manufacturing. Due to the high ductility of the alloy, during fusion welding, the Heat Affected Zone (HAZ) does not experience significant hardening, meaning that as a rule post-heat treatment is not always required to restore mechanical or corrosion resistance of the material [63].

4.2 Metallurgy of Ni-based superalloys, Inconel 625

The nominal chemical composition of IN625 is shown in Table 4.2, outlined by ASTM F3056-14E1 [64]. IN625 is a solid solution strengthened Ni-based superalloy with a face centred cubic crystal structure (FCC), drawing its strength from alloying elements such as Mo and Nb. Here Mo acts as a substitute for heavier elements such as W and Re [65]. In comparison to earlier iterations of cast Ni superalloys such as IN713LC, IN625 contains lower amounts of Al and Ti to improve weldability and minimise age-hardenability, without additions of Ta [21, 52]. The FCC crystal structure means the alloy exhibits high toughness alongside ductile properties [19]. The oxidation resistance of the alloy is derived from the high Cr content (up to 23 wt.%), which leads to the formation of a thick, self-healing chromia (Cr_2O_3) scale for temperatures up to 982˚C [18, 20, 62, 65–67]. Additions of Mo and Fe have also been found to increase the alloy's resistance to localized corrosion by pitting and Stress Corrosion Cracking (SCC), by virtue of their nobility [67, 68]. Mo in particular is considered a key alloying element in stainless steels for its resistance to pitting corrosion in chlorine containing solutions. This is by it's role in the formation Mo oxides, which changes the polarity of the passive film to cationic by the presence of negative MoO^{n-} ions. Subsequently, this leads to the promoted migration of oxygen anions, and the prevention of Cl ion ingress; aiding in the stability of the chromia passive film [69–72]. Mo also plays a role in the repassivation of the protective film by destabilising nucleating and growing metastable pits, via the formation of insoluble Mo/Cl complexes in the active sites [73–76].

Some variants of Ni-based superalloy can include the addition of reactive elements such as Y, Hf, Zr, Ce and La via Oxide Dispersion Strengthening (ODS) alloying. These have been shown to significantly improve the alloy oxidation properties, by reducing the oxidation rate, as well as the increased adhesion of the protective oxide scale via grain refinement and boundary pinning [65].

Table 4.2
Nominal chemical composition of AM IN625, ASTM F3056-14e1 [64].

Alloy		**Element ($\%_{wt}$)**												
		C	Mn	Si	P	S	Cr	Co	Mo	Nb	Ti	Al	Fe	Ni
IN625	Min	-	-	-	-	-	20.00	-	8.00	3.15	-	-	-	58.00
	Max	0.10	0.50	0.50	0.02	0.02	23.00	1.00	10.00	4.15	0.40	0.40	5.00	Bal.

Alongside grain refinement, superalloys like IN625 primarily source their high mechanical properties (i.e. high temperature creep resistance) through careful control of the microstructure and key strengthening phases and precipitates; a summary of which is outlined in Table 4.3. This is generally achieved via a specific selection of cast/wrought processing followed by the application of heat treatment to maintain thermal mechanical properties and oxidation resistance [62]. A key draw for the use of IN625 as a high temperature material is the high phase stability at temperatures from room temperature to the melting point of the alloy (T = 1375°C for γ' Ni_3Al) [19]. This is due to the stability of Ni in the FCC crystal structure, preventing any significant phase transformations during service or thermal cycling, leading to an undesirable degradation of the alloy's mechanical properties. An added advantage of FCC Ni-based superalloys is that diffusion rates for alloying elements here at high temperatures tend to be lower than competitor stainless-steels, meaning phase stability and oxidation resistance of the alloy is enhanced further [19].

4.2.1 Strengthening and key precipitates

The principal strengthening phase in IN625 is the Body Centred Tetragonal (BCT) γ'' (Ni_3Nb), promoted by the large alloying additions of Fe, Nb and Ti. This results in the formation of the ordered γ'' precipitate phase rather than γ' seen in other common Ni-based superalloys [19, 21]. The γ'' phase tends to be rich in elements such as Al and Ti, forming a precipitate phase stable for low to intermediate operational temperature [62]. To prevent coarsening during heat treatment or ageing, IN625 obtains strengthening via the pinning of grain boundaries from the precipitation of carbides from the liquid phase, predominantly by secondary M_6C, or additional intermetallic precipitation (δ-phase) [77]. The high temperature primary MC carbides tend to form more readily during processing of the alloy, containing reactive alloying elements present such as Ti [62, 78]. These experience a transformation during in-service conditions (750°C < T < 982°C) into secondary carbides, and $M_{23}C_6$, M_6C, respectively [78, 79]. In comparison to their primary form, secondary carbides tend to form at lower service ageing conditions preferentially upon interdendritic regions and grain boundaries rich in segregated Cr and Mo in the case of IN625 [19, 52, 78]. Despite draining the microstructure of Cr and other key alloying elements contributing to the oxidation resistance (Mo, Ti), the formation of carbides has

been seen as key in the improvement of the high temperature creep properties of the Ni-based superalloy, vital for its application in thermal cycling in-service conditions [19]. It is of utmost importance however to limit the coarsening of such carbides, in order to prevent the formation of stress concentrators and preferential failure sites which might degrade the fracture resistance of the alloy [62].

TABLE 4.3
SUMMARY OF PHASES AND PRECIPITATES IN IN625 [19, 52, 62, 80].

Phase	**Formula**	**Element(s)**	**Effect(s)**
γ'	Ni_3Al , Ni_3 (Al,Ti)	Al, Ni, Ti	FCC ordered, provides precipitation strengthening. Geometrically close packed phase (GCP).
		Nb, Ta	
γ''	Ni_3(Nb, Mo)	Fe, Nb	BCT ordered. Main strengthening phase in IN625 and IN718, resulting in high strength at T < 649˚C due to coherency with base γ'. GCP.
δ	Ni_3(Nb,Mo)	Nb, Mo	Orthorhombic δ. Found in over-aged IN625 and IN718 at temperatures between 815-980˚C. Produces loss in tensile and fatigue properties. Acicular morphology.
Laves	$(Ni,Cr,Fe)_2$(Nb,Ti,Mo, Si)	Fe, Co, Ti	Hexagonal, Topologically close-packed phase. Lowers mechanical properties.
	Co_2(Ta,Ti)	Nb, Mo, Ta	
η	Ni_3Ti	Ti	Hexagonal ordered phase (HCP) found in high Ti content Ni superalloys. Acicular platelet morphology. GCP.
MC	TiC, NbC, MoC	Nb, Mo, Ti,	Cubic. Globular morphology, providing strengthening by pinning grain boundaries. TiC has solubility for N.
		C	
$M_{23}C_6$	$Cr_{23}C_6$, $(Fe, W, Mo)_{23}C_6$	Mo, Cr, C	FCC. Film, globules, platelets, lamellae.
M_6C	Fe_3Mo_3C, Fe_3W_3C Fe_4W_2C, Fe_3Nb_3C	Mo, W, Cr Ni, Nb, Ta Co	FCC. Randomly distributed.
M_7C_3	Cr_7C_3	Cr, C	Hexagonal. Blocky shaped, common in alloys above 1000˚C (Nimonic 80A).
MN	TiN, (Ti, Nb)N	Ti, Nb, Zr, N	Cubic structure. Blocky, rectangular morphology.
	(Ti, Nb)(C, N), NbN		

*Table modified from Donachie et al. (2002) [62], Reed (2006) [19], Floreen *et al.* (1994) [52], and adapted from Lewis, 2020 [80].

Of significant concern in Ni superalloys strengthened by γ'' (Ni_3Nb) is its susceptibility of forming the brittle orthorhombic δ-phase during long term thermal cycling conditions below the annealing temperature (650˚C < T < 980˚C). Precipitation of this phase hardens the alloy due to its incoherency with the matrix phase [21]. Particularly, this is driven by elements such as Nb, Mo, Si and C, and their high tendency to segregate into the liquid phase upon solidification [19, 81].

The degradation of the alloy yield strength in-service is attributed primarily to the heavy precipitation of the δ-phase (Ni_3Nb), and the decoration of grain boundaries after service [27, 79]. For high temperature applications 840˚C < T < 950˚C, and in the absence of Fe content, platelets of the incoherent δ-phase have been reported to form in less than 24 h, meaning careful post processing via heat treatment is vital to prevent its formation in significant amounts [19, 62]. Nb content in the alloy can be controlled to limit the stabilization of the brittle δ-phase [52]. Mu *et al.* (2018) investigated the effect of varying Nb content (from the minimum content of 3.15 to 4.15 wt.% maximum) upon the tensile properties of IN625 cast alloy, used as a candidate for Advanced Ultra Supercritical Power Plants (U-SCWR) [59]. It was demonstrated that an increase in Nb content and ageing time significantly increases the levels of segregation of Nb to interdendritic regions, and hence the precipitation of the δ-phase along grain boundaries, and intragranularly at high temperature. This is due to the fact that higher levels of segregation allow for diffusion to defects such as vacancies, dislocations and stacking faults in the γ'' matrix, reducing the critical nucleus free energy for formation, and stabilizing the δ-phase DO_a phase structure [52, 59, 82, 83]. Despite the disadvantages of this phase in terms of decreasing the elongation of the alloy, the orthorhombic phase can however provide some amount of control over grain size to provide improvements in the tensile strength of the alloy [84].

Minor alloying elements present in Ni superalloys such as Si, P, S, Pb or Bi, sometimes referred to as Tramp Elements have been observed to lead to the degradation of mechanical and chemical properties, and to influence the likelihood of carbide precipitation on grain boundaries (in the case of Si and C) [52, 62]. This is mainly often due to poor raw materials, and poor control of the melting conditions of the raw material sourced [82]. Often segregating out to grain boundaries, or having high solubility in precipitates like carbides, high concentrations of these elements can embrittle the microstructure. There are

some advantages however, where elements like Mg can soak up S contaminants present in fuel exhaust environments to prevent formation of embrittling sulfocarbides (M_2SC), or Ti can take up nitrogen impurities in the alloy itself or introduced during processing [62, 85]. For example, Singh *et al.* (2013) observed the formation of $M_{23}C_6$ at grain boundaries at temperatures far lower than their usual formation (550˚C). This was attributed to the presence of TiN particles in the alloy, forming due to high N content. Nitrides precipitated consumed any Ti content that was required to form primary MC carbides, meaning that any remaining C led to the precipitation of the secondary $M_{23}C_6$, rather than from the degradation of MC primary carbide [82].

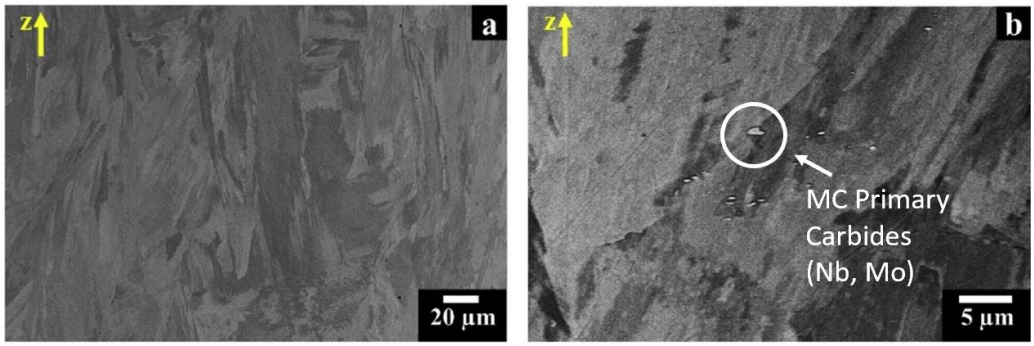
If formed in excess, heat treatments (see Table 4.1) can be applied to dissolve carbides and intermetallic formed, allowing for their redistribution throughout the microstructure [19, 52]. Carbides and intermetallics (such as δ-phase) formed upon grain boundaries can be partially dissolved when annealed at 980˚C, and dissolved entirely when solution heat treated at 1150˚C for 1 h of exposure. However, it is important to note that higher temperature treatments can lead to a degradation in the ductility, fracture toughness and corrosion resistance of the alloy via enhanced grain coarsening [48, 52, 86, 87]

Whilst post-process heat treatments are well understood for standard wrought and cast processed Ni-based superalloys; the same however, cannot be said for Additively Manufactured (AM) processed IN625, where non-equilibrium cooling and thermal gradients present lead to anisotropic microstructures.

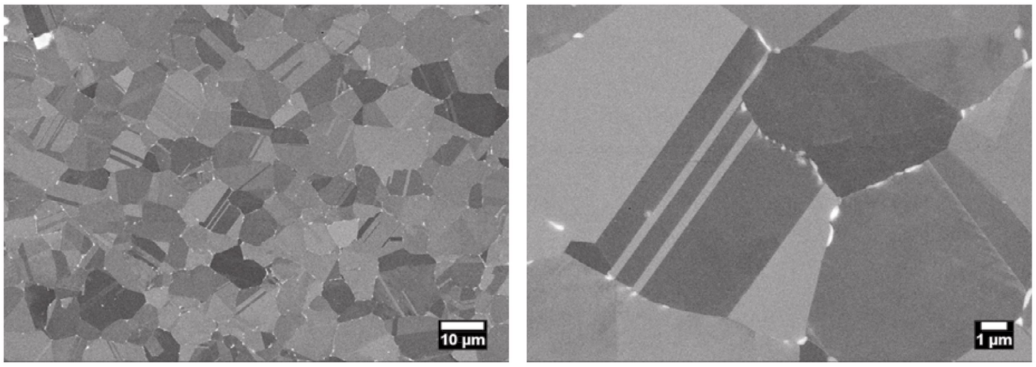
4.3 Laser Powder Bed Fusion of Inconel 625, Fundamentals and trends

Additive Manufacturing (AM) is a candidate processing route to allow for the manufacturing of highly intricate near-netshape geometry components with internal structures to high levels of dimensional accuracy, otherwise unobtainable with traditional subtractive methods.

One such method of AM is Laser Powder Bed Fusion (L-PBF), which will be the focus of this research work, which produces high density (>97%) complex near-netshape components without machining [33, 41, 88]. By firstly generating a 3D computer assisted design (CAD) model of the desired component, the part can be fused out layer-by-layer via a focused high power laser incident of a bed of metal powder. Following the selective scanning and melting of each layer, the build platform is lowered incrementally, allowing a recoater blade to cover the building plate with a fresh layer of powder to undergo melting of the subsequent layer of the part. This process is then repeated until the full part



(a) As-Built L-PBF IN625



(b) Wrought IN625

Figure 4.2: BSE-SEM micrographs depicting (a) the microstructure of L-PBF IN625, where Z = build direction. Taken from Marchese *et al.* (2020) [34]. (b) Wrought microstructure of IN625. Taken and adapted from Arnold *et al.*, (2017) [9].

is complete. This unique melting and solidification route leads to highly anisotropic microstructures compared to traditional manufacturing methods common to wrought and cast Ni superalloy.

A large number of studies have investigated the microstructure of L-PBF IN625 compared to wrought material [28, 34, 35, 38, 44, 47, 49, 89–94, 94]. Figure 4.2 shows the microstructure obtained in as-built L-PBF IN625 condition compared to wrought alloy. Fast solidification rates common to L-PBF (measured ~10^6 K/s compared to 1 - 1000 K/s in standard wrought and casting processing routes) produce fine dendritic microstructures, with columnar grains extending in the build direction [35, 47, 48, 95–98]. This is due to the epitaxy between the melted layers, and the temperature gradient present along the building direction, where heat is lost vertically when moving toward the substrate [33, 99]. The continuous nature of the process' localised heating and cooling cycles produces high tensile strength, dislocation densities, and residual stresses in as-built materials, often exceeding those found in wrought IN625 [33, 39, 44, 47, 94]. This is to detriment of ductility however, where tensile and fatigue properties are highly anisotropic as a result. Here stresses in as-built alloy tend to exist most prominently within the surface of the component [33, 34, 100].

4.3.1 Microsegregation in L-PBF Inconel 625

The aforementioned segregational effects of heavier elements in wrought materials are also exacerbated by the fast cooling and solidification rates encountered in L-PBF, resulting in strong chemical inhomogeneity and compositional gradients in the melt pool compared to wrought alloy. This leads to severe levels of enrichment (9 – 11 wt.%) in Nb and Mo at interdendritic regions upon the cooling of each fused layer of powder; over 2 times higher than the ASTM bulk powder composition [38, 48]. Microsegregation describes the partition of elements during solidification due to differences in their solubility in the liquid and solid phases formed at equilibrium during dendritic growth [28, 35, 38, 42, 44, 83, 101]. Here the inner core of the solidified dendrite will have a chemical composition different from the outside, due to the rejection of heavier solute.

For IN625 in particular, heavy elements like Nb and Mo are rejected into the liquid phase, congregating in interdendritic regions, see Figure 4.3 [34, 38, 47, 101, 102]. This leads to the enhanced precipitation of Nb and Mo rich MC primary carbides and the brittle

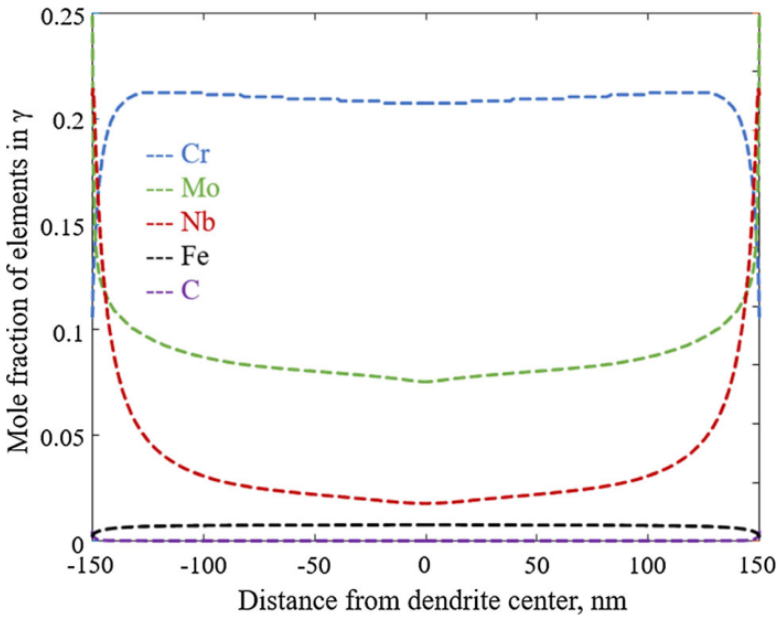


Figure 4.3: Compositional profiles in γ-matrix of L-PBF IN625, as predicted by DICTRA as a function of distance from the secondary dendrite core. Taken and adapted from Lindwall *et al.* (2019) [47].

Ni_3(Nb, Mo) δ-phase upon grain boundaries and inside grains following heat treatment, as well as some unexpected phases upon solidification due to the non-equilibrium compositions present (See Figure 4.2 (a)) [33, 34, 48, 98]. Nb segregation to grain boundaries has been shown to lead to environmentally enhanced crack growth (EECG) in Ni-based superalloys such as IN718. Miller *et al.* (2001) studied the effects of intergranular embrittlement of IN718 via precipitation of NbC and δ-phase at grain boundaries, confirmed via XPS. When placed under isothermal oxidative conditions, the δ-phase was found to oxidise preferentially to form a brittle Nb_2O_5 film ahead of the crack tip, increasing the surface concentration of Nb in this region; and increased rates of crack propagation [103].

Heat treatments are thus necessary to relieve the significant residual stresses (up to 575 MPa) and microsegregation inherent to AM, and to achieve the desired grain size and microstructure [34, 38, 83, 88, 98, 100, 104]. Whilst vital, these post-heat treatments add steps to the manufacturing process, adding to costs and reducing the advantages of the so-called near-netshape manufacturing [33].

4.3.2 Post-processing L-PBF Inconel 625, Heat treatments

Table 4.4 shows an overview of all current heat treatments applied to L-PBF IN625 in literature, and the phases and intermetallic encountered. Table 4.5 shows a set of key selected heat treatments and their outcomes [34, 38, 83, 89, 105].

Attention must be brought to the fact that different forms of carbide formed across the literature have been observed in L-PBF IN625, driven most likely due to a difference in the heat treatments applied (parameters such as the heating zone, ramp rates and cooling rates), as well as variations in the powder composition [34, 43, 106]. For example, morphology and powder particle size distribution can have an effect on the L-PBF process, where smaller particle sizes can promote improved mechanical properties and surface finish [43, 106]. AM process parameters (volumetric density (J/mm^3, power (W) (see Equation (4.1)), scan speed (mm/s), hatch spacing (µm), layer thickness (µm) (typically 10 - 50 µm), contour (°), laser spot size (µm), laser modes e.g. continuous wave, modulated melting) will also vary depending on the equipment and desired geometry, resulting in a host of different defects, surface morphology and microstructural differences [88, 93, 107–110].

Carter *et al.* investigated the 2D energy density parameter validity for various Ni-based superalloys by way of a parametric study (absence of layer thickness in Equation (4.1)) [111]:

$$\text{Volumetric Energy Density (J/mm}^3\text{)} = \frac{\text{Laser Power (W)}}{\text{Scan Speed (mm/s)} \times \text{Hatch (µm)} \times \text{Layer Thickness (µm)}} \tag{4.1}$$

It was observed that typically for Ni-based superalloys, there is a minimum threshold of 85 J/mm^3 before which parts are not considered to be fully dense, though this does not always fully illustrate the full outcome, where cracking density can become increased [110, 111]. Li *et al.* (2017) also studied the interfacial characteristics between the deposited material and the substrate with L-PBF IN625, where it was demonstrated that laser power predominantly controls primary cell spacing, as well as defect formation (un-melted powder and porosity) [88, 93, 98, 110]. The formation of process maps from design of experiments are key for the full optimization of any additively manufactured part [88, 110].

TABLE 4.4
SUMMARY OF HEAT TREATMENTS IN LITERATURE FOR L-PBF IN625, AND THE REPORTED PHASES AND PRECIPITATES OBSERVED.

Condition	Heat Treatment(s)	Phases/Precipitates	Lattice Parameter (Å)	Reference
As-built	–	γ, γ'', δ, (Nb, Ti, Mo)C $Cr_{23}C_6$, $(Ni, Cr, Fe)_2(Ni, Ti, Mo)$	3.597	[28, 35, 36, 44, 91, 104, 112–116]
Stress relief	870˚C 1 – 8 h	δ, (Nb, Mo)C, $(Nb, Mo, Si)_6C$	3.602	[28, 34, 35, 38, 44, 83, 89–91, 99, 104, 117]
Anneal	700 – 1100˚C 1 – 8 h	δ, (Nb, Mo)C, $(Nb, Mo, Si)_6C$	–	[34, 35, 44, 89, 91, 92, 99, 104, 114, 116, 118]
Solution	1040 – 1200˚C 1/4 – 2 h	γ'', δ, (Nb, Ti, Mo)C $(Nb, Mo, Si)_6C$	3.609	[12, 28, 34, 44, 83, 89–92, 99, 104, 114, 116, 117, 119]
Solution + Age	1120˚C, 760˚C 1 – 24 h	γ'', (Nb, Ti)C, $(Nb, Mo, Si)_6C$ $Cr_{23}C_6$	–	[44, 89]
Direct Age	600 – 720 ˚C, 760˚C 18 – 100 h	γ''	–	[12, 44, 118]
HIP	1120 – 1240˚C 1 – 4 h, 100 – 165 MPa	$(Ni, Cr, Fe)_2(Ni, Ti, Mo)$ $NiCr_2$, (Ni,Mo)Nb, Nb_5Ni	–	[91, 104, 112, 113, 117]

TABLE 4.5
SELECTED KEY HEAT TREATMENTS IN LITERATURE FOR L-PBF IN625.

Author	Heat Treatment(s)	Phases/Precipitates	Ref.
Li *et al.* (2017)	As-built	γ, γ''	[28]
Marchese *et al.* (2018)	As-built Aging 700˚C, 24 hrs Solution HT 1150˚C, 2hrs Aging + Solution	MC (Nb, Mo-rich) γ'', MC (Nb rich),$M_{23}C_6$ MC (Nb, Ti-rich) γ'', MC (Nb, Ti), $M_{23}C_6$ (Cr)	[44]
Lass *et al.* (2018)	Anneal 800˚C, 1-4 hrs Anneal 870˚C, 1 hrs	γ'', δ	[83]
Zhang *et al.* (2018)	Stress relief 870˚C, 8 hrs Solution 1150˚C, 1 hrs	δ, MC (Nb, Mo-rich) MC (Nb,Mo-rich)	[38]
Inaekyan *et al.* (2019)	Stress relief 870˚C, 1 hrs Anneal 980˚C, 1 hrs Solution 1120˚C, 1hrs	δ, M_6C M_6C (Nb,Mo,Si-rich) MC (Nb, Mo-rich), M_6C	[89]

Taken and adapted from Lewis (2020) [80].

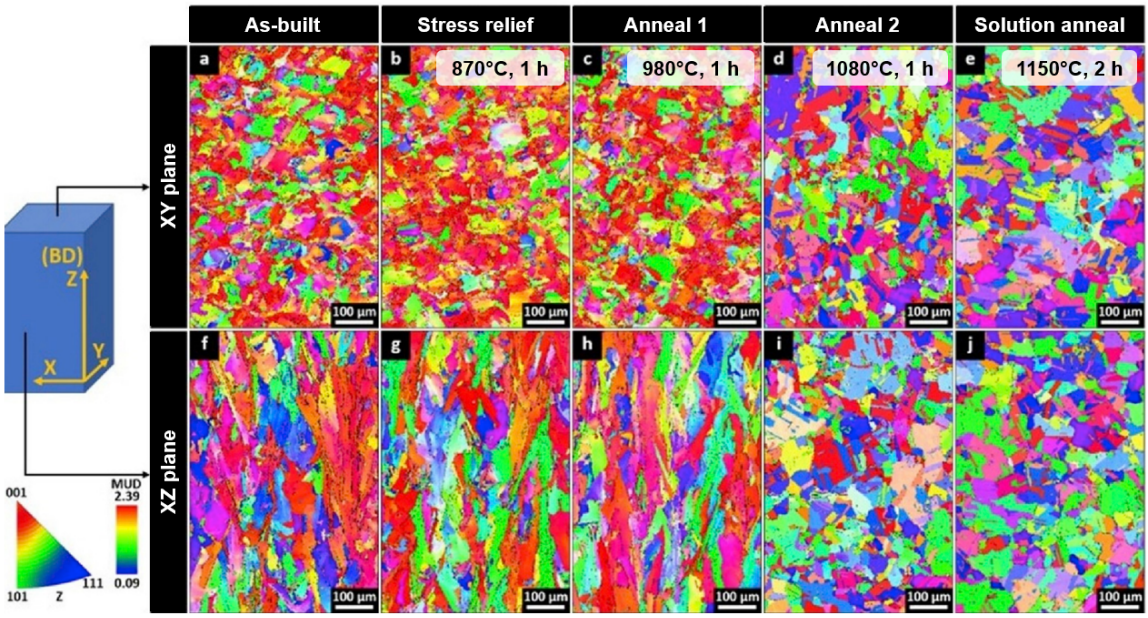


Figure 4.4: Summary of EBSD IPF maps showing the microstructures obtained following standard heat treatment of L-PBF IN625. IPF maps (c,d) show partial recrystallisation of the AM anisotropic microstructure in (a), which can be seen to be fully recrystallised in (e). Taken and adapted from Marchese *et al.* (2020) [34].

In particular for AM, a stress relieving treatment is key prior to the sample's removal from the building plate, without leading to significant changes in the microstructure (see Figure 4.4) [34, 47]. A pre-heated substrate may also be applied during building to reduce the residual stresses induced through control of the temperature gradient generated between the melt pool and base plate (up to ~90˚C) [110, 120, 121]. It is important to note that heat treatments applied to L-PBF IN625 are

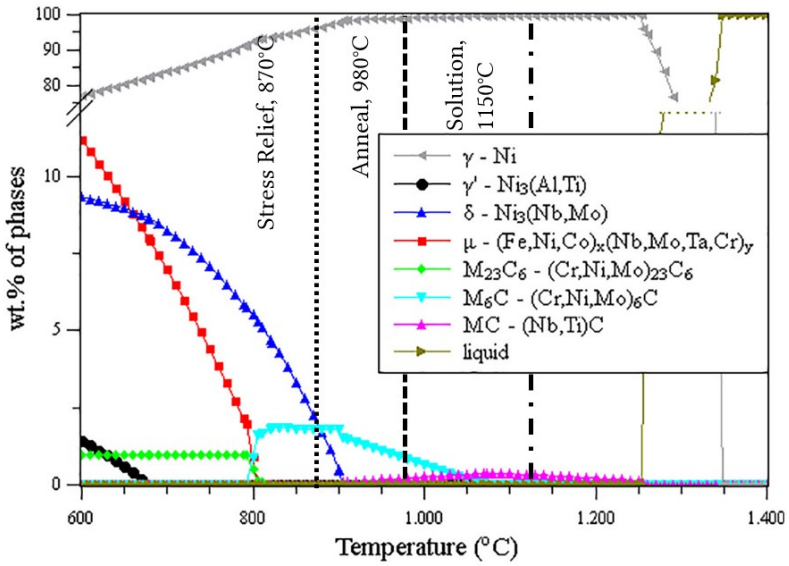


Figure 4.5: Simulation of the phases (wt.%) in IN625 as a function of temperature, with standard stress relief (870˚C), anneal (980˚C) and solution heat treatments (1150˚C) overlaid [122]. Note, stress relieving treatments at 870˚C result in the formation of δ-phase. Taken and adapted from Mariano de Sousa Malafaia *et al.* (2020) [11].

designed for wrought microstructures, based upon their nominal powder compositions and their equilibrium phase diagrams and kinetics (see Table 4.1). This means that there is some debate upon whether or not the treatments are suitable for achieving the desired outcomes required for use in industry [48, 61]. Annealing and solution treatments however are applied to induce recrystallisation with reduced grain growth, or to promote more prominent recrystallisation and grain growth to enhance creep resistance, respectively (see Figure 4.4) [34]. Figure 4.4 shows a series of EBSD IPF maps, showing the resultant microstructure obtained following the application of standard heat treatments to L-PBF IN625, taken and adapted from Marchese *et al.* (2020) [34]. For comparison, Figure 4.5 shows a summary of the phases (in weight %) expected to form in IN625 as a function of exposure temperature, calculated using the JMatPro modelling software, taken from Mariano de Sousa Malafaia *et al.* (2020) [11]. This shows that in terms of thermodynamics (and not including the effects of the kinetics of phase transformation), above 1000˚C, the brittle δ-phase should not be stable, with a decrease presence of MC and M_6C carbides.

As of yet it is unclear as to which of the industry recommended heat treatments provide the optimum mechanical and oxidation properties for highly segregated AM alloys like IN625. This is evident following research by Lass and Stoudt at the National Institute of Standards and Technology (NIST). USA, who observed that microsegregation lead to the enhanced precipitation kinetics of $D0_a$ orthorhombic δ-phase and intermetallic in significantly shorter time periods than in wrought IN625 following heat treatment [35, 48]. Indeed, Lindwall *et al.*, produced a Time-Temperature-Transformation (TTT) diagram comparing AM IN625 to wrought material

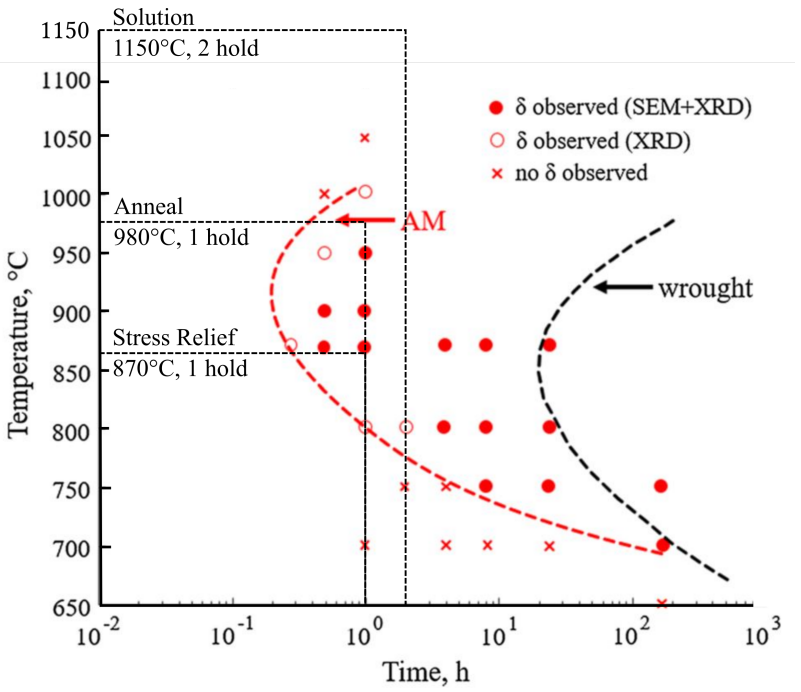


Figure 4.6: Time-Temperature-Transformation (TTT) diagram showing δ-phase (Ni_3Nb) volume fraction change in L-PBF material (red line) and wrought IN625 (thick black line). Standard heat treatments for IN625 are overlaid. Taken and annotated from Lindwall *et al.* (2019), and Floreen *et al.* (1994) [47, 52].

(see Figure 4.6), showing the accelerated growth kinetics of the brittle δ-phase (Ni_3(Nb,Mo)) using thermodynamic simulation with DICTRA [47]. This was attributed almost exclusively to the microsegregation of Nb and Mo, where is it expected that high dislocation density and vacancy concentration (also present in rapidly solidified melt spun IN625) in AM material may also contribute to the accelerated precipitation kinetics present [47, 123]. This correlates strongly to research by Suave *et al.* who observed accelerated precipitation kinetics of δ-phase following the introduction of strain energy due to applied mechanical deformation in wrought IN625 [124].

In AM IN625, stress relieving treatments (at 870˚C) have been observed to lead to the initial dissolution of the dendritic microstructure, to produce significant amounts of δ-phase, as well as leading to the precipitation of carbides enriched in Nb and Mo (see Figure 4.5) [11, 38, 89]. Additional work by Zhang *et al.* reported that δ-phase could form in t<5 minutes when undergoing stress relief compared to 10s of hours in traditional wrought materials; indicating a low nucleation barrier associated with the high dislocation density present in AM alloy [38, 48]. For instance, Floreen *et al.* determined that the δ-phase would take up to 20 hours to precipitate in wrought annealed IN625, further demonstrating the degree of enhanced kinetics [52]. Platelets of δ-phase at 870˚C have also been observed to begin to coarsen after a period of 0.5 h inside interdendritic regions preferentially, noticeably increasing in size following 4 h of exposure (see Figure 4.7) [38, 48].

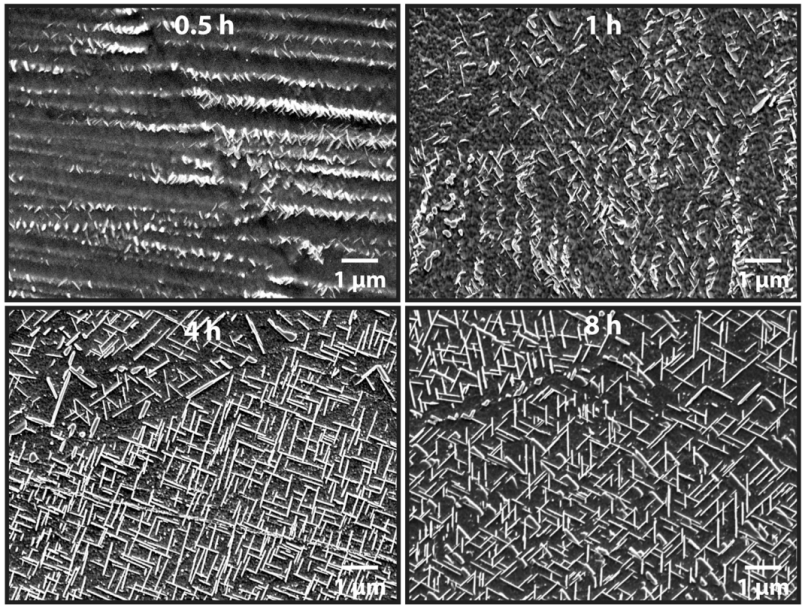


Figure 4.7: BSE-SEM micrographs showing the enhanced precipitation of δ-phase in L-PBF IN625 following stress relieving at 870˚C after (a) 0.5 h, (b) 1 h, (c) 4 h, (d) 8 h. Taken from Zhang *et al.* (2018) [38].

It can be viewed in Figure 4.4 that below 1000˚C, heat treatments such as stress relief or anneals are unable to fully recrystallise grains, further demonstrating the thermal stability of IN625 [34, 121]. Annealing heat treatments are successful in bringing about the partial homogenisation and dissolution of sub-micron carbides present, although this is yet insufficient to remove all of this entirely. Solution heat treatments at 1150˚C are hence deemed most effective in dissolving δ-phase and precipitates, producing fully homogenized and equiaxed microstructures similar to wrought IN625. This has been determined both experimentally, see Figure 4.8, and using diffusion simulations [38, 44, 83, 89, 116, 121, 125]. Solutionising treatments have also been shown to be successful in the removal of residual stresses in the build [28, 104]. However, in literature it has observed that solution heat treatments are not always sufficient for the full solution redistribution of microsegregated elements in the as-built L-PBF IN625 microstructure. Models using DICTRA by Lindwall *et al.* (Figure 4.9) for the maximum composition of Nb in IN625 (4.15 wt.%) determined that even at T = 950 – 1000˚C the δ-phase can remain stable [47]. In fact, with further enrichment due to microsegregation, the stability of δ-phase increases with temperature up to this threshold, where it has been accepted that larger degrees of segregation lead to faster formation of the brittle phase, as shown in Figure 4.9 for various distances from the theoretical interdendritic region centre (10 - 30 nm). Recent studies using Selected Area Electron Diffraction (SAED) and Scanning Transmission Electron Microscopy (STEM-EDS) in the γ-matrix of solutionised IN625 have also observed that even following treatment the intercellular boundaries present remained enriched in Nb and Mo and depleted in Ni, Cr and Fe; increasing the nucleation driving force for δ and Nb

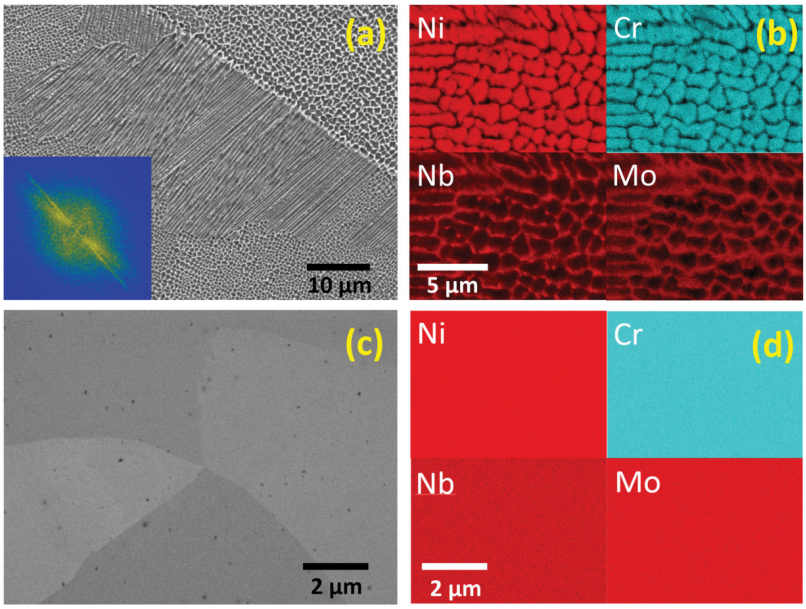


Figure 4.8: (a) SE-SEM micrograph, with inset image (left-hand corner) showing the Fourier transform of the SE-SEM micrograph, (b) shows the corresponding EDS maps of (a) as-built IN625 at higher magnification (Ni, Cr, Nb and Mo). (c) SE-SEM micrograph, and (d) corresponding EDS maps (Ni, Cr, Nb and Mo) of 1150℃, 1 h heat-treated L-PBF IN625. Taken from Zhang *et al.* (2017) [116].

and Mo containing secondary carbides (see Figure 4.8) [126].

Studies have investigated the effects of high temperature ageing to remove microsegregation to varying levels of success [12, 34, 44, 59, 79, 91, 104, 109, 127, 128]. The successful redistribution of the solute appears to be highly dependent on the minor alloying elements present in the powders used. Building upon previous research by Khayat and Palmer (2018) [129], Zuback *et al.* (2019) investigated the effects of Fe and minor Si and Ti content within the allowable ASTM standard ranges (Fe: < 5.0 wt.%, Si: < 0.5 wt.%, Ti: < 0.4 wt.%), finding that small variations influenced the resultant grain size and in turn the precipitation, and mechanical properties of the alloy. High Fe and Ti content (Fe: up to 4.0 wt.%, Ti: 0.19 wt.%, Si: 0.0035 wt.%) was revealed to produce MN nitrides enriched in Ti and Nb, which are not commonly encountered in the wrought material, see Figure 4.10 [52, 130]. Microsegregation of Nb, and the higher Ti content is thought to have enhanced the precipitation of these nitrides in the liquid phase before solidification. On the other hand, in the sample set with low Fe content (Fe: 1 wt.%, Ti: 0.019 wt.%, Si: 0.37 wt.%), laves phase was produced during solidification, promoted by the higher Si content here. Thermodynamic simulations determined a limit for Si content before Laves precipitation could be observed, showing that an excess of 0.05 wt.% was required. Ageing HIP heat treatment at 1163˚C, 101 MPa for 4 h were applied to remove the aforementioned anisotropy. This was unsuccessful in the dissolution of precipitates in the high Fe content samples, where the MN became more enriched in Ti, and depleted in Nb. Laves phase in the low Fe content IN625 however was found to experience

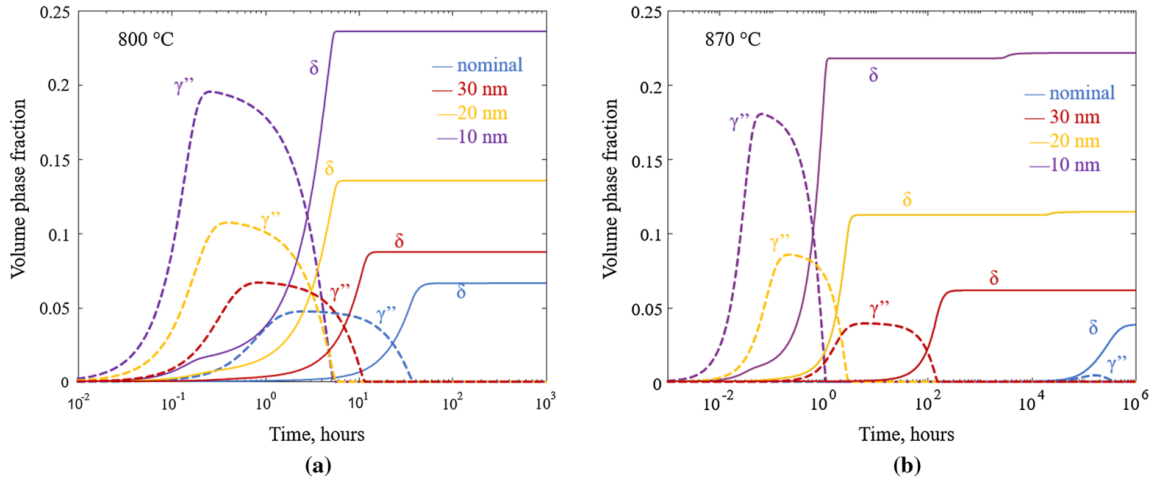


Figure 4.9: TC-PRISMA calculated volume phase fraction of δ-phase at stress relief temperatures from (a) 800˚C to (b) 870˚C, for the nominal composition of L-PBF IN625. Note the accelerated kinetics with temperature. Taken from Lindwall *et al.*, (2019) [47].

a change in morphology into a set of blocky precipitates, with partial transformations into (Nb, Cr, Mo)$_2$N [130]. This study in particular highlights the importance of understanding the effects of minor alloying elements following the unique solidification routes experienced in AM and its post-processing.

The unique cooling and heating cycles also tend to lead to strong textures along the build direction following solidification (<001> direction, commonly shown by the red colouring in an EBSD IPF map, see (a), (b) and (c) Figure 4.4) [17, 34, 98]. This is strongly dependent on the direction of heat input i.e. the laser and build height, leading to grain growth along the thermal gradient resultant of the process [98]. As-built IN625 tends to show a very low fraction of High Angle Grain Boundaries (HAGBs, defined as $\theta > 10^{\circ}$), dominated predominantly with Low Angle Grain Boundaries (LAGBs, defined as $\theta < 10^{\circ}$), as a consequence of the cellular microstructure and high dislocation density (around 80% majority). The selection of printing parameters can directly influence this via grain refinement and the grain boundary density. Huang *et al.* (2022) found that an increase in the applied scan speed from 750 – 900 mm/s lead to an increase in the Coincident Site Lattice (CSL) fraction (e.g. twin boundaries) by increasing the solidification rate during the fusion of metal powders to give and average grain size of <15 µm [17, 98].

Heat treatments are able to remove this preferential aligned texture, where the application of higher temperatures common to anneal and solution treatments result in a partial to fully recrystallised microstructure with a random texture throughout, as well as an increase in the fraction of HAGBs up to a reported 58.5% (see Figure 4.4) [34, 90, 104, 112, 131]. Texture can have strong influence upon the mechanical properties of the as-built alloy, where higher tensile strengths and poor ductility were observed along the XY orientation than samples in the XZ plane, as reported

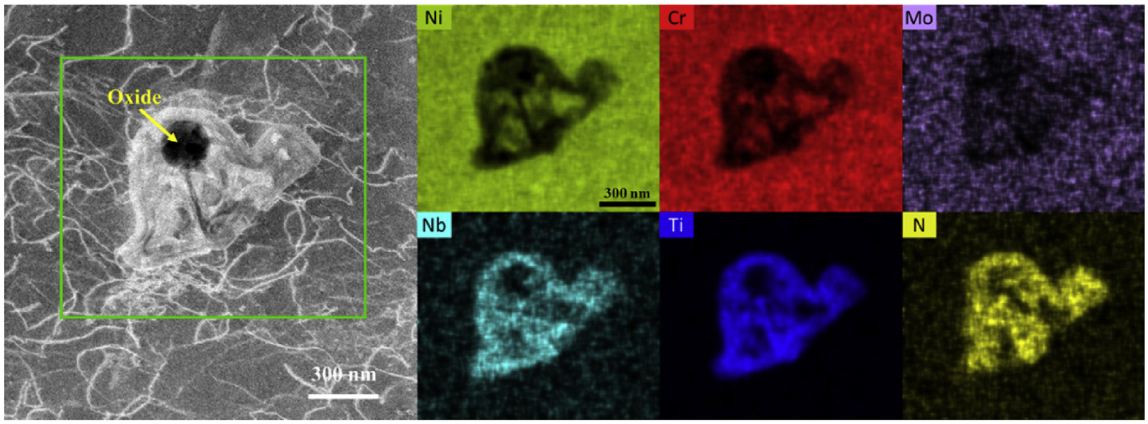


Figure 4.10: HAADF-STEM micrograph and corresponding EDS maps showing a (Ti,Nb)-rich MN precipitate in as-built IN625, manufactured using powders with high Fe content (4 wt.%). Taken from Zuback *et al.* (2019) [130].

by Marchese *et al.* (2020). These effects were removed following the application of heat treatment to promote a more random texture [33, 34, 90].

As outlined by Stoudt *et al.* (2018), it is hence of the utmost importance the effects of post-process heat treatment are fully understood as pertaining to AM Ni-based superalloy components, not only in terms of precipitation but also texturally. This is especially important given the growing focus on recycling and reusing metal powders in manufacturing. Variations in powder composition, not only in terms of Nb and Mo content but also in minor alloying elements like Si, N, and C, can significantly impact the formation of non-equilibrium phases at higher temperatures. Whilst it is unclear what the effect we will be upon the mechanical properties of the alloy, further work is also required to elucidate the effects of minor compositional differences and precipitate formation upon the oxidation and corrosion resistance of the alloy.

4.3.3 Post-processing L-PBF Inconel 625, Surface finishing

As well as anisotropic microstructure, a key difference, and indeed drawback, encountered with Laser Powder Bed Fusion and other related AM processes is the high surface roughness (R_a > 30 µm) often deemed insufficient for use in-service [88, 132, 133]. Poor surface finish is primarily driven by the large temperature gradient present in AM and the motion of the input laser heat source, causing a rippling effect by surface tension shear forces in the melt pool. Full relaxation of the pool is prevented by high viscous forces of the molten metal and high solidification rates [132]. This can be worsened in AM due to non-optimal design, powder feed stock and process parameter selection (e.g. laser power, scan speed, and layering giving insufficient energy density leading to balling of the powders), the chamber leaking argon gas, or low quality feed stock (low packing density, oxygen contamination) [33, 110, 120, 134]. These are detrimental to the mechanical prop-

erties of the alloy in terms of the fracture toughness and fatigue life, but also oxidation resistance by increasing the surface area for oxidative attack through the presence of partially/un-melted powder particles [66, 100, 110, 134–136]. Surface finishing and polishing is therefore an essential requirement for AM components application in-service to reduce dimensional inaccuracies, poor fatigue and oxidative performance and surface quality in terms of aesthetics [110]. This can be particularly difficult for intricate geometry parts with complex internal surfaces. The techniques that follow can be applied with various different pros and cons to their use.

Several studies have been conducted to investigate the best current methods available and the optimization of these applicable to AM components in an industrial setting. So far, for this study the candidate methods include the following: Chemical, electrochemical etching, milling, abrasive flow machining, magnetic abrasive polishing, vibrational mass-finishing, and laser shock peening [13, 133, 134, 137]. For the purpose of this study, AM surfaces prior to finishing, simple metallographical grinding and polishing, electropolishing, shot peening, and Centrifugal High Energy Finishing (CHEF) will be outlined and discussed.

4.3.3.1 Laser parameters and polishing

Standard polishing, machining or milling of AM parts are known to produce high mirror-like surface finishes (as low as ~0.25 μm), and improved oxidation and corrosion properties [134]. These can however contribute to generation of tensile residual stresses from the grinding or machining process, leading to poorer fatigue life, increased defect population, and porosity in the surface [42, 100, 110, 134, 136]. Components common to AM with complex shapes prove difficult to polish using traditional softening and smearing of surface layers, where it is often impossible for the necessary tooling to reach crevices or internal channels present [42, 134].

Various studies have investigated the effect of process parameters upon final part surface finish with L-PBF IN625, and other alloys manufactured using L-PBF [16, 88, 100, 132, 133, 136, 137]. Findings by Mumtaz and Hopkinson determined that in order to lower top and side surface roughness, low speed scans with high laser powder were required, alongside a small hatch spacing to ensure complete melting of the feed stock powders [88, 110, 132]. This was by way of increasing the wettability of the melt pool, therefore reducing balling effects in the powder, yielding final surface roughness values of 9 – 10 μm [132]. Different laser modes may also promote high surface finish, particularly via laser pulsing modes, by continuously remelting the melt pool and stabilizing it [138]. Mumtaz and Hopkinson further observed that short pulsing times and increased remelting rates lead to higher degrees of surface integrity (low R_a) through the generation of a lower volume of molten metal during melting [132]. More recently Balbaa *et al.* achieved average R_a values of

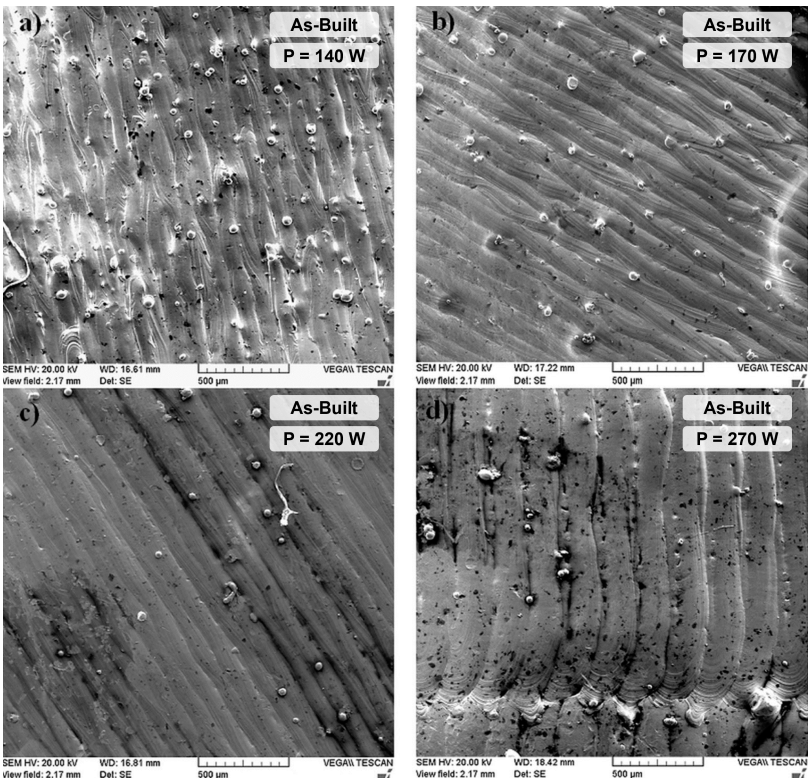


Figure 4.11: SE-SEM micrographs showing the surface profiles of L-PBF IN625 fabricated with the following parameters: 600 mm/s, 1 mm hatch spacing, (a) 140 W, (b) 170 W, (c) 220 W, (d) 270 W. Taken and adapted from Balbaa *et al.* (2019) [88].

>5µm, by careful control of scan speed and power (increasing from 170 to 270 W), leading to an increase in the diameter of the melt pool, see Figure 4.11 [88]. When measuring residual stresses however, it was found that there was no specific relationship between the printing parameters, with the exception that residual stresses were mainly located at the surface of the component, ranging from 1 – 575 MPa depending on the process parameters applied [88].

Whilst improvement is possible by simple design of experiments and careful selection of parameters, the results achieved are limited to the quality of the powders used, the control of the vacuum environment, etc. [139].

4.3.3.2 Electropolishing

Electrolytic polishing, or electropolishing (often referred to as electrochemical etching) involves the removal of particles on the surface of a component via the application of an electrical circuit; without imparting or relieving stresses inherent to the manufacturing process [134, 140]. Here, following the necessary pre-cleaning / masking steps, the sample is submerged in a specific electrolyte and attached to a DC power supply (using voltages 20 – 70 V, current densities ~50 A/dm^2) [42, 134, 141]. The specimen (M) acts as the anode, allowing positive surface ions (M+) to be repelled, and attracted towards a sacrificial negatively charged cathode. The electrolyte applied (e.g.

perchloric acid and methanol, perchloric-acetic acid) selectively attacks and dissolves active asperities and raised projections on the surface of the fabricated part (e.g. partially/un-melted powder particles and scan tracks), to produce a low R_a smooth surface (~ 8 – 0.8 µm) [17, 42, 134, 140, 142]. Upon removal, the polished part is neutralised and rinsed to ensure the end of the reaction.

The effectiveness of the process is controlled by several parameters: the size of the component, the applied voltage, the duration of time polished, the distance between the anode and cathode, as well as the concentration of the electrolyte/acid solution used [134, 143]. Here the aim is to reach a high efficiency of electropolishing (i.e. a maximum rate of reduction) whilst maintaining a minimum thickness loss [133].

Traditional methods as well as novel methods of electrochemical polishing as a means for the post-processing of AM components has been extensively investigated for L-PBF IN625, IN718 and other AM Ni-based superalloys for multiple geometries, reaching submicron surface finishes up to 0.25 µm [133, 139, 141, 144–146]. Ali *et al.* studied the application of electropolishing upon the internal roughness of L-PBF IN625 with various different geometries for different times with high degrees of success, aiming for maximum surface roughness reduction, and minimum thickness loss [133]. Results obtained using surface profiling (by confocal microscopy) showed an average 80% decrease in surface roughness R_a, with a thickness reduction of 8.5%, with reduced surface variability, see Figure 4.12. Here roughness reduction increased with longer duration periods of

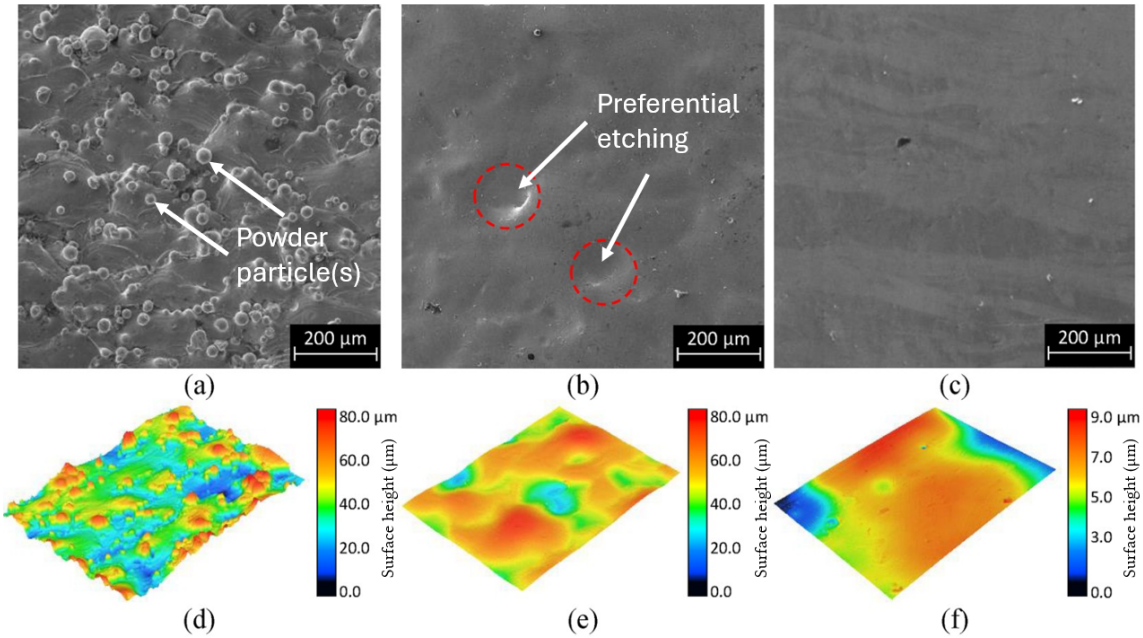


Figure 4.12: SE-SEM micrographs and confocal microscope surface profiles of the external surfaces of L-PBF IN625 following electropolishing at 30 V, in a 4:1 ratio of sulfuric acid to methanol solution, room temperature. (a)-(f) As-built IN625, (b)-(e) 120 s, (c)-(f) 240 s. Taken from Ali *et al.* (2020) [133].

immersion, S_a values of 0.91 μm were achieved after 240 s of immersion, producing smoother profiles with homogenised surface variability, without altering the chemical composition of the bulk. Similar results were obtained by Urlea and Brailovski with L-PBF manufactured Ti-6Al-4V with internal surfaces, giving R_a values of 1 – 3 μm with uniform roughness across the specimens [140].

The key draw for electropolishing is the ability to polish internal surfaces (e.g. threads, undercuts or hanging edges) otherwise inaccessible with methods requiring a nozzle, without inducing residual stresses in the component and affecting the bulk properties of the part (e.g. machining, shot peening) [141]. In particular, the ability to finish sides on AM parts which often exhibit higher R_a values than flat surfaces present makes electrochemical finishing techniques attractive for AM component post-processing. Jiang *et al.* studied both flat surface and angled L-PBF tubes of IN718, showing an average 80% improvement in the surface roughness R_a after the electropolishing process [42, 132, 133, 139]. Such improvements in roughness can be achieved in times less than 10 minutes [133, 141].

However, electropolishing can be a challenge where Ni-based superalloys are concerned, due to their characteristic corrosion resistance (via high wt.% Mo alloying) at high temperatures and aqueous environments [73, 143]. Any pitting corrosion or sub-surface porosity as a result of electrolytic anodic dissolution have also been predicted to affect the roughness, future wear, fatigue and cracking mechanisms of the component in question, by providing stress concentrators and crack sites [134]. Precipitates with non-conductive properties, such as Nb-rich MC carbides, $M_{23}C_6$ and Laves have also been reported to reduce the quality of the surface finish following electropolishing with AM Ni-based superalloys, where often the surrounding γ-γ' matrix is etched preferentially [141, 145]

Attention must also be drawn to the fact that electropolishing requires the use of highly hazardous strong acid solutions (e.g. sulfuric acid, hydrochloric, perchloric acids, etc.), often applied at high temperatures up to 80°C to dissolve the metal surfaces [134, 139, 143, 145, 147]. Care must be taken to avoid the low boiling points of these acids and to avoid spillage. Correct storage and ventilation are key, where hazardous fumes and gases, as well as waste are byproducts of their use. These are generally difficult to dispose of making lean and green manufacturing processes complicated and hard to achieve [134]. Work is being done to tackle this issue, where it is thought that ionic electrolytes (ethylene glycol, and choline chloride ionic liquid ($HOC_2H_4N(CH_3)Z_3{}^+Cl^-$) exhibiting low volatility, high ionic conductivity and high electrochemical stability could be key in improving the efficiency of the process and in providing a greener route for finishing in an industrial setting [148].

4.3.3.3 Shot peening

Shot peening is a cold working approach applied to reduce the roughness of a component, but to also improve the surface mechanical properties. In this method, the desired component surface is struck and indented repeatedly with shot, usually balls manufactured of steel, ceramic or glass, flattening the adhered powders on the surface of the AM material [100]. Here the resultant surface finish is dependent upon: (i) the size and the morphology of the media used, (ii) the Almen intensity (defined by the amount of strain energy imparted to the surface and the arc height deflection of a sample thin metal strip), and finally (iii) the percentage coverage of the component finished [134, 149]. Due to the force of impact, the material undergoes plastic deformation at the surface, inducing high compressive residual stresses (up to 550 MPa) [42, 100, 134, 137]. This leads to some levels of localised grain refinement, increasing the hardness of the surface [134].

Balbaa *et al.* (2022) investigated the effectiveness of shot peening on L-PBF IN625 for increased fatigue life, see Figure 4.13. Following shot peening, a large decrease in the surface roughness was measured, with an improvement of 40% observed upon the side surfaces of the coupons (R_a ~3 µm). High surface compressive stresses were measured following shot peening, found to penetrate at

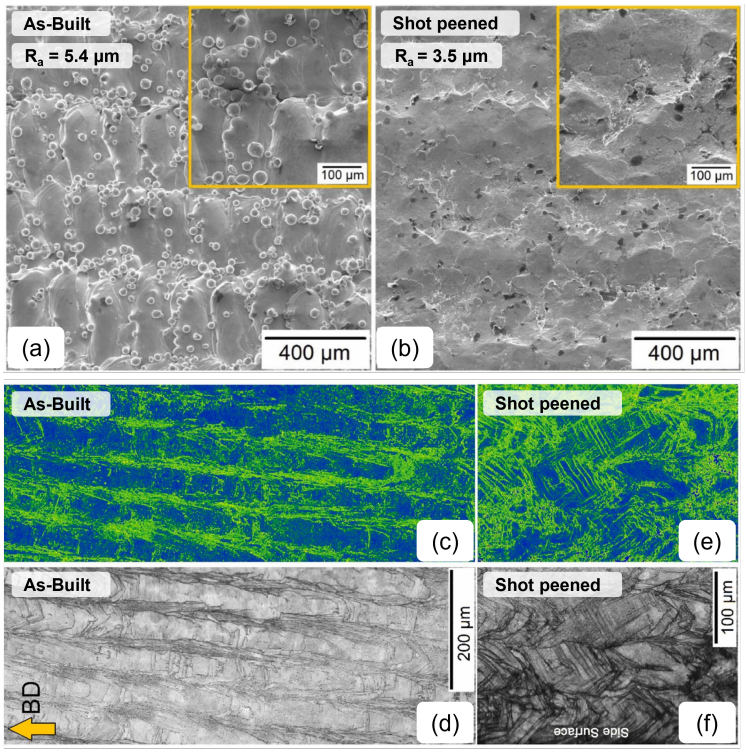


Figure 4.13: SE-SEM micrographs of (a) as-built IN625, and (b) shot peened L-PBF IN625, (c) (d) KAM (Kernal Average Misorientation) map and corresponding band contrast image of as-built IN625, (e) and (f) KAM map and corresponding band contrast image of shot peened IN625. For KAM maps (c) and (e), green coloring indicates a region with a high density of dislocations. Taken and adapted from Balbaa *et al.* (2022) [100].

depths up to 250 μm. This resulted in the formation of sub-grains and high dislocation densities at the boundaries between these in this region due to plastic deformation (see KAM (Kernal Average Misorientation) map for shot peened IN625, Figure 4.13 (e)). Altogether, shot peening was seen to reduce the frequency of crack initiation sites present, increasing the fatigue life and elongation of the specimens to levels comparable, if not superior to shot peened traditional wrought IN625 [100]. Similar results have been reported in literature by Lesyk *et al.* for AM IN718, showing an enhancement in the fatigue, and corrosion properties of the component following shot peening [134, 150].

This makes shot peening a strong candidate for AM IN625 surface finishing. Limitations arise however where internal surfaces are concerned, where again the tooling may not be able to physically access all features present. Thin sections common to AM designed parts can also risk being eroded in the process [134].

4.3.3.4 Centrifugal High Energy Finishing

Centrifugal High Energy Finishing (CHEF) is a high energy mass-finishing technique applied to remove surface roughness left behind from the manufacturing process, in this case partially melted powder particles upon the surface of the desired part, and any visible evidence of supports. This involves a cutting, smoothing and polishing set of steps, with various finishing media (of different densities, abrasive content and compositions), times and chemical agents applied at each stage [134]. The components are firstly placed in barrels containing a mixture of abrasive media (commonly pellets of a ceramic, e.g. carbide free bainitic, CFB, or semi-friable brown fused alumina, SFB), and a carrying chemical agent, often mildly acidic to oxidise the surface and prevent build-up of dust (e.g. LQ18, LQ16 - see Chapter 5 for descriptions).

The barrels are rotated and vibrated at a high velocity to create large centrifugal forces. Here the abrasive media impacts the part inside in random directions, smoothing and rounding the surfaces to leave behind a isotropic, mirror-finish (S_a < 2.5 μm) with a large compressive residual stresses in the surface of the component [137, 151]. The residual stresses imparted by the CHEF process have been measured to reach up to 550 − 800 MPa, making CHEF a comparable finishing route to the likes of shot peening [137]. Significant increases in hardness are thus also experienced following CHEF, attributed to work hardening [134]. This may have significant implications for the oxidation resistance of a component, where an increase in surface defect population and dislocation density may increase the rates of diffusion and hence reduce the oxidation resistance of the component, despite improvements to the surface finish [13].

Compared to common traditional routes of machining used for IN625, CHEF does not require

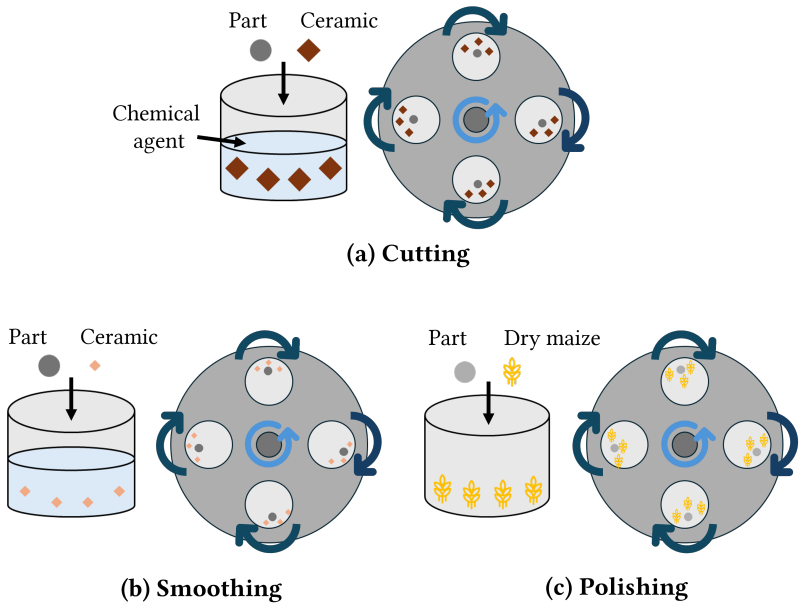


Figure 4.14: A schematic outlining the standard (a) cutting, (b) smoothing and (c) polishing steps involved in Centrifugal High Energy Finishing (CHEF). Note the barrels rotate in the opposite direction to the wheel they are attached.

tooling, making it applicable to hard Ni-based superalloys which are often difficult to machine without significant wearing. The size of the ceramic media used to deburr parts may also be varied depending on the dimensions and internal surfaces of the component, making CHEF a key candidate for the development of surface finishing for complex geometry parts encountered with AM, though this may affect the speed of the finishing process i.e. smaller ceramic leads to lengthier polishing times required. This may prove lengthy in the case of harder materials such as Ni-based superalloys which experience slow rates of material loss [134]. It is therefore important that mass loss and a decrease in wall thickness is considered during the design of the component before CHEF to compensate. Limitations also arise when aiming to target specific features, due to the isotropy of the techniques, as well as with the finishing of small diameter holes and features [134, 137].

Overall, it is clear that there is no one-size fits all approach to the post-processing of AM IN625 components with complex geometries, where there is a continuous balance between optimizing for surface finish, surface stress state and dimensional accuracy. Combining this with different applications of heat treatment, further work is required to ascertain which processing routes are optimal to reach the standard oxidation performance outlined by wrought Ni-based superalloy, with the aim to optimize and enhance these properties for use in industry settings. Table 4.6 shows a summary of all of the surface finishing techniques investigated and their respective R_a, S_a values.

TABLE 4.6
AN OVERVIEW OF THE SURFACE ROUGHNESS VALUES OBTAINED WITH STANDARD SURFACE FINISHING TECHNIQUES FOR AM IN625, AND SIMILAR NI-BASED SUPERALLOYS FROM LITERATURE.

Surface	R_a (µm)	S_a (µm)	Comments	Ref.
Additive	1.50 < AD < 80.00	~30.00	High residual stress, process dependent (power, scan speed, hatch)	[132, 133] [88, 137]
Machined	< 1.00	< 1.00	–	[134]
Electropolish	0.40 < EL < 11.00	< ~30.00	Process dependent (time, voltage, distance)	[133, 145] [17, 141]
Shot peen	< 4.00	< 10.00	High residual stress (~500 MPa), process dependent (time, media size)	[88, 137] [150]
CHEF	–	< 2.00	High residual stress (~550 MPa) process dependent (time, media size)	[137]

*CHEF (Centrifugal High Energy Finishing).

4.4 High temperature oxidation of Ni-based superalloys in air, Thermodynamics and kinetics

High temperature oxidation resistance is defined as the materials ability to form a protective oxide scale when placed under aggressive conditions at T>400˚C in the presence of oxygen [66, 135]. At such temperatures, most metals will oxidise over time, leading to the loss of material and a change in the near surface composition of that component. Therefore, it is key to understand the mechanisms by which this occurs in terms of the rate of growth, and the morphology of the films produced.

Oxidation occurs either due to the simultaneous transport of electrons and ions throughout the metal to the oxide/gas interface, and/or via the transportation of oxygen to the surface of the metal/oxide scale. For this reaction to occur, one or both of the reactants (metal ions, or oxygen anions) must penetrate the scale [66]. The transport of ions is controlled by the defect structure of the oxide via point (oxygen anions, or metal cations), line (e.g. dislocations) and surface defects (e.g. grain boundaries)[66]. Figure 4.15 shows a schematic of the process, where electrons are shown to be lost from the metal substrate and oxygen anions are gained, resulting in the formation of an oxide and a metal cation vacancy concentration gradient across the scale, taken from Birks *et al.* (2006) (see Equation (4.2)) [18, 66, 152]:

$$M + O_2 = M \cdot O_2 \tag{4.2}$$

where M is a metal atom, combining with oxygen (O_2), to form a metal oxide (MO_2).

At initial stages, all alloy components will oxidize, and discrete metal oxide islands will nucleate upon the surface, with some oxides being more thermodynamically stable than others depending upon the alloy composition, the holding temperature and oxygen partial pressure, as well as their diffusion coefficients [18]. This is controlled by the second law of thermodynamics. This is primarily due to their respective Gibbs Free energy change, determined by the following equations, Equation (4.3) and Equation (4.4) [66, 67]:

$$\Delta G^{\circ} = R \cdot T \cdot lnPO_2 \tag{4.3}$$

where G˚ is the Gibbs free energy (KJ/mol), R is the molar gas constant, T is the temperature (K) and PO_2 is the oxygen partial pressure.

$$\Delta G = \Delta H - T\Delta S \tag{4.4}$$

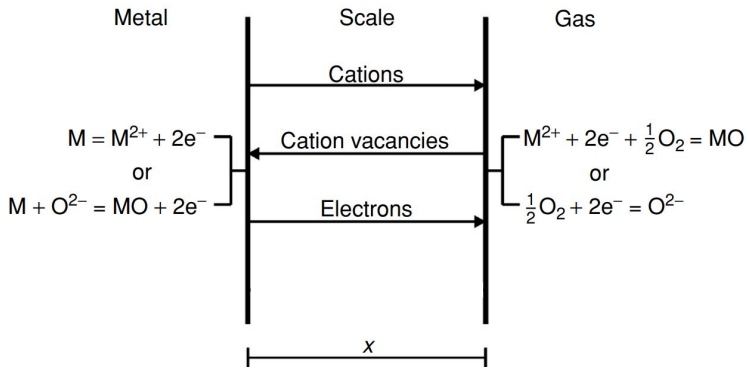


Figure 4.15: Simplified model for diffusion-controlled oxidation in metals, where M is the metal (e.g. Cr). Taken from Birks *et al.* (2006).

where H is the enthalpy, and S is the entropy, for a constant pressure and temperature (K).

Oxides with a more negative ΔG° are more thermodynamically stable and will thus form preferentially. These oxides grow laterally until a local equilibrium is formed between the scale the and the parent alloy, as well as the scale and gas environment [66, 135, 152]. This can be graphically demonstrated by Ellingham-Richardson diagrams (see Figure 4.16), which show the standard Gibbs free energy of formation for oxides G, as a function of temperature T [153]. Note this is a normalised plot, showing the Gibbs free energy of reactions for one mole of the element consumed, in this case oxygen. The thermodynamic stability of each oxide tends to decrease with an increase in temperature before dissociating or becoming unstable [66, 135, 152].

Once stable, the reaction kinetics of the desired oxide film can be measured to determine its oxidation resistance. Wagner's theory of oxidation describes the high temperature oxidation of metals where diffusion of ions is rate controlling; derived from Fick's first law of diffusion [67]:

$$J_x = -D_v \cdot \frac{dc}{dx} \tag{4.5}$$

where J is the diffusion flux (mol), D is a constant diffusion coefficient (cm^2/s), and $\frac{dc}{dx}$ is the derivative of the concentration flux across a thickness x (cm).

This approach assumes a metal-lost to oxide thickness relationship, which is parabolic for most common Ni-based superalloys. The classical equation by Carl Wagner demonstrates this rate of mass transfer per unit time [66, 135]:

$$\left(\frac{m}{A}\right)^2 = K_p \cdot t \tag{4.6}$$

where m is the mass change (g), A is the surface area (cm^2), K_p is the parabolic oxidation rate constant ($g^2cm^{-4}s^{-1}$) and t is the time (s).

If the growth regime is not perfectly parabolic, an exponent n may be determined to better describe the oxidation behaviour as either: linear (n = 1), parabolic (n = 2), or cubic (n = 3), using Equation (4.7):

$$\left(\frac{m}{A}\right)^n = K_n \cdot t \tag{4.7}$$

where m is the mass change (g), A is the surface area (cm^2), K_n is the oxidation rate constant ($g^2cm^{-4}s^{-1}$) assuming the exponent n, and t is the time (s).

Assuming non-equilibrium thermodynamics, as is the case during oxidation, for a parabolic rate to be maintained, the oxide layer must be dense, compact and adherent to the surface of the alloy (to allow diffusion of lattice species), with thermodynamic stability at both the scale/alloy interface, and scale/gas interface (to establish a chemical potential gradient and thus, driving force for diffusion). In addition, the diffusion of ions and electrons must be rate controlling [66, 152]. The growth rate of oxide films is determined by the reactions taking place between the environment and alloying elements present in the base metal. The following key properties influence rate in alloys [66, 135]:

- Alloying elements with differing affinities for oxygen;
- Differences in solid solubility of oxides formed in the parent metal;
- Differences in metal ion mobility and diffusivity in oxide;
- Formation of sub-surface oxide and phases near the scale/alloy interface.

For an oxide scale to be considered protective in the long term, it must demonstrate the following characteristics [66, 135, 152]:

- The growth rate of the oxide must occur slowly;
- The scale must show low stoichiometry (i.e. a low density of lattice defects to lower diffusion of ions);
- Low dislocation density (to limit diffusion of reactive species);
- The scale must be thermodynamically and chemically stable (to prevent formation of volatile species and thickness reduction);
- Macro/Micro crack free (again, to limit short circuit diffusion pathways);
- Compact and adherent to the metal surface;
- Stress-free / low stress over the required temperature range of use to minimise scale loss.

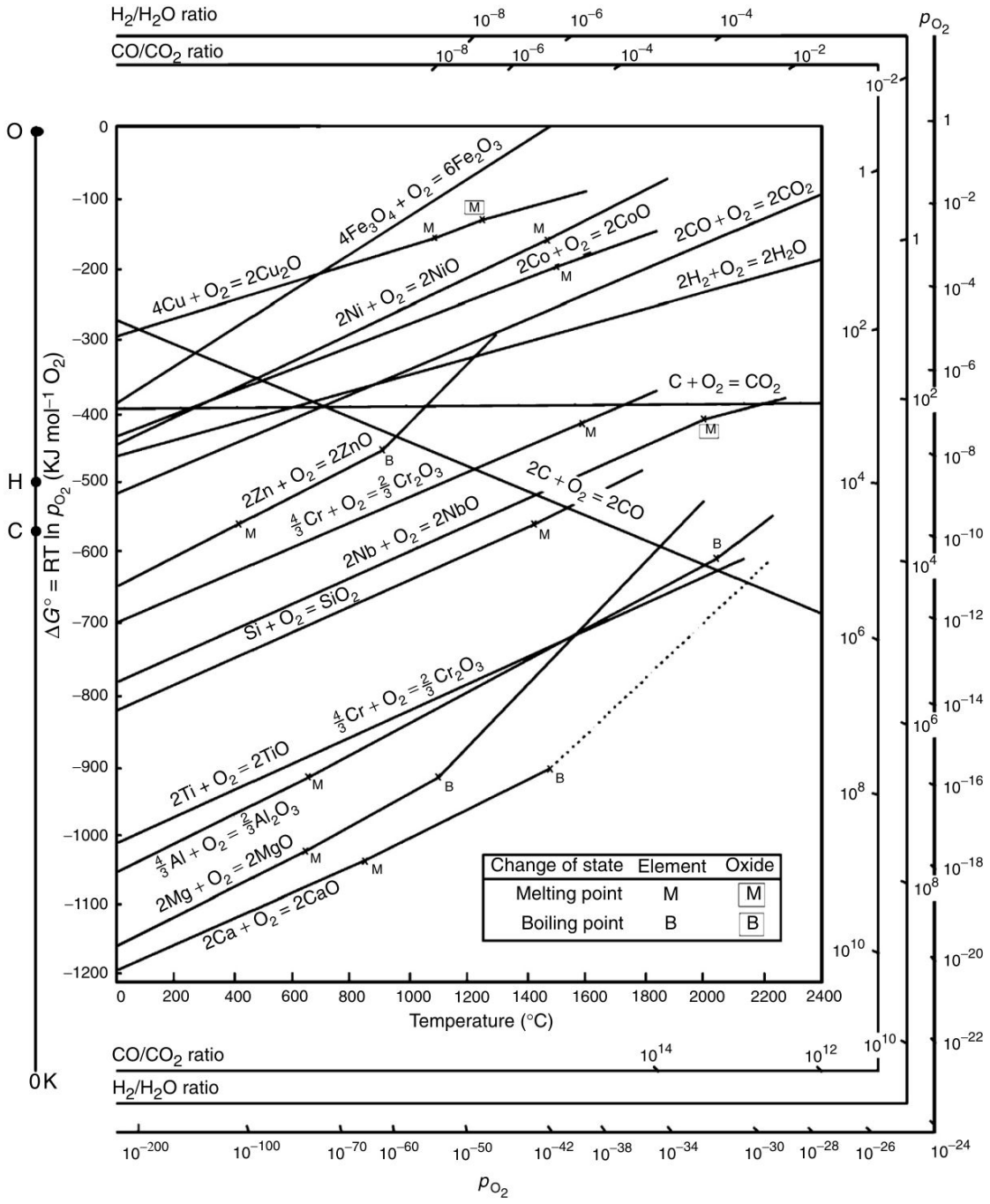


Figure 4.16: Standard Ellingham-Richardson diagram, showing the standard energy of formation of selected oxides against temperature. Taken from Birks *et al.* (2006).

Common properties which can affect the formation of oxide can include the environment the material is exposed to, defects, the surface roughness and stress-state of a component, as well as impurities elements present such as a pre-existing external oxide. Once investigated, film growth may be controlled and modified to extend component lifetime by limiting excessive environmental degradation by material loss and phase changes in the alloy. Most alloys or protective coatings used are primarily based on iron, nickel-based superalloys, or cobalt, where Cr and Al are selectively

oxidised to generate a continuous protective oxide scale [19, 65, 66, 135]. These are known to form dense, stable and protective chromium and/or aluminium rich oxide scales. These films grow at a slow rate and are favoured thermodynamically over other oxides containing Fe, Ni or Co which may form at early transient stages of oxidation [135]. The extent of an elements enrichment inside the oxide film is determined by the composition of the alloy, the element's diffusivity in the scale, as well as its oxide stability, as determined by the Ellingham-Richardson diagram. The following series of elements are placed in order of their stability for the standard Ellingham-Richardson diagram shown in Figure 4.16: Al > Ti > Si > Nb > Cr > Mo ~Fe > Co > Ni [2].

4.4.1 Chromia (Cr_2O_3)

Chromia (Cr_2O_3) is a key protective oxide scale used by virtue of its high thermodynamic stability to temperatures 600 – 900˚C (see Figure 4.17) [2, 9, 135]. One mole chromia forms via the following route:

$$2Cr(s) + \frac{3}{2}O_2(g) = Cr_2O_3 \tag{4.8}$$

Chromia demonstrates the aforementioned qualities well: it is a slow growing, stable and continuous oxide scale, often compact and fully adherent to the surface of the metal. For a Ni-based superalloy, the chromia scale acts to block the diffusion of Ni cations to the oxide/gas interface, preventing the formation of the non-protective NiO scale [154]. For common chromia forming

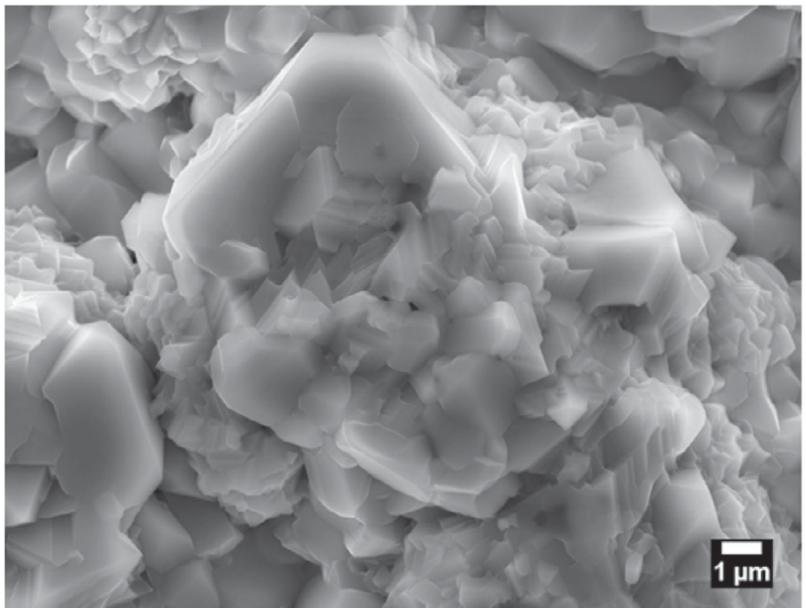


Figure 4.17: BSE-SEM micrograph showing the external oxide scale formed upon wrought IN625 following isothermal oxidation for 1000 h at T = 900˚C in air. Taken from Arnold *et al.* (2018) [9].

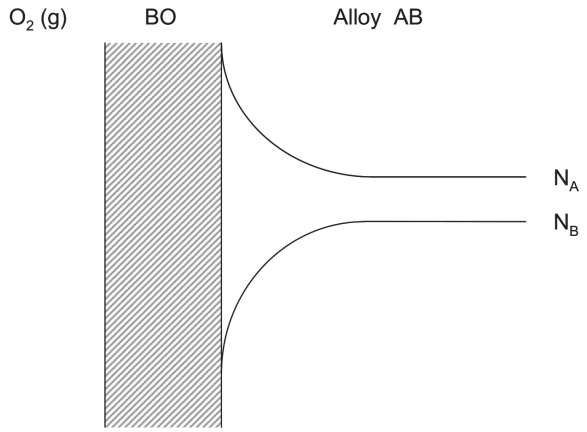


Figure 4.18: A schematic illustrating the oxidation process (BO), which results in the depletion of element B within the near-oxide region of a selectively oxidized metal alloy, AB. Adapted from Young (2016). [67].

Ni-based superalloys (of 15 – 25 wt.% Cr) exposed to high temperatures, the oxidation rate of the alloy is governed by the supply, outward cationic diffusion of Cr^{+3} and the selective oxidation of chromium at the metals surface [62, 135, 142, 155]. Here the reaction involves the diffusion of chromium ions Cr^{3+} to the scale/gas interface where it reacts with oxygen in the environment to form chromia. Whilst chromium diffusion is the dominant transport mechanism, inwards oxygen anion diffusion into the scale is also a contributor to the rate of oxidation. Here for Cr-rich Ni-based superalloys, the larger the concentration of Cr, the faster the continuous chromia layer will tend to establish itself. As the scale thickens over time, a Cr depletion zone forms beneath the oxidation affected region, where the concentration profile increases moving towards the bulk of the material, see Figure 4.18 and Figure 4.19. This change in the microstructure composition can lead to significant changes in the chemical potential of other key alloying elements, driving their diffusion from the bulk to the external scale [135]. As a result of the thickening oxide over time, the diffusion pathway for Cr through the chromia scale increases, meaning the overall rate decreases to a plateau once a critical thickness is reached [18, 66]. In terms of IN625, the Ti and Nb content is kept to a minimum in order to prevent the formation of detrimental fast-growing oxides containing the aforementioned elements which may interfere with the growth of the slower, more protective oxide scales [65]. Alloying elements in high amounts such as Ti may also act to dope the chromia scale, as viewed by Cruchley *et al.* for RR1000 [149, 156]. This leads to enhanced oxidation kinetics than typically observed in Ti-free chromia scale, and the establishment of a Ti-depleted zone in the sub scale for increasing depths at increased periods of exposure.

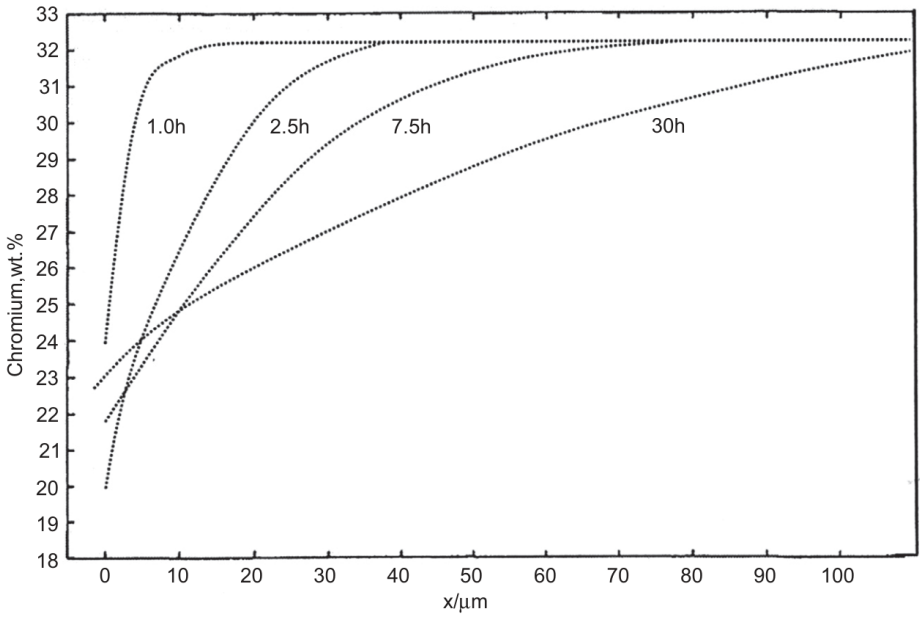


Figure 4.19: Graph showing the depletion of Chromium from the bulk to the scale for Fe-32Cr, measured using Electron Probe Microanalysis (EPMA) after exposures of T = 977°C. Reprinted from G. L. Wulf *et al.* (1969). Taken from Young (2016) [67]

4.4.2 Internal oxidation

Internal oxidation may also occur beneath the scale inside the matrix during exposure to high temperatures. This involves diffusion of oxygen into the surface of an alloy, and the subsequent formation of sub-surface oxides beneath the protective scale, commonly precipitating upon grain boundaries preferentially (acting as short-circuit diffusion pathways). The oxides forming here tend to be enriched in slow diffusing elements (with a more negative ΔG° than the protective oxide scale) such as Al or Ti, which are unable to diffuse to the surface quickly enough to develop an external scale [67]. Here it is a requirement that the composition of this element must be low enough to ensure that it will not lead to the formation of an outer scale [18]:

$$N_m \times D_m << N_s \times D_O \tag{4.9}$$

where N_m is the nominal concentration of the metal matrix ions, D_m is the diffusion coefficient of the matrix phase, and N_s is the nominal concentration of the solute, D_O is the diffusion coefficient of the solute oxide.

Formation of an internal oxide can form simultaneously alongside the external scale [67]. Internal oxides are generally undesirable, not only depleting the alloy from its intended composition in the oxidation-affected region, but also exhibiting a different coefficient of thermal expansion (CTE) than the parent metal, contributing to the spallation, crack initiation and possible delamination of the oxide scale [66]. If the protective oxide scale is successful in preventing the ingress and

dissolution of oxygen into the parent alloy, internal oxide cannot occur. This is very uncommon however, where most protective scales will allow some amount of permeation, establishing an oxygen concentration gradient through it. Here the least/less noble elements in the parent alloy will react to form oxides, namely Alumina (Al_2O_3) in the case of IN625 [66]. As a rule, the higher the Cr content, the shallower the depth of penetration of internal oxide [67]. This is on account of the faster establishment of an external protective chromia scale, and reduced amounts of the ingress of oxygen through the scale via micro-cracks as a result.

4.4.3 Stress generation in the oxide scale

As mentioned previously, different oxides and their parent base metal can exhibit vastly different CTE. When an oxide or precipitate forms, it is accompanied by change in volume, due to the fact each component will have its own unique lattice parameter and/or crystal structure [66, 152]. Differences between these characteristics will result in the oxide experiencing amounts of elastic strain and in the extreme case, plastic deformation, fracture and failure of the protective layer. During isothermal oxidation two main sources of stress are encountered as a result of the expansion or contraction between the base and the layer growing over time: (i) Growth stresses, and (ii) Thermal stresses. A strong understanding of how these form and present themselves is needed to ensure the prolonged lifetime of critical components in high temperature environments, where the protectiveness of the scale is characterised by its adherence to the surface, and thus, its stress state [155]. A key example of this can be the history of the use of PWR systems during the 1970s, outlined by Evans (1995), who described the denting of IN600 secondary circuit tubing via the formation of magnetite. This led to a loss of efficiency in the steam generator unit [157].

4.4.3.1 (i) Growth stresses

Growth stresses in the external oxide formed upon a material can occur during the isothermal oxidation of an alloy for a range of different reasons and sources [66, 154]. As previously mentioned, volume changes in the material are one of the major sources for stress, where the growing oxide will have a different volume than the base parent metal. This mismatch generates elastic strains that form and accumulate during the isothermal oxidation of the metal. The Pilling-Bedworth ratio (PBR) (1923) can be calculated as a useful, qualitative indication of the stress type and level within the growing oxide, given by the following relationship [66, 158]:

$$PBR = \frac{V(\text{per metal ion in the oxide})}{V(\text{per metal atom in metal})} \tag{4.10}$$

where V is the molar volume of the oxide / the molar volume of the metal upon which the oxide layer forms.

Here if the PBR > 1 (where the volume of the oxide is greater than the metal consumed), the oxide growing experiences compressive stresses. The scale formed will tend to be protective, i.e. compact and non-porous. If PBR < 1 however, the oxide is under tension, and will appear to be discontinuous and non-protective. This is due to the fact the volume of the oxide is less than the metal consumed, meaning it will act to stretch itself across the surface of the metal. Most protective oxides (e.g. Chromia, PBR = 2.07 - 2.42, Alumina = 1.28, Rutile = 1.70 – 1.78) will generate compressive stresses, with the exception of K, Mg, Na oxides which show tensile stress generation [66, 154, 155, 157]. In cases where the PBR > 2.0, the oxide is likely to be mostly protective and non-porous, but subjected to higher compressive stresses, exacerbated as the scale thickness increases over time, making it more likely to spall [159]. Such compressive stresses are expected to be located at the scale/alloy interface, where the oxide grows due to the inward diffusion of oxygen anions to the interface, growing in the direction with the least resistance i.e. the free surface. Here the oxide formed at the scale/alloy interface must occupy the volume previously occupied by the consumed metal, meaning it must expand or contract; thus generating stress.

It is important to note, that the Pilling-Bedworth relationship is deemed to be more of a qualitative quantity, where the relationship is limited by its lack of inclusion of the stress magnitude experienced by the scales and metal substrates, as well as subsequent cracking [157, 159]. For example, many other factors can affect the growth stress generation, such as the adherence of the scale to the substrate in terms of epitaxy between the metal oxide and base metal lattice parameters. This stress mismatch will decrease with time as the scale grows thicker [155].

As the formation of oxide scales leads to the selective oxidation and depletion of elements in the metal substrate, a significant compositional change is experienced in both the alloy and the protective scale. This causes there to be an evolution in the lattice parameters of the alloy and oxide leading to further mismatch and stress generation. The internal oxidation of an alloy (forming alumina in the case of IN625), and/or carbide formation also leads to local compositional changes along grain boundaries resulting in stress [155].

The accumulation of point defects, namely vacancies (when an atom is not present at its lattice site) can lead to high levels of non-stoichiometry in the metal substrate, leading to a change in lattice parameter and hence stress generation. For chromia forming metals (growing oxide by the outward diffusion of Cr ions to the scale/gas environment), a vacancy gradient can form beneath the scale. These vacancies lead to a change in the local density of the substrate, generating a relaxation effect around the vacancies. This can decrease the contact area between the protective

oxide and the base metal.

At high temperatures, during oxidation, metals can experience some level of recrystallisation, leading to the coarsening of grains and the generation of special grain boundaries. As the grains grown in size, this can lead to volume mismatch between the grain and the oxide growing upon it, once again generating stress.

The specimen geometry is also an important factor to consider, especially for the case of AM components with complex geometries. Curvature (concave and convex surfaces), as well as the mechanism of oxidation will influence the stress generated in the protective scale. There are four cases identified by Hancock and Hurst (1974) [160] to characterise these, summarised as follows [66]:

- **Oxides growing on convex surface by cation migration** - The metal moves away from the oxide is formed at the scale/gas interface, and compressive stresses accumulate inside the oxide as it chases the metal substrate;
- **Oxide formation on convex surfaces by anionic diffusion** - Tensile stress generation and accumulation at the outer surface of the external oxide;
- **Oxides growing upon concave geometries via cation diffusion** - Initial compressive stresses in oxides grown. As this scale grows thicker, a transformation from compressive to tensile stress occurs at the scale alloy interface.
- **Oxides growing upon concave surface by anion diffusion** - Compressive stress generation, increasing in magnitude as the scale becomes thicker over prolonged periods of oxidation.

4.4.3.2 (ii) Thermal stresses

During the oxidation of a metal the stresses generated are dominated by growth effects inside the metal substrate and oxide. However upon cooling or thermal cycling of the component, significant thermal stresses are also formed as a result of differences in the coefficient of thermal expansion of each component layer [154, 155, 157]. This was shown for NiCr alloy by Daghigh (1996), who demonstrated stress relaxation by oxide elastoviscoplastic deformation (elastoviscoplastic, behaves elastically as a solid below a critical stress, once exceeded, flows like a viscous liquid) tends to occur at $T > 700^{\circ}C$, making growth stresses during isothermal oxidation negligible [154, 161].

This is expressed using Equation (4.11) [162]:

$$\sigma_{oxide} = \frac{E_{oxide} \cdot \Delta T \cdot (\alpha_{oxide} - \alpha_{metal})}{1 + 2\left(\frac{E_{oxide} \cdot t_{oxide}}{E_{metal} \cdot t_{metal}}\right)} \tag{4.11}$$

where σ is the in-plane stress generated in the oxide layer (MPa), E is the elastic modulus of the metal substrate and oxide (GPa), ΔT is the change in the exposure temperature (i.e. the difference between the initial and final exposure temperature), α is the CTE, and t is the thickness of the component.

As a rule, for a protective oxide under compressive stress the CTE of the growing oxide will tend to be less than that of the metal substrate, where the overall level of stress is determined by the difference between these two values. For example, for Chromia $\alpha_{Cr_2O_3} = 8.1 \times 10^{-6}$ K^{-1}, compared to IN625 $\alpha_{IN625} = 17.3 \times 10^{-6}$ K^{-1} (for 20°C – 900°C) [157, 163–166]. Another general rule of thumb for chromia, alumina and NiO scale is that if the following criteria shown in Equation (4.12) is met, compressive stresses are expected to form during cooling from in-service to room temperature [155]:

$$\frac{\alpha_m}{\alpha_{ox}} > 1 \tag{4.12}$$

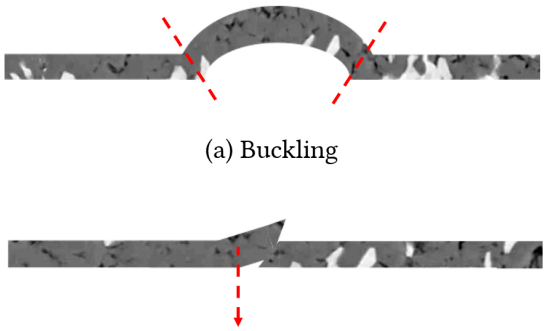
where α is the thermal expansion coefficient for both the metal, m, and the oxide, ox, respectively.

A. M. Huntz (1995), determined this ratio for Chromia for Ni-Cr alloys, ranging between values of 2.1 – 2.25 [155]. Measured values for the compressive residual stress contained in a chromia scale exposure exposures of 700 – 1000°C tend to vary between -1.2 to - 3.30 GPa, recorded using a combination of both XRD techniques and Raman spectroscopy [154, 167–171]. Note, measured stresses only take into account the system in purely elastic conditions, with no consideration for the stress relaxation effects taking place. Therefore, these values may be taken as an upper limit [154].

4.4.3.3 Relieving stresses and their quantification

During operation, creep and recrystallisation of the alloy can relieve a large portion of these accumulated stresses, by way of plastic deformation of the substrate and oxide, and the subsequent cracking and spallation of the oxide film, particularly during cooling [66, 155, 157, 168, 171]. This is of a particular concern should the protective scale be lost, and the selectively oxidised element be depleted in the parent alloy, it may make the re-passivation of the scale difficult [157].

The mechanism for this relaxation is heavily dependent on the scale and substrate properties, such as the mechanical properties, differing creep rates etc. The thickness of the scale has a large



(a) Buckling

(b) Wedging

Figure 4.20: Schematic showing the stress-failure response of an oxide when placed under compressive stress, (a) Buckling, (b) Wedging. Adapted from Evans (1997) [159].

impact upon spallation of the oxide during cooling, where thermal shock may occur at outer layers of the scale where the thermal gradient is steepest [155]. Figure 4.20 shows the two classic types of spallation mode. Buckling occurs for thinner scales where adherence between the oxide and the substrate is low i.e. preexisting defects / stress concentrators are present within the scale / scale/alloy interface. Wedging however, occurs as the scale becomes thicker, and shear cracks are able to form upon cooling. Fracture of the scale will occur once the stress accumulated reaches a critical value which exceeds the interfacial fracture energy of the scale [154].

It is key these stresses can be predicted / quantified to evaluate the effectiveness and endurance of the protective scale in high temperature environment. Stresses can be determined in the scale both qualitatively and quantitatively using a range of techniques either in-situ or following cooling. This is summarised from reviews by Evans (1995), Huntz (1995), Kemdehoundja *et al.* (2006) and the National Physics Laboratory in the following [154, 155, 157, 159, 171, 172]:

- **Deflection and extension techniques** - measurement of deflection in the sample, D, produced by strain induced in-situ during isothermal oxidation i.e. creep relaxation. This takes into account changes to the sample length over the period of exposure, implying formation of compressive stress;
- **Curvature** - Determination of stress distributions at room temperature for both the scale and substrate from the external scale penetrating into the bulk;
- **Hole drilling** - Involves stress relaxation by drilling, allowing for the measurement of macroscopic stress by changes in several strain gauges surrounding the drilled hole;
- **Raman Spectroscopy** - Non-destructive method analysing small volumes of material. Stress measured by the shift in the Raman peak vibrational frequencies for comparison to a perfect, non-stress crystal;

- **X-ray diffraction, $\sin^2(\psi)$ method** - Static or continuous measurement of the interplanar spacing changes and strain experienced by the crystal lattice before and after oxidation to inform the associated residual compressive stress induced. The $\sin^2(\psi)$ method is a key example of this which will be discussed in the methodology of the thesis.

Empirical equations can also be used to predict properties of the scale, such as the critical temperature drop that leads to spallation on a planar surface. Evans (1997) developed an equation to determine the temperature change necessary for the spallation of an oxide or protective coating. This equation accounts for instantaneous crack growth during a temperature shift, assuming that all stored energy within the oxide is available to drive crack formation [157, 159]. The equation for spallation due to wedging of the oxide scale is derived as follows [159]:

$$\Delta T_c = \left(\frac{\gamma_F}{\epsilon \cdot E_{ox} \cdot (\Delta\alpha)^2 \cdot (1 - \nu_{ox})} \right)^{1/2} \tag{4.13}$$

where ΔT_c is the change in temperature (K), γ_F is the fracture energy of the oxide scale (J/m^2), ϵ is the oxide thickness (μm), E_{ox} is the Young's modulus of the oxide layer (GPa), $\Delta\alpha$ is the difference between the linear expansion coefficients between the growing oxide and the base alloy metal, and ν_{ox} is the Poisson's ratio of the oxide.

From this equation, it can be concluded that a slower temperature drop improves the spallation resistance of the alloy, permitting thicker oxide scales to be grown at a particular temperature. For layered oxides or protective coatings, this also demonstrates how by careful selection of α CTE, it is possible to relax the surface of a metal. Should the $\Delta\alpha$ be large, large amounts of sliding displacements will occur upon the wedge crack tip, leading to a lower temperature drop required before initiation and spallation [159].

4.5 Oxidation of Inconel 625, A comparison of wrought and AM alloy

Research into L-PBF IN625 at high temperatures is primarily focused on the isothermal oxidation properties of the alloy in air, where there have been several studies investigating the oxidation performance of AM IN625 at short (< 200 h) exposures (with the exception of Arnold *et al.,* (2018) who investigated an ODS Spark Plasma Sintered (SPS) variant for 1000 h) across L-PBF, and Electron Beam Melting (EBM) fabricated alloy at T = 800 – 1050˚C [1–6, 8–11, 13–17, 173–176]. Short exposures investigated in the literature are less reflective of the material in service, where the oxide film and key phases, particularly the δ-phase, are not fully established. So far L-PBF and Laser Beam Melted (LBM) IN625, when surface finished, is reported to perform to approximately the same standard as wrought IN625 and similar Ni-based superalloys, in terms of their oxidation rate, the thickness, chemistry and morphology of the scales formed, see Figure 4.22 and Figure 4.23 [1, 7, 10, 15].

4.5.1 Oxidation kinetics of L-PBF Inconel 625

A summary of the research covering wrought, and AM isothermal and thermal cycling (TC) oxidation is shown in Figure 4.21 and Table 4.7, where each IN625 data point is summarised in Table 1 and Table 2 in the Appendix. Data was extracted from each paper, allowing the oxidation rate constants and n-values to be extrapolated according to the classical Wagner equation for oxidation Equation (4.6) [66].

Research into the oxidation kinetics of IN625 has shown that wrought and AM IN625 exhibit mainly sub-parabolic (n~2) to cubic growth (n~3) behaviour with spallation of the oxide scale after 100 h of exposure, dependent on the microstructure and surface finishing applied [1]. Higher temperatures of exposure increase the oxidation rate, as expected. In general, AM IN625 shows a greater resistance to oxidation than AM IN718, attributed to the higher Cr and Ni content and faster establishment of a protective passive chromia scale [174].

4.5.2 External oxide

Figure 4.22 shows the standard oxide scale and microstructure formed for wrought IN625 following thermal exposure at 900˚C for 1000 h in laboratory air and pressure [7]. For comparison, Figure 4.23 shows the standard oxide scale and microstructure formed for L-PBF IN625 following thermal exposure at 900˚C for 168 h in laboratory air and pressure; where it can be seen that the scale chemistry and morphology is approximately the same despite the microstructural anisotropy introduced by the AM process [1].

For temperatures ranges of 800 – 1200˚C for 10s – 10,000s h, the scale has been observed to consist of a thick, adherent protective chromia scale (Cr_2O_3), with a critical thickness of 10 µm [1]. The protective scale observed following exposure is uniformly wrinkled and porous, indicating growth/thermal stress effects during formation. Further to this, photoelectrochemistry (PEC) testing by de Sousa Malafaia *et al.* (2020) determined that at 800˚C the chromia scale exhibited p-type semiconductor character, indicating that the oxide grows via the outward diffusion of metal cations (Cr^{3+}) via cation lattice vacancies [11, 152]. Thus, the enrichment of Cr in the scale tends to increase with an increase in the oxidation exposure temperature until T > 1000˚C, where a mixed chromite (Ni,Fe)Cr_2O_4 has been reported to form [2, 14].

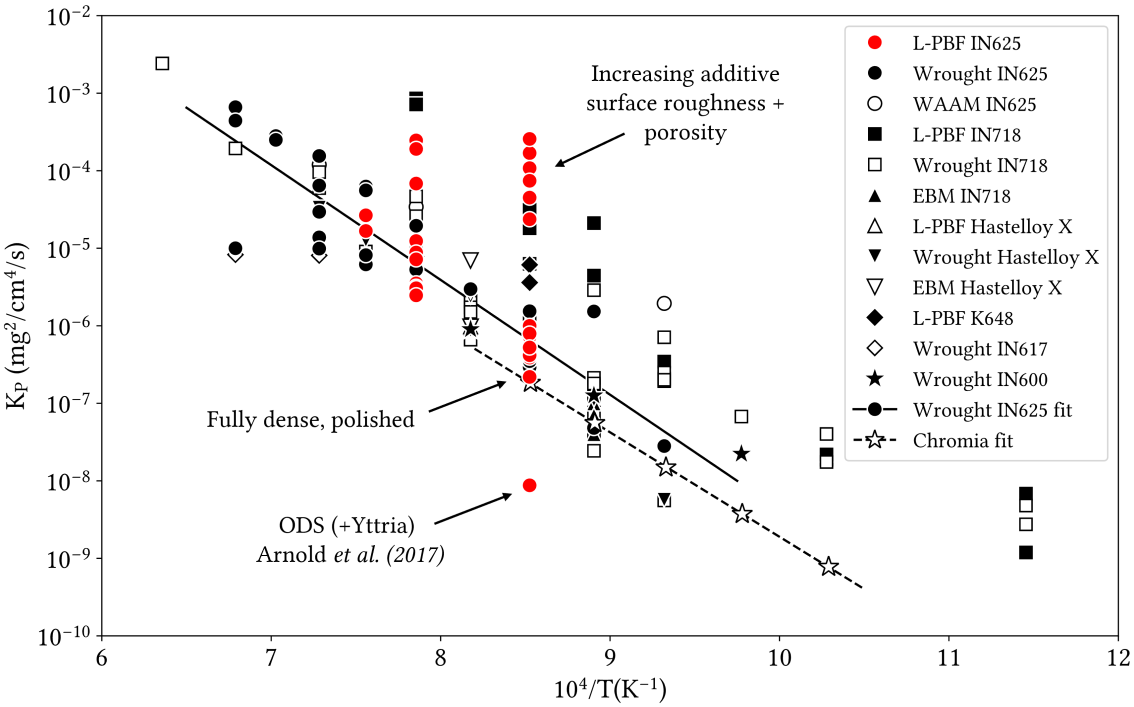


Figure 4.21: Arrhenius Plot of K_P values from literature, comparing the oxidation performance of AM and wrought IN625 to similar chromia forming Ni-based superalloys, as well as a chromia formation on a high chromium austenitic steel. See as-built L-PBF IN625 and SPS ODS IN625 highlighted in red [2–7, 9–11, 14–17, 53, 144, 166, 173–184].

TABLE 4.7
SUMMARY OF KEY ISOTHERMAL OXIDATION STUDIES INVESTIGATING AM IN625, AND THE OXIDES OBSERVED FROM LITERATURE.

Author	Time (h)	T (°C)	1/ 10^4/T	K_p ($mg^2/cm^4/s$)	Oxides	Comments
Arnold et al. 2017 [9]	1000	900	8.53	8.75E-09	Cr_2O_3	ODS (+Yttria) via SPS
Chen et al. 2020 [13]	100	900	8.53	1.69E-04	Cr_2O_3, $Ni(Cr,Fe)_2O_4$	As-built TiC nano-composite
	100	900	8.53	1.01E-04	Cr_2O_3, $Ni(Cr,Fe)_2O_4$, NiO	Laser shock peened (1×)
	100	900	8.53	4.50E-05	Cr_2O_3, $Ni(Cr,Fe)_2O_4$, NiO, TiO_2	Laser shock peened (2×)
	100	900	8.53	2.37E-05	Cr_2O_3, $Ni(Cr,Fe)_2O_4$	Laser shock peened (3×)
Chen et al. 2020 [115]	100	1000	7.86	2.46E-04	Cr_2O_3, $Ni(Cr,Fe)_2O_4$	As-built
	100	1000	7.86	6.83E-05	Cr_2O_3, $Ni(Cr,Fe)_2O_4$	As-built+TiC
	100	1000	7.86	1.91E-04	Cr_2O_3, $Ni(Cr,Fe)_2O_4$	Heat treated (1070℃, 1 h)
	100	1000	7.86	2.47E-06	Cr_2O_3	Heat treated (1070℃, 1 h)+TiC
Chyrkin et al. 2022 [1]	300	900	8.53	8.78E-07	Cr_2O_3, $NiCr_2O_4$, TiO	As-built Y-direction
	300	900	8.53	9.97E-07	Cr_2O_3, $NiCr_2O_4$, TiO	As-built Z-direction
	100	1000	7.86	1.24E-05	Cr_2O_3, $NiCr_2O_4$, TiO	As-built Y-direction
	100	1000	7.86	8.80E-06	Cr_2O_3, $NiCr_2O_4$, TiO	As-built Z-direction
	300	900	8.53	2.19E-07	Cr_2O_3, $NiCr_2O_4$, TiO	Coarse grained, annealed
	300	900	8.53	7.93E-07	Cr_2O_3, $NiCr_2O_4$, TiO	Hot rolled at 980℃
Condruz et al. 2020 [14]	96	900	8.53	7.23E-07	Cr_2O_3, (Ni, Fe)Cr_2O_4	As-built
	96	1050	7.56	1.67E-05	Cr_2O_3, (Ni, Fe)Cr_2O_4	As-built
Huang et al. 2022 [17]	40	1000	7.86	7.19E-06	Cr_2O_3, $NiCr_2O_4$,NiO	As-built, v = 600 mm/s
	40	1000	7.86	2.86E-06	Cr_2O_3, $NiCr_2O_4$,NiO	As-built, v = 750 mm/s
	40	1000	7.86	3.52E-06	Cr_2O_3, $NiCr_2O_4$,NiO	As-built, v = 900 mm/s
	40	1000	7.86	3.18E-06	Cr_2O_3, $NiCr_2O_4$,NiO	As-built, v = 1050 mm/s
	40	1000	7.86	3.05E-06	Cr_2O_3, $NiCr_2O_4$,NiO	As-built, v = 1200 mm/s
Parizia et al. 2020 [15]	96	900	8.53	3.89E-07	Cr_2O_3, TiO_2	As-Built
	96	900	8.53	5.97E-07	Cr_2O_3, $NiCr_2O_4$, Nb_2O_5,TiO_2	Solution treated
Ramenatte et al. 2020 [10]	50	900	8.53	5.25E-07	Cr_2O_3, $NbCrO_4$	Laser Beam Melted
	50	1050	7.56	2.66E-05		Laser Beam Melted
Sun et al. 2020 [16]	100	900	8.53	2.57E-04	Cr_2O_3, $NiCr_2O_4$, $NiFe_2O_4$, NiO	VED = 76 J/mm^3
	100	900	8.53	1.08E-04	Cr_2O_3, $NiCr_2O_4$, $NiFe_2O_4$, NiO	VED = 104 J/mm^3
	100	900	8.53	7.42E-05	Cr_2O_3, $NiCr_2O_4$, $NiFe_2O_4$, NiO	VED = 167 J/mm^3

Small differences in the oxide scale can occur dependent on the powder composition used and the oxidation conditions, where an increased bulk composition in Ti, Nb and Fe wt.% for example can lead to the increased formation of imperfect chromia scales at temperatures above 1000˚C, with the presence of mixed spinel containing $Ni_2Cr_2O_4$ and $Ni(Cr,Fe)_2O_4$ protrusions, as well as rutile (TiO_2), NiO, and multiple mixed Nb-rich oxides (NbO, NbO_2, Nb_2O_5, $NbCrO_4$) along external oxide ridges. These were inspected via X-ray photoelectron spectroscopy (XPS), Auger Electron Spectroscopy (AES) and Raman Spectroscopy [1, 2, 8, 10, 11, 14–17, 128, 144, 166, 171, 174, 175, 179, 185–188]. Oxides such as these are often porous in nature (in comparison to protective chromia), meaning their presence may reduce the protective qualities of the external oxide scale often leading to spallation after 10s of hours of exposure to relieve compound stresses [176, 181]. Mixed oxides like this with high PBR > 2.0, i.e. presence of Nb_2O_5 (PBR = 2.61) detected in the oxide

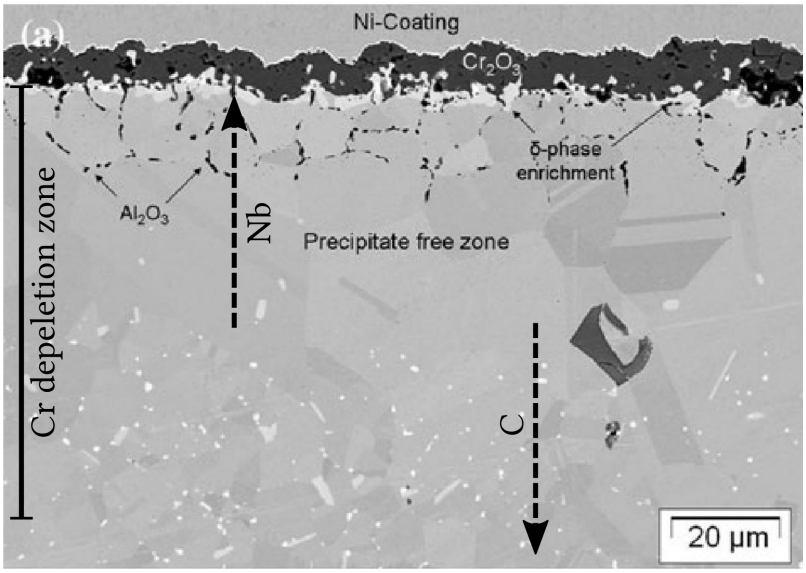


Figure 4.22: BSE-SEM micrograph showing the oxide film cross-section through wrought IN625, following thermal cycling at 900˚C for 1000 h. See the Cr depletion depth and the diffusion directions of Nb and C. Taken and adapted from Chyrkin *et al.* (2011) [7].

scales upon L-PBF IN718 formed at 1000˚C have been reported to experience severe spallation and delamination of the oxide layer via micro-cracking [128].

However, some research has stated the advantages of a mixed oxide, where Staszewska *et al.* (2016) argued the simultaneous formation of a $NiCr_2O_4$ alongside chromia was successful in the reduction in the diffusion velocity of metal ions to the scale, reducing the rate of oxidation and the bonding rate of metal ions and oxygen [179]. Local nobility variations may also occur due to the aforementioned nucleation of carbide and nitride precipitate alongside / inside the oxide scale. This can lead to strong microgalvanic interactions, increasing rates of oxidation further [98].

Some studies have reported Mn enrichment throughout and on the outer layer of the scale in IN625, IN718, and IN601, determined to be Mn spinel ($MnCr_2O_4$, Mn_3O_4) using Atom Probe Tomography (APT), Electron Probe Micro-analyser (EPMA) and Transmission Electron Microscopy (TEM) [3, 3, 5, 9–11, 15, 53, 57, 135, 176, 177, 181, 185, 188, 189]. This presence of Mn throughout protective chromia scale has been widely reported in literature for common Ni-based superalloys, where it is believed to improve the adherence of the external scale, specifically by reducing the activity of the Chromia, and hence the formation of their more volatile species (CrO_3, at T > 900˚C) [5, 152, 181, 188].

Stott et al. explained that the mechanism for the spinel formation is firstly transient oxidation at the surface of the alloy (where the ΔG of MnO is more negative than the protective Cr_2O_3), which then allows for the diffusion of Mn through the chromia outer scale. Here Mn-rich spinel can form either homogeneously throughout the scale, or on the outermost layer, as shown by Arnold

et al. (2018) which can be viewed in Figure 4.24 [9]. This is possible even with minor amounts of Mn (~ 0.04 wt.%) due to the rapid diffusion of Mn through chromia, where the diffusion coefficient of Mn is recorded to be two orders of magnitude higher than Cr ions [188, 189].

4.5.3 Internal oxide

Alumina (Al_2O_3) internal oxide is formed inter/intragranularly beneath the oxide scale, due to the ingress of oxygen from the atmosphere through the scale, and via micro-cracks here (see Figure 4.23 and Figure 4.22) [5, 7, 9, 15, 187]. This occurs due to aluminium's higher reactivity with oxygen than chromium, allowing alumina to form at lower oxygen partial pressures in the sub-scale region inter/intragranularly [17, 187]. Presence of the Alumina internal oxide at grain boundaries have been observed to stabilize the parent metal alloys original microstructure prior to exposure, by effectively pinning the grain boundaries and preventing small grains from undergoing coarsening in the oxidation effected zone [1, 7, 166]. Internal oxides have further been shown to lead to a change in the stress state of the oxidation affected region in the substrate, lowering residual stresses compared to the oxide surface [155]. Alumina at grain boundaries can generate compressive stresses in the substrate due to the volume increase and difference in the CTE between itself and the bulk. Here the bulk acts to constrain the alumina by placing it under compression (PBR > 1.0) [157, 168]. Overall, increased rates of internal oxidation have been reported in L-PBF IN625, leading to poorer resistance to oxidation than in traditional wrought alloy [1]. This has been attributed to minor chemical compositional variations, particularly in Si, and the rapid formation of a protective SiO_2 subscale in the unique case of L-PBF IN625.

4.5.4 Precipitation and δ-phase in the oxidation-affected region

A thin layer of δ-phase (<10 μm) is reported to form at the scale/alloy interface for both IN625 and IN718, occurring as small islands at short exposure and forming a near-continuous layer at the interface at longer periods at high temperatures (See Figure 4.24) [7, 9, 11, 15, 176, 182, 190]. This has been observed to remain chemically stable for temperatures ranging from 700 – 1000°C, its presence has been detected and confirmed across multiple studies both experimentally and via diffusion and thermodynamic modelling using DICTRA. The exact effects of this phase at long thermal exposures are yet unknown, as are the effects of the enhanced microsegregation of Nb in AM material [1, 7, 9–11, 14, 15, 53, 175, 191, 192].

Primary carbides (Nb,Ti)C and nitrides (TiN) have been reported to precipitate in the bulk microstructure of as-received and isothermal oxidised IN625 at size ranges of 10 – 12 μm, fabricated

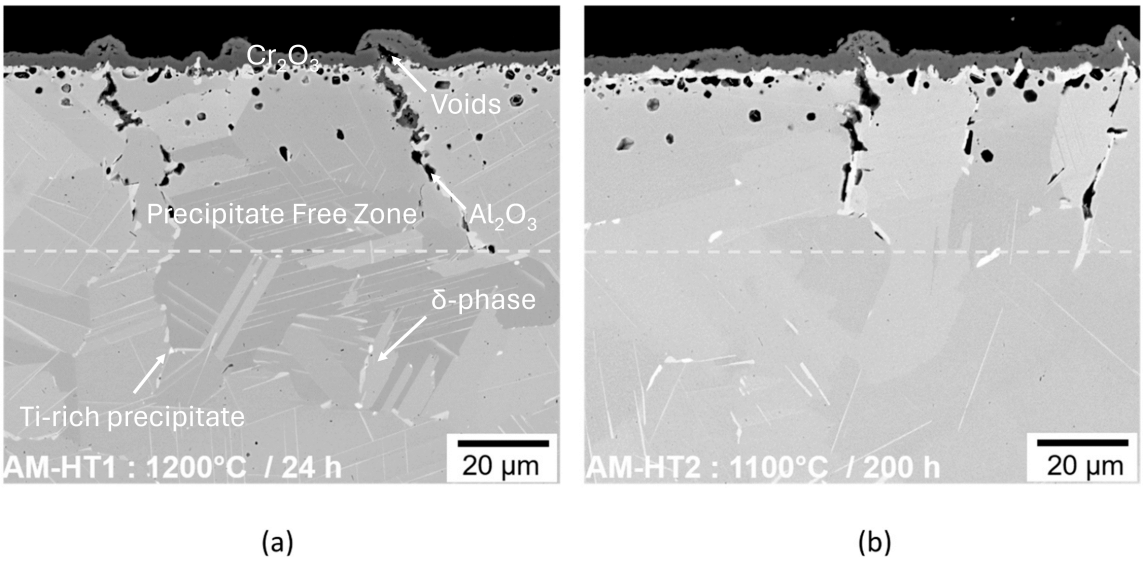


Figure 4.23: BSE-SEM micrograph showing an oxide cross-section through L-PBF IN625 following isothermal oxidation at 900˚C, for 168 h. (a) L-PBF IN625 heat treated at 1200˚C for 24 h, (b) Coarse grained L-PBF IN625 heat treated at 1100˚C for 200 h. Taken and adapted from Chyrkin *et al.* (2022). [1].

via wrought and AM methods, as shown in Figure 4.24 [9, 10, 57]. M_6C carbides enriched in Cr, Ni and Mo have been found to form and coarsen in the sub-scale region during high temperature exposures, as well as δ-phase upon grain boundaries and inside of grains [7, 9, 47, 128]. Here microsegregation of Nb acts as nucleation sites for the intermetallic to form, where similar to alumina, δ precipitates are able to provide a pinning effect upon grain boundaries to limit their coarsening [13, 176]. At long exposures (100s – 1000s h), the distribution of these precipitates in the sub-scale region varies with time, where a precipitate free zone is demonstrated to form beneath the oxide scale at increasing depths with time [7]. Due to this depletion in Nb, grains in the vicinity of the precipitation free zone have been observed to experience coarsening, appearing larger than grains inside the bulk of the alloy [1].

Chyrkin *et al.*, proposed a mechanism for the growth of δ-phase and the migration of precipitates into the bulk from the sub-scale region at 900 – 1000˚C [7]. During oxidation, Cr is depleted from the microstructure to form chromia at the surface of the alloy. This produces a sub-scale depletion profile of Cr from the scale to the bulk of the alloy, which increases with depth over time (See Figure 4.25, showing ~15 wt.% Cr at the surface of the bulk alloy, with a depletion depth of approx. 60µm after 1000 h exposure). This Cr depletion produces a change in the chemical potential, μ (the rate of change of the Gibbs free energy w.r.t to the number of moles of the i^{th} component), of other elements in the sub-scale region; particularly Nb, Mo and C (See Figure 4.26) [7, 66, 152]. In areas with a lower mass fraction of Cr (near to the oxide surface), the activity of Nb (and to a lesser extent Mo) decreases, causing diffusion of Nb and Mo from an area of high to low activity;

from the bulk of the alloy to the scale/alloy interface to form δ-phase. The opposite occurs with C, where activity increases in areas of low Cr mass fraction. Hence C diffuses from the sub-scale, back into the bulk of the alloy; dissolving $(Ni,Mo)_6C$ and creating a precipitate depleted zone (~60 μm deep when oxidized for 1000 h at 900°C). Chyrkin *et al.,* (2011) demonstrates these mechanisms through the use of Glow Discharge Optical Emission Spectroscopy (GDOES) depth profiles of each element in the scale. It is stated that the amount of Nb depleted is approximately equal to the peak of Nb enrichment at the scale alloy interface; demonstrating that Nb diffuses towards the oxide scale during exposure. The opposite occurs for C, where depletion and enrichment do not correlate, showing that C diffuses back into the bulk alloy [7].

The mechanism of δ-phase formation has not been explored in L-PBF material, where it is unclear how the highly segregated microstructure will affect oxidation mechanisms, the morphology of the film and its stress state. Elliot and Hampton investigated the effects of Nb (from 7.7 – 10 at.%) upon the cyclic oxidation of wrought Ni-Cr alloy, where it was observed that contributions of Nb lead to reduced spallation of the protective oxide scale, as well as fewer instance of internal

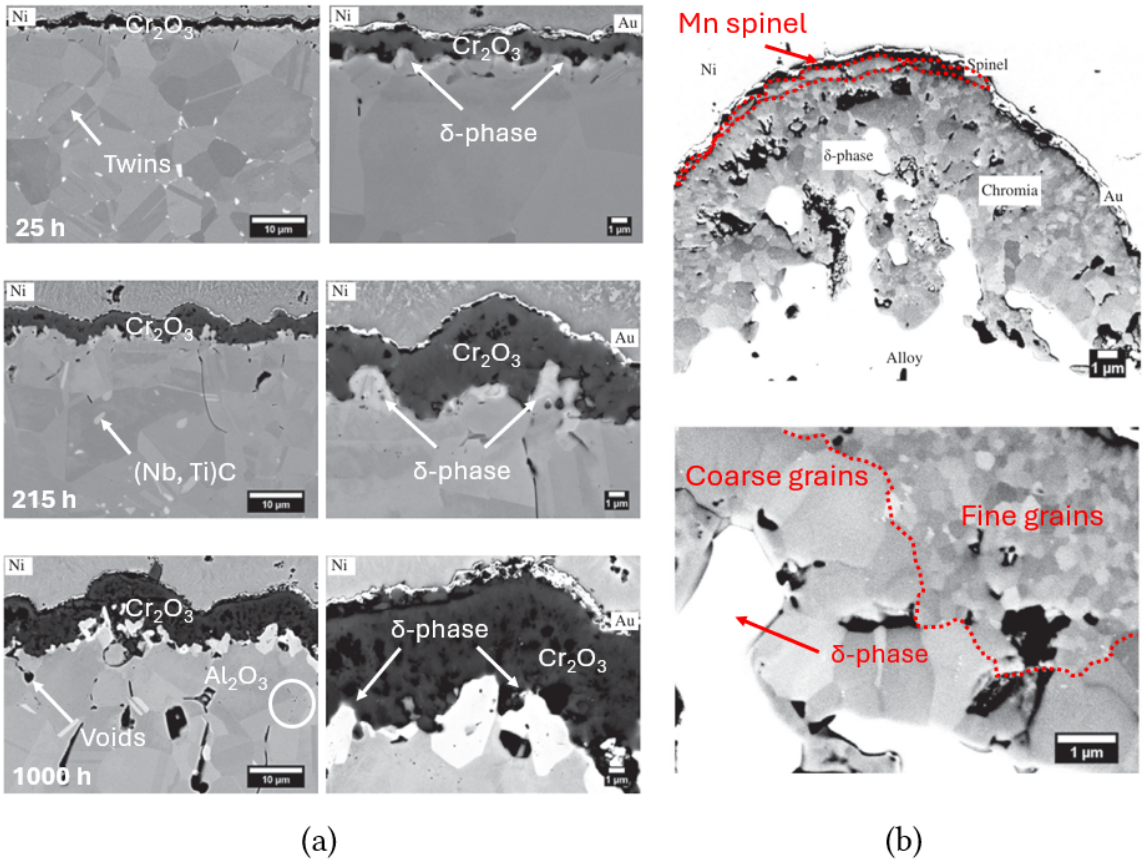


Figure 4.24: (a) BSE-SEM micrographs showing wrought IN625 following isothermal oxidation at 900°C, for periods up to 1000 h showing the oxide cross sections after 25 h, 215 h, and 1000 h. (b) Channelling electron contrast (ECCD) micrographs illustrating the duplex fine/coarse grain scale observed after 1000 h. Note the Mn-rich spinel at the outermost layer of the external oxide. Taken and adapted from Arnold *et al.* (2018) [9].

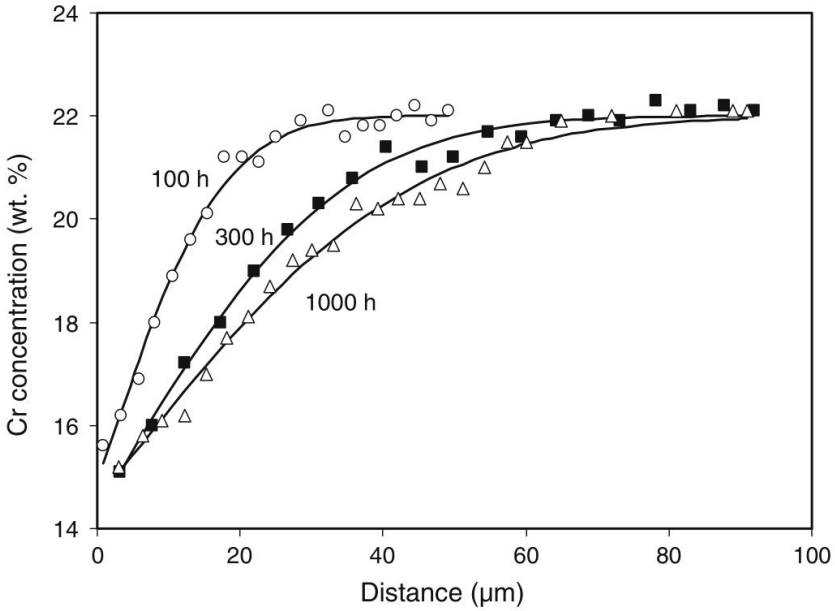


Figure 4.25: Cr depletion in Wrought IN625, 900˚C for t= 100 - 1000h. Chyrkin *et al.* (2011) [7].

oxidation, so much so that the mechanism of oxidation tended more towards cubic rates compared to traditional parabolic behaviour [193]. An improvement in the protective qualities of chromia via Nb was further corroborated by findings by Delaunay *et al.* who suggested that δ-phase formation at the scale/alloy interface may improve oxidation properties of Ni-based superalloys, by acting as a barrier for the diffusion of ions [11, 185, 191]. This is by virtue of Cr low solubility in the Ni_3Nb δ-phase. Kumar *et al.* (1996) explored similar themes, where it was revealed that the presence of Nb, Ta and Al near the oxide surface was advantageous in the control of oxygen diffusion through the bulk, hence limiting the thickness of the external oxide formed; though this was mostly prominent below 1000˚C where the solubility of Nb is highest [2].

On the other hand, many have postulated the deleterious effects of the near-continuous δ-phase layer at the scale/alloy interface. Parizia *et al.* (2020) observed severe wrinkling of the chromia scale occurring directly above islands of the δ-phase, generated by growth stresses as a result of the mismatch in volume expansion between the precipitate, external oxide and bulk material. This change in volume during exposure was expected to have led to micro-cracking of the protective chromia, and the accelerated oxidation of the bulk alloy [7, 9, 15, 127]. It is also argued by Chyrkin *et al.* (2011) who observed significant spallation of wrought IN625 after 1000 h exposure at 900˚C, attributed to the micro-cracking of chromia, driven by the presence of the δ-phase particles at the scale/alloy interface [7].

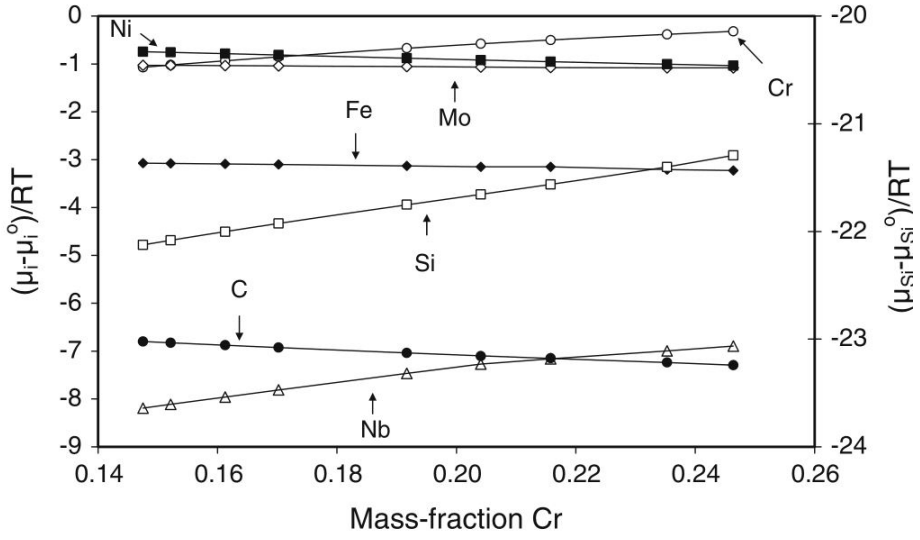
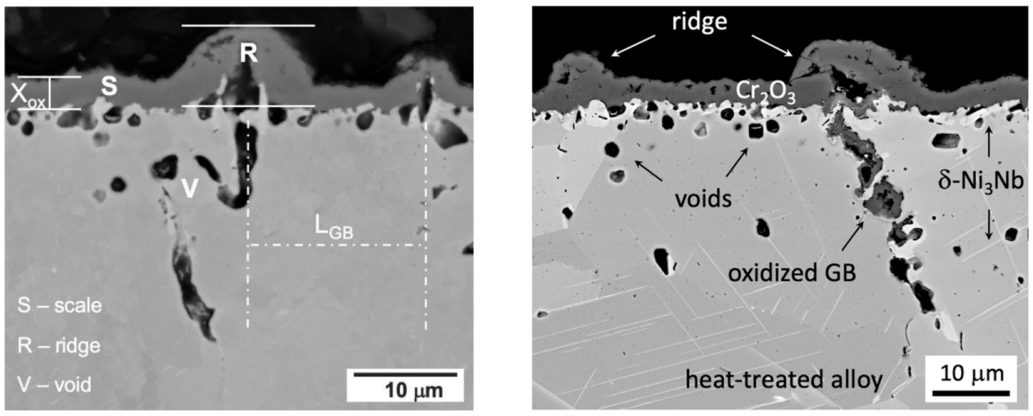


Figure 4.26: Chemical potentials of elements in IN625, 900˚C, plotted as a function of Cr content. Chyrkin *et al.,* (2011) [7].

4.5.5 Voids and cavities in the sub-scale

Kirkendall voids and cavities (reported to have diameter < 5 µm by Sanviemvongsak *et al.* (2018)) are reported to form readily in the oxidation affected region (at interfaces, the bulk and grain boundaries) beneath chromia and alumina scales following high temperature exposure (T = 850˚C – 1050 ˚C) for both wrought and AM Ni-based superalloy [1, 3, 5, 7, 10, 14, 16, 17, 128, 144, 174, 175, 187]. This effect has been shown to be more pronounced in AM Ni-based superalloys such as 625 and 718, forming in times as little as 2 h in L-PBF IN625 oxidised at 900˚C [1, 144, 187]. As well as higher temperatures, the dimensions of a component can also worsen this effect, where void



(a) Ridge void

(b) Spherical voids + Backfilled voids

Figure 4.27: SEM-BSE micrographs showing the two morphologies of Kirkendall voids observed in L-PBF IN625 exposed to 900˚C, for 168 h. (a) Ridge voids, and (b) Spherical voids. Taken and adapted from Chyrkin *et al.* (2022) [1].

formation is enhanced in thinner sections of material, particularly for foils of Ni-based superalloys, shown by England and Virkar (1999).

Two different void morphologies are commonly observed: individual randomly distributed spherical voids, or alternatively elongated voids forming under ridges in the oxide. Chyrkin *et al.* (2022) outlined a possible mechanism for ridge void formation, whereby the protective chromia becomes corrugated over time by growth stresses generated between the base metal and the growing oxide. Plastic deformation is required to alleviate these stresses in the growing film. This causes the scale to buckle and form ridges, thus, delaminating from the metals surface, allowing for the ingress of oxygen and the opening up of inter/intragranular voids (see Figure 4.27(a)) [1, 144, 155]. The ridges forming above voids tended to occur upon grain boundaries, showing oxides twice as thick than the that of the adjacent scale, showing enhanced rates of oxidation [1]. Similar results were reported by Parizia *et al.* (2020) who observed ridges and evidence of buckling after 96 h of oxidation [15].

Spherical voids (see Figure 4.27(b)) however form as a result of significant Cr depletion in the sub-scale region Figure 4.25, exacerbated by spallation of the protective scale and possible Cr evaporation via volatilisation [144]. This is by way of oxidation, leading to vacancy injection at the surface of the alloy. The steeper the Cr concentration gradient, the greater the net flux of vacancy injection at the scale/alloy interface via the loss of Cr ions in the bulk metal. As these vacancies increase in density and coalesce, voids begin to form. These occurs more readily along grain boundaries due to the faster rate of Cr loss from the bulk to the scale along the interface, acting as a short circuit diffusion pathway [1, 10, 194].

Regardless of the morphology, voids present can lead to direct contact between the gas phase and the metal substrate, leading to enhanced rates of oxidation, as well as a loss of coherency and the eventual spallation of the oxide film by the concentration of localised stresses [1, 17, 157]. Void formation was reported to be more prominent in L-PBF IN718 than in wrought alloy by Sanviemvongsak *et al.* (2018), who attributed this affect to the higher dislocation density in AM alloy, allowing for a greater amount of annihilation of vacancies by dislocation climbing at the metal/oxide interface and thus recrystallisation [187].

4.5.6 The effect of grain size and heat treatment

The effect of solution heat treatment was investigated by Parizia *et al.* (2020), where it was demonstrated that as-built L-PBF IN625 showed higher oxidation resistance compared to the solution heat treated condition when exposed to 900˚C for a period of 8 – 96 h [15]. This was postulated to be due to the faster formation of a compact oxide layer due to faster rates of diffusion along a

higher density of grain boundaries owing to the finer grain structure encountered with AM IN625, supported by works by Trindade *et al.* (2010) investigating the effects of grain size in wrought IN625 [142, 195]. In the case of the solution treated IN625, coarsening of the precipitates (namely δ) lead to an increase in lattice parameter of the bulk Ni phase.

Further to this, more recently Chyrkin *et al.* (2022) investigated the impact of grain size, AM anisotropy and texture by way of the application of hot rolling and heat treatment (ageing), where it was determined that significant differences in grain size (Coarse grained alloy ~100 µm, fine grained ~15 µm,) significantly affected the oxidation rate, but not the intergranular oxidation morphology. The accelerated kinetics observed in AM material was attributed to significant intergranular oxidation, as well as differences in the minor chemical composition of the powders used (i.e. Ti, Mn, Si, Al and S) compared to wrought materials in literature [1, 196]. Similar conclusions were made by Kim *et al.* (2009) when investigating the oxidation of Alloy 617 and Haynes 230 at 900°C and 1100°C, who argued the effects of Ti and Mn alloying content on the accelerated formation of mixed spinel such as $MnCr_2O_4$ and TiO_2 [188]. Here differences between the CTE for each spinel phase contributed to stress generation and consequently spallation of the oxide.

4.5.7 Oxide Dispersion Strengthened (ODS) Inconel 625 alloy

An ODS variant of SPS IN625 with additions of nano yttria investigated by Arnold *et al.* also studied the effect of grain size, where it was found to show oxidation rates which were 100 times slower than wrought IN625 and competitor alloys, even outperforming rates observed for the

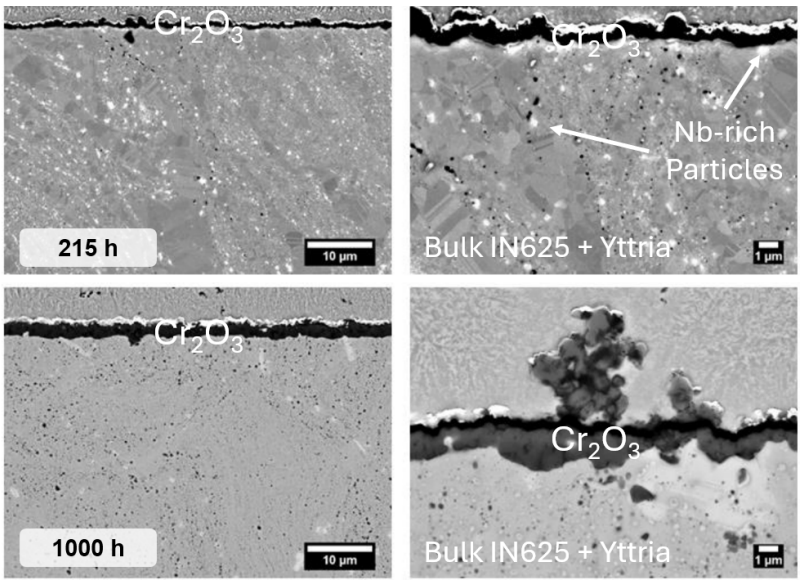


Figure 4.28: SEM-BSE micrographs showing the oxides formed upon ODS IN625 manufactured using SPS after 215 h – 1000 h exposure to 900°C in air. Taken and adapted from Arnold *et al.* (2018) [9].

likes of a pure chromia scale (see Figures 4.21 and 4.28) [9, 149]. This is postulated to be due to less doping of the chromia by Nb compared to wrought alloy. Increased Nb content in ferritic steels has been shown to lead to an increased rate of oxidation if free to diffuse in the bulk [197]. This effect was lessened in the ODS variant of IN625, where Nb was confined in carbides, preventing the effect. Cruchley *et al.* reported similar effects, where Ti-doping (the Wagner-Hauffe effect) of chromia in RR1000 Ni-based superalloy led to increased rates of oxidation, where Ti ions have enhanced mobility through the chromia scale to form oxides in the outermost layer [156, 181]. Quadakkers (1990) produced a literature review covering the ODS effect for a range of high Cr Ni-based superalloys, attributing the improvement in oxidation rate via control over the grain refinement over non-ODS alloy compositions. This is thought to have occurred via a change to the oxidation mechanism, whereby the ODS presence led to a reduction in the cation diffusion within the scale, preventing formation of a non-adherent, convoluted mixed spinel, as well as increased vacancy density at the scale/alloy interface. Smaller surface grain size also alloys for enabling of ease of relief of surface stresses, reducing the likelihood of micro-crack formation [66, 154, 198]. ODS effects can also be beneficial in reducing the compressive residual stresses experiences by the substrate during isothermal oxidation. This is by suppressing internal oxidation in the alloy, and reducing strain induced by lattice mismatch [155].

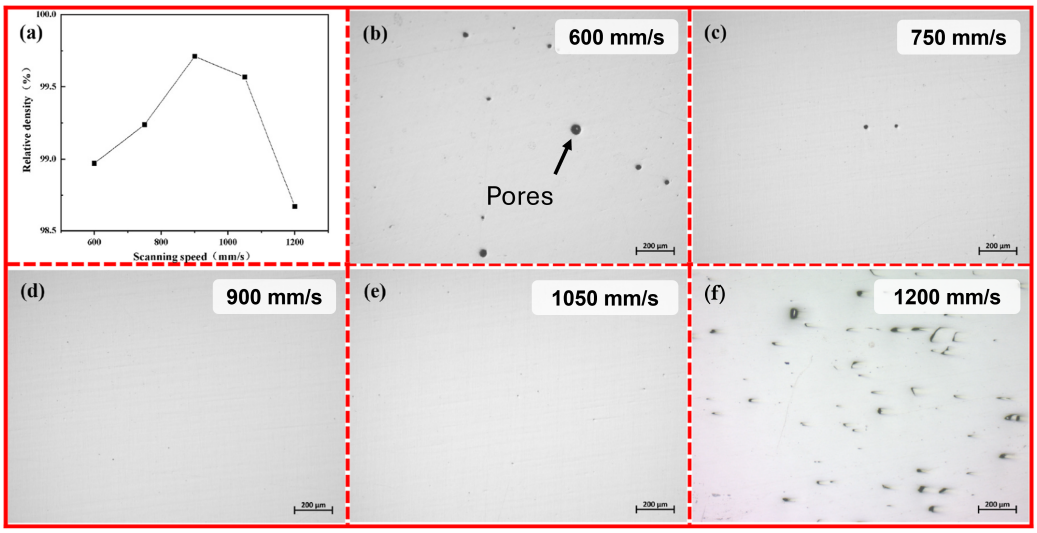


Figure 4.29: SE-SEM micrographs showing the relationship between scan speed and the relative measured densities for L-PBF IN625. (a) depicts a line graph of the relative density (%) recorded for increasing scan speed, (b) 600 mm/s, (c) 750 mm/s, (d) 900 mm/s, (e) 1050 mm/s and (f) 1200 mm/s. Note the high density of defects in (f), showing incomplete melting and lack of fusion of powder particles. Taken and adapted from Huang *et al.* (2022) [17].

4.5.8 The effects of additive surface roughness and porosity

When studied with its as-built surface roughness, AM IN625 (and similar Ni-based superalloys e.g. IN718) exhibits poorer oxidation resistance due to the high surface roughness (R_a = 10 − 12 μm) and dislocation density inherent to the process (see Figure 4.21) [10, 13, 16, 17, 88, 98, 100, 133, 137, 187]. In the roughest case investigated by Sun *et al.* (2020) (R_a = 10.5 μm, using a 76 J/mm^3 energy density), the oxidation rate was measured to be 100 times faster than for wrought IN625, showing more cubic rates of oxidation (n=3) [16]. This was attributed to poor surface quality due to insufficient laser energy input, leading to lower part density and higher amounts of porosity (see similar results by Huang *et al.* (2022), Figure 4.29) [17]. Here pores are able to acts as nucleation sites from which pits can form from, allowing for stress concentration and the onset of SCC by reducing the threshold stress for crack initiation [98]. This has been reported to occur selectively at grain boundaries, leading to enhanced oxidation here as well as along weld tracks [98, 199].

Porosity induced by low scan speeds (size ranging 3 − 8 μm according to Wang *et al.* (2020) for Laser Metal Deposited (LMD) high Cr superalloy K648) have the potential to reduce oxidation resistance by accelerating the diffusion of oxygen within and into the bulk of the metal [16, 17, 144, 166]. Indeed, it was discussed that samples manufactured with the highest sample density exhibited the most continuous, uniform and adherent scales, and those with < 99.0% density formed loose, non-protective oxides (see Figure 4.30. This was discussed by Jia *et al.* (2014) who investigated L-PBF IN718 in high temperature air. Here samples with higher volumetric density (~97.8% with VED = 70 J/mm^3) tended to show improved oxidation resistance, where more porous samples (~92.5% with VED = 130 J/mm^3) oxides experienced severe amounts of spallation. At higher VED where pore density is decreased, the chromia scale morphology become more homogeneous, showing denser granular oxides with little to no spallation or cracking [144, 176].

This was similar to Julliet *et al.* (2018) and Sanviemvongsak *et al.* (2018) whose investigations with L-PBF IN718 which both determined that unoptimized parameter selection led to large internal oxidation attack and a resultant large mass gain (see Figure 4.31) [176, 187]. Hot Isostatic Pressing (HIP) treatments can be applied to close pores resultant of low VED, and to densify AM samples to improve the oxidation resistance to rates lower than that achieved with solution ageing. HIP treatments applied above 1020˚C have also been reported to dissolve any δ-phase resulted of the manufacturing [128].

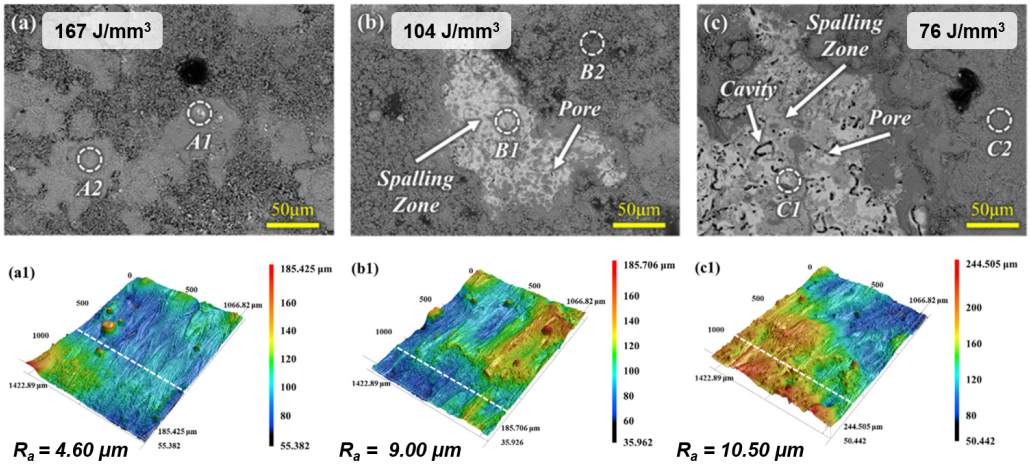


Figure 4.30: A selection of SEM-BSE micrographs showing the external oxide formed after 100 h of isothermal oxidation at 900°C for L-PBF IN625 samples manufactured with a VED of (a) 167 J/mm^3, (b) 104 J/mm^3, and (c) 76 J/mm^3. (a1), (b1) and (c1) displays the 3D surface topographies of the aforementioned samples prior to oxidation, respectively. Taken and adapted from Sun *et al.* (2020) [16].

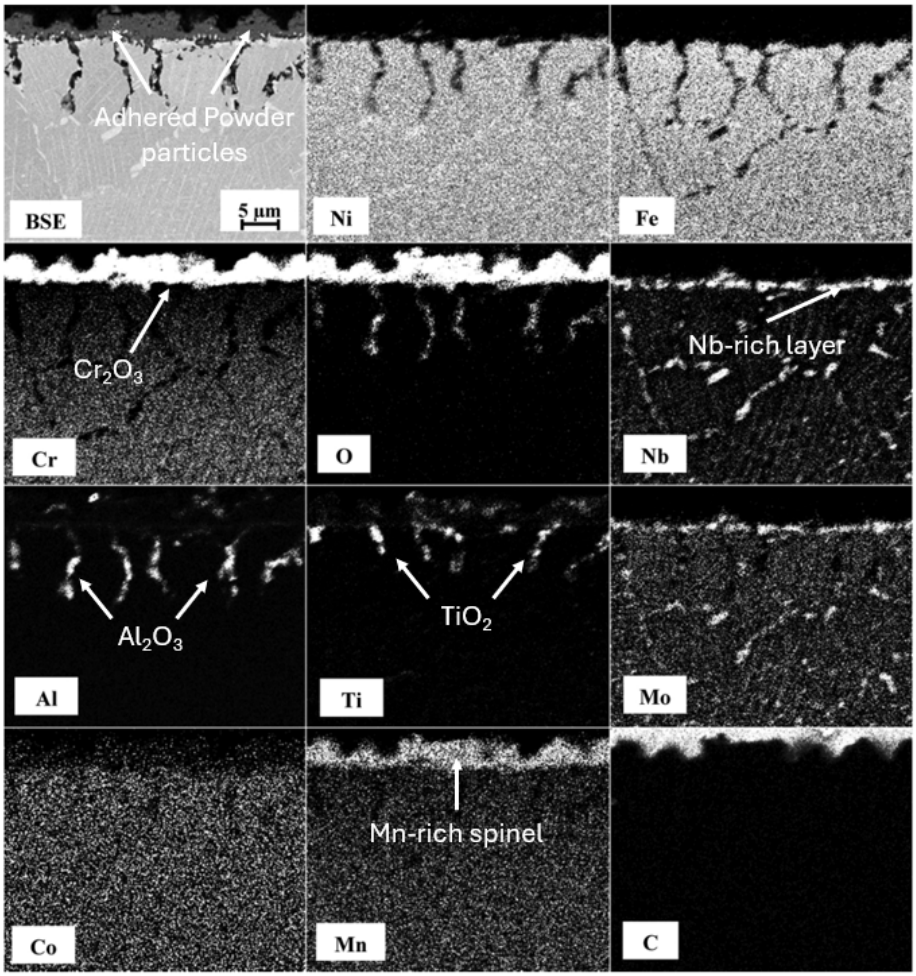


Figure 4.31: BSE-SEM micrograph and corresponding EDS maps showing the distribution of elements in the cross-sectioned oxide scale formed upon electron beam melted IN718 exposed to 850°C for 1000 h. Taken and adapted from Sanviemongska *et al.* (2018) [187].

4.5.9 The effects of high surface residual stresses

The effects of high stress surfaces (i.e. shot peening) have been widely investigated upon Ni-based superalloys in high temperature oxidative environments in the literature [98, 200]. Reynolds *et al.* (2018) studied the effects of grain size and shot peened surface finish for RR1000 after isothermal exposure to 650˚C for up to 4000 h. Here it was found that shot peening influenced the external oxide morphology more significantly in coarser grained alloy than finer grained RR1000, where chromia was seen to buckle. This was not the case for the traditional ground specimens, which did not show buckling or spallation of the protective scale. Buckling was attributed to the chromia acting to relieve the compressive in-plane growth stresses present. Shot peening is thought to have contributed to these stresses and the buckling behaviour of the protective scale [200].

Similarly, Chen *et al.* (2020) investigated the effects of laser shock peening upon the surface finish and subsequent oxidation rate in high temperature air. Here it was postulated that the high dislocation and defect concentration in the sample surface acted to provide short circuit diffusion channels for the transport of Cr ions to the external scale to allow for the accelerated growth of a dense protective oxide layer [13, 115]. Other works investigating the additive surface in isothermal oxidation environments suggest that the high dislocation density present in as-built alloy surfaces may actually improve the oxidation resistance, by their similarity to highly deformed structures [98].

4.5.10 Summary

Collectively, these results suggest that further work is needed at longer exposures to determine the full effect of surface roughness upon the oxidation of IN625. It is also very important to note that any surface finish with an irregular surface profile (i.e. adhered powder particles, ridged surfaces from CHEF or shot peening) that the surface topography is assumed to be perfectly planar when calculating the sample surface area for use in Equation (4.7) to calculate the growth rate of the oxide. Sanviemvongsak *et al.* (2018) discussed the impact of these inaccuracies upon the rates determined for L-PBF and EBM manufactured IN718 [187]. Quantitative correlations were made to relate the parabolic growth rate constants calculated to the surface area for non-planar AM surfaces with adhered powder particles and balling effects. Here it was observed that the surface areas measured for tokens with AM surfaces are often underestimated; and the resultant growth rates calculated an overestimation (up to 16× higher for EBM IN718 samples). This also becomes an issue when measuring for oxide thickness, where a non-planar oxide with a convoluted shape can prove difficult to measure consistently. Therefore, it may be concluded that oxidation rates in the literature for AM alloy could be considered to be conservative values.

4.6 Corrosion of Ni-based superalloys in nuclear applications

With ever increasing demands for improved efficiency in new build generation IV fission and fusion reactors, materials resistance to higher temperatures has become a critical design criterion for components with complex geometries [24, 29]. The Nuclear industry is therefore currently exploring how additively manufactured Ni-based superalloys might be applied in current and new Light Water Reactor (LWR) designs. Wrought alloys such as IN625, IN825, IN718, IN600, as well as multiple ferritic-martensitic steels have been thoroughly characterised for their common range of operation temperatures and pressures for use in cladding, steam generator tubing, heat exchanger piping, and control rod components [23, 29, 57, 68, 201, 202]. The same cannot be stated however for additively manufactured Ni-based superalloys.

4.6.1 Sub-to-Supercritical, Current and future generation fission reactors

Pressurised Water Reactor (PWR) environments are designed to operate at temperatures ranging from 260 – 350˚C, and pressures of 12 – 15 MPa [24, 25, 29, 30, 32, 55, 203–205]. Newer designs for sub-critical, supercritical and ultra-critical water reactors (SCWR) tend to exist within the temperature range of 425 – 620˚C for pressures up to 22.5 – 25.5 MPa, and O_2 presence of 500 ppb – 8 ppm [24, 25, 29, 30, 32, 55, 203–205]. It is of paramount importance alloys in these environments are tolerant to a combination of high temperatures, pressures, water chemistry variations, as well as high radiation flux [206, 207]. Across these systems, components experience irradiation levels of a maximum of 15 – 100 dpa (displacements per atom) across their lifetime. This is a key step in the oxide failure mechanism, where irradiation not only affects the component mechanical properties via irradiation embrittlement, but the surrounding water chemistry as well. Irradiation leads to radiolysis and the formation of H_2O_2 which raises the corrosion potential of alloys in the environment by increasing the dissolved oxygen content [29, 204]. It must be noted however, that the effects of irradiation will not be explored out of simplicity for the duration of this work, and were deemed outside of the scope of the study.

The nominal chemistry of primary water in PWRs is maintained alkaline (pH ~ 10.5) to limit corrosion. This is achieved via small additions of Li in the form of LiOH [29, 208]. Here oxidation rates increase with pH levels > 10, where a dependence relationship occurs between pH and Fe cation flux across the protective oxide scale. This is due to the concentration of ionic defects and

vacancies in the external oxide scale, which changes with varying pH in the system. For alkaline solutions common to PWRs, the primary defect for ion transport in the oxide is the Fe^{2+} vacancy [209].

Ni-based superalloys are chosen as a candidate material due to their superior oxidation resistance over ferritic-martensitic steels [29, 57, 206, 210, 211]. A key motivator in their selection is that at T > 375˚C and P > 22.1 MPa, the primary water experiences a change in its properties, becoming less dense, increasing the likelihood of corrosion [68]. This occurs as the solubility for organic compounds (such as Cl, S, and P impurities), and oxygen content in the primary water increases [32, 206, 212].

Hydrogen additions (~25 – 30 cm^2/kg) can be added to absorb oxygen presence and to hydrogenate the reactor primary water. This results in a slower oxidation rate of the alloy at higher temperatures, and the destabilising of the non-protective NiO oxide via diffusion of Ni to the surface via grain boundaries [68]. Here the hydrogen present acts to produce a more reducing environment in the primary water, making the reduction reaction of NiO to Ni and water more favourable. The transition of the NiO layer from stable to unstable occurs when the hydrogen content in the primary water reaches ~9.16 cm^3/kg, for standard operational temperatures of 320˚C [202]. It is important that hydrogen levels are carefully controlled around this value in order to limit the initiation and propagation of cracks, where Ni-based superalloys tend to exhibit the highest susceptibility to SCC or Primary Water Stress Corrosion Cracking (PWSCC) under reducing conditions close to the Ni/NiO transition [202, 213]. PWSCC has been deemed the predominant mechanism for the degradation of Ni-based superalloys in PWRs, leading to the rupture and failure of components such as steam generator tubing and nozzles [202, 206, 207, 212, 213]. The effects of hydrogen partial pressure upon the corrosion behaviour of Ni-based superalloy and stainless-steel were investigated by Kim *et al.* (2016) using u-bend specimens. Results showed that little to no cracks were observed for samples corroded with 5 – 25 cm^3/kg hydrogen content in PWR water, at times < 100 h [202]. Despite their poorer susceptibility to SCC compared to the ferritic-martensitic steels, it is believed that Grain Boundary Engineering (GBE) approaches via CSL boundaries and grain texture control could be applied to rectify this weakness [29].

For the purpose of this study, PWR hydrogenated primary water conditions will be discussed primarily, using key literature covering IN625 and Ni-based superalloys performance in various supercritical designs for comparison, and to inform key corrosion mechanisms present. Thus, attention must be brought to the fact that differing oxygen content across various PWR and future designs will lead to changes in the composition and structure of oxides formed [204]

4.6.2 Oxide kinetics

In terms of kinetics, IN625 and other similar Ni-based superalloys exhibit low rates of corrosion in PWR primary water, following parabolic behaviour with rate constants independent of the O_2 partial pressure according to Kumar *et al.* (1996) [2, 23, 25, 214].

Parabolic rates calculated by Ziemniak (2003) showed the growth rate to be equal to 0.074 $mg^2/dm^2/h^{\frac{1}{2}}$ when held at 260˚C for 10000 h [214], where as expected, higher temperatures lead to thicker oxide scales grown. Potentiodynamics have shown this directly, where the corrosion current density of IN625 has been demonstrated to increase with increasing exposure temperatures, resulting in decreased corrosion resistance of the Ni-based superalloy [212]. For higher operational temperatures and pressures common to SCW (T = 600˚C, P = 24.8 MPa), Chang *et al.* (2011) determined the following parabolic relationship:

$$w^{2.21} = 1.4 \times 10^{-5} \cdot t \tag{4.14}$$

where w was the weight change (mg/cm^2) and t was the duration of the corrosion test (h).

Here Chang *et al.* (2011) determined a weight change of 0.15 mg/cm^2 for IN625 in SCW conditions. Generally, higher weight gain is experienced in corrosive PWR environments than supercritical temperatures (T > 360˚C), attributed to the increase dissolved oxygen in the primary water [204]. Was *et al.* (2007) discussed the effects of increasing temperature with SCW deaerated conditions at temperatures of T = 400 − 500˚C compared to PWRs, where it was shown that IN625 demonstrated 3× less corrosion than the likes of 316L stainless-steel [29]. This was supported by findings by Fujisawa *et al.* (2006) [210]. Further to this, the activation energy for the oxides formed upon Ni-based superalloy (IN625 and 690) was calculated to be equal to 140 KJ/mol compared to 210 KJ/mol for oxides grown upon stainless-steels (Type 304 and 316L) [29].

Corrosion rates of IN625 in the literature were seen to be affected by the sample geometry and dimensions, where lower oxide growth rates were recorded in thick-walled material, compared to thinner strips and foils, determined by Garcia and Fresnillo *et al.* (2014) [57]. This is supported by findings from England and Virkar (1999) for IN625 [3]. This is simply attributed to the lower sample area present, and a higher surface area to volume ratio for oxidative attack.

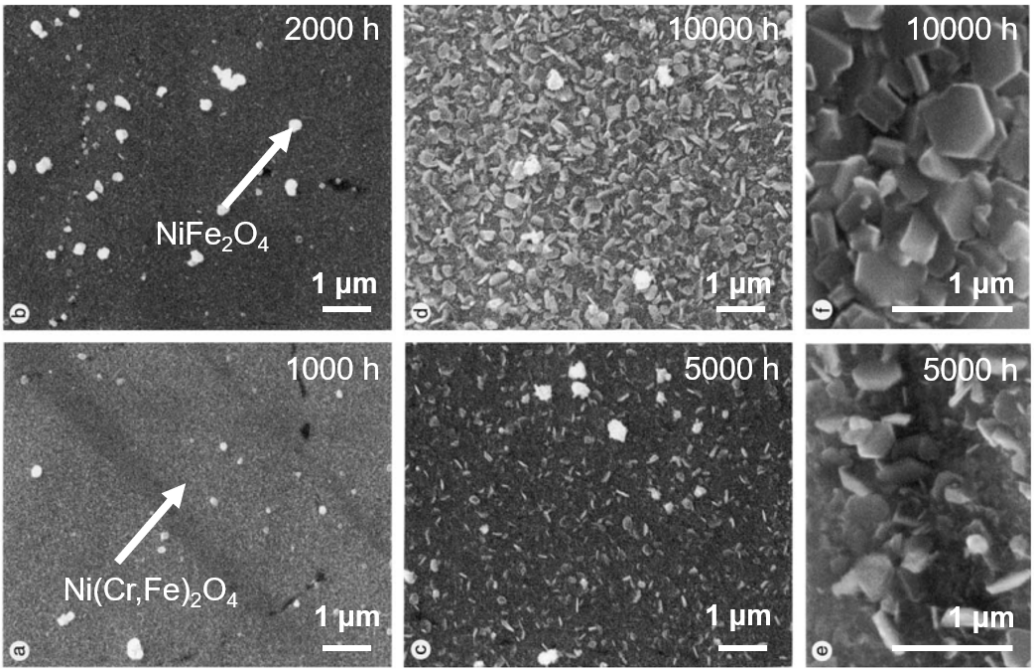


Figure 4.32: A summary of SE-SEM micrographs showing the external oxides formed upon wrought IN625 following exposure to PWR hydrogenated water, held at 260˚C for 1000 – 10,000 h. Taken and adapted from Ziemniak *et al.* (2003) [214].

4.6.3 External oxide scale

In PWR hydrogenated primary simulated conditions, IN625 forms a passive protective duplex scale, acting as a diffusion barrier to oxygen and organic solvents in the system to reduce the oxidation rate [29]. This is key to reduce the likelihood of releasing Ni-58, which upon activation with high energy neutrons can form the radioactive isotope Co-58 of metal cations into the primary water [205]. This is vital to keep the levels of radiation in the system to amounts as low as reasonably practicable (ALARP), according to the Safety Classification of Structures, Systems and Components in Nuclear Power Plants: SSG-30, as outlined by the IAEA (2014) [215].

Findings applying techniques such as SAED, grazing incidence XRD and SIMS revealed the oxide consists of a mixed M_2O_4-type $Ni(Cr,Fe)_2O_4$ spinel forming as irregular hexagonal shaped crystallites randomly embedded onto a Cr-rich thin oxide layer (see Figure 4.32) [23, 29, 30, 68, 201, 204, 205, 209, 212, 214]. The duplex layout of the oxide formed suggests non-selective oxidation behaviour, commonly viewed in Fe, Ni or Co alloys, meaning all component alloying elements oxidise in amounts proportionate to their composition [29, 209, 214]. Oxide here grows by the diffusion of Ni^{2+} ions to the surface of the alloy to form a protective oxide layer [214]. Despite relatively low Fe content in IN625, Fe-rich spinel is able to form by means of over-saturation of the primary water in Fe^{2+} due to degradation of the stainless-steel autoclave during service [205, 209, 214]. These Fe cations are able to diffuse through the outer later via pores to the interface

to form large islands of the mixed $Ni(Cr,Fe)_2O_4$, free from volume constraints [68, 209]. These oxide islands were found in increase in size and number with longer periods of corrosion [29, 214]. Here the Fe-rich spinel tends to coarsen more readily, due to its faster diffusion coefficient through the Cr-rich layer, developing into rods and platelets at longer exposure periods at T > 450˚C [212]. Due to the irregular nature of the scale, the outer layer can exhibit porous behaviour and spallation, where the looser oxide reduces the alloys resistance to corrosion, shown by Behnamian *et al.* (2016) via EDS and TEM [201, 206, 209, 212].

The inner layer however, is reported to consist of fine, dense equiaxed grains enriched in Cr, which cover the entire surface of the alloy equally [24, 25, 55, 201, 205, 209, 214, 216]. This is reported to be very thin compared to the (Ni,Fe)-rich outer layer, with thicknesses values on average $\leq$1µm, often too small measure accurately without TEM [29, 30, 205, 214, 216]. It can however become thicker with higher exposure temperature and time to reach thicknesses up to 1.55 µm after 1000 h when moving towards more SCWR behaviour [24, 25, 30, 55]. For IN600 in standard PWR primary water conditions, Panter *et al.* (2005) identified the compact Cr-rich layer to be Cr_2O_3 via TEM. At higher operational temperatures, Chang *et al.* (2011) confirmed presence of chromite inside the inner layer using TEM, measured at a thickness of 27 nm following exposure to SCW for 24h at 600˚C [25]. Yang *et al.* (2017) and Robertson (1991) also detected the presence of Fe_2O_3 and Fe_3O_4 presence in the surface outer layer, predicted to occur due to the Fe saturation present in the primary water [68, 209].

It is suggested that the mechanism for formation of the inner chromite/chromia layer involves the selective oxidation of Cr. This relies upon the access of primary water transported through the oxide via defects such as micropores, grain boundaries and vacancies, where Cr^{3+} and Cr^{6+} cations are found to leach into the coolant water [25, 209, 212]. From this, elevated areas of oxide appear directly above grain boundaries during exposure, by means of short-circuit diffusion compared to the matrix [55, 57, 68, 206]. Here the duplex layers are able to form due to the inherent differences in the diffusion coefficients of the metal cations through the oxide layers. Faster diffusing cations (Ni^{2+}, Fe^{2+}) present in the bulk alloy are able to be transported to the outer layer, whereas slower cations such as Cr are retained closer to the surface of the as-received material. The order of decreasing diffusion rate is as follows: $Mn^{2+} > Fe^{2+} > Co^{2+} > Ni^{2+} \gg Cr^{3+}$ [55, 68, 209]. Consequently, the growth rate of chromia is considerably slower than that of the $Ni(Cr,Fe)_2O_4$ upon the surface, leading to Cr depletion (as low as 5 wt.%) in the sub-scale region, viewed experimentally using sputtering [25, 29, 201, 206, 209, 212]. The continuous diffusion of Fe and Ni cations from the bulk leads to a higher concentration of Cr and vacancies at the surface of the alloy, which hence drive the reaction [29, 55].

For low hydrogen environments, acicular shaped NiO is also reported to form on top of the mixed $Ni(Cr,Fe)_2O_4$ external oxide layer, increasing in diameter and thickness for increased exposure time (up to 1.42 µm after 250 h at exposures of 500˚C). [24, 25, 30, 55, 68, 204–206, 208, 212, 216]. This was confirmed using a combination of XPS and XRD by Tan *et al.* (2008), and via TEM and SAED patterns recorded by Sun *et al.* (2008) [23, 212]. Due to the lower free energy of formation of chromia compared to NiO, the non-protective oxide commonly forms on top of the spinel [25]. Studies involving Raman spectroscopy revealed that instances of NiO tended to form preferentially at low dissolved hydrogen conditions. This was more widespread at lower operational temperatures common to SCWR of ~400˚C and tended to decrease in presence as temperatures moved towards ultra-critical (~525˚C) [30, 55, 212]. This effect is attributed to the higher concentration of Ni^{2+} ions released into the primary water by the porous outer layer, where higher amounts of Ni^{2+} cation transport was observed compared to Cr^{3+}. As a p-type oxide (positively doped, electron deficient), the mixed NiO/M_3O_4 spinel outer layer of the external oxide is said to be formed and controlled primarily by the diffusion of Ni^{2+} cations from the bulk to the surface of the scale via grain boundaries [29, 208].

Altogether, the two layers and protective composite oxides interact with each other via the following reactions. Initially, NiO and chromia react via a solid solution reaction to form islands of the mixed $NiCr_2O_4$ [204, 206]. Alongside this, solid solution reactions between the non-protective NiO and Fe_2O_3 is also reported to occur, resulting in the precipitation of $NiFe_2O_4$. The formation of the Fe-rich $NiFe_2O_4$ is favoured in low oxygen partial pressure environments compared to the likes of the protective chromia scale [30]. Small presence of $Ni(OH)_2$ and NiOOH were observed by both Merwin *et al.* (2014) and Sennour *et al.* (2010) via XPS and TEM, respectively when exposed to sub-critical waters. [30, 205, 212]. It is understood that the outer layer was able to form by the

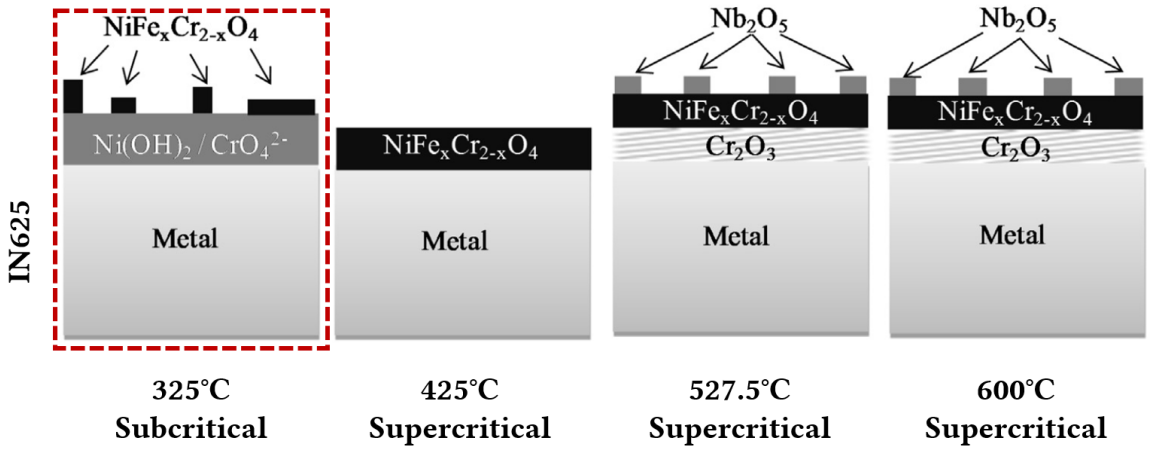


Figure 4.33: A schematic showing the duplex oxide films formed upon IN625 when exposed to sub-to-supercritical primary water. Taken and adapted from Rodriguez *et al.* (2017) [24].

outward diffusion of Cr^{3+} and Ni^{2+} to the primary water. Here the cations were able to react to with OH^- ions present [212].

A summary of the standard oxide scales formed for sub-to-super critical reactor conditions can be viewed in Figure 4.33.

4.6.4 Pitting corrosion

At higher temperatures of corrosion standard to newer SCWR designs (T > 500 – 600˚C), pitting corrosion occurs and competes with general oxidation mechanisms for IN625 [25, 32, 55, 206]. Compared to oxidation, this is a more targeted form of corrosion where holes or 'pits' are generated over time due to the stochastic loss of metal cations from the surface of the alloy [55, 217]. These pits have been recorded to vary from size ranges of 4.3 - 12.9 µm from 100 to 1000 h, respectively, occurring at inclusions in the surface of the metal [68, 204]. Inclusions include the likes of (Ti,Nb)-rich MC primary carbides and (Ti,Nb)-rich oxides, where local galvanic coupling effects take place between the precipitate and the matrix to produce instability in the protective scale and accelerated rates of oxidation and weight losses at early stages (~ 100 h) [23, 32, 206, 212, 216]. However, rapid levels of weight gain are experienced after longer periods (300 h), where the mass

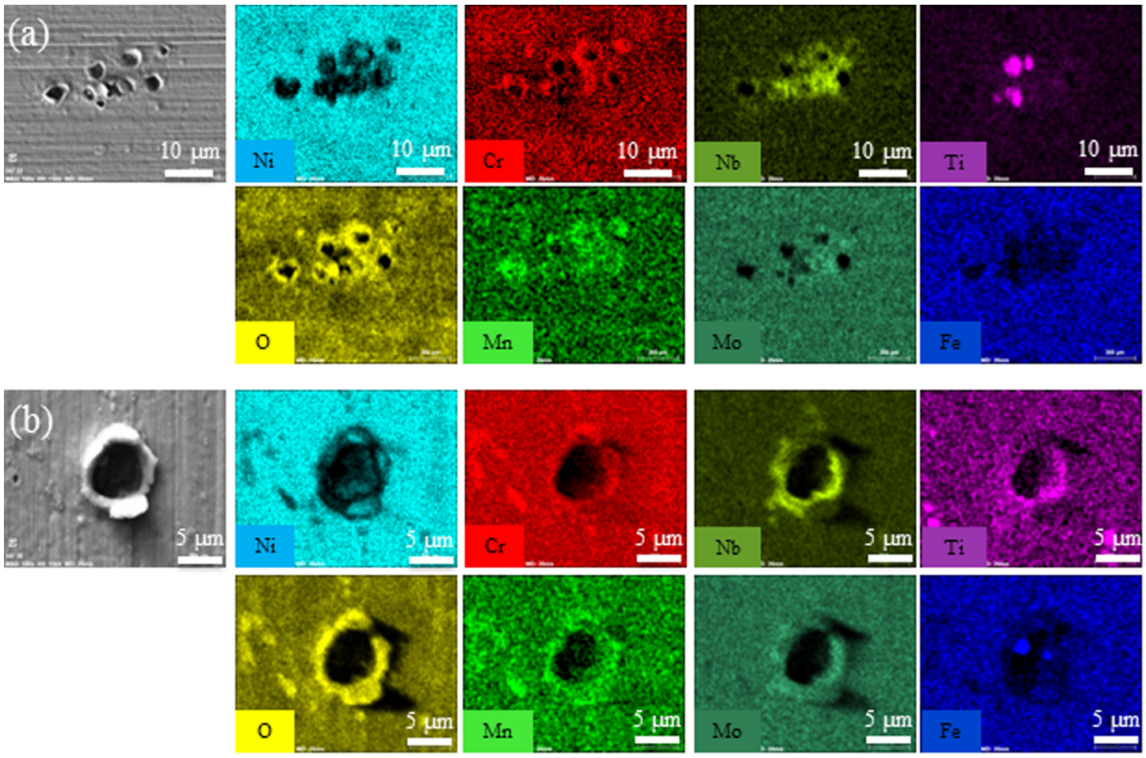


Figure 4.34: SE-SEM micrographs (a) and (b) with their corresponding EDS maps, showing the elements (Ni, Cr, Nb, Ti, O, Mn, Mo, Fe) present in and around pits formed upon the surface of wrought IN625 following exposure to SCW held at 800˚C for a period of 12 h. Taken from Behnamian *et al.* (2016) [206].

gained exceeds the amounts of oxide lost to via spallation and pitting [29, 216] .

Tan *et al.* (2008) and Rodriguez *et al.* (2017) reported the presence of Nb_2O_5 within pits imaged upon IN625 following exposure to SCW using XPS and EDS scanning, respectively. These can be viewed in Figure 4.34, where Nb and Ti enrichment is present in and around the pits formed [23, 25, 55, 206]. It is accepted that NbC inclusions in the surface can lead to the subsequent formation of Nb_2O_5 following oxidation [23, 25, 29, 203]. Here the high Ni, Nb content in IN625 contributed to the enhanced pitting, despite its high Cr and Mo content compared to similar alloys such as IN718 [24, 68, 147, 206]. The effects of pitting can be mitigated by an increase in the oxygen content, or indeed higher exposure temperatures common to SCWR designs. This is due to the faster establishment of a protective stable oxide [55, 204, 206].

Various literature suggests that the predominant cause for pitting stems from the formation and subsequent dissolution of Mo-rich oxides [68, 206, 212, 214]. Indeed, Nb and Mo precipitates were detected to be present in the surface of PWR hydrogenated water corroded samples of IN625 via GIXRD after 10,000 h exposure [212, 214]. Galvanic coupling effects with Mo-rich precipitates are predicted to be more significant, where the calculated electrical conductivity of Mo is 8× greater than Ti, and 3× than Nb, according to Tan *et al.* (2008) [23].

4.6.5 Surface finish effects and cracking in PWR and SCWR environments

As discussed in subsections 4.5.8 and 4.5.9, surface finish and surfaces stresses have a direct effect on the oxide crystallite chemistry and morphology, as well as inducing different concentrations of defects and dislocation densities. [205, 207, 218]. In particular, this has been found to influence the cracking mechanisms observed in IN625, where varying concentrations of metal ions can initiate cracking. The effects of machining have been widely investigated, where it is assumed to be deleterious to the alloy's resistance to PWSCC due to the roughness and machining marks left behind [25, 29, 207, 218]. Here machined and milled surfaces experience high levels of residual stress, exhibiting deep levels deformation up to 90μm [207]. These provide short circuit diffusion pathways to aid the accelerated diffusion of ions to form oxide. In addition, the peaks and troughs resultant of the milling process leads to the preferential nucleation of oxide upon raised areas of the sample [205].

Chang 2018 *et al.* (2018) studied the effects of such machining upon PWSCC, taking into account the roughness orientation, machining marks, and tensile residual stresses induced in the surface for Ni-based superalloy compared to stainless-steel. Here 316L type stainless-steel showed

accelerated rates of oxidation in high temperature hydrogenated water following slow strain rate tensile testing (SSRT). It was revealed that SCC propagated preferentially alongside marks left behind that were perpendicular to the surface loading direction, where the presence of a near-surface 'ultrafine grained layer' resultant of the machining process inhibited the progression of cracks. This layer was not present in low stressed ground samples, which exhibited longer and wider cracks. For comparison, a set of un-strained electropolished samples were also investigated. The oxides upon the electropolished samples were denser, and more stable in morphology, making these surfaces ideal for use in LWR environments [207, 218]. Although it was stated by Robertson *et al.* (1991) that electropolished surfaces begin to experience more accelerated rates of oxidation once a T > 350°C is exceeded, more common to newer SCW designs [209]. It was suggested by the authors that a grinding step be included to remove the tensile residual stresses resultant of the machining process, leading to a stress reduction of a maximum of ~335 MPa. This did not however, result in a decrease in the crack depth and rate reduction [218]

Epitaxial relationships between the growth orientation of the Cr-rich inner layer and the outer $NiCr_2O_4$ oxide layer were reported by Sennour *et al.* (2010) for Alloy 690 in aqueous PWR high temperature water [205]. Here certain grain orientations exhibited greater rates of oxide growth than other. Was *et al.* (2007) expanded upon this, showing IN690 grain orientation enhanced oxidation using EBSD IPF mapping [29].

4.6.6 Summary

With this information in mind, and the lack of literature covering the effects of high temperature hydrogenated water for AM IN625, it is clear more research is needed to elucidate the AM alloys usability in this environment and similar generation IV designs. Attention must be drawn to the fact that if pitting corrosion is the key corrosion mechanism for the alloy at short time periods by the formation of Nb, Ti and Mo inclusions, microsegregational effects common to AM IN625 could pose an issue for the protective qualities of the scales formed.

4.7 Grain boundary engineering and oxidation, control of microstructure and texture

Ni superalloys and austenitic steels may also be controlled in terms of their morphology, in particular the grain-aspect ratio and their texture/orientation by means of thermomechanical treatments such as cold rolling and heat treatment, or in this case through careful design parameter selection via AM [46, 62, 219].

Microstructural grading is defined as the variation of a particular structural feature i.e. grain morphology, size or texture within a component [50]. Grading in L-PBF can be achieved by changing parameters such as the laser power, speed, hatch spacing, and scanning strategy to modify the thermal gradient and solidification rate of a melt pool, and has been achieved for alloys such as IN718, 316L and Ti-6Al-4V [50, 68, 131, 220–225]. Careful selection of the heat input via the laser scan strategy can result in the formation of different localised grain sizes and textures, shown in L-PBF IN718 for use in aerospace turbine blades by Attard *et al.* (2020) [45]. This may allow for unique customization of functionality and performance, by controlling sub-grain features like cell size, grain growth and direction [226, 227]. Such features are key in the control of diffusion related phenomena involved in the degradation of alloys in-service, including SCC, creep, and fatigue cracking [228].

In addition to texture, research has shown that the introduction of plastic deformation prior to heat treatment promotes the formation Coincident Site Lattice (CSL) grain boundaries; introduced as a concept by Watanabe (1984) [34, 46, 173, 228–231]. CSL boundaries describe two crystal lattices which when translated can bring the lattices to a point of coincidence, i.e. where they perfectly overlap in a geometrical relationship. Grain Boundary Engineering (GBE) approaches can take advantage of the fast solidification rates in AM, to produce as-built components with significant levels of residual stress, as well an highly textured microstructures with columnar grains [34, 35, 38, 45, 83, 88, 98, 110]. FCC materials are applicable to this, due to their low stacking fault energy [230]. Grain Boundary Engineering (GBE) processing firstly requires that the strain level required exceeds 20-30% plastic deformation before a GBE effect is observable, following subsequent heat treatment for a long (t > 1 h) high temperature hold. [46, 230, 232].

CSL boundaries follow the Coincident Site Lattice model, where each characteristic boundary with a particular misorientation and axis is defined by its Σ values. For FCC Ni-based superalloys, CSLs with special character are categorised as $\Sigma < 29$, where Σ is determined by the reciprocal of the number of 'coincident' lattice sites between two adjacent grains[46, 219, 233, 234]. These low CSL boundaries ($\Sigma < 29$) are classed as special boundaries by virtue of their unique properties. This

includes the following characteristics [23, 235, 236]:

- Low grain boundary energy (1/50 of a random misoriented grain boundary);
- Lower susceptibility to solute segregation;
- Higher resistance to grain boundary sliding and shear stress;
- Lower rates of diffusion, giving greater resistance to intergranular degradation processes.

Twin boundaries, or twin family boundaries are especially important, defined as $\Sigma = 3^n$. These boundaries occur within the {111} direction, as a 'mirror' plane, showing high levels of resistance for diffusion related phenomenon. First order twins form initially during the recrystallisation of highly deformed grains, and subsequently the second, until a set of twin families are created (Σ3, Σ9, Σ27...) [219]. Here the grain boundary acts to minimise its inherent energy via the process of twinning and grain boundary misorientation.

When measuring for particular CSL boundaries, EBSD techniques are key. Multiple coincidence model criteria exist to apply a geometrical threshold for the accurate determination of one grain boundary misorientation to another. Most literature tends to apply either the Brandon Criterion (1966), or the more recent and updated Palumbo–Aust Criterion (1998). These provide the allowable angular deviation a grain boundary can show to be classed as a particular CSL Σ boundary. The classical Brandon's Criterion is detailed below in Equation (4.15) for the maximum allowable deviation from the coincidence [234, 236]:

$$\Delta\theta \leq 15 \cdot \Sigma^{\frac{-1}{2}} \tag{4.15}$$

where θ is the misorientation of the grain boundary, and Σ is the reciprocal of the number of coincident sites between two neighbouring grains.

All criteria depend upon the Read–Shockley relationship where $\theta \sim$ b/d, where b is the Burgers vector of that particular grain boundary dislocation, and d is the dislocation spacing. Palumbo *et al.* introduced the concept of grain boundary control to improve the resistance to localised oxidative attack in Ni-based superalloys in high temperature critical environments [235]. This was primarily by increasing the number of CSL boundaries with low Σ orientation ($\Sigma < 29$), shown to demonstrate improved resistances to SCC by means of slower diffusion of oxygen along the interface. This is by means of their lower excess free volume and energy associated with them (1/50 of a random oriented boundary) [228, 237].

Palumbo and Aust evaluated the validity of the Brandon Criterion in relation to instances of

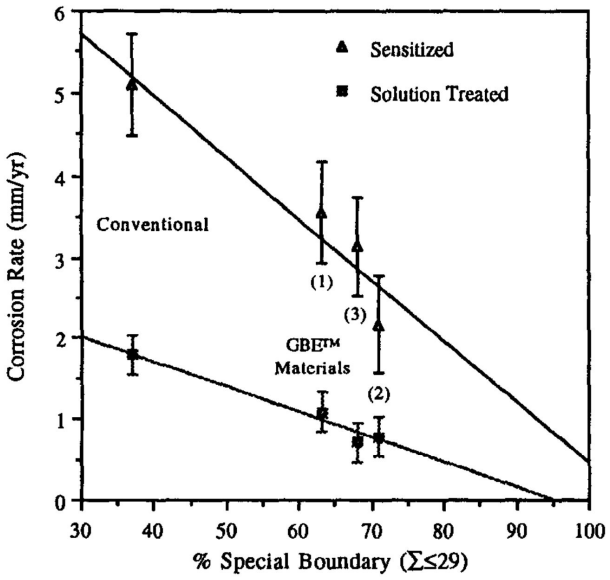


Figure 4.35: The proportion of CSL grain boundaries in conventional and GBE IN600 showing the effects upon the corrosion rate. Taken from Lin *et al.* (1995) [229].

internal oxide and the resultant intergranular stress corrosion cracking, and creep cavitation. The application of the criterion lead to the incorrect classification of special boundaries, which did not display the expected characteristics (i.e. slow diffusion and lower instances of internal oxide). Research using automated EBSD and advancements in structure property databases allowed a more restrictive criterion to be developed, reducing the instances of the misclassified grain boundaries.

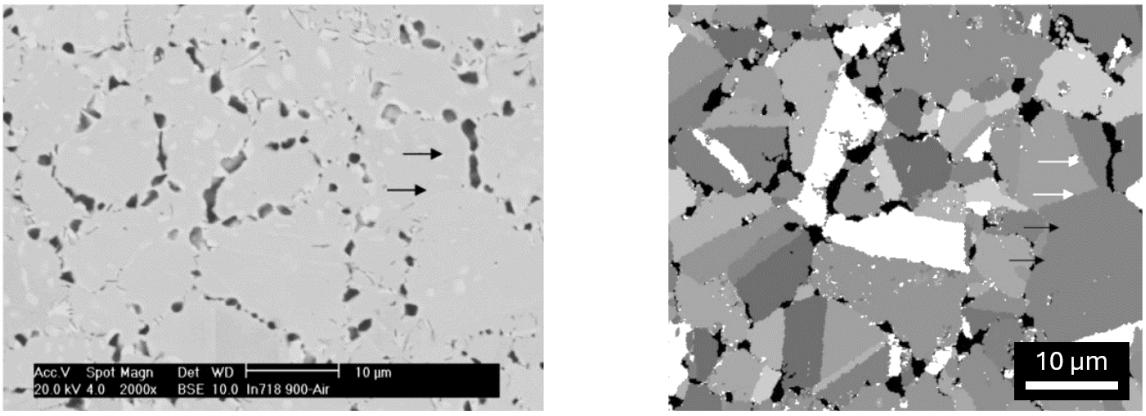
The Palumbo-Aust Criterion is defined as follows in Equation (4.16):

$$\Delta\theta \leq 15 \cdot \Sigma^{\frac{-5}{6}} \tag{4.16}$$

where θ is the misorientation of the grain boundary, and Σ is the reciprocal of the number of coincident sites between two neighbouring grains.

Here the inclusion of the $\Sigma^{\frac{-5}{6}}$ dependence takes into account the third burgers vector present in the Displacement Shift Complete (DSC) lattice being independent of the Σ. DSC refers to the displacements available to a grain which conserves the symmetry of the CSL boundary dislocations [236]. For example, a study was carried out investigating the corrosion of boundaries present in Alloy 800 (40Fe-35Ni-25Cr). With the Brandon Criterion applied, 12% of the boundaries classified as special showed evidence of corrosion. With the more stringent Palumbo–Aust criterion, only 3% of the boundaries classified as special indicated corrosion [236].

Figure 4.35 shows a study by Lin *et al.* (1995) with IN600 nuclear steam generator tubing, where an increase in the proportion of Twin Grain Boundaries (TGBs) and LowΣ CSLs (of up to 71% via cold rolling and subsequent heat treatment), lead to significant improvements in corrosion



(a) Intergranular oxidation of sub-scale IN718

(b) Corresponding EBSD orientation map

Figure 4.36: Wrought IN718 following oxidation at 850°C in static air. (a) BSE-SEM micrograph of the oxide sub-scale following external oxide removal. Note high contrast internal oxide upon grain boundaries. (b) EBSD IPF map of the corresponding area, showing presence of internal oxide upon randomly orientated grain boundaries. Taken and adapted from Krupp *et al.* (2013) [228].

resistance. It was hypothesized that this occurred because intergranular corrosion paths were blocked when they intersected with annealing twin boundaries, thereby preventing intragranular stress corrosion cracking (SCC) [23, 29, 46, 229]. This was more recently discussed by Athreya *et al.* (2018), who improved the cyclic oxidation resistance of IN617 for superheater and reheater tubing. By applying thermomechanical processing, the density of low-energy grain boundaries, including twin and twin-family boundaries, as well as triple junctions, was increased. Hence improvements to oxidation resistance was attributed to the interruption of the random high angle grain boundary network present, overall decreasing the levels of Cr depletion during oxidation [237]. This was also supported by findings by Tan *et al* (2008) for IN800H, where oxide scale stability was superior following an increase in CSL fraction [230].

Trindade and Yang *et al.* (2005), and Krupp *et al.* (2013) conducted additional investigations into the effects of special grain boundaries in both wrought IN625 and 718, showing an improvement in oxidation rate by increasing the density of CSLs compared to random high angle grain boundaries (see Figure 4.37 and Figure 4.36), showing reduced presence of internal oxides upon CSL boundaries). Here internal oxides in particular formed preferentially along random oriented grain boundaries due to the faster diffusion of oxygen anions here, leading to premature brittle failure of the protective oxides formed [4, 233]. Yamaura *et al.* (1999) studied the phenomenon in polycrystalline Ni-Fe alloy, deeming that specific grain boundary CSL types were more immune to intergranular oxidation than others, due to their inherent geometry, orientation and therefore grain boundary energy. Twin boundaries ($\Sigma 3$, with 60° misorientation) boundaries were deemed

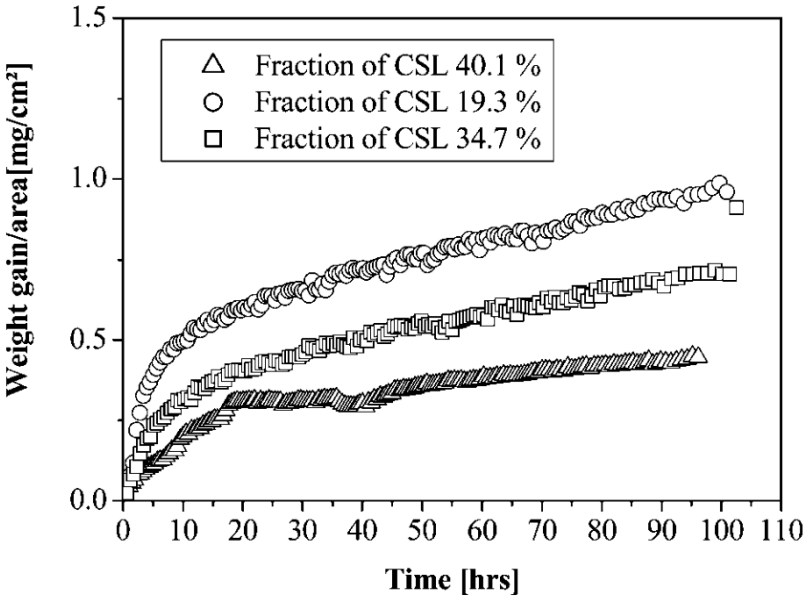


Figure 4.37: Graph showing the TGA oxidation kinetics taken for a set of IN718 samples with differing CSL fractions following oxidation at 850°C in air. Taken from Krupp *et al.* (2013) [228].

most significant in the reduction of internal oxide and intergranular degradation [219, 238].

The aforementioned effects are especially prevalent in AM alloys showing enhanced alumina formation [1, 187]. Therefore, it is thought that by increasing the fraction of CSL boundaries up to the maximum available fraction (2/3 in an FCC material, approx. 66%), this approach could be key in the improvement of the oxidation resistance of AM alloy, by disrupting the network of connectivity between random high angle boundaries present in the matrix [34, 131, 219, 229, 230, 233].

For L-PBF IN625 and similar AM Ni-based superalloys, research into texture has been primarily focused on improving tensile properties. Solution heat treatments are reported to significantly increase the fraction of TGBs compared to as-built materials, leading to tensile properties surpassing the standard expected for wrought IN625 [34, 104, 113, 121]. Marchese *et al.* (2020) reported up to 56% twinning in solution heat treated L-PBF IN625, though it is expected that the AM manufacturing process, and printing parameter selection in particular may influence the level of twinning experience by the component following heat treatment by virtue of the level of residual stress and dislocation density following printing of the build [34, 108].

For research into oxidation rates at high temperatures, crystal anisotropy was reported to directly influence oxidation performance in L-PBF IN625. Huang *et al.* (2022) found that samples showing a textural deviation from the (100) plane, to the (101) and (111) planes, saw the formation of a denser oxide scale, suggesting diffusion rates appear to be higher for grains showing (111) preferred orientation [17].

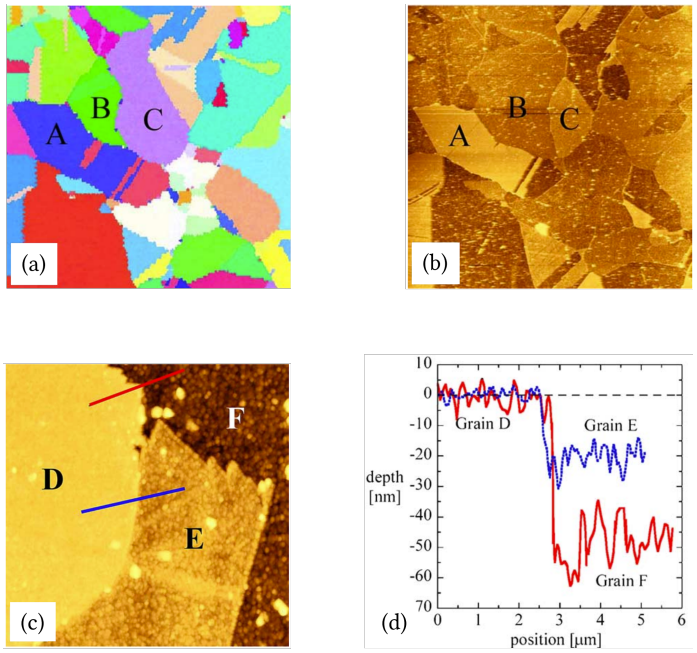


Figure 4.38: (a) EBSD IPF map showing the external oxide formed on Haynes 230 alloy, with corresponding AFM maps (b,c), and surface roughness line scan (d), correlating the effects of surface grain orientation upon oxidation. (a) and (b) show the EBSD IPF map and AFM map analysis of the same area upon the same sample, respectively. Darker contrast in AFM map (b) indicates a region of thicker oxide scale. (c) outlines an alternative area upon the oxide sample shown in (a). Grain D is a {111} orientation grain. (d) Shows the corresponding surface profile line scan across the sample area outlined in (c), where the oxide thickness was measured to be lower in Grain D than the neighbouring grains. Taken and adapted from Schuh *et al.* (2003) [239].

Similar results were obtained with L-PBF IN718. Sanviemvongsak *et al.* (2018) observed that special boundary fractions even up to as little as 35% lead to improved oxidation resistance and shallower intergranular oxidation depth [187]. Alloy texture inherent to the AM process is also thought to have played a role in the reduced rates of oxidation for as-built microstructure IN718. As previously outlined, L-PBF alloys tend to show strong preferential orientation along the <001> direction, with the build direction. This effect was lost following heat treatment [34, 187].

Wang *et al.* (2015) investigated this relationship with texture and oxidation for wrought Haynes 230 superalloy using a combination of EBSD and Atomic Force Microscopy (AFM), who established a qualitative relationship between texture and oxidation [240, 241]. Here surfaces parallel to the {111} plane tended to show improved oxidation resistance compared to others, where oxidation rates for grains in terms of oxide thickness was as follows: (111) < (110) < (100). Similar results were presented by Schuh *et al.* (2003) investigating IN600 for use in acidic corrosive environments with HCl, who stated that corrosion rates increase as the grain normal vector diverges from the ⟨111⟩ (see Figure 4.38 [239].

Attention must however be drawn to the fact that the aforementioned investigations were

performed over short exposure times of ~5 mins compared to the likes of Huang *et al.* (2022), making the effect an early-stage mechanism of oxidation. Sanviemongska *et al.* (2020) also commented as such, carrying out oxide scale measurements on L-PBF IN718 in both the XY (strongly texture to 100 orientation) and the XZ direction following 48 h, 1000 h and 3000 h exposures at 850˚C. Here no significant difference was found in the measured intergranular oxidation depths and thicknesses with texture [242]. It must also be noted that Wang *et al.* (2015) found that following oxidation EBSD IPF mapping, the indexing of certain grains was poor, attributing this affect to oxide thickness via preferential diffusion and growth via texture. Whilst possible deterioration in the index rate could come from formation of the oxide, contributions from the epitaxy between the oxide and alloy could also lead to preferential electron channelling, making the correlation of grain orientation to oxide thickness inaccurate. Strain affects in the near surface of the substrate may also contribute to such effects.

Evidently, more work is required to fully understand the mechanism and combined influence of special boundaries and texture upon the oxidation resistance of L-PBF IN625, where it is predicted that a GBE approach could be applied to tailor microstructure for improved oxidation performance.

4.8 Summary

It is clear that oxidation of L-PBF IN625 has not yet been fully investigated at long exposures (1000s h). More work is required to ascertain how AM microstructures will affect chromia growth, the establishment of the δ-phase, and its affects upon the growth rate of chromia scale. It may be possible to take advantage of the flexibility of parameters in L-PBF to produce microstructures optimized for oxidation resistance. However, limitations remain in terms of the surface roughness of as-built components, where further surface modifications must be researched to evaluate the future of AM components for oxidation resistance. There is also a lack of literature showing the performance of L-PBF IN625 in common operational environments such as steam generators and heat exchangers. These points altogether impact the production efficiency, limiting AM's industrial application as of yet. A summary of proposed research topics to rectify some of these issues can be viewed in Figure 4.39.

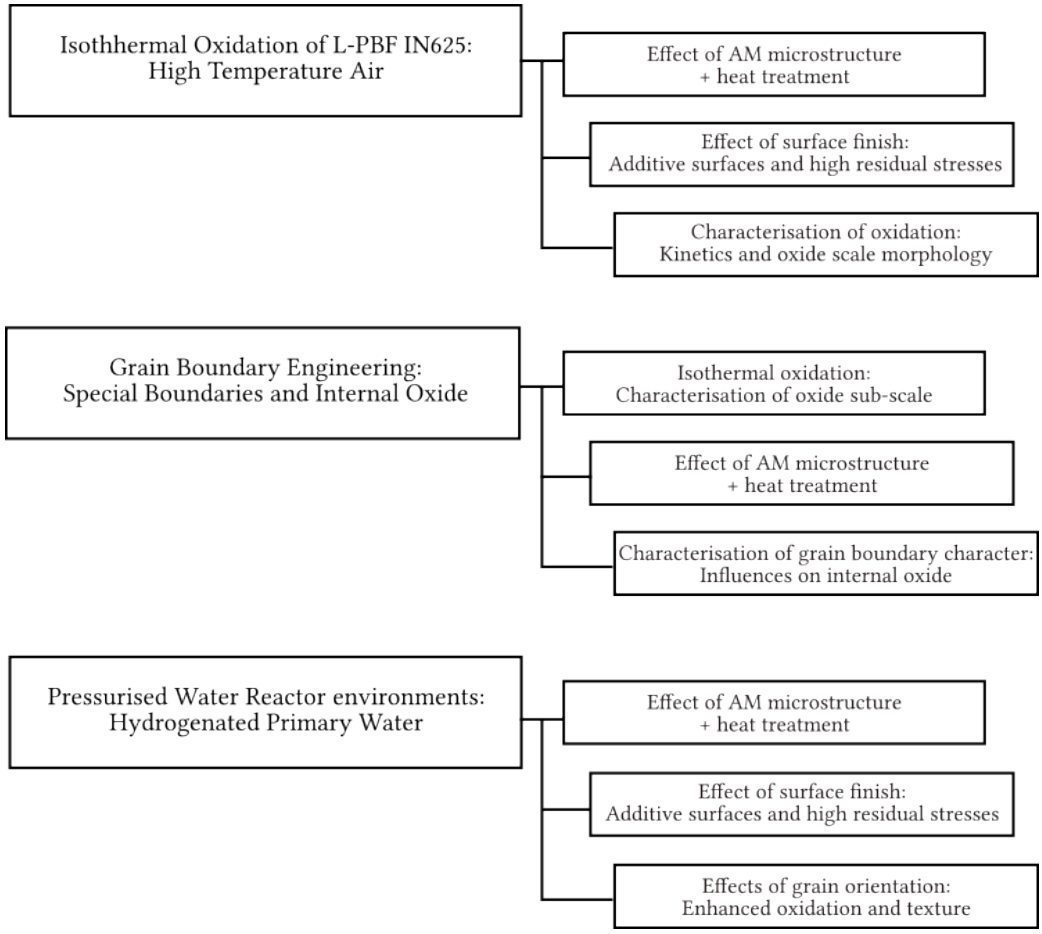


Figure 4.39: A flowchart showing the key research topics carried out for the PhD project.

Chapter 5

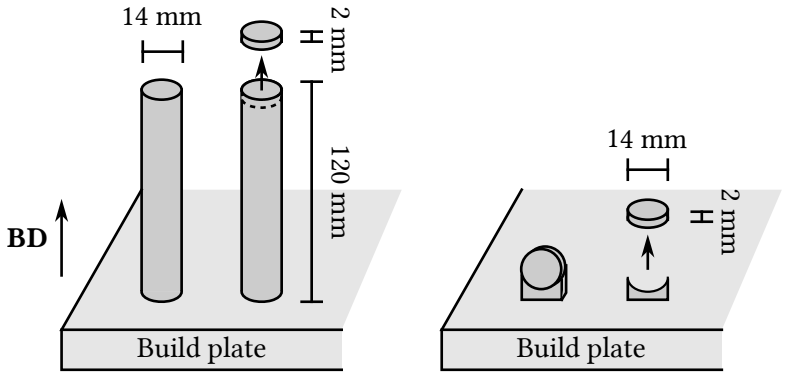
Experimental procedure and theory

5.1 Materials, Laser Powder Bed Fused and Wrought Inconel 625

5.1.1 Laser Powder Bed Fused Inconel 625

Two builds were completed for the period of the PhD project, built using an EOS M280 (400 W) laser powder bed fusion machine: the first, Build 1 by Parker Aerospace, and an additional build, Build 2, at the Manufacturing Technology Centre (MTC). Figure 5.1 shows the dimensions of the samples built.

Build 1 consisted of 72 fully dense cylindrical rods of L-PBF IN625, built using powder particle sizes ranging from 15 – 45 µm). Rods were manufactured using the default IN625_Performance_110 parameter set, with a layer height of 40 µm. The selected geometry (diameter 14 mm and height 125 mm) was applied to investigate the effect of the as-built microstructure, and the effects of heat treatment upon oxidation. The samples fabricated were taken from a batch obtained from a previous work by the authors [80, 191], for which the build plate can be viewed in the appendix, see Appendix Figure 1. In the previous study by the authors, possible microstructural variation along



a) Build 1
Effect of microstructure

b) Build 2
Effect of surface finish

Figure 5.1: A schematic showing the two L-PBF builds carried out for the duration of the PhD project. Build 2 included support struts. BD indicates the building direction.

TABLE 5.1
SET CHEMICAL COMPOSITIONS OF CONVENTIONAL AND L-PBF IN625.

Alloy		Element ($\%_{wt}$)												
		C	Mn	Si	P	S	Cr	Co	Mo	Nb	Ti	Al	Fe	Ni
AM IN625[1]	Min	-	-	-	-	-	20.00	-	8.00	3.15	-	-	-	Bal.
	Max	0.10	0.50	0.50	0.015	0.015	23.00	1.00	10.00	4.15	0.40	0.40	-	Bal.
Wrought IN625[2]	Min	-	-	-	-	-	20.00	-	8.00	3.15	-	-	-	58.0
	Max	0.10	0.50	0.50	0.015	0.015	23.00	1.00	10.00	4.15	0.40	0.40	5.0	-

[1] Data from ASTM F3056-14 [243].
[2] Data from ASTM B564-18 [244].

TABLE 5.2
MEASURED POWDER COMPOSITION FOR L-PBF IN625 USED IN THE PRESENT STUDY.

Alloy	Element ($\%_{wt}$)												
	C	**Mn**	**Si**	**P**	**S**	**Cr**	**Co**	**Mo**	**Nb**	**Ti**	**Al**	**Fe**	**Ni**
IN625	-	<0.01	0.07	<0.01	0.00	21.27	0.04	9.02	3.65	0.10	0.11	3.66	Bal.

the 120 mm rod sample length due to thermal gradient effects was investigated. Here no changes in grain size or texture were observed from the base to the tip, regardless of the rod position on the build plate [191].

Build 2 consisted of 420 fully dense individual disks of L-PBF IN625 (diameter 14 mm and thickness 2 mm). This was also completed using the standard IN625_Performance_110 parameter set. The token geometry was selected to allow for the investigation of tokens with a fully additive surface roughness for comparison to the cylindrical rod specimens, and for comparison to industrial applications of additive component surfaces. The small individual tokens also allowed for the use of specific weight gain quantification for the calculation of oxidation growth rates. Further images showing the layout of the build plate for Build 2 can be viewed in the appendix, see Appendix Figure 2.

IN625 powders were supplied by the MTC. The standard powder composition used is shown in Table 5.2 for comparison to the minimum and maximum allowable compositions, shown in Table 5.1. This was confirmed using a combination of LECO, ICP-OES (Inductively Coupled Plasma Optical Emission Spectroscopy) and XRF (X-Ray Fluorescence) collected externally by AMG Analytical, AMG Chrome Ltd. [61]. LECO and ICP-MS was also carried out on as-received materials from both Build 1 and 2, as well as a set of wrought IN625 tokens fabricated for comparison to the standard alloy performance. The quantities for these elements were found to be in accordance with ASTM F3056-14 for the standard specification for additively manufacturing nickel alloy (UNS N06625) with powder bed fusion, making all materials comparable to each other [243, 244]. The compositions can be viewed in Table 5.3.

The powder morphology and structure were examined using a Hitachi TM3030+ scanning

TABLE 5.3
WROUGHT AND L-PBF IN625 SAMPLE CHEMICAL COMPOSITION.

Alloy	Element ($\%_{wt}$)												
	C	**Mn**	**Si**	**P**	**S**	**Cr**	**Co**	**Mo**	**Nb**	**Ti**	**Al**	**Fe**	**Ni**
Build 1	0.021	0.020	0.110	< 0.005	0.004	21.940	0.050	9.690	3.880	0.120	0.160	3.950	Bal.
Build 2	0.026	< 0.020	0.050	<0.005	0.004	21.510	< 0.020	9.480	3.870	0.110	0.130	3.500	Bal.
Wrought	0.025	0.090	0.120	0.005	0.004	21.640	0.110	8.730	3.460	0.080	0.130	3.520	Bal.

electron microscope (SEM) with back scattered electrons and energy dispersive spectroscopy (EDS) analysis using an accelerating voltage of 15 kV. The powders were found to be spherical in shape.

5.2 Post-processing: Surface finishes and heat treatments

A variety of conditions were considered, investigating the effect of as-built and heat treated microstructures (i.e. grain size variation and texture), as well as various different surface roughness conditions upon the oxidation performance of L-PBF IN625.

5.2.1 Heat treatments

To investigate the effect of microstructure, as-built microstructure samples from Build 1 were produced, as well as a set of solution-treated tokens, outlined in Table 5.4, following guidance outlined in AMS2774D [61]. A solution-treatment was applied to as-built material in order to see the effects of a fully recrystallized microstructure with large twin boundary fractions, combined with the removal of microsegregated Nb and Mo on cell boundaries. This was conducted to study their combined effects on the oxidation mechanism of L-PBF IN625, particularly on chromia growth, and the precipitation of the brittle δ-phase (Ni_3(Nb,Mo)).

Two methods were applied to heat treat samples depending on their geometry. Cylindrical rods received from Build 1 were placed into a pre-heated box furnace for a solutionising heat treatment at 1177˚C for 1 hour, before their removal and water quenching to room temperature. In order to heat treat the individual tokens from with additive surface roughness taken from Build 2, tokens were firstly encapsulated in an argon back-filled quartz ampule. The ampules then underwent solution-treatment in a pre-heated box furnace, were they were subsequently water quenched to room temperature upon completion.

TABLE 5.4
STANDARD HEAT TREATMENTS FOR IN625 - AMS2774E [122].

Condition	Heat Treatment	Details
AB	As-built	N/A
ST	Solution-treated	1177°C, 1 hr dwell 60°C/min forced air cool/water quench

5.2.2 Surface finishing

A variety of different surface finishes were applied with the aim of devising a suitable post-processing route for L-PBF IN625. Alongside standard ground samples, three additional surface finishes were selected based on their applicability to complex additive geometries seen with additive manufacturing: Additive surface roughness tokens, Centrifugal High Energy Finishing (CHEF), and electropolished tokens. Electropolishing and CHEF in particular were applied to examine the effects of strain induced in the surface of the component upon the oxide films produced. Here CHEF was considered to be highly strained, and electropolished tokens were considered to have a very low surface strain.

5.2.2.1 Grinding and polishing

Specimens of L-PBF IN625 were made to size from cylindrical rods taken from Batch 1. These were cut perpendicular to the build direction using Electrical Discharge Machining (EDM) to produce disks of diameter 14 mm and thickness 2 mm. The surfaces were successionally ground, and the edges chamfered to approximately 45° to 400 to 4000-grit (approximately 5 μm, R_a = 0.15 μm, R_a = 0.10 μm, respectively) using a combination of wet SiC papers, and an automated Struers Ltd. Tegramin-30. This was to remove any residual surface damage produced following cutting. This was carried out using both as-built and solution-treated tokens to investigate the effects of the as-built microstructure.

5.2.2.2 Centrifugal High Energy Finishing (CHEF)

Solution-treated tokens from Build 2 underwent Centrifugal High Energy Finishing (CHEF). This involved putting coupons of L-PBF IN625 into a barrel, mounted upon a large rotating wheel. Small barrels containing abrasive media and agents (see Table 5.5) were mounted on the edge of the wheel which then rotated with opposing spin. High centrifugal force and contact pressure between components and media reduces the surface roughness of the sample by abrading each sample surface to produce highly finished samples, albeit leading to a small loss in the sample

geometry. The centrifugal finishing was performed using three stages outlined by the machine, provider ActOn Finishing Ltd [245]: (i) cutting for 120 mins with ceramic media (carbide-free bainitic, CFB, medium abrasive) 10 × 10 with 50 ml of LQ18 reagent and water, (ii) smoothing for 120 mins with ceramic media (Semi-Friable Bainitic, SFB, highly abrasive) 6 × 10 with 50 ml of LQ16 reagent and water, then (iii) polishing for 60 mins in dry maize. Following their removal samples were cleaned in an ultrasonic bath with ethanol to remove any remaining media upon the surface. This produced samples with a mirror-like finish (R_a = 0.40 μm) and sample edges which were rounded.

5.2.2.3 Electropolishing

A set of solution-treated tokens from Build 2 underwent electropolishing. Using a power supply, a stainless-steel coil was connected as the sacrificial cathode, and the sample to be polished was connected to act as the anode. Both were placed into a 500 ml beaker containing a 4:1 ratio solution of sulfuric acid and methanol kept at room temperature (20-22°C). The power supply was set to 30 V. This was according to the ASTM standard for the electropolishing of Ni-based superalloys (E1558-09) [246], with adaptations to ASTM G1-03 [247]. The voltage was applied, and the samples were swirled in the mixture using metal tongs. To produce a mirror finish, samples were electropolished for 10 minutes each, stopping at 20 s intervals to rotate the sample to allow for full coverage, and to wash away surface contaminants using ethanol. The procedure resulted in samples with an even surface finish (R_a = 1.8 μm), and sample edges which were rounded.

A summary of all sample token types is outlined in Table 5.6.

Table 5.5
Chemical agents applied during CHEF, ActOn Finishing Ltd. Adapted from [245].

Compound name	Description	pH
LQ16	A concentrated cleaner agent used for polishing and brightening non-ferrous alloys	8.5 – 9
LQ18	A light descaling agent applied to remove metal oxides following heat-treatment to give a bright surface finish	1 – 2

TABLE 5.6
SUMMARY OF THE HEAT-TREATED AND SURFACE FINISH CONDITIONS OF THE MATERIAL INVESTIGATED FOR WROUGHT AND L-PBF IN625.

Alloy	Heat treatment(s)	Surface(s)
L-PBF Batch 1	As-built	4000-grit 0.25 µm (OPS)
	Solution	4000-grit 0.25 µm (OPS)
L-PBF Batch 2	As-built	0.25 µm (OPS)
	Solution	Additive surface CHEF Electropolished
Wrought	Solution	0.25 µm (OPS)

5.3 Characterisation of as-received materials

5.3.1 Sample density and porosity validation measurements

In order to assess that the fabricated tokens were fully dense, a combination of Archimedes density testing, and SEM imaging was carried out. Archimedes testing was performed using a variation on methods laid out in ASTM B962-17, where tokens were measured in both air and ethanol at room temperature [248]. To confirm these measurements, XY and XZ cross-sections of tokens from Builds 1 and 2 were imaged using SEM using 3 repeat locations across the sample surfaces. Using FIJI Image J software, an image threshold approach was taken, where pores or voids are filled allowing the % porosity to be calculated [249]. Both methods confirmed the tokens to be approximately fully dense at 99.6%, on average showing tokens to have a density of 8.41 g/cm^3 compared to 8.44 g/cm^3 for wrought IN625 [20].

5.3.2 Surface roughness measurements

Surface roughness measurements were taken using a combination of confocal microscopy and physical recordings taken using a surface Rugosimeter.

An Alicona InfiniteFocus optical 3D measuring instrument was used at 5× magnification. Analysis of the data was completed using the Infinite Focus Measurement Suite by Alicona. In this work, the areal surface texture parameters S_v (the maximum valley depth of the selected area) and S_a (arithmetical mean height of the selected area) are used. Surface height maps were also measured to analyse the peaks and valleys of all conditions and to show improvements of the surface conditions compared to additive surface roughness specimens. When taking line measurements

R_a and line profiles, care was taken to measure perpendicular to machining marks for ground and additive roughness samples.

A Surfcorder SE1700 surface analyser was used to measure surface roughness profiles for all conditions investigated in this study. Values for R_a (the arithmetic average of the height profile over the measured length), R_{max} (the maximum value of the vertical distance between the highest peak and lowest trough in the profile) and R_z (the average arithmetic height, calculated from the distances between the highest peaks and lowest troughs in the profile). Three repeat values were recorded for each specimen type, at random areas on the surface. For the additive roughness and ground samples, where topography is directional, measurements were taken both parallel and perpendicular to the weld tracks and grinding marks, respectively.

5.3.3 Metallurgical sample preparation

Both XY and XZ cross-section metallographic samples were produced for all conditions of the as-received materials investigated, including all heat-treated and surface finish conditions. To examine the microstructure, materials were hot mounted in Bakelite and successively ground and polished to a mirror-like finish using 0.25 μm OP-S colloidal silica (R_a = 0.05 μm) . To etch samples and reveal the microstructure, samples were excessively polished with the OP-S solution for times up to 2 hours.

5.3.4 Scanning Electron Microscopy, Assessing the as-received microstructures

Scanning Electron Microscopy (SEM) was performed using the following microscopes over the duration of the project: a Hitachi TM 3030Plus tabletop SEM, a JEOL 6060 SEM with Oxford Inca EDS capabilities, a JEOL 7000F Field Emission Gun Scanning Electron Microscope (FEG-SEM), and a Zeiss EVO-15 SEM with Bruker Quantax EDS. SEM using both Backscattered Electrons (BSE) and Secondary Electrons (SE) were used to obtain images and compositional data from the as-received microstructures of all conditions and surface features, respectively, where an accelerating voltage of 20 kV was used throughout imaging.

5.3.5 Electron Backscatter Diffraction (EBSD)

A JEOL 7000F Field Emission Gun Scanning Electron Microscope (FEG-SEM) equipped with an HKL Nordlys EBSD unit with Oxford Aztec capabilities was used to image the microstructure samples of as-received material in both the XY and XZ orientations. Samples were tilted by 70°

and scanned at 20 kV, using step sizes and scanning areas of 2.5 μm and 680 × 400 μm^2 for the as-built alloy conditions, and 1.5 μm and 500 × 400 μm^2 for solution-treated alloy conditions due to the differing grain sizes observed.

EBSD ctf. files obtained were reconstructed using the MATLAB MTEX toolbox to generate the inverse pole figure (IPF) maps. These were plotted and analysed using code taken and adapted from the MTEX MATLAB framework, allowing for the calculation of average sample grain sizes (D50 measurements). MTEX is a free open-source library containing the tools needed to analyse and model crystallographic texture by means of EBSD IPFs. The codes written in the present work build upon existing codes produced by Bachman, Hielscher, Krakow and Nolze [250–254].

5.3.5.1 Determination of grain size

To calculate the grain size, IPF maps were recorded over scanning areas spanning 1200 μm × 900 μm^2 to provide a large enough sample number of grains representative of the sample. An automated MATLAB code was created which applied the Heyn Lineal Intercept procedure to the generated EBSD IPF maps of the same size area, according to ASTM E112-13 [255]. The code estimated the mean average grain size by layering a 15 x 15 square grid upon each EBSD IPF map. Care was taken to ensure each line would intercept at least 50 grains each to allow for the calculation of an average grain size. Additional attention was given to begin each measurement at the start of a new grain to prevent sampling of incomplete grains. The grain diameters were then plotted as cumulative grain size fractions for both XY and XZ orientation samples. This then allowed for the grain diameters to be plotted as a cumulative grain size fractions for direct comparison to each other.

5.3.5.2 Grain misorientation and texture

To investigate the fractions of special grain boundaries and random misorientation boundaries, IPF maps were analysed to determine local grain misorientation. The percentages of Low Angle Grain Boundaries (LAGBs, $\theta < 15$ °) and High Angle Grain Boundaries (HAGB, $\theta > 15$ °) were measured, taking a particular interest in the frequency of Twin Grain Boundaries (TGBs) ($\theta = 60°$) for each condition of L-PBF IN625. In order to classify each type of grain boundary within the Coincidence Site Lattice (CSL) framework ($\Sigma \leq 29$), the Palumbo-Aust Criterion was chosen and applied to calculate the maximum geometrically allowable deviation from the exact CSL misorientation (see Equation (5.1)). The frequency of special boundaries was then calculated as the length fraction of the total grain boundary length in the IPF map:

$$\Delta\theta = \theta_0 \cdot (\Sigma)^{\frac{-5}{6}} \tag{5.1}$$

where $\Delta\theta$ is the allowable angular deviation, θ_0 is the misorientation angle.

Qualitative measurements of texture variations in the samples were made from IPF maps generated.

5.4 High temperature isothermal oxidation in air

A collection of isothermal oxidation tests was conducted, characterising the performance of L-PBF IN625 across various heat treated and surface finish conditions. All testing was done in accordance with the standardised procedures outlined in ASTM G1-03 (2011), and methods adapted from ASTM B487-85 (2013) using SEM for oxide thickness measurements [247, 256].

5.4.1 Laboratory air and pressure, 950˚C

Isothermal oxidation testing was conducted at 950˚C in laboratory air and pressure for 24 - 1000 h using a Lenton Thermal Designs horizontal tube furnace, calibrated to give temperatures correct to ±1˚C using calibrated R-type and K-type thermocouples. Calibration testing was conducted by testing the furnace temperature in 50˚C increments from 500 – 950˚C. The hot zone of the furnace was determined by measuring temperature in 5 cm increments along the furnace working tube. The exposure temperature of T = 950˚C was selected in order to investigate the oxidation of the alloy near it's operational limit of T = 980˚C, and to accelerate the formation of a protective oxide, and the associated key precipitate phases for inspection.

An additional set of oxidation tests were also carried for short time periods of oxidation at 950˚C in laboratory air and pressure for 0.5 to 100 h to investigate the evolution of the oxide scale, and the early stages of recrystallisation experienced by as-built and solution-treated L-PBF IN625 material. These were oxidised using a Nabertherm horizontal metal tube furnace at the University of Malta. Prior to starting these tests, the furnace was also calibrated to give temperatures correct to ±1˚C using a calibrated K-type thermocouple. Calibration testing was conducted in the same manner as the Lenton Thermal Designs tube furnace.

An oxidation testing matrix outlining all specimen types, surface conditions and times investigated is shown in Table 5.7. Oxidation behaviour was investigated using a combination of two methods: Specific weight gain calculation, and cross-sectional oxide thickness measurements.

To measure the specific weight gained by each specimen, the surface area and thickness of all samples was measured in six locations using a micrometer. Sample mass was measured using a calibrated micro-mass balance (accurate to ±0.00001 g). Prior to oxidation, all specimens were degreased in acetone in an ultrasonic bath for 5 minutes and subsequently dried with hot air (See Figure 5.2). Batches of 4 – 6 specimens were placed in open ceramic alumina crucibles and placed into the centre of a pre-heated tube furnace. These were all removed, and air cooled to room temperature after exposures of: 0.5, 1, 8, 24, 100, 500 and 1000 h (see Table 5.7). At each time period, each specimen was re-weighed 3 times to determine the net mass increase per unit area, then kept in a desiccator ready for inspection of the oxide scale. Samples and crucibles were examined for visual signs of spallation upon removal.

For each time period, at least 2 samples from each batch were selected to undergo surface and cross-sectional analysis using the following techniques: Scanning Electron Microscopy (SEM) with both BSE and SE, Transmission Electron Microscopy (TEM) with STEM-EDS (selected samples of interest only), X-ray Diffraction (XRD), Electron Backscatter Diffraction (EBSD), and surface roughness measurements using a confocal microscope and non-contact profiler.

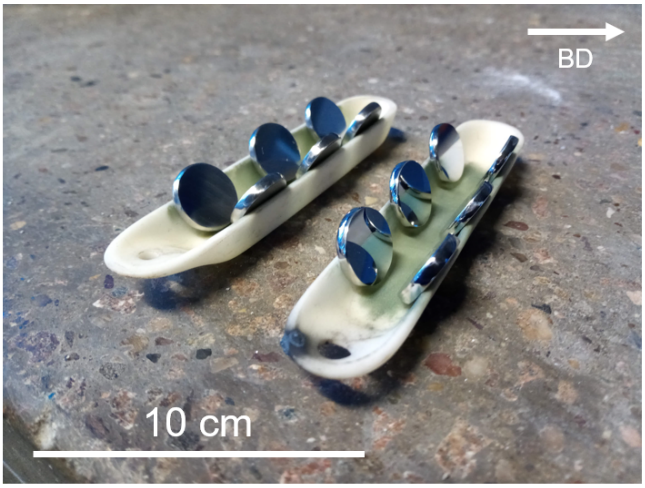
5.5 Oxide sample preparation post-exposure

Following isothermal oxidation, analysis of the oxide cross-section, chemical composition and sub-scale elemental depletion depth was carried out. To protect against cracking or spallation of

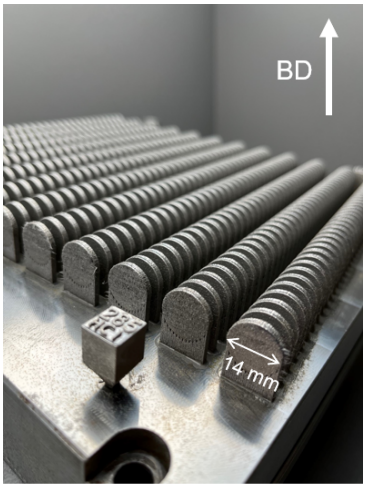
Table 5.7
Oxidation testing matrix for L-PBF IN625, T = 950°C, t = 0.5 – 1000 h.

Sample condition		**Time (h)**						
Microstructure	**Surface**	**0.5**	**1**	**8**	**24**	**100**	**500**	**1000**
As- built	4000-grit				✓	✓	✓	✓
	0.25 µm	✓	✓	✓		✓		
Solution	4000-grit				✓	✓	✓	✓
	0.25 µm	✓	✓	✓		✓		
	Additive				✓	✓	✓	✓
	CHEF				✓	✓	✓	✓
	Electropolish				✓	✓	✓	✓

CHEF = Centrifugal High Energy Finishing



(a) 0.25 µm (OP-S polish), L-PBF Build 1



(b) Additive surface tokens L-PBF Build 2

Figure 5.2: (a) L-PBF IN625 - Batch 1, polished to an OP-S mirror-finish, (b) L-PBF IN625 - Batch 2. Build 1 and 2 token dimensions: 14 mm diameter, 2 mm thickness. Note the building direction (BD) annoted for each build.

the oxide, the following Ni electroplating method was applied, adapted from methods outlined by Cruchley *et al.* [149]:

- Specimens were sputtered with gold, producing a conductive layer upon the surface.
- Specimens were Ni-plated using a Watt's bath electrolyte solution (25 – 40 g/l $NiSO_4 \cdot 6H_2O$, 20 – 60 g/l $NiCl_2 \cdot 6H_2O$ and 30 – 45 g/l H_3BO_3) at 46 – 71°C, using a temperature controlled hot plate. A current density of 1 – 10 A/dm^2 was applied using a power supply. The Ni-plate aids in the protection of the scale during sectioning, as well as acting as marker to indicate where the scale started and ended.
- Samples were mounted in low-shrinkage cold resin (Struers Duracit-3), and sectioned into half-moons using a Struers Accutom-5 precision cutting machine at <0.05 mm/s.

All mounted cross-section specimens were ground using wet SiC papers to 4000 grit, and subsequently polished to a 0.25 µm finish using a Struers MD-Chem disc with OP-S solution. Prior to imaging, samples were cleaned in an ultrasonic bath with ethanol for 5 mins.

5.6 Characterisation of oxidation products

5.6.1 Scanning Electron Microscopy and optical microscopy

Scanning Electron Microscopy (SEM) was performed to image the external oxide and oxide-cross-sections using the following: A JEOL 6060 SEM with Oxford Inca EDS capabilities, a Hitachi TM 3030Plus SEM. SEM with Backscattered Electrons (BSE) was used to obtain images and compositional data from the surface oxide and to conduct cross-sectional analysis of the through sample specimens via EDS point, line and map scanning. An accelerating voltage of 20 kV was used throughout, except for the Hitachi TM 3030Plus, where a maximum voltage of 15 kV was applied. Additional imaging using optical microscopy was also performed on specific areas of interest using a Zeiss Axioscope 5 microscope for comparison.

5.6.1.1 Analysis of oxide cross-sections

Fiji Image J was used to characterise the oxide cross-section. A grid was overlaid onto each cross-sectional image, producing 5 equally spaced intersections from which to measure the thickness/depth of the oxide using the line tool. 50 measurements of the desired feature were recorded to produce a representative average and standard deviation. The following measurements were made across 10 repeat images:

(a) ***External chromia scale***

Chromia scale thickness measurements were taken by drawing lines from the surface of the oxide to the oxide scale/alloy boundary. To confirm the presence of chromia, EDS line scans from the scale surface to the bulk of the alloy were taken. For more non-uniform surface finish oxides such as the oxides grown on the additive roughness tokens (with adhered powder particles on the surface), separate measurements were taken (i.e. measurement of thickness over the powder particles, and measurements of oxide thickness on the flat surfaces of the token.)

(b) ***Internal oxide scale***

Internal oxide penetration was measured by drawing lines from the external chromia/substrate boundary to the end each instance of internal oxide. EDS maps and line scans were taken to inform the presence of Al, Ti, etc.

(c) ***Precipitate free zone***

The precipitate free zone was measured by drawing lines from the oxide scale to the bulk of the alloy where precipitate was first encountered.

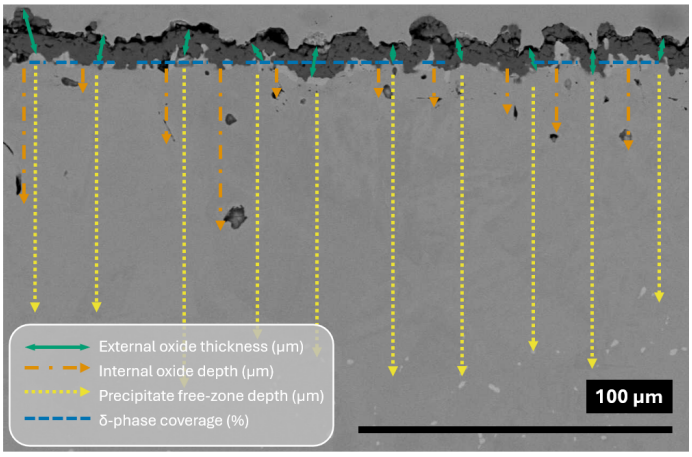


Figure 5.3: A BSE-SEM micrograph depicting a summary of the oxide scale measurements carried out. (a) Chromia thickness (µm), (b) internal oxide depth (µm), (c) precipitate free zone depth (µm), (d) δ-phase percentage coverage across the scale/alloy interface (%). 10 individual measurements were taken for each cross-section feature present, to allow for an average value and standard deviation to be calculated.

(d) ***Internal oxide scale – δ-phase characterisation*** The δ-phase layer was measured by drawing a line across the scale/alloy boundary and measuring the percentage coverage of the line by δ-phase.

A summary of these measurements is shown in Figure 5.3.

5.6.1.2 Cr depletion profiling

In order to investigate the growth mechanism differences between different conditions of L-PBF IN625, it is necessary to examine the microstructure beneath the oxide scale, particularly Cr depletion in the near-oxide affected region. To inform this, EDS line scans approximately 150 µm length were performed from the centre of the scale/alloy interface down through to the bulk of the sample. To improve the repeatability of the measurements, 3 repeat EDS lines scans were taken for each sample at 3 random regions across the surface of the cross-section. For each condition, the line scans were plotted, solved and fitted to Fick's 2nd law of diffusion for diffusion into or out of a semi-infinite solid using python code, see Equation (6.1) [66, 67]:

$$N_{Cr} = N_{Cr}^{(S)} + (N_{Cr}^{(B)} - N_{Cr}^{(S)}) \cdot erf \cdot (\frac{x}{2\sqrt{Dt}}) \tag{5.2}$$

where N_{Cr} is the Cr content in mol fraction, $N_{Cr}^{(S)}$ is the Cr content at the scale/alloy interface, $N_{Cr}^{(B)}$ is the Cr content in the bulk of the alloy, D is the diffusion coefficient of Cr in Ni-Cr alloy in mm^2/s, t is time in seconds, and x is the line distance.

For the fit, the diffusion coefficient of Cr in a Ni-Cr alloy was taken to be approximately 2.64×10^{-16} m^2/s, extrapolated from data reported by Ruzikova *et al.* (1981) [257]. From the fit, values of the diffusion coefficient of Cr in the IN625 bulk could be determined, along with the approximate depletion depth for comparison across the different conditions of L-PBF IN625.

5.6.2 X-ray Diffraction (XRD)

An automated Proto AXRD Benchtop X-ray Diffractometer was used to identify key phases in the as-received material (XY cross-sectioned), as well as the oxide scales formed on all conditions exposed to high temperature air and PWR hydrogenated water. This was conducted using a Cu Kα radiation source, indexed between a 2θ range of $20^\circ - 100^\circ$, with a step size of 0.02°. A combination of MATCH! (by Crystal Impact Ltd) [258] and Crystal Diffract (by CrystalMaker Software Ltd) software [259] was used to analyse the XRD data obtained. The data was compared to imported ICSD database files for key phases and oxides curated by the PSDS (The Physical Sciences Data Science Service), as well as resources from NIST [260].

5.6.2.1 Determination of residual stress using the $\sin^2(\psi)$ method

In order to determine the residual stress within the near surface of the oxide scales produced for t = 0.5 h − 1000 h, macroscopic scale measurements were obtained using conventional X-ray diffraction with the $sin^2(\psi)$ method. An automated Rigaku Ultima IV X-ray diffractometer was used to obtain this measurement by following the standard method outlined by the National Physical Laboratory (NPS) [172]. The method involves the determination of residual stress by measuring the strain in the crystal lattice via peak shift. This accounts for the elastic constants of the material and the assumption that there is linear elastic distortion of the crystal plane. Plane stress conditions are assumed, where stress normal to the surface is set to zero.

The principle of the analysis relies on the interaction between the incoming wave front of the X-ray beam and the crystal lattice, following Bragg's Law Equation (5.3) [172]:

$$n \cdot \lambda = 2d \cdot sin(\theta) \tag{5.3}$$

where n is the diffraction order, λ is the wavelength, d is the interplanar spacing, and θ is the diffraction angle.

The incoming X-ray interacts with the crystal to produce a diffraction pattern, which can be related to the distance between the atomic planes in the material. An interplanar space which is free from strain allows for the production of a pattern characteristic of the material. When the

material becomes elastically strained, the contractions and elongations produce a change in the materials interplanar spacing, d, which causes a shift in the characteristic pattern. An example of the observed peak shift can be viewed in Figure 5.4 for chromia formed upon L-PBF IN625. It is this shift in the diffraction pattern which can be measured to give a Δd [172]:

$$d_n = \frac{n \cdot \lambda}{2 \cdot sin(\theta)} \tag{5.4}$$

where d_n is the interplanar spacing for diffraction n.

Assuming the measurement is made in the surface of the oxide and the orthogonal coordinate system shown in Figure 5.5 is applied, strain in the lattice can be determined. This involves a comparison between the perfect unstrained lattice interplanar spacing with the strained interplanar spacing, assuming plane stress conditions where $\sigma_\psi = 0$. Experimentally, this can be achieved by measuring the strain along a direction ψ, by altering the tilt of the specimen in the diffractometer an various angles of ψ to give the following relationship, Equation (5.5) [172]:

$$\epsilon_\psi = \frac{d_{\phi\psi} - d_0}{d_0} \tag{5.5}$$

where ϵ_ψ is the strain measured for the angle ψ, and$d$ is the interplanar spacing for directions of the angles ψ and ϕ.

It is then possible to use the measured values of strain to determine the stresses present in the oxide surface via the application of Hooke's Law Equation (5.6) [172]:

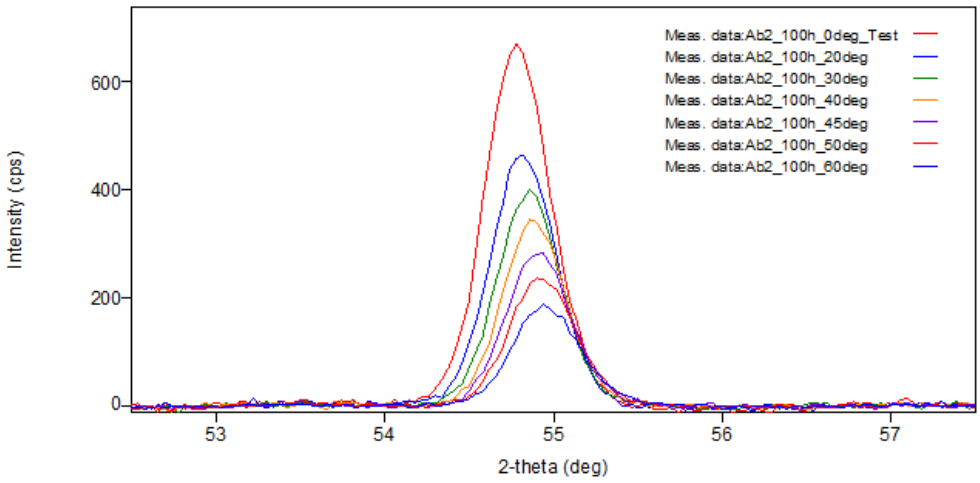


Figure 5.4: A plot showing the peak shift experienced by chromia grown upon an as-built token of L-PBF IN625, exposed to 950˚C for 100 h in air. Peaks were measured over a range of 0 - 60˚, showing decreased peak intensity with increasing tilt.

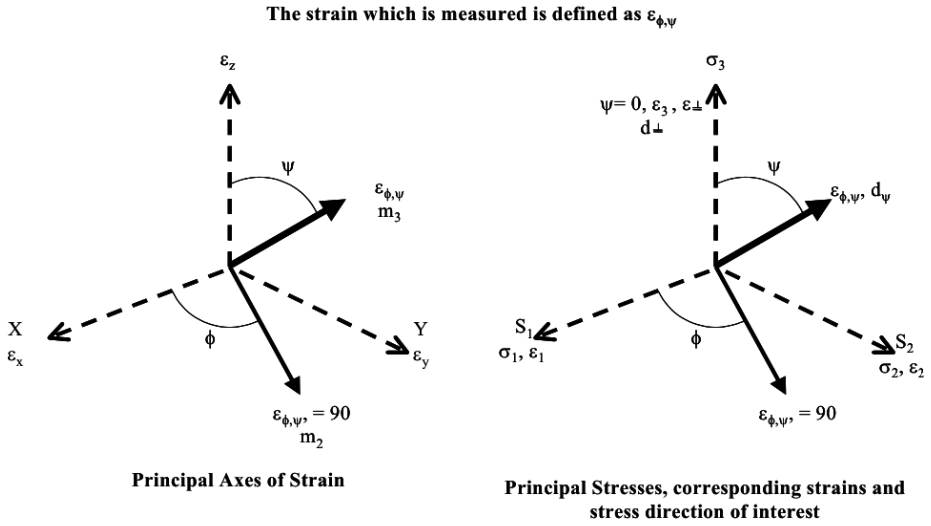


Figure 5.5: A diagram showing the co-ordinate system used to calculate the strain and stress in the surface of an oxide. Oxide scale through thickness assumed through z-direction. Taken from the Measurement Good Practice Guide No. 52, National Physical Laboratory, NPL [172].

$$\sigma_y = E \cdot \epsilon_y \tag{5.6}$$

where σ_y is the stress in direction y, E is the elastic modulus of the oxide, and ϵ_y is the strain in the y direction.

By the assumption that plane stress exists and that biaxial stresses are present in the sample surface, the following equation to be derived [172]:

$$\epsilon_x = \epsilon_y = -\nu \cdot \epsilon_z = \frac{-\nu \cdot \sigma_y}{E} \tag{5.7}$$

where ϵ_x and ϵ_z is the strain in the x and z direction, respectively, and ν is the Poisson's ratio.

Then by rearranging Equation (5.7) to assume plane stress conditions, the following equation takes form [172]:

$$\epsilon_z = -\nu \cdot (\epsilon_x + \epsilon_y) = \frac{-\nu}{E} \cdot (\sigma_x + \sigma_y) \tag{5.8}$$

Through the combination of Equation (5.5) and Equation (5.8), it is possible to measure a single stress acting in the surface Equation (5.9) [172]:

$$\sigma_\phi = \frac{E}{(1+\nu) \cdot sin^2(\psi)} \cdot (\frac{d_\psi - d_n}{d_n}) \tag{5.9}$$

where σ_ϕ is the stress in angle ϕ, and E is strain in the crystal lattice.

In this fashion, stress can therefore by calculated for any chosen direction from the change in interplanar spacing Δd, via measurement in the plane perpendicular to the sample surface and the direction through which stress is desired to be measured. A plot was generated for each sample, of $sin^2(\psi)$ against the measured interplanar spacing, for the d (116) of Cr_2O_3. An example of this plot can be viewed in Figure 5.6.

By calculation of the gradient of the line, m, and knowledge of the elastic constants of pure chromia (E_{116} = 334.5 GPa, ν_{116} = 0.264, taken from Guerian *et al.* (2017) [167], and Panicuad (2004) [261]), stress can be given by Equation (5.10) [172]:

$$\sigma_\phi = \left(\frac{E}{1+\nu}\right) \cdot m \tag{5.10}$$

where m is the gradient of the line of d vs $sin^2(\psi)$.

To achieve this, the Inorganic Crystal Structure Database (ICSD) was referred to in order to obtain a value for the characteristic interplanar spacing for a perfect, pure chromia (Cr_2O_3). This was calculated to be approximately d_0 = 0.1672124 nm for the (116) plane of a hexagonal close-packed crystal, taken from Sawada (1994) [262]. A high intensity 2θ peak characteristic of chromia was chosen (55˚) to ensure that small changes in d and the angular position of the peak were significant enough for the accurate determination of the residual stress.

Multiple XRD measurements were carried out for the 55˚ peak over a selected 2θ range of 52.5˚ – 57.5˚. A step size of 0.03 – 0.04˚ was applied throughout measurements, as well as a dwell time of 20 – 40s. These values were dependent on the thickness of the oxide film examined, where a longer dwell time and a smaller step size was required for the measurement of thinner oxide scales. The measurements were carried out for seven values of ψ: 0, 20.705˚, 30˚, 37.761˚, 45˚, 52.239˚ 60˚. The

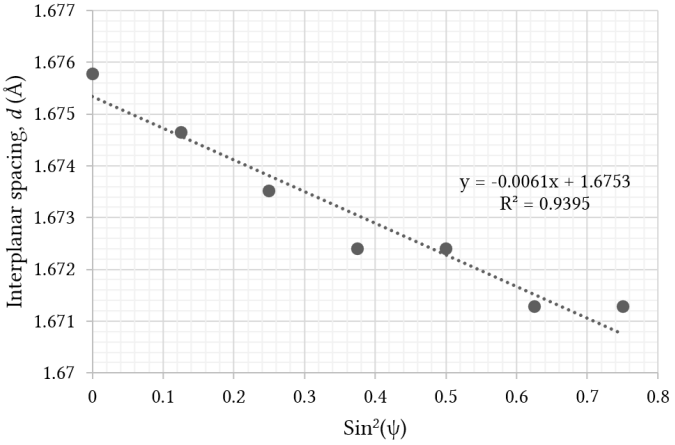


Figure 5.6: An example of an interplanar spacing, d, vs $sin^2\psi$ graph for chromia growth upon L-PBF IN625 in the (116) plane of Cr_2O_3.

values of ψ were selected to replicate the methods outlined by Guerain *et al.* (2017), allowing for direct comparison and validation of the results obtained for chromia. These were chosen to obtain equidistant values of $sin^2(\psi)$ ranging from 0 – 0.8 [167].

5.6.3 Characterisation of oxidation products, contact profilometry

Surface profiles were collected to investigate the oxide topography formed on the surface of tokens exposed to high temperatures. This was carried out using a NanoMap-LS 3D contact profilometer, using a 1 µm stylus tip, over areas of 500 µm × 500 μm^2 to generate a 3D surface topography map. A speed of 20 µm/s was selected to occur over a limit of 5000 positions, measuring out at 150 points measured per scan. A contact force of 15 mg was selected to limit damage to the oxide surface. Care was taken at the start of each measurement to manually calibrate the sample by varying X and Y until the surface was deemed to be approximately planar.

5.7 Corrosion testing, Simulating a Pressurized Water Reactor (PWR)

A recirculating autoclave loop was used to simulate the corrosive environment inside a PWR with high temperature hydrogenated primary water. The temperature of the autoclave was set to 300˚C, and water pressure was monitored at 10.8 MPa. Samples were exposed for interrupted periods of 500 h to 1500 h. Water chemistry inside the autoclave was controlled and set to contain: 2 ppm Li (added as 30.23 mg of LiOH), 3 ppm H_2 (33.7 cc/kg), and <5 ppb of O_2. The feed tank volume of water was at 2.5 litres capacity and was maintained alkaline at 10.5 pH.

To assess the effect of the as-built microstructure and surface finishing techniques on oxidation performance, disks (14 mm diameter, 2 mm thick) of as-built material, solution-treated material, and cuboidal tokens of wrought IN625 (10 mm × 10 mm × 2 mm) were investigated for comparison to conventional materials used in PWR environments. A series of different surface finishes were investigated, as informed by Rolls-Royce Nuclear: additive surface tokens, polished (0.25 µm OP-S), electropolished, and CHEF. These are outlined in Table 5.8.

Each sample condition was exposed to the PWR simulated environment for two time periods of 500 h and 1500 h to allow for the evolution of the oxide scale with time to be investigated. At each time period, the samples were removed, and re-weighed 3 times to measure the net mass gain, then stored in a desiccator.

Table 5.8
Corrosion testing matrix for: L-PBF IN625 and wrought IN625, T = 300°C, P = 10.8 MPa, t = 500 h, 1500 h.

Sample condition		Time (h)	
Microstructure	**Surface**	**500**	**1500**
L-PBF, As-built	0.25 µm	✓	✓
L-PBF, Solution	0.25 µm	✓	✓
	Additive	✓	✓
	CHEF	✓	✓
	Electropolish	✓	✓
Wrought, Solution	0.25 µm	✓	✓

5.8 Characterisation of corrosion products

5.8.1 External oxide scanning electron microscopy

A Zeiss EVO15 VP ESEM microscope with Backscattered Electrons (BSE) and Bruker eFlash EDS capabilities was used to obtain images and compositional data from the surface oxide. A combination of EDS point, line and map scans were carried out to identify the oxide and embedded precipitates. An accelerating voltage of 20 kV was applied throughout imaging.

5.8.2 Characterisation of oxidation products, X-ray diffraction

As laid out in Section 4.6.3, an automated Proto AXRD Benchtop X-ray Diffractometer was used to identify the corrosion product produced upon all specimens investigated.

5.8.3 Characterisation of oxidation products, Raman Spectroscopy

Due to overlap between key phases present in the XRD measurements collected for L-PBF IN625 following exposure to PWR hydrogenated waters, Raman spectroscopy was applied to resolve them. A Renishaw InVia confocal Raman microscope equipped with WiRE 4.2 software was used to collect and characterise the Raman peak shift values obtained from the oxide surface. This was carried out on samples exposed for 1500 h. The microscope was operated using a 633 nm edge

laser, focused at a working distance of 50× with a beam power of 20 mW. Samples scanned were indexed across an area of 900 μm^2 with a step size of 1 μm. Scan dwell times were selected based on the roughness of the token and the resolution obtained for periods of 8 – 25 s. The RRUFF™ Project database was consulted to collect peak shift values of key oxides formed upon the PWR exposed tokens [263].

5.8.4 Oxide removal and grain orientation correlations

To correlate oxide thickness to specific grain orientations the following multi-step method was applied. Four individual rectangular sites of area 500 μm × 500 μm^2 were chosen across the L-PBF solution-treated specimens (of 0.25 μm finish), following exposure to 1500 h in PWR hydrogenated water. To mark out these sites, a Buehler Wilson VH1102 Micro Hardness machine with a Vickers indenter was used to place 4 indents, one in each corner. A load of 1 kg was applied, with a dwell time of 10 s. SE-SEM micrographs were then collected for later comparison to EBSD IPFs.

Following indentation, a gentle vibropolish was applied to oxides grown upon flat XY orientation samples (cut perpendicular to the building direction) using a Buehler VibroMet-2 Tabletop vibratory polisher. A napless porous synthetic MetPrep Chemicloth was mounted and covered with 500 ml of OP-S (0.25 μm) as a polishing lubricant. Individual samples were mounted in weighted sample holders (50 g) and placed onto the table. A vibration amplitude of 60% was selected to give 6 rpm. The samples were polished for 50 h each to remove the oxide, and visually inspected intermittently using an optical microscope. Following removal, tokens were submerged in ethanol and placed into an ultrasonic bath for 5 minutes.

EBSD IPF maps of the revealed sites were then collected using the same microscope, method and parameters as outlined in Section 5.3.5. EBSD IPF maps were correlated with the corresponding SE-SEM micrographs of the external oxides to allow for a grain orientation-oxidation relationship to be established.

5.8.5 Focused ion beam milling - Dual-Beam cross-sectioning

In order to cross-section thin oxides and examine their thickness and morphology, Focused Ion Beam (FIB) milling was applied. An FEI Quanta 3D FEG FIB-SEM was used, applying a variation on the method used by Cruchley *et al.* (2014) [264]. First the sample was attached to a five-axis motorised stage and a eucentric height was set (the location at which the ion and electron beams intersect). This was then tilted to 52° to allow for the positioning of the sample perpendicular to the ion beam. To protect the oxide film from delamination during ion milling, a thick layer of

platinum, Pt (30 μm × 2 μm × 2.5 μm) was deposited on the desired area using a Pt needle. An initial rectangular area of 12 × 12 μm was milled away using the Ga ion beam at the following applied currents: 65 nA current to remove bulk material, 30 nA to mill a crude flat surface, and two subsequent cleaning cross-sections at 7 nA, and 0.5 – 1 nA until the oxide and the sub-scale microstructure was revealed to a sufficient clarity. SE micrographs were then taken at 20 kV accelerating voltage.

5.8.6 Focused ion beam milling and TEM of oxides

To characterise the sub-micron sized precipitates embedded in the surface of the oxide scales and any voids in the sub-scale, TEM was required. To investigate the microstructure and the elemental composition of the precipitates, thin lamellae were prepared using a Thermofisher Helios 660 Xe plasma FIB. This was performed using a standard FIB-lift out technique [265]. The following currents were applied during milling and cleaning steps at 30 kV: trenches via 15 nA, and cleaning at 4 nA and 1 nA. Following this the sample was undercut at 4 nA and 30 kV, lifted-out and attached to a Cu grid. Final polishing of the sample lamellae was carried out at 5 kV, and 2 kV at both 57° and 47° for 20 s each.

A FEI Talos F200x fitted with Oxford Super-X-Detectors EDS capabilities was used to examine variations in the chemical composition via point scanning, mapping and STEM-EDS line scans. Here a beam energy of 200 kV was used, with a dwell time of 10 μm. Note, images were taken off-axis (i.e. the incident beam was not aligned to a particular crystal orientation direction). A series of High-angle annular dark-field imaging (HAADF), Dark Field (DF), and Bright Field (BF) micrographs were produced.

Chapter 6

The effect of microstructure and surface finish on the high temperature oxidation of Laser Powder Bed Fused IN625

6.1 Abstract

Isothermal oxidation of Laser Powder Bed Fused (L-PBF) IN625 was investigated in air at 950°C for 1000 h, across multiple heat-treated and surface conditions. Findings indicated that ground L-PBF IN625 performed to a similar standard to wrought Ni-based superalloys, regardless of microstructural anisotropy. Additive surface roughness and Centrifugal High Energy Finished (CHEF) tokens exhibited accelerated kinetics and a departure from sub-parabolic to cubic behaviour, showing spallation, severe void formation and intergranular oxidation. Growth of the near-continuous Ni_3(Nb,Mo) δ-phase differed across conditions and is suggested to improve the adherence of chromia by reducing the critical temperature change for spallation.

Authors: E. R. Lewis, B. Attard, Z. Gao, N. Cruchley, A. C. Cruchley, M. M. Attallah, S. Cruchley.

Keywords: Oxidation, Superalloys, SEM, X-ray diffraction, Rapid solidification, Stress relaxation

6.2 Highlights

- Laser Powder Bed Fused IN625 oxidised at a similar rate to wrought Ni-superalloy.
- The anisotropic as-built microstructure did not alter oxidation kinetics overall.
- AM surface roughness and CHEF residual stresses lead to accelerated oxidation.
- Surface finish altered the precipitation of δ-phase near-continuous layer.
- δ-phase at Cr_2O_3/IN625 interface lowers the temperature change for spallation.

6.3 Introduction

High temperature degradation via oxidation is a life-limiting factor in the design of components for extreme environments. Ni-based superalloys are used extensively in the manufacturing of critical components in nuclear reactors for steam generator tubing and valving, and many other applications in the aerospace, automotive and marine industries [18–20, 31, 33, 42, 65].

Chromia forming Ni-based superalloys, such as Inconel 625 (IN625), have been designed and optimised for such environments, able to provide a combination of high fatigue and creep resistance at elevated temperatures $T \leq 980^{\circ}C$, whilst maintaining excellent oxidation and corrosion resistance [18–20, 23, 26, 27, 29, 42, 53, 65, 156, 266–268].

Additive Manufacturing (AM) techniques like Laser Powder Bed Fusion (L-PBF) provide a promising route for the manufacture of complex components common to high temperature environments, without the need of costly machining steps [42]. IN625 is well-suited to L-PBF due to its superior weldability (linked to low Al, Ti wt.%) and is found to produce high density parts without cracking or defects [33, 269]. L-PBF IN625 has been widely investigated in both its as-built and heat-treated forms. Key differences in the microstructure compared to wrought materials arise due to the fast solidification rates common to L-PBF ($\sim 10^6$ K/s) [35, 270]. This typically produces columnar grains extending in the building direction with a cellular sub-structure, and consequently anisotropic mechanical properties with high residual stresses [33, 35, 126, 271–274]. Furthermore, heavy elements such as Nb and Mo segregate to interdendritic regions in the as-built microstructure, leading to localised compositions exceeding the standard composition for IN625 [12, 28, 34, 35, 38, 48, 118, 243].

Heat treatments counteract these effects by removing microstructural anisotropy, resulting in similar mechanical performance to wrought alloy [34]. Chemical inhomogeneity via microsegregation however remains an issue. Selected area electron diffraction (SAED) in the γ-matrix of heat-treated L-PBF IN625 has shown that intercellular boundaries remain enriched with Nb and Mo, and depleted in Ni, Cr and Fe, even following solution treatment at 1177°C for 1h. [61, 117]. Interdendritic regions saturated in Nb and Mo aid in the accelerated formation of the brittle orthorhombic Ni_3Nb δ-phase, forming in $t < 5$ minutes compared to $t > 10$ h in wrought IN625 when stress relieving at 870°C for 1 h [38, 47, 61]. Oxidation studies of L-PBF IN625 are limited to short periods of $t < 1000$ h, at $T = 850 - 1050$℃ in isothermal laboratory air and pressure [1, 9, 10, 13–17, 175, 191]. Results obtained for L-PBF IN625 are nonetheless promising, shown to perform to a similar standard to wrought chromia forming Ni-based superalloys.

Findings by Chyrkin *et al.* [1, 196] determined that the AM microstructure did not affect the

oxidation characteristics in air. Instead, kinetics were driven by the intergranular oxidation following buckling, and minor alloying differences in Ti, Mn, Si, Al, and S. It was also observed that variations in grain size (up to 100 μm) altered oxidation behaviour but not the intergranular oxidation morphology. Internal oxidation at grain boundaries, and formation of voids were found to be more pronounced in L-PBF IN625, due to steep Cr depletion profiles underneath the scale and alloying additions of Si [1, 196].

For IN625, a near-continuous Ni_3Nb δ-phase layer forms at the scale/alloy interface, remaining stable at T = 700 – 1000˚C [1, 7, 9–11, 13–15, 175, 191, 192, 196]. It is understood that δ-phase grows following changes in the chemical potential of Nb and Mo beneath the scale due to Cr depletion [7]. It is unclear how microsegregation of Nb and Mo, and minor alloying variations may affect the oxidation characteristics of AM alloy by possible changes to the growth and nucleation of this phase. Elliot and Hampton [193] reported the effects of Nb on the cyclic oxidation of Ni-Cr alloys, reporting that Nb led to reduced spallation, an improvement in oxide self-healing, and a reduction in internal oxidation. Delaunay *et al.* investigated the protective qualities of the Ni_3(Nb,Mo) layer, reporting improvements in the oxidation resistance of IN718 by acting as a diffusion barrier against Cr [185]. Contradictory findings state that δ-phase may deteriorate the protective qualities of the oxide scale. Parizia *et al.* [15] stated that the formation of the Ni_3(Nb,Mo) layer leads to wrinkling of the scale, generated by growth stresses via mismatch in the volume expansion coefficients between chromia, δ-phase, and the bulk [7]. This is believed to accelerate oxidation by causing microcracking in the protective chromia via a volume change in the scale/alloy interface [7, 9, 15].

Surface roughness and residual stresses in Ni-based superalloys directly influence oxidation rates by affecting the grain boundary and dislocation density in the surface [67]. A key drawback for the application of AM is that the additive surface roughness is high ($R_a \sim 15$ μm for vertical surfaces), often too rough and non-uniform for use in industry [10, 13, 133, 187]. This can lead to oxidation rates 100 × higher than the standard expected for wrought alloys [16]. Surface topology may affect the precipitation of the δ-phase, by altering the Cr depletion profile underneath the scale.

Research is needed to establish post-process heat-treatments and surface finishes optimised for oxidation resistance in AM components, and to characterise their influence on mechanisms of oxidation. An investigation of the isothermal oxidation behaviour of L-PBF IN625 at 950℃ for 1000 h was conducted, using as-built and solution-treated tokens to evaluate the effects of grain size and microsegregation. A series of surface finishes applicable to AM were selected to evaluate their effect on the oxidation rate, the oxidation-affected region, and growth of the δ-phase layer.

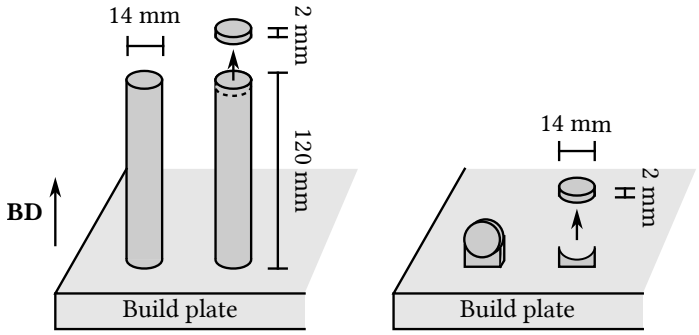
6.4 Material and Methods

6.4.1 Materials

Specimens were built using an EOS M280 (400W) L-PBF machine with the default IN625 Performance 1.10 parameter set. Two builds were completed: Builds 1 and 2 (Figure 6.1). IN625 powder particle sizes of 15 – 45 µm were used with a layer thickness of 40 µm. The powder chemical composition was measured using inductively coupled plasma mass spectroscopy (ICP-MS) and X-ray fluorescence (XRF), in accordance with ASTM F3056-14 (see Table 6.1) [243].

In order to compare the oxidation behaviour of the as-built and solution treated microstructures, 72 fully dense cylinders (Figure 6.1(a)) (14 mm diameter, 125 mm height) were manufactured. A set of cylinders underwent solution-treatment at 1177°C for 1 h in air, followed by a water quench [122]. Disks (14 mm diameter, 2 mm height) were cut from both as-built and solution-treated cylinders using electrical discharge machining (EDM). Specimen surfaces were then ground, and the edges were chamfered at 45° using wet SiC papers to 4000-grit (approximately R_a = 6 µm).

To investigate the effect of additive surface roughness, a set of 420 fully dense individual disks (14 mm diameter, 2 mm thickness) of L-PBF IN625 were manufactured (Figure 6.1(b)). To remove



a) Build 1
Effect of microstructure

b) Build 2
Effect of surface finish

Figure 6.1: A Schematic showing the orientations of L-PBF IN625 samples fabricated in Build 1 and 2. Build 2 tokens include bar-supports. BD indicates the building direction.

TABLE 6.1
MEASURED COMPOSITION FOR L-PBF IN625 POWDERS, BATCH 1 AND BATCH 2 FOR THIS STUDY.

Alloy	Element (wt.%)												
	C	Mn	Si	P	S	Cr	Co	Mo	Nb	Ti	Al	Fe	Ni
IN625 Powder	-	<0.01	0.07	<0.01	-	21.27	0.04	9.02	3.65	0.10	0.11	3.66	Bal.
Batch 1	-	0.02	0.11	<0.01	-	21.94	0.05	9.69	3.88	0.12	0.16	3.95	Bal.
Batch 2	-	<0.02	0.05	<0.01	-	21.51	<0.02	9.48	3.87	0.11	0.130	3.50	Bal.

TABLE 6.2
OVERVIEW OF MATERIALS, HEAT TREATMENTS AND SURFACE FINISHES INVESTIGATED.

Build no.	**Sample condition**	**Surface finish**			
		R_a **(µm)**	R_z **(µm)**	S_a **(µm)**	S_v **(µm)**
1 – Microstructure	Ground (AB)	0.14	0.01	-	-
	Ground (ST)	0.14	0.01	-	-
2 – Surface finish	Additive (ST)	9.10	33.80	6.80	33.50
	CHEF (ST)	0.40	2.20	0.90	15.00

AB = As-built.
ST = Solution-treated (1177°C 1h, water quench).
R_a = Arithmetical average relative to base length.
R_z = Maximum valley depth below the mean line.
S_a = Maximum valley depth of a selected area.
S_v = Arithmetical mean height of the selected area.

microstructural anisotropy, the specimens underwent solution-treatment in an argon back-filled quartz ampule [122]. Centrifugal High Energy Finishing (CHEF) was selected as an alternative surface finish applicable to complex AM components, producing a smooth surface finish with high compressive residual stresses similar to that of shot-peening (~550 MPa) [137]. The CHEF tokens were produced in three stages: (1) cutting for 120 minutes with ceramic and 50 ml of LQ18 reagent/water mix (light descaling agent to remove oxides, pH = 1 – 2); (2) smoothing for 120 minutes with ceramic and 50 ml of LQ16 reagent/water mix (concentrated cleaner for polishing, pH = 8.5 – 9.0); (3) polishing for 60 minutes in dry maize. Fresh media was used at the start of each stage [137].

Sample surface roughness was determined using a combination of techniques. An Alicona InfiniteFocus confocal microscope at ×5 magnification was used, and the data analysed using the InfiniteFocus Suite. Area measurements were investigated to take into account the non-uniform surface of AM components. For comparison, a Fowler Surf-corder SE1700 Rugosimeter surface analyser was also used, applying a Gaussian fit to peaks recorded.

A summary of the sample specimen types can be viewed in Table 6.2.

6.4.2 Isothermal oxidation testing

Isothermal oxidation testing was conducted at 950°C in laboratory air and pressure for t = 24, 100, 500, and 1000 h in a Lenton Thermal Designs horizontal tube furnace. The furnace was calibrated to give a heat zone correct to ±1°C using calibrated R-type and K-type thermocouples.

Prior to exposure, samples were degreased in acetone in an ultrasonic bath, then dried with

air. Specimen dimensions were measured using a screw gauge micrometer. Samples were placed in open ceramic alumina crucibles (6 repeat tokens per condition, per exposure time) and placed directly into the heat zone of the pre-heated furnace. After exposure, the samples were removed from the furnace and left to cool to room temperature. Specific mass gain/area curves were generated by measuring the sample mass prior to, and after exposure using a Sartorius ME5 micro balance (± 0.00001 g).

6.4.3 Microstructural characterisation, SEM, TEM, XRD

Prior to exposure, metallographic specimens were cut via EDM and mounted in Bakelite. Following their oxidation, oxide cross-section specimens were also produced for each condition, per time period. This was carried out by sputtering the tokens with gold, Ni-plating and then mounting in low-shrinkage cold-setting resin. The mounted samples were cut into halves using a Struers Accutom-50 with a SiC blade to reveal the oxide cross-section. Metallographic samples were ground using wet SiC papers, and polished to 0.25 μm mirror-finish using colloidal silica solution (OP-S). The microstructure was examined using SEM with backscattered electrons (SEM-BSE) and energy dispersive spectroscopy (EDS), conducted using a JEOL 6060 SEM, with Oxford INCA EDS at 20 kV. Cr depletion profiling underneath the oxide scale was carried out using EDS line scan data fit to Fick's second law of diffusion. This allowed for the calculation of depletion depth, and approximation of Cr diffusion coefficients in each condition, see Equation (6.1) [67]:

$$N_{Cr} = N_{Cr}^{(S)} + (N_{Cr}^{(B)} - N_{Cr}^{(S)}) \cdot \mathrm{erf} \cdot \left(\frac{x}{2\sqrt{Dt}} \right) \tag{6.1}$$

where x is the distance from the scale/alloy interface, N_{Cr} is the Cr content in mol fraction, $N_{Cr}^{(S)}$ is the Cr content at the scale/alloy interface, $N_{Cr}^{(B)}$ is the Cr content in the bulk, D is the diffusion coefficient of Cr in the alloy in m^2/s, and t is time in seconds. For the fit, the initial prediction for the diffusion coefficient of Cr in a Ni-Cr alloy was taken to be approximately 2.64×10^{-16} m^2/s, taken and adapted from Ruzikova *et al.* [257].

External oxides were examined using SEM with BSE and secondary electrons (SE). Fiji image processing software was applied to measure oxide thickness and to quantify the amount of Ni_3Nb δ-phase formed at the scale/alloy interface [249]. The δ-phase was measured as a percentage coverage along the line of the scale/alloy interface, across 10 repeat micrographs of the same magnification, for each condition, per time period.

Electron backscatter diffraction (EBSD) was carried out to determine texture and grain size using a JEOL 7000F FEG-SEM at 20 kV, equipped with an Oxford Instruments Nordlys EBSD detec-

tor. Depending on the microstructure examined, step sizes ranging from 1.5 – 2.5 μm were applied, over maximum scanning areas of 800 × 600 μm^2 to produce inverse pole figure (IPF) maps representative of the sample. MATLAB was used with the MTEX toolbox to generate IPF maps from EBSD data [250–254]. Average grain size (D50) measurements were calculated using the Heyn Lineal Intercept method (ASTM E112-13) in the XY and XZ directions using IPF maps generated [275].

To examine voids present in the oxidation-affected sub-scale, Transmission Electron Microscopy (TEM) was performed. Thin lamellae were prepared via a Thermofisher Helios 660 Xe plasma Focused Ion Beam (FIB) using a standard FIB-lift out method to mill and clean the sample [265]. TEM was carried out using a FEI Talos F200x fitted with Super-X-Detectors EDS capability. A beam energy of 200 kV was used, with a dwell time of 10 μms to collect EDS maps and line scans.

To identify the oxide crystal structure, X-ray Diffraction (XRD) was performed using a Proto AXRD Benchtop X-ray Diffractometer with a Cu Kα radiation source, indexed between 2θ = 20 – 100°, with a step size of 0.03°.

6.4.4 Measuring oxide residual stress

To investigate residual stress in the surface of the scale, the XRD $\sin^2(\psi)$ method was applied using a Rigaku Ultima IV automated multipurpose XRD, as outlined by the National Physical Laboratory (NPL) standard [172]. Data from the Inorganic Crystal Structure Database (ICSD) was used to obtain the characteristic interplanar spacing (d_0) for a perfect, non-stressed chromia of d_0 = 0.16721 nm for the (116) plane [262]. The high intensity 55° 2θ reflection of chromia (corresponding to the (116) plane) was selected to ensure small changes in d and the angular position of the reflection were significant enough for the accurate determination of residual stress in the oxide surface. The interplanar spacing shift in the 55° reflection was measured over a 2θ range of 52.5 – 57.5°, using a step size of 0.03 – 0.04°, and dwell times of 20 – 40 s, dependent on the thickness of the scale investigated. Seven values of ψ were investigated: 0.000°, 20.705°, 30.000°, 37.761°, 45.000°, 52.239°, and 60.000°. The values of ψ were selected to provide equidistant values of $\sin^2(\psi)$ from 0 – 0.8, for comparison to results obtained for pure chromia by Guerain *et al.* [167]. The elastic constants for pure chromia were taken as follows: E_{116} = 334.5 GPa, and ν_{116} = 0.264, taken from Guerian *et al.* [167] and Panicuad *et al.* [261]. The stress state of the oxide was determined by plotting a straight-line graph of the interplanar spacing of chromia, d, against $\sin^2(\psi)$, then calculating the gradient of the fit, m, [172, 276]:

$$\sigma_\phi = \left(\frac{E}{1+\nu}\right) \cdot m \tag{6.2}$$

where σ_ϕ is the stress in the oxide, E is the Young's modulus of the oxide, ν is the Poisson's ratio of the oxide, and m is the gradient of the fit line.

6.5 Results

6.5.1 Microstructural characterisation

Figure 6.2 shows the SEM-BSE micrographs and EBSD IPF maps of as-built L-PBF IN625, and the microstructure following solution-treatment. The as-built material demonstrated a fine cellular microstructure, with grains <22 µm in size, and cells in the XY direction approximately 1 µm in diameter across both builds [275]. Fine cells extended parallel to the build direction, with strong texturing effects observed in the ⟨100⟩ direction. The as-built microstructures observed across Builds 1 and 2 were deemed to be similar, showing no significant difference in chemical composition using EDS, or in cell/grain size and morphology.

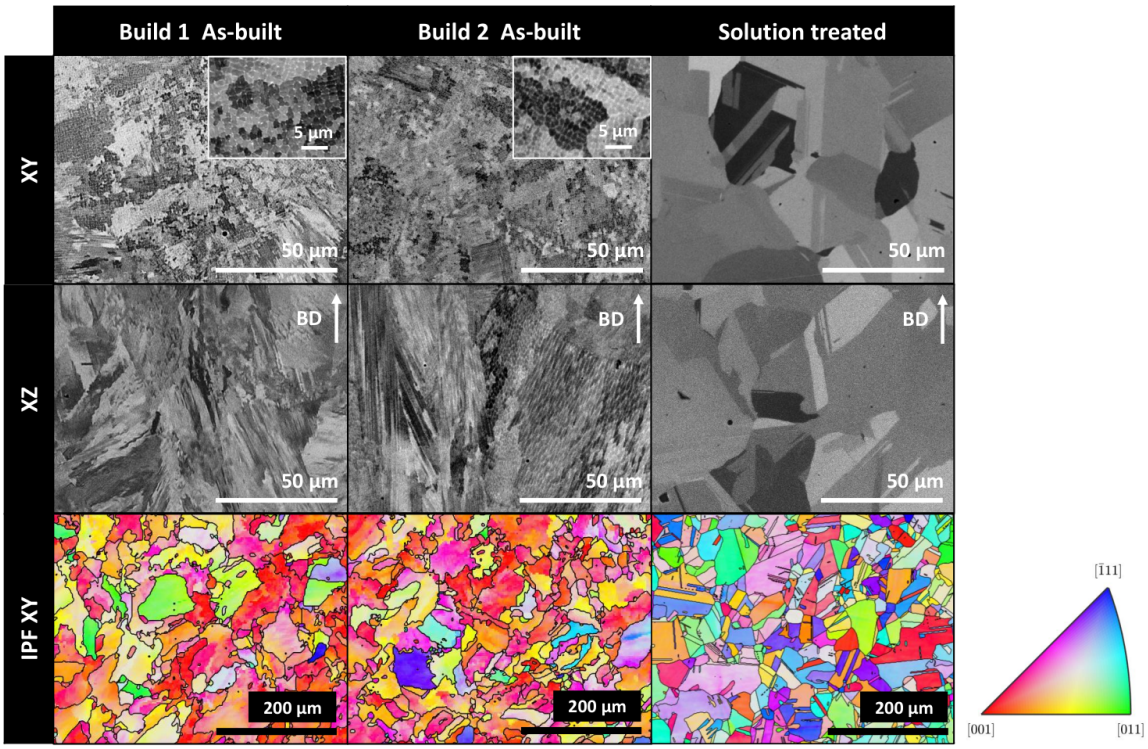
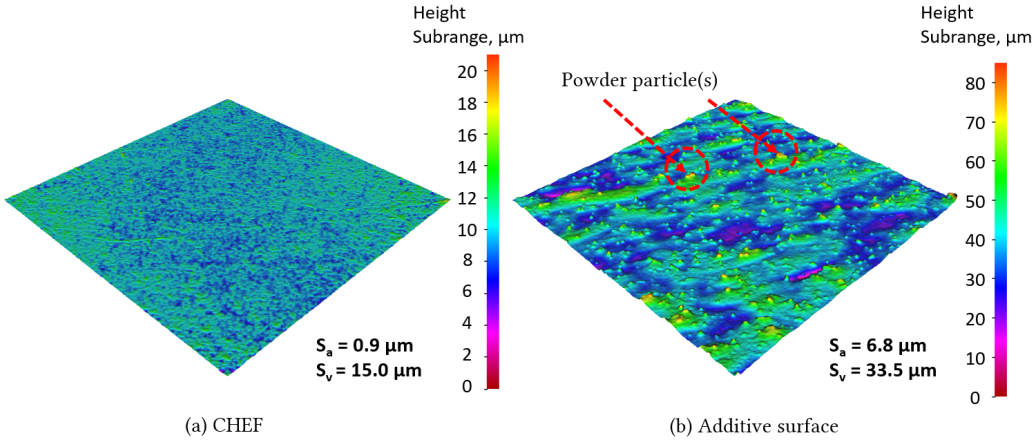


Figure 6.2: SEM-BSE micrographs and IPF maps of the as-built and heat-treated microstructures of L-PBF IN625 across Build 1 and Build 2, where BD indicates the building direction. Solution-treated material across both builds showed the same equiaxed and recrystallised microstructure. Solution-treated micrographs were taken using Build 2 materials.

The solution-treated microstructure was revealed to be fully recrystallised, with equiaxed grains <25 µm in size, demonstrating a complete transformation from the as-built structure. A random texture was exhibited throughout the microstructure, showing the elimination of texture effects resultant of the L-PBF process. When compared to as-built material, the solution-treated IN625 (see Figure 6.2) showed a decrease in the number and size of precipitates observed, suggesting the successful redistribution of solute during the heat treatment [191].

6.5.2 Surface roughness

The surface roughness measurements recorded for L-PBF IN625 can be viewed in Table 6.2, and the associated surface profile height variation maps for the CHEF (ST) and additive (ST) tokens are shown in Figure 6.3 (a) and (b), respectively. Following AM, un-melted powder particles were observed to be adhered to the additive surfaces, see Figure 6.3 (b). In the absence of any surface finishing, additive surfaces yielded mean surface S_a values of 6.80 µm, with mean average height variation $S_v \leq 33.50$ µm. This was deemed representative of AM surfaces investigated in literature, where surfaces are reported to show $S_a \geq 10$ µm, with best cases reaching $S_a = 1.5 - 6$ µm along the surface of an additive component [41, 88, 132, 277]. Following CHEF, a significant improvement in the surface finish was observed, where roughness was reduced to sub-micron levels of S_a = 0.90 µm, with S_v = 15.00 µm. This was within the range observed for similar L-PBF components finished using CHEF [137].



(a) CHEF (b) Additive surface

Figure 6.3: Confocal images showing the height variation observed across the (a) CHEF (ST) surface, and (b) as-received additive (ST) surface L-PBF IN625 samples, both measured in the XY orientation. The two conditions use two different colour styles, in order to highlight the features present, e.g. the labeled powder particles present in the case of the additive surface tokens.

6.5.3 Isothermal oxidation

The oxidation data for all conditions of L-PBF IN625 was collected and fit to the classical Wagner equation, (Equation (6.3)), and log-log plots were generated for each data set, to determine the exponent *n*. For comparison, the parabolic and cubic rate constants (Table 6.3) were calculated for all conditions:

$$(\Delta m)^n = K'_n \cdot t \tag{6.3}$$

where Δm is the specific mass gain/area (g/cm^2), K'_n the growth rate constant (g/cm^2)^n/s), and t is the exposure time (s).

The fit applied to the mean mass gain data for all conditions can be viewed in Figure 6.4, plotted using their respective *n*-values into Equation (6.3), against standard wrought IN625 data taken from Chyrkin *et al* (using tokens with a comparable starting surface finish of 0.25µm) [1]. Sub-parabolic oxidation behaviour ($n>2$) was observed (see Figure 6.4, Table 6.3), with the exception of the additive (ST) tokens, which showed a departure to cubic behaviour ($n = 3$). This contrasted the typically parabolic behaviours observed in wrought Ni-based superalloys [1–4, 7, 9–11, 173, 278]. Ground (AB, ST) tokens showed approximately the same mass gain over 1000 h exposure, showing lower rates of oxidation compared to wrought IN625. Higher surface area and residual stresses in the additive (ST) and CHEF (ST) led to accelerated growth of oxide, respectively.

Table 6.3
Values of the exponent, n, parabolic, K_P, and cubic, K_C, rate constants for the oxide growth at 950°C, 1000 h for L-PBF, and wrought IN625 (with starting surface finish of 0.25µm) from literature.

Condition	K_P **(mg^2/cm^4/s)**	***n***	K_C **(mg^3/cm^6/s)**
Ground (AB)	$7.60\,(\pm0.04)\times10^{-7}$	2.6 (±0.1)	$0.88\,(\pm0.04)\times10^{-6}$
Ground (ST)	$6.00\,(\pm0.04)\times10^{-7}$	2.7 (±0.1)	$0.71\,(\pm0.03)\times10^{-6}$
Additive (ST)	$2.41\,(\pm0.38)\times10^{-6}$	3.0 (±0.2)	$2.30\,(\pm0.09)\times10^{-6}$
CHEF (ST)	$1.35\,(\pm0.06)\times10^{-6}$	2.4 (±0.2)	$7.90\,(\pm0.58)\times10^{-6}$
Wrought [1]	1.61×10^{-6}	2.0	

[1] Data taken from Arrhenius plot, taken from Chyrkin *et al.* [1].

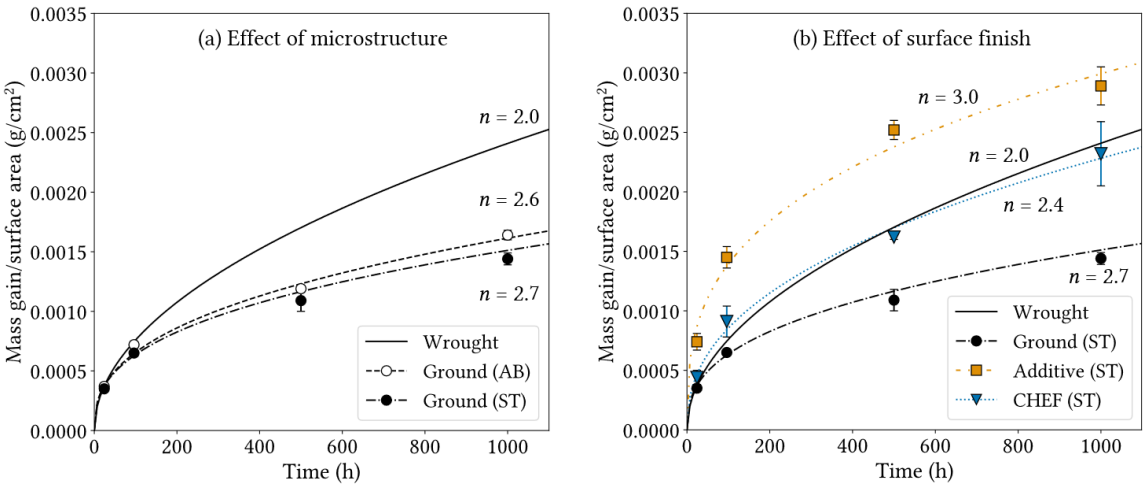


Figure 6.4: Mean mass gained/area vs time for each condition of L-PBF IN625, oxidised at 950˚C for up to 1000 h compared to wrought IN625: (a) Plots comparing the effect of microstructure, (b) Plots comparing the effects of surface finishing. Wrought data taken from Chyrkin *et al.* [1].

6.5.4 Oxide cross-section analysis

6.5.4.1 External oxide

Figure 6.5 shows SEM-BSE cross-sections and the top view of the oxide scales produced for L-PBF IN625 after 24 h – 1000 h at T = 950˚C. A combination of EDS maps, point scans and XRD patterns, Figure 6.6 and Figure 6.7, determined that all conditions formed Cr_2O_3 external oxide with slight Mn enrichment incorporated throughout. The Mn enrichment in the scale was most prominent in the additive (ST) samples (Figure 6.7), identified via XRD to be $Ni(Mn_{0.2}Cr_{1.8})O_4$ spinel.

For Ground (AB) and Ground (ST) samples, the morphology of the protective chromia appeared to be porous (Figure 6.8), and fairly uniform in thickness (Table 6.4), increasing from an average of <2.5 µm to <10 µm at 24 h and 1000 h, respectively [1, 191]. From SE external oxide micrographs obtained after 24 h (Figure 6.5), it was observed that the Ground (ST) tokens showed enhanced oxidation along grain boundaries. This was less apparent in the Ground (AB) samples.

The additive (ST) surface tokens investigated showed a non-uniform and wrinkled scale, where un-melted IN625 powder particles adhered to the surface oxidised preferentially. A thicker oxide scale was observed along these powder particles, measured on average to be 4.0 (± 0.4) µm thick, compared to 1.0 (± 0.2) µm across the smoother surfaces of the sample after 24 h. In some cases, the un-melted powder particles were observed to be consumed by oxidation completely, as shown in Figure 6.5 and Figure 6.9. Cracking was also observed inside the oxidised powder particles after 24 h of exposure, see Figure 6.5. The CHEF oxide tokens showed a highly wrinkled oxide scale after 1000 h of exposure. Thinner oxide scales were observed in the more complex surface finishes investigated, additive (ST) and CHEF (ST) compared to ground tokens.

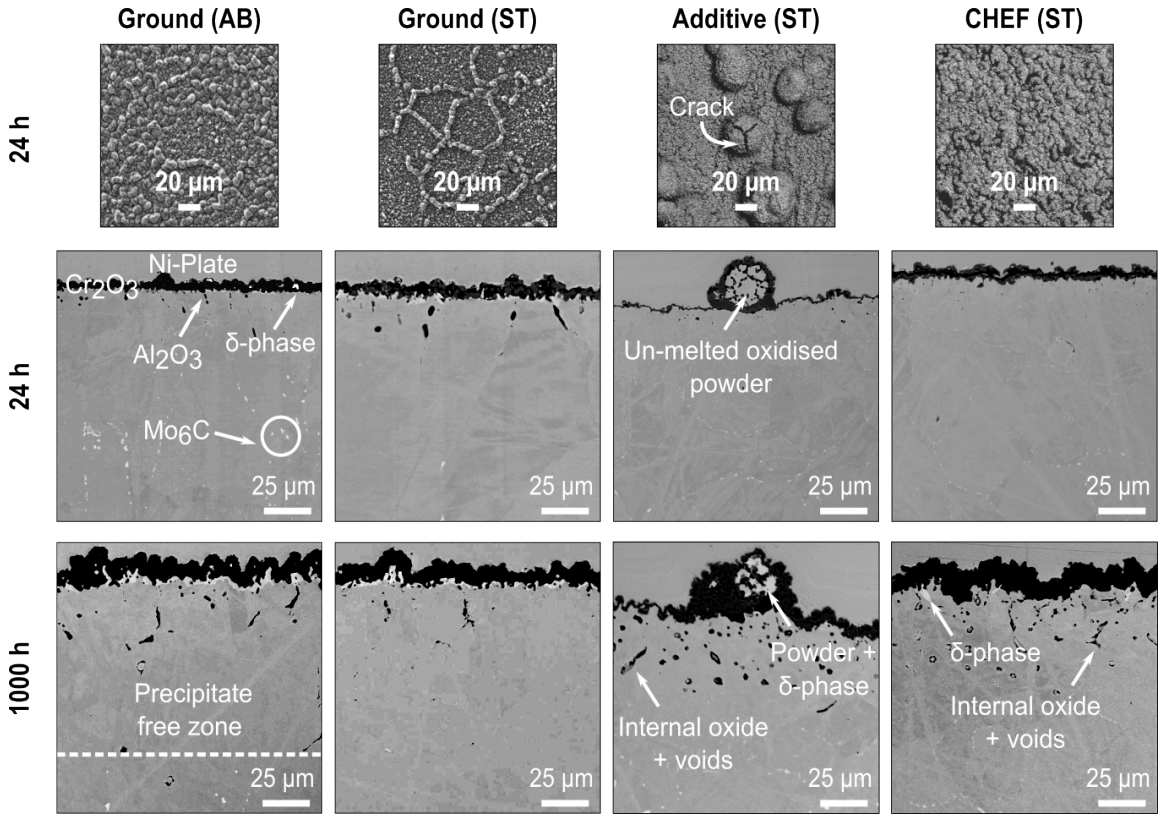


Figure 6.5: Summary of SEM-BSE oxide cross-sections for L-PBF IN625 exposed to 950 ˚C in laboratory air and pressure for 24-1000 h. SE image inserts show the XY external oxide formed upon the surface of each sample condition after 24 h exposure.

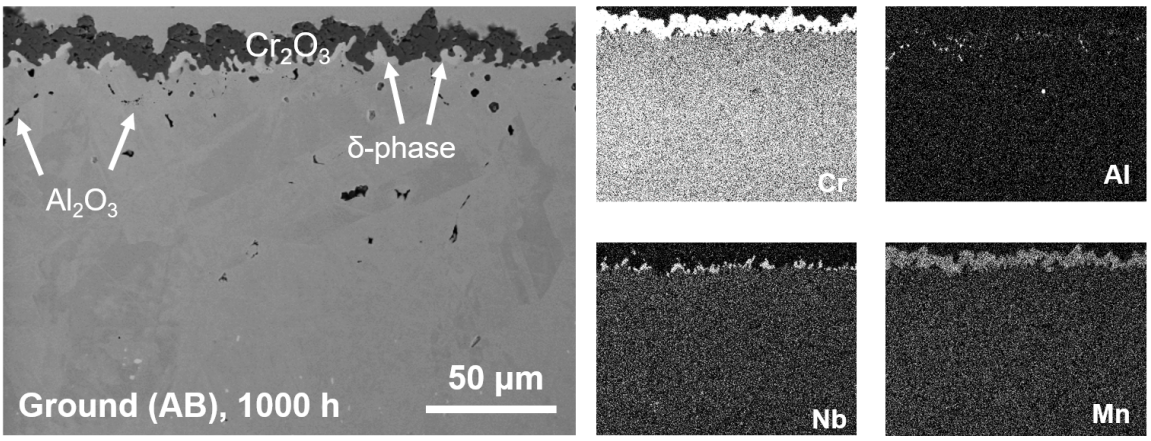


Figure 6.6: BSE-SEM micrograph showing the oxide cross-section through as-built L-PBF IN625 exposed to 950˚C in laboratory air and pressure for 1000 h, with the corresponding EDS maps: Cr, Al, Nb, Mn.

6.5.4.2 The near-continuous δ-phase (Ni_3Nb) layer

A Nb-rich phase was detected as discrete islands at the scale/alloy interface from 24-1000 h, becoming near-continuous with extended exposures of t >500 h (see Figure 6.5 and Figure 6.6). A combination of XRD and EDS identified this phase to be the Ni_3(Nb,Mo) δ-phase [7, 9, 53, 191]. The percentage coverage of the δ-phase across the scale/alloy interface from 24 and 1000 h of exposure

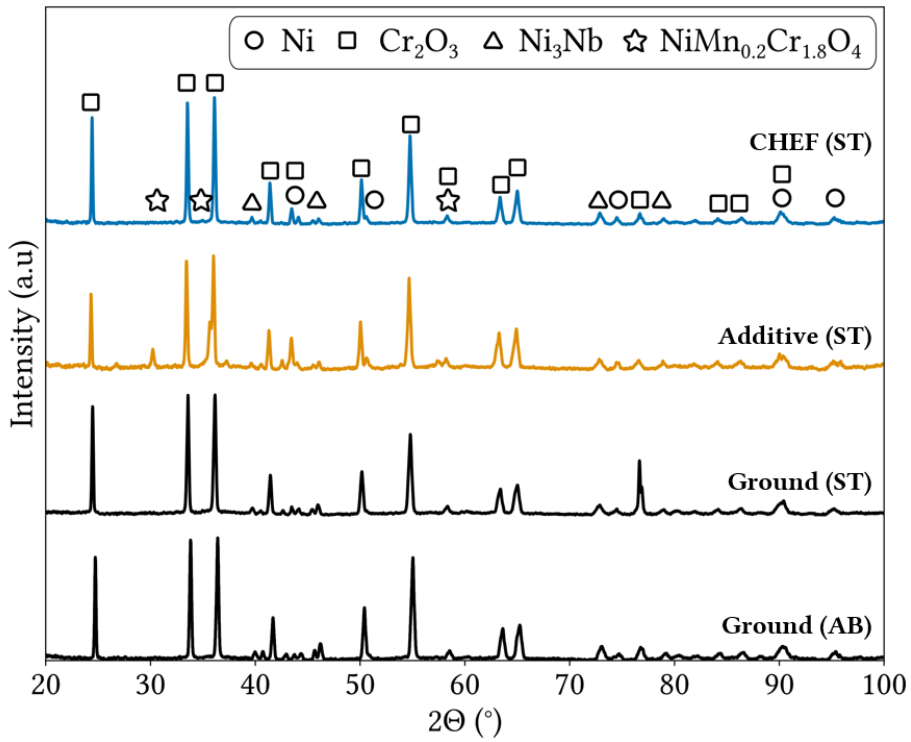


Figure 6.7: XRD patterns obtained for L-PBF IN625 exposed to 950 ˚C for 1000 h. The identified peaks are labelled and outlined in the legend. ICSD collection codes: Ni – 8688, Cr_2O_3 – 261801, Ni_3Nb – 105175, $NiMn_{0.2}Cr_{1.8}O_4$ – 9407.

is shown in Figure 6.8. The δ-phase coverage was observed to increase from 50% at the scale/alloy interface after 24 h, to up to 75% for the Ground (AB) and Ground (ST) samples after 1000 h.

The coverage and morphology of the δ-phase was observed to have evolved differently across the additive (ST) and CHEF (ST) tokens. Significantly less δ-phase was measured to cover the interface in the additive (ST) and CHEF (ST) tokens, with only 40% coverage after 1000 h. In particular, the additive (ST) tokens showed preferential formation of δ-phase as islands inside of the un-melted powder particles adhered to the surface of the tokens, rather than alongside the scale/alloy interface as seen throughout literature for oxidised IN625 and the ground surface samples in this study (see Figure 6.5 and Figure 6.9). The CHEF (ST) tokens however, exhibited δ-phase growth inside the wrinkled and suspected buckled areas of the oxide film.

Spallation of the scale was observed visually in all cases after 100 h. This was more significant in the additive (ST) and CHEF (ST) cases, where chromia was found to delaminate from the surface, leaving behind the exposed δ-phase islands at the scale/alloy interface. An example of this phenomenon can be viewed in Figure 6.8(b), (c) and (d), showing delamination of the oxide scale from the near-surface δ-phase following oxidation periods of 1000 h.

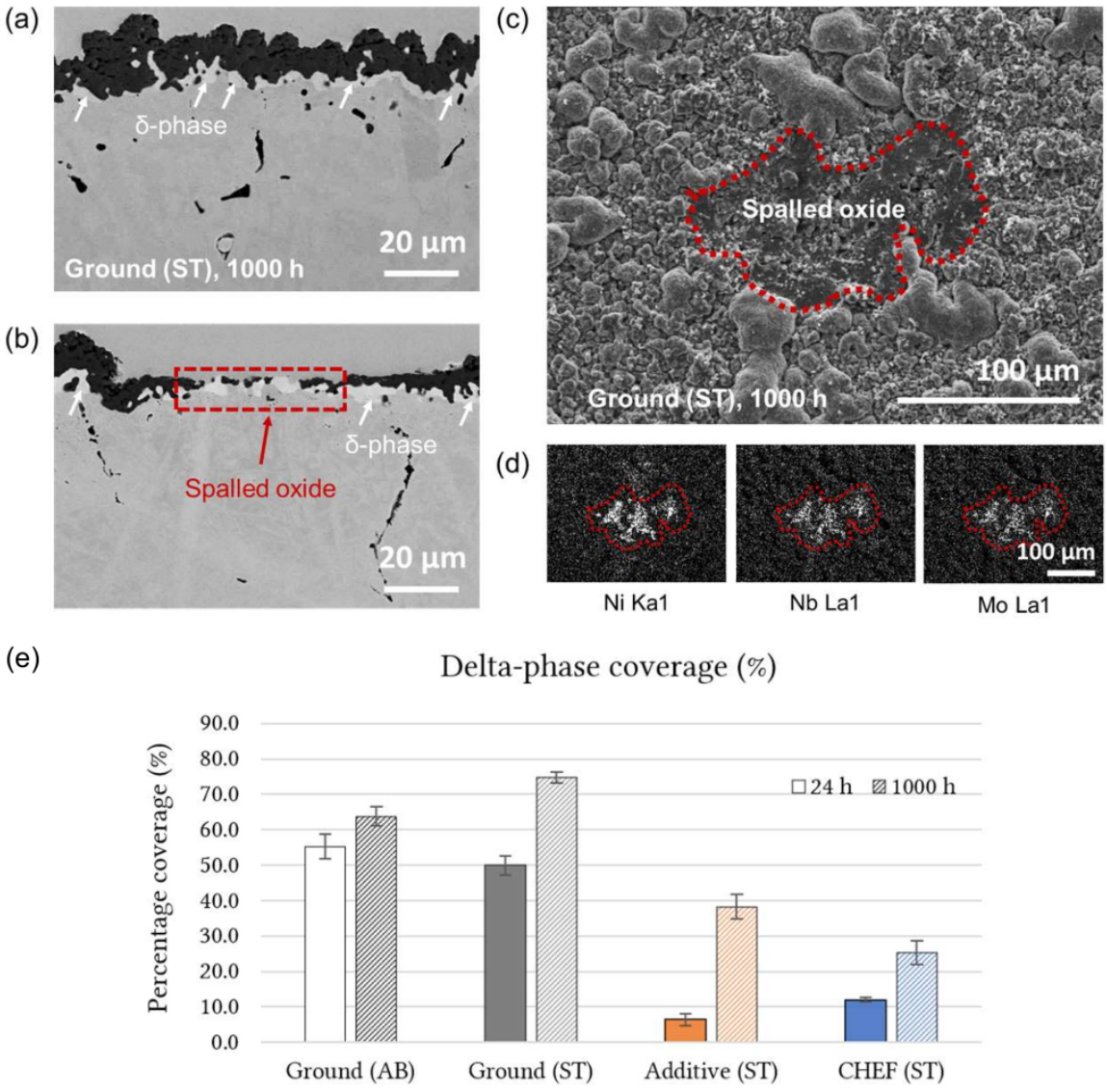


Figure 6.8: Spallation of the oxide revealing δ-phase presence beneath the scale, for solution-treated ground L-PBF IN625 exposed for 1000 h. (a) BSE-SEM oxide cross-section showing a well adhered chromia scale, (b) BSE-SEM oxide cross-section showing a spalled area of oxide, (c) external oxide SE-SEM showing spalled oxide, (d) EDS maps showing enrichment in Ni, Nb, Mo underneath the spalled region, indicating oxide delamination from the near-continuous δ-phase, (e) a bar chart showing growth of the δ-phase as percentage coverage at the scale-alloy interface for all conditions of L-PBF IN625.

6.5.4.3 Internal oxides and voids

Beneath the scale, extensive inter/intragranular Al-rich oxides were detected and identified to be Al_2O_3 using EDS mapping and point scanning (Figure 6.6(c) and Figure 6.9 (e)). These formed at the substrate grain boundaries, penetrating depths from 30 – 55 µm for all conditions [135]. An additional small presence of Ti-enriched oxide, taken to be TiO_2, was detected using EDS mapping at the scale/alloy interface as internal oxide along grain boundaries in the Ground (ST) samples after 1000 h. Powder particles adhered to the surface of the additive (ST) tokens were also shown

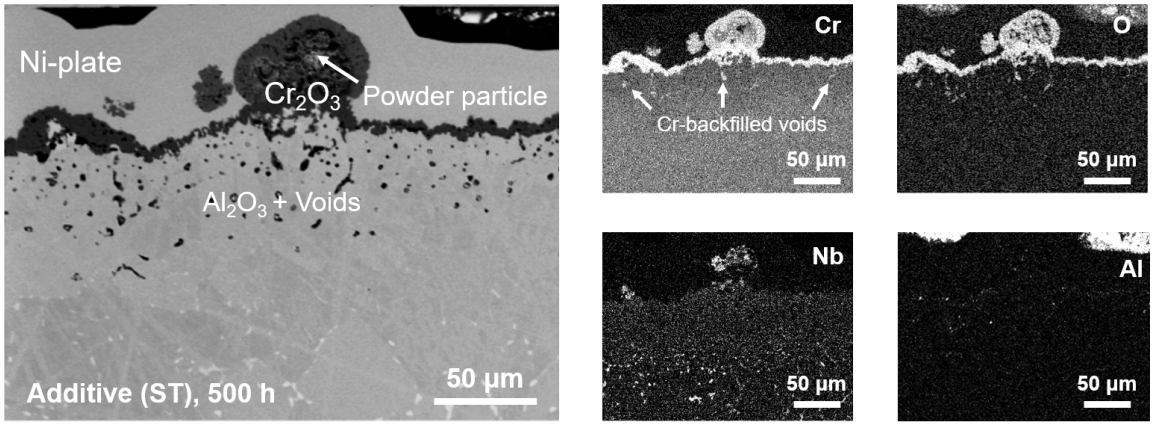


Figure 6.9: BSE-SEM micrograph and corresponding EDS maps (Cr, O, Nb, Al) showing oxide cross-sections for additive (ST) tokens of L-PBF IN625, oxidised for 500 h. Note the Nb distribution localised to the centre of the oxidised powder particle, and Cr enrichment in voids present in the sub-scale.

to exhibit severe internal oxidation (Figure 6.5).

Alongside alumina internal oxide on grain boundaries, voids formed in the oxidation-effected region from 24 – 1000 h. In particular, the additive (ST) and CHEF (ST) tokens showed the most evidence of void formation, see Figure 6.9, particularly visible after 500 h where ridge and spherical voids appeared beneath the oxide scale. Ridge voids were present more so in the Ground (AB) tokens along grain boundaries and have interestingly not been observed previously in conventionally manufactured materials in the literature [1]. Possible ridge void presence was confirmed via FIB lamellae thinning, where STEM-EDS mapping and line scans revealed voids to be absent of any oxide, as shown in Figure 6.10. Some interfacial voids present in the additive (ST) tokens were also found to have become back-filled with Cr_2O_3 (see Figure 6.9) due to the higher oxygen partial pressure here, a common feature observed in the literature for IN625 due to Cr depletion in the oxidation-effected region [1].

6.5.4.4 Oxidation-affected region: Cr depletion and precipitation

Nb and Mo-rich precipitates formed inter/intragranularly in the bulk following exposure for all cases but were most apparent in the Ground (AB) samples, particularly after 24 h of exposure at 950˚C (Figure 6.5). EDS point scanning and evidence posed from modelling using Thermo-Calc (TCNI8 Ni-based superalloy database) suggests these were most likely a combination of Ni_3(Nb,Mo) and $(Nb,Mo)_6C$, supporting findings in the literature for IN625 [7, 9, 47, 191]. The distribution of these precipitates changed over time, where a precipitate free zone from 5 to 150 µm was formed following from 24 – 1000 h exposure, respectively, agreeing with findings by Chyrkin *et al.* [7]. Coarsening of grains was observed in the oxidation-affected region for all conditions,

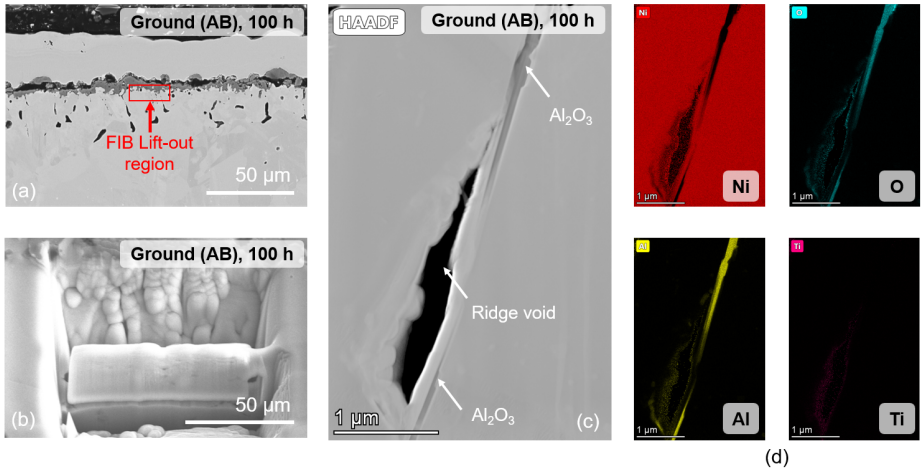


Figure 6.10: (a) SE-SEM micrograph showing an oxide cross-section through Ground (AB) L-PBF IN625 oxidised for 100 h at T = 950°C, indicating the region of a FIB lift-out. (b) Shows the trenching of the FIB lift-out sample during the thinning stages. (c) A High Angle Annular Dark Field (HAADF) micrograph showing a ridge void formed in the Ground (AB) sub-scale after 100 h, with the corresponding STEM-EDS maps (d) showing the elemental distribution of Ni, O, Al, and Ti.

where an increase from (21.95 ± 0.80) µm to (28.44 ± 2.31) µm) was observed in the most extreme case of the CHEF (ST) tokens.

To further understand the oxidation mechanism, the microstructure and composition in the oxidation-affected zone underneath the oxide scale was investigated. To examine chromia growth and void formation, Cr depletion profiles were generated using Equation (6.1) and can be viewed in Figure 6.11 [66]. From the fit, values for the Cr depletion depth (µm) and Cr diffusion coefficients (m^2/s) were extracted, shown in Table 6.4. Cr depletion profiles were found to extend into the bulk at depths up to 140 µm. Additive (ST) and CHEF (ST) tokens showed a deeper Cr depletion profile beneath the oxide scale compared to the Ground (AB,ST) conditions, showing depletion of < 14 wt.% Cr at the scale/alloy interface.

Overall, the oxide morphology obtained in the ground samples (Figure 6.5) were representative of those typically observed in the literature for IN625, AM and wrought Ni-based superalloys [1, 3, 7, 15, 16, 173, 175, 176, 187].

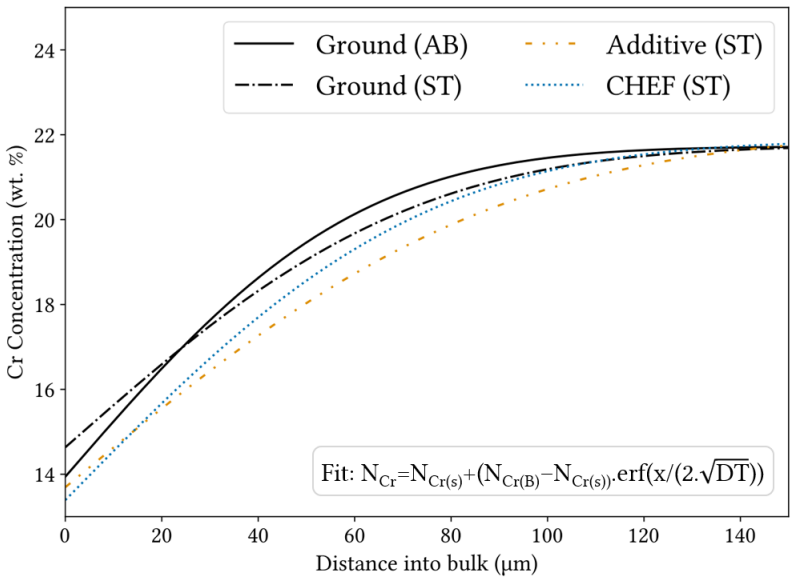


Figure 6.11: Chromium depletion profiles generated for all conditions of L-PBF IN625 after oxidation at 950˚C for 1000 h. Profiles generated from EDS line scan measurements averaged and fitted to Fick's second law of diffusion, Equation (6.1) [66].

TABLE 6.4
OXIDE THICKNESS, CHROMIUM DEPLETION DEPTH AND CALCULATED CHROMIUM DIFFUSION COEFFICIENTS MEASURED FOR ALL SAMPLE CONDITIONS OF L-PBF IN625, AFTER 1000 H EXPOSURE AT 950˚C.

Sample	Oxide thickness (μm)	Depletion depth (μm)	Diffusion coeff. (m^2/s)
Ground (AB)	10.3 (± 0.6)	110.0 (± 10.0)	2.9×10^{-16} ($\pm 6.1 \times 10^{-17}$)
Ground (ST)	10.6 (± 0.4)	120.0 (± 14.0)	4.1×10^{-16} ($\pm 9.9 \times 10^{-17}$)
Additive (ST)	6.9 (± 0.4)	140.0 (± 3.0)	7.0×10^{-16} ($\pm 1.2 \times 10^{-16}$)
CHEF	8.4 (± 0.5)	140.0 (± 0.6)	4.3×10^{-16} ($\pm 7.9 \times 10^{-17}$)

6.5.4.5 Stress in the oxide scale: XRD $\sin^2(\psi)$ oxide stress measurements

The XRD $\sin^2(\psi)$ method for measuring surface stress was applied to all sample conditions after 1000 h exposure [172, 276]. The compressive stresses of the oxides obtained after 1000 h, for all conditions of L-PBF IN625 were calculated according to Equation (6.2) and can be viewed in Figure 6.12. The compressive stresses measured in the oxides ranged from −0.64 to −2.20 GPa, where samples with ground surfaces exhibited higher levels of compressive stresses in the oxide surfaces after 1000 h of exposure. The additive (ST) and CHEF (ST) conditions showed diminished levels of compressive stress in the external oxide, indicating possible relaxation of the scale via spallation.

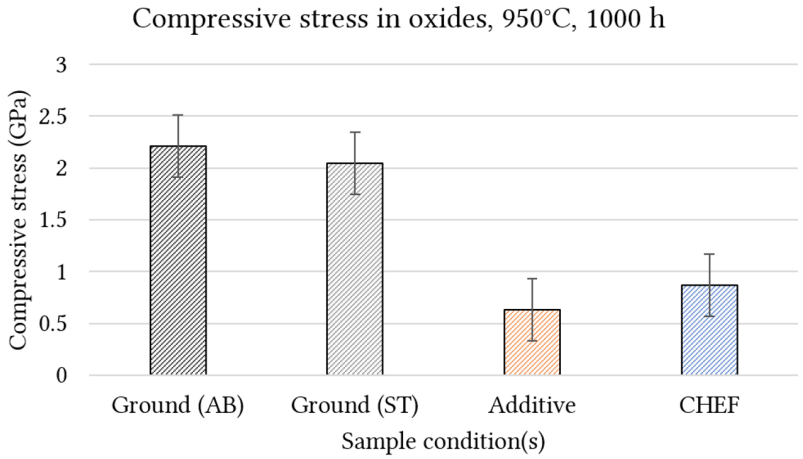


Figure 6.12: A bar chart showing the compressive stresses measured using the XRD $\sin^2(\psi)$ method, for surface oxides formed for all conditions of L-PBF IN625, exposed to 950˚C for 1000 h.

6.6 Discussion

6.6.1 The effects microstructure upon oxidation

6.6.1.1 Microstructure characterisation - Ground (AB, ST)

The results obtained were in-line with observations found throughout literature for AM IN625 [35, 44, 116, 118, 191]. Precipitates observed were taken to be likely a mixture of MC primary carbides (Nb, Mo, Ti), and δ-phase. In a previous study by the authors using the same L-PBF IN625 material and heat-treated conditions, sub-micron globular intermetallic precipitates enriched with Nb (approx. 7 wt.%) were found to decorate grain boundaries in small amounts [191]. These precipitates were identified to be primary NbC from similar findings in literature [36, 38, 89, 92, 191]. The strong texturing effects observed in the ⟨100⟩ direction were also consistent with previous research for the AM IN625, and other similar AM superalloys such as IN718 [34, 99, 104, 176].

The solution-treated microstructure obtained was comparable to conventional wrought annealed IN625 found in literature, where SEM-EDS found the composition of both the as-built and solution-treated alloy to be in line with the specified composition for the alloy [1, 7, 9, 243, 279].

6.6.1.2 Oxidation kinetics - Ground (AB, ST)

From Figure 6.4(a), it was shown that anisotropy resultant of the AM microstructure did not significantly alter the oxidation kinetics, leading to similar mass gain values in the Ground (AB, ST) samples compared to wrought IN625 observed in literature [1]. Parabolic growth rates calculated were slower than those found in wrought Ni-based superalloys, regardless of heat treatment. It is important to note, that the exposure temperature of 950˚C is close to IN625's solutionising temper-

ature of 1050˚C, therefore it is likely the as-built material experienced recrystallisation during the early hours of exposure. This would produce an equiaxed grain structure similar to the solution-treated alloy, and a similar density of grain boundaries for ion transport. Note, the wrought data extracted from Chyrkin *et al.* [1] was based upon samples fabricated with a 0.25 µm mirror-finish, meaning accelerated growth rates would be driven by microstructural feature differences, such as compositional variations between samples. The samples investigated in by Chyrkin contained 0.30 wt.% Al, approximately twice the amount present in the samples built in this study (0.13–0.16 wt.%) [1]. This is likely to have contributed to greater amounts of internal oxidation, and thus a greater mass gain overall.

The Ground (ST) samples exhibited a slightly slower growth rate, supporting previous finding by the authors and Parizia *et al.* [15, 191]. The authors attribute this effect to the lower density of grain boundaries for diffusion of Cr in the equiaxed heat-treated material, compared to the fine microstructure shown in Ground (AB) material [4, 195].

The alternative surface finish tokens, the additive (ST) and CHEF (ST) tokens (Figure 6.4(b)), however showed accelerated oxidation rates compared to the ground tokens, as well as similar wrought Ni-based superalloys in the literature [1, 7, 10, 11, 278, 280]. It was noted that spallation of the protective oxide was observed on cooling of the additive surface and CHEF cases after 24 h exposure, leading to a larger variation in the mass gain. This was also observed in the Ground (ST) cases, though to a lesser extent.

6.6.1.3 Oxide film analysis - Ground (AB, ST)

Ground samples (AB and ST) showed approximately the same oxide morphology and chemical composition. The only noticeable difference was that enhanced grain boundary oxidation was observed after 24 h of exposure in the Ground (ST) samples (Figure 6.5), due to grain boundaries acting as short circuit diffusion pathways for ion transport to the scale. This led to the formation of external oxide ridges over grain boundaries [173, 187, 237]. This effect was diminished after 100 h, where the oxide became thicker and more evenly distributed across the surface. Literature has reported these oxide ridges to be decorated with Ti, but this was not found in the present study [1]. This phenomenon was less apparent in the Ground (AB) sample external oxides due to the cellular sub-grain structure. Overall, it was determined that despite differences in the oxide morphology at short periods ($t > 24$ h), that the resultant oxide scale morphology was not significantly affected by L-PBF microstructure; supporting work by Chyrkin *et al.* [1].

6.6.1.4 Oxidation affected region: Delta-phase - Ground (AB, ST)

Underneath the oxide scale, a near-continuous layer of Nb-rich δ-phase formed at the scale/alloy interface. A significant fraction of the scale/alloy interface was covered in both the cases of the Ground (AB) and Ground (ST) tokens, where 50% – 75% of the scale was measured after 24 h and 1000 h of exposure, respectively (see Figure 6.8). This suggests that the majority of the δ-phase coverage nucleated and coarsened laterally during the early stages of oxidation t < 24 h. These samples also showed similar oxide thicknesses (~ 10 μm) and Cr depletion depths (~ 115 μm), indicating that microstructural differences did not significantly influence the δ-phase's nucleation at the scale/alloy interface.

6.6.1.5 Oxidation affected region: Internal oxide and Cr depletion - Ground (AB, ST)

The Cr depletion measured in the Ground (AB, ST) conditions correlate well with the growth rate constants obtained for these conditions, and confirms the thermodynamic relationship between Cr depletion and the nucleation of precipitates containing Nb, Mo and C, as shown by Chyrkin *et al.* [7]. In addition, indications of both spherical and ridge voids were detected in all conditions of L-PBF IN625. Void formation commonly occurs due to the Kirkendall effect and vacancy injection, following Cr depletion in the oxidation-affected region beneath the protective oxide scale [135]. Multiple morphologies of voids have been reported in literature across several AM Ni-based superalloys, most recently by Chyrkin *et al.* [1] for L-PBF IN625 oxidised at 900 – 1000°C [5, 10, 26, 128, 181, 187]. These were reported to form in t < 2 h of exposure, with some interfacial voids becoming back-filled with oxide (Cr, Al, Ti rich) during longer exposures. This occurred more excessively at higher temperatures where oxidation rates were accelerated, leading to faster depletion of Cr, void formation, and direct contact between the gas phase and the metal substrate [1].

Elongated ridge voids formed along grain boundaries following buckling and the subsequent delamination of the oxide scale, accompanied by a corresponding oxide ridge, where the oxide wrinkles above a grain boundary, see Figure 6.5. More ridge voids were observed in Ground (AB) samples compared to Ground (ST). This may be due to the faster oxidation growth rate experienced by the Ground (AB) materials, leading to larger growth stresses and hence buckling of the protective oxide scale [10].

Spherical voids formed in the microstructure due to steep chromium diffusion profiles in the oxidation-affected region. This was driven by accelerated oxidation rates and spallation of the oxide. Possible Cr and Mo volatilisation is also possible due to the high exposure temperature

of 950°C, and the open flowing system present in the horizontal tube furnace. It was noted that spherical void formation was more prominent in the Ground (ST) samples after 24 h, appearing as long streaks along grain boundaries. This is thought to be due to the larger initial grain size compared to the anisotropic Ground (AB) material, where fewer grain boundaries lead to slower diffusion of Cr to the sample surface, and thus a steeper Cr depletion profile. This is supported by recent findings by Chyrkin *et al.* [1], who reported that following heat treatment to remove grain boundaries via coarsening that a slower diffusion rate was achieved. It has been discussed in literature, that severe internal oxidation and void formation is a driving force for the faster high temperature oxidation of AM Ni-based superalloys [1, 187]. Despite this, whilst the micrographs obtained indicate the presence of ridge/spherical shaped voids in the subscale, further work using FIB and TEM is necessary to fully confirm this is not resultant of oxide delamination above the scale.

Internal oxide and void formation appears more so in AM material than wrought conditions, particularly reported in the works by Chyrkin *et al.* [1] and Sanviemvongsak *et al.* [187] when working at temperatures above 850°C [1]. It is yet unclear as to why severe formation of internal oxide and voids is so prominent in AM materials. Arguments can be made that the phenomenon is not directly related to microstructural differences, but rather small variations in alloy composition and microsegregation of key (Nb and Mo) and minor alloying elements (Si) following the L-PBF process.

6.6.2 The effects of surface finish on oxidation

6.6.2.1 Microstructure characterisation - Additive (ST), CHEF (ST)

No significant difference was noted in the bulk microstructures observed in the additive (ST) and CHEF (ST) tokens compared to Ground (ST) in terms of average grain size, texture and precipitates. This was to be expected, as they both shared the same solution-treatment prior to oxidation.

6.6.2.2 Oxidation kinetics - Additive (ST), CHEF (ST)

The additive (ST) and CHEF (ST) tokens exhibited faster oxidation rates compared to both the Ground (AB, ST) samples. This can be attributed to multiple factors, firstly, that the additive (ST) samples have a rougher, non-uniform finish, providing a larger surface area to volume ratio for oxidative attack. It can also be assumed that the CHEF tokens had a higher level of surface residual stress (~ 550 MPa [137]) present than the ground cases. Higher stress, dislocation density and an increased defect population is assumed to have driven accelerated rates of oxidation. Spallation

observed in these cases may have also driven re-passivation and increased rates of diffusion of Cr to the surface to re-form chromia.

6.6.2.3 Oxide film analysis - Additive (ST), CHEF (ST)

The morphology of the additive (ST) and CHEF (ST) tokens differed greatly from those typically observed in the literature due to their high surface roughness and surface residual stresses, respectively, showing non-uniform, wrinkled oxide scales. Both the additive (ST) and CHEF (ST) samples showed visual evidence of spallation, exhibiting thinner oxide thicknesses than their ground counterparts after 1000 h, measuring thickness on average of 6–8 μm compared to 10 μm, respectively. This was an effect of the spallation of the oxide scale, which was exacerbated in these cases due to the higher surface roughness of the additive (ST) tokens, and surface residual stress in the case of the CHEF (ST) tokens.

The additive (ST) samples also showed preferential oxidation of adhered powder particles on the surface of the tokens, resultant of the L-PBF process. Many of these powder particles observed after 24 h of oxidation showed significant cracking (Figure 6.5) indicating a high level of stress in these regions. It is suggested by the authors that these areas are most likely to experience spall. SEM and EDS mapping of oxide cross sections revealed that in areas of spallation, the protective scale here tended to delaminate, removing the powder particle/oxide scale from the surface completely to leave the underlying δ-phase layer exposed to the environment (see Figure 6.8). This supports similar findings by Kang *et al.* [128] who observed the same delamination phenomena with chromia growing on near-continuous δ-phase upon AM IN718. This may affect additive (ST) and CHEF (ST) IN625 usability in critical high temperature environments, where the re-passivation of the protective chromia may be limited due to the low solubility of Cr in δ-phase (of up to 4 wt.%); effectively making the δ-layer a diffusion barrier against diffusion of Cr to the surface. [13, 181, 185, 191].

The additive (ST) oxide in particular showed a deviation in chemical composition compared to the other conditions investigated, where a stronger presence of the Mn-enriched spinel phase was detected using XRD and EDS mapping (Figure 6.7). It is predicted that this was due to the faster oxidation rates observed in the additive (ST) tokens resultant of the high surface roughness. Stott *et al.* outlined the mechanism for the Mn spinel formation, where MnO is able to form via transient oxidation at the alloy surface prior to chromia ($\Delta G_{MnO} < \Delta G_{Cr_2O_3}$) [189]. The MnO likely established itself quicker than in the other conditions, allowing for the formation of $NiMn_{0.2}Cr_1.8O_4$ spinel by accelerated Mn diffusion through the growing chromia scale.

The enhanced presence of the Mn-rich spinel may provide an explanation for the more cubic

TABLE 6.5
ELASTIC CONSTANTS AND FRACTURE ENERGIES TAKEN FROM LITERATURE FOR Cr_2O_3, Ni_3Nb AND IN625 [20, 157, 165, 200, 208, 281–284].

Phase	E (GPa)	ν	ΔT (°C)	γ_f (J/m^2)	Ref.
Cr_2O_3	273 – 280	0.29	930	4.4 – 6.0	[157, 200, 208, 283, 284]
Ni_3Nb	212 – 268	0.34	930		[281, 282]
IN625	206 – 208	0.28	930		[20, 165]

behaviour of these oxides, where competing growth of the spinel may disrupt the growth of the perfect stoichiometric chromia scale and reduce Cr evaporation by volatilisation [181]. Mn enrichment in oxide scales has been widely investigated across multiple Ni-based superalloys from T = 700 – 1100°C, and has been found to provide both complementary and adverse effects on oxidation resistance at high temperatures [1, 9–11, 53, 181, 185, 189, 192, 278]. Presence of Mn spinel such as $MnCr_2O_4$ have been found to alter oxidation kinetics when present in minor amounts, providing improved oxide adherence through reduced chromia activity [181]. The accelerated diffusivity of Mn compared to Cr ($\times 10^2$ faster), means that Mn spinel tends to form first at the scale/alloy interface, and quickly diffuses through to the external oxide [189]. The Mn-spinel has been shown to decrease inward diffusion of oxygen, suppressing further oxidation of Cr and reduce oxidation growth rates up to $\times 10^3$ [53].

6.6.2.4 Oxidation-affected region: δ-phase - Additive (ST), CHEF (ST)

The δ-phase morphology was influenced by surface topography and stress effects. For the more non-uniform surfaces present in the additive (ST) and CHEF tokens, formation of the continuous δ-phase layer was delayed and inhibited, where only 40% of the scale/alloy interface was covered following 1000 h. The non-uniform morphology of these scales led to the disruption the near-continuous coverage of the δ-phase layer, forming as localised islands inside powder particles and the peaks and troughs present in the CHEF (ST) sample case.

6.6.2.5 Oxidation-affected region: Internal oxide and Cr depletion - Additive (ST), CHEF (ST)

Void formation in the sub-scale was enhanced for the additive (ST) and CHEF (ST) tokens. This may be due to the non-uniform nature of the scales and severe spallation observed here. Visually, these sample also exhibited the most relaxation in the scale via cracking, leading to significant ingress of oxygen, and subsequent internal oxidation of Al and Ti at grain boundaries [7, 9, 173]. The presence of TiO at grain boundaries however was diminished compared to that observed by

Chyrkin *et al.* and Parizia *et al.* [1, 15]. This is likely due to higher alloying amounts of Ti content (Chyrkin *et al.*: 0.33 – 0.36 wt.% [196], Parizia *et al.*: < 0.40 wt.% [15]) compared to the present study (0.11 – 0.12 wt.%).

The deeper Cr depletion profile present in the additive (ST) and CHEF surface tokens serves to explain the enhanced presence of voids in the oxidation affected regions, shown in Figure 6.9. Deeper depletion profiles were observed in this study compared to Chyrkin *et al.* [7] for wrought IN625 after 1000 h of exposure at 900°C. This may however be due to the higher exposure temperature investigated. A deeper Cr depletion profile will result in a high net flux of vacancy injection at the scale/alloy interface, and thus amplify the Kirkendall affect. This is attributed to their enhanced oxidation growth rates due to the larger surface area for oxidative attack and high levels of residual stress in the surface compared to Ground (AB, ST) conditions.

In this fashion, the CHEF and additive (ST) tokens with deeper Cr depletion profiles should have experienced the most δ-phase coverage at the scale/alloy interface (see Figure 6.8), which was not observed. This is attributed to the more non-uniform morphologies of the chromia scales formed, where a more continuous δ-phase layer was prevented from forming due to the sharp wrinkles of the CHEF token scale, or the adhered powder particles present on the additive (ST) sample cases. This led to more localised islands forming and coarsening in powder particles on the surface, as shown in Figure 6.5 and Figure 6.9, rather than the near-continuous layers seen in literature [1, 9, 191]. This is attributed to the higher surface contact angles present at the scale/alloy interfaces of the additive (ST) and CHEF (ST) sample cases. Higher contact angles result in a higher Gibbs free energy barriers ΔG required for the nucleation of a phase [285].

6.6.3 Oxidation-affected region: δ-phase and oxide spallation models

To understand the significance of the presence of the δ-phase at the scale/alloy interface across all samples, oxide scale spallation models were explored by analogy to research with layered thermal barrier coatings under compressive loads by Evans *et al.* [157, 286].

It is understood that the failure of a protective oxide scale via spallation occurs following a temperature change and/or thermal cycling during a component's lifetime in-service. This is by consequence of the superposition of growth and thermal stresses; where thermal stresses are considered most influential [155, 157, 159, 168]. On cooling, compressive in-plane stresses experienced by the oxide are generated due to a difference in the thermal expansion coefficients between the base alloy and the protective oxide, where often the expansion coefficient of the bulk metal is

much greater than that of the growing protective oxide scale [5, 157, 159]. Regions experiencing the largest stresses become points of failure along the scale, leading to promoted crack formation through the scale to the scale/alloy interface, buckling, de-cohesion at the interface, and spallation of the protective scale [5, 154, 155, 157]. This may occur when continuous / near-continuous phases precipitate at the oxide scale/alloy interface, shown to lead to the formation of wrinkled scales decorated with cracks [15, 18, 65, 181, 237]. As this paper investigates isothermal conditions, the initial spallation conditions will be considered.

It is common to evaluate the protective quality of a scale or thermal barrier coating by its resistance to spallation following a temperature change. This can be modelled by taking into account the elastic strain energy of the growing oxide scale per unit volume, W^*, following extensive work by Evans *et al.* [157, 286]. With this knowledge, and the assumption that all stresses experienced by the scale are only experienced during cooling to room temperature, an equation for the critical temperature change required to initiate spallation, ΔT_c of the scale can be generated, Equation (6.4) [157, 286]:

$$\Delta T_c = \left(\frac{\gamma_F}{\epsilon \cdot E_{ox} \cdot (\Delta\alpha)^2 \cdot (1 - \nu_{ox})} \right)^{1/2} \tag{6.4}$$

where γ_F is the fracture energy of the oxide (J/m^2), ϵ is the oxide thickness (μm), E_{ox} is the Young's Modulus of the oxide (GPa), α is the coefficient of thermal expansion (/K) and ν_{ox} is the Poisson's ratio of the oxide. An extensive derivation of this equation by Evans can be found in [157].

If the elastic energy inside the scale increases beyond the fracture surface energy, then spallation of the scale will occur; making the alloy only as strong as its protective oxide scale and by extension its adherence to the bulk alloy [155, 157, 208].

The required information and elastic constants for chromia, IN625 and δ-phase were collected and can be viewed in Table 6.5 [20, 165, 208, 281–284]. These values were applied in Equation (6.4) to generate curves showing the temperature change for spallation with increasing oxide thickness, shown in Figure 6.13, for: chromia growth on IN625, chromia growth on δ-phase, and δ-phase on IN625.

It was found that when chromia grows on δ-phase, ΔT_c of the protective scale increases significantly, preventing instantaneous crack growth and relaxation of the scale. For a critical chromia thickness of 10 μm, $\Delta T_c \sim 200$°C for chromia on IN625, compared to $\Delta T_c \sim 400$°C for chromia growing on δ-phase [1]. Therefore, it would appear that having a near-continuous δ-phase at the scale/alloy interface may serve to improve the adherence of the film and its protective qualities.

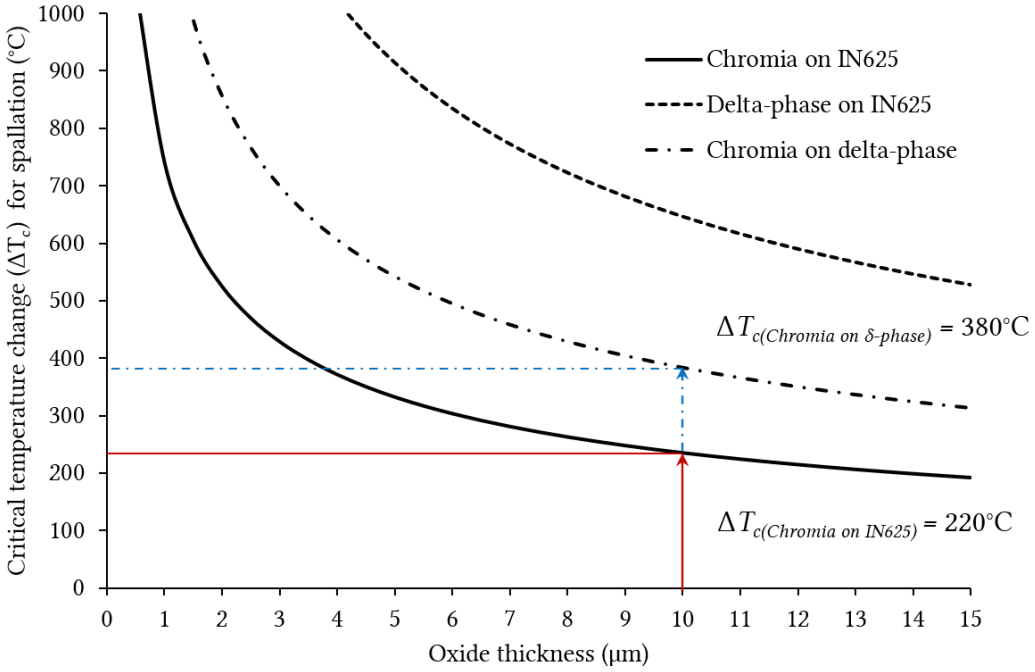


Figure 6.13: Curves showing the critical temperature change, (ΔT_c), required to initiate spallation for increasing oxide thickness for: chromia growing on L-PBF IN625, chromia growing on Ni_3Nb δ-phase, and Ni_3Nb δ-phase growing on IN625.

This correlates well with visual observations made, where the Ground (AB,ST) samples showing the most δ-phase coverage showed little visual spallation at all. This was compared to the additive (ST) and CHEF (ST) tokens which showed significant spallation and accelerated oxide growth kinetics with less than half the δ-phase coverage at the scale/alloy interface. It is understood that the quality of the scale/alloy interface and defect concentration here will affect the adherence of the scale, where non-uniformity and large Cr depletion in these scales will contribute to stress generation in these samples by enhanced cracking [155]. This contrasts findings by Parizia *et al.* [15] and Chyrkin *et al.* [7], where δ-phase formation was stated to be the causation of spallation by virtue of the differences in the thermal expansion coefficients of the bulk, chromia and δ-phase.

6.6.4 $\mathbf{Sin^2(\psi)}$ oxide stress measurements

To evaluate levels of spallation and thermal stress experienced by the scale, XRD $\sin^2(\psi)$ measurements of the oxides were carried out (see Figure 6.12). The values obtained showed the oxide scales to be under compressive stress from −0.6 to −2.0 GPa on cooling from exposure to room temperature. The values of compressive stress measured were deemed to be representative of those observed for chromia forming alloys in literature, determined using a combination of both XRD and Raman spectroscopy for residual stress measurement across multiple exposure temperatures from 700 − 1000˚C. Values from literature show that compressive stress in chromia scales tend to

vary from −1.2 to −3.30 GPa, depending on the exposure temperature and time [154, 167–171]. This is also to be expected for chromia, due to the Pilling-Bedford ratio, PBR > 1 ($PBR_{Cr_2O_3}$ = 2.07), leading to compression of the scale [66, 154, 155, 157, 168]

The additive (ST) and CHEF (ST) tokens showed lower levels of compressive stress compared to Ground (AB, ST) tokens investigated, indicating relaxation in the oxide scale by scale cracking and spallation. This result shows good correlation with the visual observations made, where spallation was more prominent in the additive (ST) and CHEF (ST) tokens. It is important to note that these tokens showed the least δ-phase coverage (around 40%), and according to Figure 6.13, will therefore require a much smaller ΔT_c before cracks initiate in the scale and spallation occur. It appears that the surface finish controls the oxide stress state on cooling from exposure to room temperature, and that the anisotropic as-built microstructure did not contribute to stress generation significantly.

It is important to note, that thicker oxide scales tend to show a decreased T_c for spallation. Whilst the Ground (AB, ST) showed on average thicker oxide scales than the additive (ST) and CHEF (ST) tokens (see Table 6.4), they did not show significant spalling on cooling for times t < 100 h. This poses further evidence for the relaxing effects of the near-continuous δ-phase layer. [157]. The non-uniform morphology of the additive (ST), and residual compressive stress present in the CHEF (ST) surfaces will have also likely contributed to their spallation. More poorly adhered scales tend to buckle at sharp points of curvature leading to the formation of tensile cracks and enhanced spallation in these regions, in this case the adhered powder particles, and the sharp wrinkles in the additive (ST) and CHEF (ST) cases, respectively [157].

One drawback of the XRD $\sin^2(\psi)$ method is that it is difficult to separate contributions of the oxide stress state from growth stresses generated during isothermal oxidation, and the thermal stresses generated from thermal mismatch between oxides and the base metal, as well as strains induced by phase changes [157]. However, good agreement has been shown between methods using XRD against repeat measurements with Raman Spectroscopy for chromia by Guerain *et al.*, hence stress values can be taken as a good reflection of the overall superimposition of stress in the oxide scale [167]. Whilst the results obtained do not directly inform the exact stress mechanism, it is clear that the surface morphology has a large influence on the stress state of the oxides formed, as well as the precipitation of the near-continuous δ-phase. Modelling of the ΔT_c for the alloy with δ-phase present at the scale/alloy interface suggests that this phase is key in improving the adherence of the protective film, as evidenced by the lack of relaxation in the Ground (AB,ST) cases with the largest coverage in δ-phase.

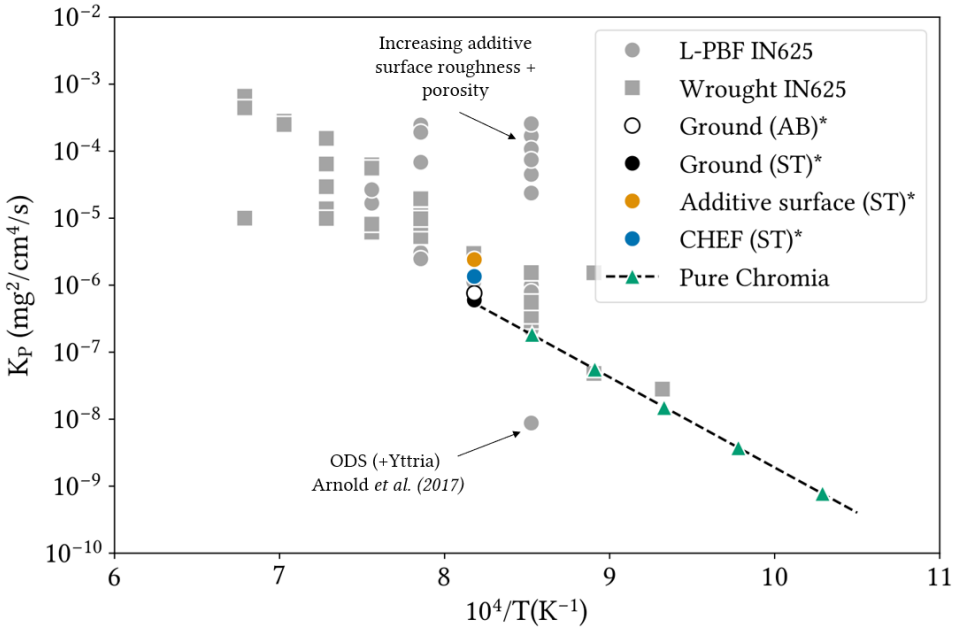


Figure 6.14: Arrhenius graph, showing the temperature dependence of the parabolic K_P rate constants for the oxidation of L-PBF and wrought IN625 taken from literature. Note, * indicates results obtained from this study. [2–5, 7–11, 13–17, 173, 180, 287].

6.6.5 Summary

In summary, it appears that L-PBF microstructure anisotropy does not affect the oxidation kinetics of IN625, but rather surface finish is more critical in the effect upon oxidation rate. Non-uniform surface morphology led to a larger surface area for oxidative attack, where a large residual stresses, dislocation density and defect concentration contributed to rates of oxidation, leading to severe void formation, and cracking and spallation of the protective scale. The non-uniform oxides in the additive (ST) and CHEF (ST) cases led to the disruption of the precipitation of the near-continuous δ-phase layer, leading to lower levels of coverage. This was shown to have implications on the relaxation of the dual-layered scale when cooling to room temperature, where it is discussed that δ-phase may aid in the adherence of the protective scale.

To compare the oxidation kinetics observed to standard performances in literature for wrought and AM IN625, and the ideal case of pure chromia grown on a high chromium stainless steel, an Arrhenius relationship diagram was generated (see Figure 6.14). Overall, oxidation growth rates were comparable to wrought IN625, as reported by Chyrkin *et al.* [1] and England *et al.* [3], in some cases showing similar performance to pure chromia formed on a high chromium steel [180]. Despite similarities in performance, it is clear that further research is required to optimize the use of the alternative surface finishes, where non-uniform morphology and high residual stresses appear to have led to increased rates of oxidation and changes to the typical parabolic behaviour observed in Ni superalloys.

6.7 Conclusions

The high temperature isothermal oxidation behaviour of L-PBF IN625 has been studied at 950°C for 1000 h in laboratory air and pressure, for different microstructures and surface finishes selected for their applicability to additively manufactured geometries.

- Oxidation growth rates calculated showed the performance of L-PBF IN625 was similar to wrought Ni-based superalloy, regardless of anisotropy in the as-built microstructure.
- A protective chromia scale was formed, with small additions of $Ni(Mn_{0.2}Cr_{1.8})O_4$ spinel throughout the external scale. This was most prominent in the additive (ST) tokens, where the authors attributed cubic behaviour to the spinel phase disrupting the diffusion of Cr to the surface to form perfect stoichiometric chromia.
- Both Ground (AB, ST) tokens showed approximately the same morphology chromia scale, thick and wrinkled, with a near-continuous δ-phase layer at the scale/alloy interface.
- The additive (ST) and CHEF (ST) surface tokens showed more non-uniform morphology oxides, with strong wrinkling and indications of stress. Severe void formation beneath the scale occurred due to accelerated growth kinetics and a steep Cr depletion in the oxide-affected region.
- The effect of the near-continuous δ-phase layer was investigated using strain energy modelling and physical stress measurements of the surface oxides formed. It was demonstrated that chromia scale growing on a continuous δ-phase layer shows a theoretically larger ΔT_c, required before the spallation of the protective scale is experienced, improving the adherence of the oxide scale.

6.8 Acknowledgements

The authors are grateful for the financial support of the Manufacturing Technology Centre (MTC). The authors would like to acknowledge Ing. James Camilleri for his expertise and assistance with XRD stress measurements, taken at the University of Malta. SEM was carried out at the Centre for Electron Microscopy, University of Birmingham. This work was carried out with the support of Parker Aerospace (UK).

6.9 Funding

This research did not receive any specific grant from funding agencies in the public, commercial, or not-for-profit sectors.

6.10 Data availability

All raw data required to reproduce these findings can be made available on request through the University of Birmingham thesis repository.

6.11 CRediT authorship contribution statement

E. R. Lewis: Writing - original draft, Writing - review & editing, Visualisation, Data Curation, Formal Analysis, Investigation, Methodology; A. C. Cruchley: Supervision, Writing - review & editing, Resources; B. Attard: Writing - review & editing, Methodology, Resources; Z. Gao: Methodology, Investigation, Resources; N. Cruchley: Supervision, Writing - review & editing, Methodology, Resources; M. M. Attallah: Supervision, Writing - review & editing, Methodology, Project Administration, Resources; S. Cruchley: Conceptualization, Supervision, Formal Analysis, Writing - review & editing, Methodology, Project Administration, Resources.

6.12 Declaration of interests

No conflict of interest is known/can be identified by the authors.

Chapter 7

The effects of grain boundary character on the internal oxidation formation in Laser Powder Bed Fused IN625

7.1 Abstract

This study explores the behaviour of Coincident Site Lattice (CSL) grain boundaries encountered in Laser Powder Bed Fusion (L-PBF) manufactured IN625 and their resistance to internal oxidation. The oxidation kinetics for as-built and solution-treated L-PBF IN625 are presented following isothermal oxidation in laboratory air and pressure at 950˚C for times up to 1000 h. Sub-parabolic oxidation behaviours were observed, showing oxide growth rates in the range expected for wrought IN625 ($K_P \sim 1.00 \times 10^{-7}$ mg/cm^2/s – 1.00×10^{-6} mg/cm^2/s). Oxide growth and microstructure in the sub-scale was examined using contact profilometry, SEM, EBSD, and STEM-EDS. The characteristics of the grain boundaries were examined in relation to the nucleation of internal oxide. Significant fractions of CSL boundaries were formed, up to 60% following heat-treatment and high temperature oxidation. EBSD mapping revealed that CSL boundaries demonstrated a higher resistance to internal oxidation, attributed to lower rates of diffusion compared to random misorientation grain boundaries. A higher fraction of CSL boundaries were found to correlate to a shallower depth of internal oxide penetration as a result. Oxidation growth rate however was unaffected by the slight variations in CSL fraction.

Authors: E. R. Lewis, B. Attard, Z. Gao, J. P. Magnussen, Y. L. Chui, N. Cruchley, A. C. Cruchley, M. M. Attallah, S. Cruchley,

7.1.0.1 Keywords:

Oxidation, Coincident site lattice, Ni alloys, Electron backscattering diffraction (EBSD), Rapid solidification

7.2 Highlights

- Laser Powder Bed Fused IN625 showed sub-parabolic oxidation behaviour similar to wrought Ni-based superalloys.
- CSL boundary fractions ($\Sigma \leq 29$) were significant following heat-treatment ($\leq$62% compared to 4%), and high temperature oxidation.
- Random misorientation grain boundaries showed enhanced internal oxidation, acting as short circuit diffusion pathways.
- CSL boundaries showed greater resistance to internal oxidation compared to random misorientation boundaries.
- A higher fraction of CSL boundaries in the sub-scale corresponded to shallower depths of internal oxidative attack.

7.3 Introduction

Ni-based superalloys are susceptible to intergranular oxidation at the high temperatures typically encountered in the nuclear, aerospace and automotive industries [19–21, 62, 66, 67]. This causes embrittlement of the microstructure by vacancy injection and subsequent oxygen transport to the bulk, leading to cracking and failure of the protective oxide scale [201]. It is crucial that the external scales formed are protective to inhibit oxygen ingress and enhanced ionic transport across the interface [66, 67].

Additive Manufacturing (AM) techniques like Laser Powder Bed Fusion (L-PBF) have been adopted to allow for greater freedom of design for complex near-netshape components for use at elevated temperatures [33, 41, 98, 121, 274, 288]. The oxidation performance of L-PBF IN625 has been widely investigated in high temperature air, producing parabolic oxidation rates similar to traditionally fabricated Ni-based superalloy via forging or casting [1, 9, 10, 13–17, 115]. Any deviations in performance are attributed to the grain size, quality of the sample density by sub-optimal parameter selection, high additive surface roughness, and minor alloying element variations (Si, Mn) [16, 17, 144, 166, 176, 187, 196]. Studies have also reported that AM Ni-based superalloys show enhanced internal oxidation along grain boundaries in the substrate, leading to accelerated oxidation kinetics compared to wrought alloy [1, 10, 187, 196, 242]. This is of special concern, where in-service lifetime is strongly dependent on the alloys resistance to key degradation mechanisms involving grain boundary diffusion, particularly Stress Corrosion Cracking (SCC) [29, 201, 202, 207, 211, 213, 218].

The classical dynamic embrittlement cracking mechanism involves the diffusion of oxygen into a highly-stressed grain boundary ahead of the crack tip. This lowers the grain boundary cohesion allowing for the propagation of an intercrystalline crack [228, 289]. Grain boundary character has been found to influence dynamic embrittlement and the oxidation resistance of FCC materials. Coincident Site Lattice boundaries (CSLs) such as low energy twin boundaries (Σ = 3, with 60˚ misorientation) have been reported to reduce the formation of internal oxides, thus reducing the effects of dynamic embrittlement compared to high-angle grain boundaries [46, 173, 219, 236, 238]. This is attributed to reduced diffusivity rates resulting from their lower excess free volume energy (1/50 compared to that of a random oriented grain boundary) [228, 230, 233, 237].

It is understood that increasing the fraction of special CSL boundaries with low diffusivity of oxygen it is possible to disrupt the network connectivity of random high-angle boundaries present in the matrix, thereby improving resistance to interface controlled properties such as, creep, corrosion, oxidation, and fatigue [173, 228, 233, 235–238]. This can be achieved through a multi-step process of plastic deformation and subsequent heat-treatment to induce recrystallisation and twinning; introduced as a concept by Watanabe (1984) [131, 231, 235, 236, 238]. Past research into the Grain Boundary Engineering (GBE) of wrought IN600 showed that an increase in special boundaries reduced the corrosion rate and intergranular SCC [229]. This effect was also reported for wrought IN718 following works by Trindade *et al.*, Yang *et al.* and Krupp *et al.*, who observed fewer instances of internal oxides along CSL boundaries. A shallower internal oxide attack depth was also reported following the GBE approach [173, 228, 233].

There are few reports investigating the relationship between L-PBF IN625 grain boundary characteristics and oxidation behaviour. Marchese *et al.* investigated the effect of heat-treatment upon texturing and microstructure evolution in L-PBF IN625. Following solution-treatment (1150˚C for 2 h), up to 58.5% of grain boundaries present were classified as Twins, with 60˚ misorientation. This was then compared to as-built alloy which showed a majority of Low Angle Grain Boundaries (LAGBs) with 1 – 10˚ misorientation. Heat-treatments at higher temperatures closer to recrystallisation produced an increased number of twins. This was close to the theoretical limit of ~2/3 of the grain boundaries exhibiting special character in FCC materials [34]. Sanviemongska *et al.* investigated the oxidation resistance of L-PBF IN718, reporting that low CSL fractions of 35% could lead to a marked improvement in performance by limiting the internal oxide penetration depth into the substrate [187, 242]. It is believed that through manipulation of the microstructure via parameter selection and heat treatment that it may be possible to improve oxidation resistance by increasing the CSL fraction. In this study, samples of as-built and solution-treated L-PBF IN625 were exposed to 950˚C for 0.5 – 1000 h. Samples were cross-sectioned, and the oxide scale removed to

allow the inspection of internal oxide along grain boundaries using Electron Backscatter Diffraction (EBSD). The influence of heat treatment on CSL fraction and subsequent internal oxidation will be explored.

7.4 Materials and Methods

7.4.1 Materials

Fully dense cylindrical rods of IN625 (diameter 14 mm, height 125 mm) were manufactured using an L-PBF EOS M280W machine with the default IN625 parameter set. Powder size ranges of 15 – 45 μm were used with a layer height of 40 μm. The chemical composition was confirmed using a combination of LECO and ICP-OES (Inductively Coupled Plasma - Optical Emission Spectroscopy) testing is shown in Table 7.1 [243].

A set of cylinders underwent solution-treatment at 1177˚C for 1 h, followed by a water quench to room temperature [122]. Tokens (diameter 14 mm, thickness 2 mm) of as-built and solution-treated alloy were cut to size using Electrical Discharge Machining (EDM), and were ground using wet SiC papers from 120-grit to 4000-grit. A final polish of 0.25 μm (R_a = 0.05 μm) was applied using OP-S colloidal silica. The token edges were chamfered to remove stress concentrators.

7.4.2 Microstructural characterisation, pre-oxidation

The as-received microstructure of both sample types was inspected following hot mounting in Bakelite. To inspect the microstructure, samples were imaged using a JEOL 7000F Field Emission Gun Scanning Electron Microscope (FEG-SEM), with a HKL Nordlys EBSD unit with Oxford Aztec software. Backscatter Electron (BSE-SEM) micrographs were collected using an accelerating voltage of 20 kV. Electron Backscatter Diffraction (EBSD) was carried out to examine the microstructure before and after isothermal oxidation. Samples were tilted to 70˚ and scanned at 20 kV using a step sizes and scanning areas dependent upon the sample condition: as-built tokens

Table 7.1
Measured composition for L-PBF IN625 powders and cylinders, wt.%, used in the present study.

Alloy	Element, wt.%)												
	C	Mn	Si	P	S	Cr	Co	Mo	Nb	Ti	Al	Fe	Ni
IN625 Powder	-	<0.01	0.07	<0.01	-	21.27	0.04	9.02	3.65	0.10	0.11	3.66	Bal.
IN625 Cylinders	-	0.02	0.11	<0.01	-	21.94	0.05	9.69	3.88	0.12	0.16	3.95	Bal.

scanned areas of 680 × 400 μm^2 at steps of 2.5 μm, and solution-treated alloy areas of 500 × 400 μm^2 at steps of 1.5 μm. EBSD data obtained was plotted and analysed using code from the MTEX MATLAB framework [250–254]. The average grain size (diameter μm) was calculated from the IPF maps generated using the Heyn Lineal Intercept method [255].

Grain boundary character was analysed according to the Palumbo-Aust criterion and applied to EBSD IPF maps obtained for each condition. The Palumbo-Aust criterion classifies each type of boundary within the CSL framework ($\Sigma \leq 29$), calculating the maximum geometrically allowable deviation from the misorientation [236]:

$$\Delta\theta \leq 15 \cdot (\Sigma)^{\frac{-5}{6}} \tag{7.1}$$

where $\Delta\theta$ is the allowable angular deviation (°), and Σ is the reciprocal of the number of coincident sites between neighboring grains.

The frequency of CSL boundaries was calculated as a length fraction of the total grain boundary length.

7.4.3 Isothermal oxidation

Isothermal oxidation testing was carried out in laboratory air and pressure for exposure temperatures of 950°C for time periods of 0.5 h – 1000 h. A pre-heated Lenton Thermal Designs horizontal tube furnace was used. Calibration of the furnace was carried out using a combination of K-type and R-type thermocouples to determine the heat-zone correct to ±1 °C. Prior to testing, all sample types were degreased in acetone in an ultrasonic bath for 5 minutes, then dried in still air. Six repeat samples were used per time, per conditions. These were placed into open air alumina crucibles, and then into the pre-heated furnace heat-zone. Oxidation kinetics were determined using the specific weight gained by each sample upon removal using a calibrated microbalance (±0.00001 g). This was measured and fit to the classical Wagner's equation [66, 67].

7.4.4 Microstructural characterisation, post-oxidation

Optical microscopy was performed to examine the external oxide using a Zeiss Axioscope 5 microscope at ×10 magnification. To further inspect the topography of the external oxide, 2D and 3D surface profiles were collected. A NanoMap-LS 3D contact profilometer was used, equipped with a 1 μm stylus tip for scanning areas of 500 × 400 μm^2. A dwell time of 20 μm/s was selected, and a contact force of 15 mg.

To allow for EBSD analysis of the microstructure beneath the oxide scale, selected tokens were vibropolished to remove their surface oxide. A Buehler VibroMet2 tabletop vibratory polisher was used with 0.25 μm OP-S suspension as lubricant for t<50 h. To inspect the oxide cross-sections, oxide tokens were sputtered with gold, and Ni plated. To section, samples were cold-mounted using low shrinkage resin and cut in half. These were then polished to a 0.25 μm finish. Cross-sectional features such as internal oxidation penetration depth were measured and analysed using Fiji image software [249]. Discrete instances of internal oxide on each grain boundary type in the oxidation-affected sub-scale were counted manually using Fiji across 3 repeat images per condition, following 1000 h of exposure. This allowed the percentage of internal oxide on a particular grain boundary character type to be calculated via direct comparison between EBSD IPF maps and the corresponding SEM-BSE cross-section micrographs (taken at the same magnification). Nano-sized precipitates in the oxide cross-section were characterised using an FEI Talos F200X fitted with Oxford Super-X-Detectors STEM-EDS capability. A Thermofisher Helios G4 XE plasma FIB CXe dual beam SEM was used to produce a FIB lamellae using a standard FIB lift out technique [265].

7.5 Results

7.5.1 Microstructural characterisation of as-received materials

Figure 7.1 shows a summary of the sample microstructures obtained for as-built and solution-treated IN625 prior to exposure via BSE-SEM micrographs and EBSD IPF maps. The as-built microstructure consisted of fine cells, with dendrites extended in the building direction, resultant of the heat flow in the L-PBF process (XZ, perpendicular to the image). Grains were < 22 μm in diameter, with cells showing an average diameter of approximately 1 μm. A strong texture was demonstrated along the ⟨100⟩ direction, parallel to the building direction of the sample. Few CSL character boundaries were present following building, with as-built samples showing an average of 5.7% of grain boundaries classified as $\Sigma \leq 29$, with only 4.5% classified as $\Sigma 3$ twins. Only a small percentage of twin family $\Sigma 3^n$ boundaries were seen to have formed. Altogether this shows good agreement with the literature [34, 35, 117].

The solution-treated tokens showed a complete transformation from the anisotropic microstructure and the removal of melt pool lines. Fully equiaxed grains of diameter < 25 μm were observed, with a random grain orientation with respect to the building direction throughout, as found in wrought alloy [35, 104]. No significant precipitation was observed inside grains or on grain boundaries following EDS mapping. From the IPF maps and band contrast micrographs generated from

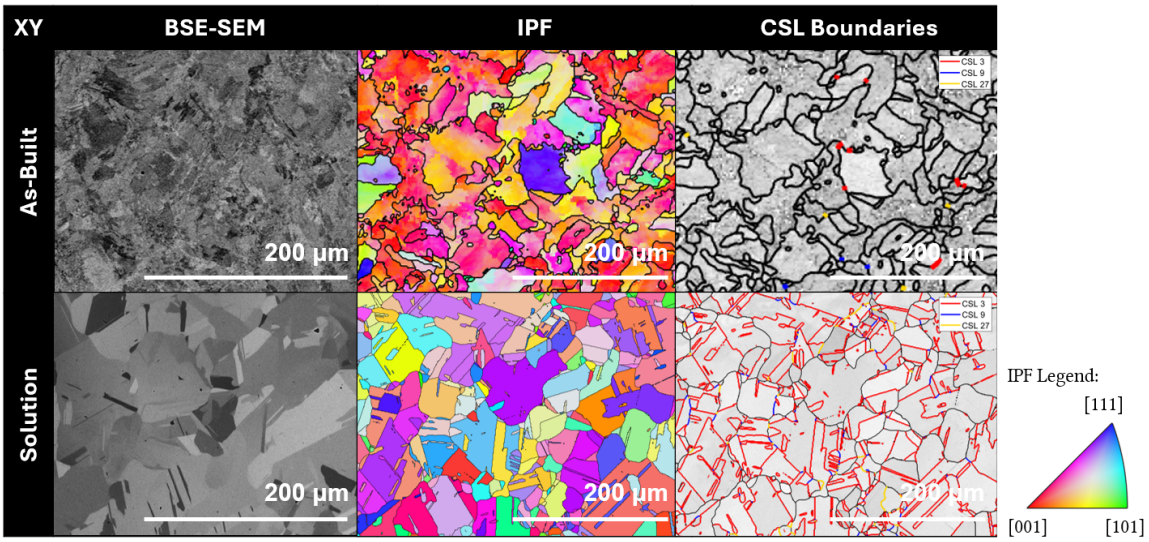


Figure 7.1: A summary of BSE-SEM micrographs, and Inverse Pole Figures (IPF) maps showing the microstructure of as-built and solution-treated L-PBF IN625. Imaged perpendicular to the build direction. Note the recrystallisation and subsequent increased occurrences of twin family boundaries in the microstructure following solution heat treatment.

Figure 7.1 it can be seen that L-PBF IN625 demonstrated a significant fraction of twin grain boundaries when heat-treated, with an average of 62.0% twin boundaries, and 64.7% classified as special grain boundaries ($\Sigma \leq 29$); highlighted in red ($\Sigma = 3$), blue ($\Sigma = 9$), and yellow ($\Sigma = 27$).

7.5.2 Isothermal oxidation kinetics

The specific mass change experienced by as-built and solution-treated L-PBF IN625 following exposure to 950°C for times up to 1000 h is shown in Figure 7.2. The associated parabolic oxide growth rate constants calculated from the data alongside the exponents n are shown in Table 7.2. Slower rates of oxidation were obtained for the solution-treated material compared to as-built IN625. Both alloys showed sub-parabolic oxidation behaviour with $n > 2.0$ compared to traditional parabolic behaviour expected for conventional Ni-based superalloy. Despite these differences, both sample conditions showed slightly slower kinetics than traditional wrought IN625, indicating superior oxidation resistance [1, 3]. Some visual spallation was observed in both sample cases at t > 100 h upon cooling.

7.5.3 External oxide

The external oxide topography was examined using a combination of optical microscopy and contact surface profilometry after t = 100 h of exposure. The summary of the external oxides formed from t = 0.5 – 100 h exposure can be seen in Figure 7.3. The 3D and corresponding 2D surface

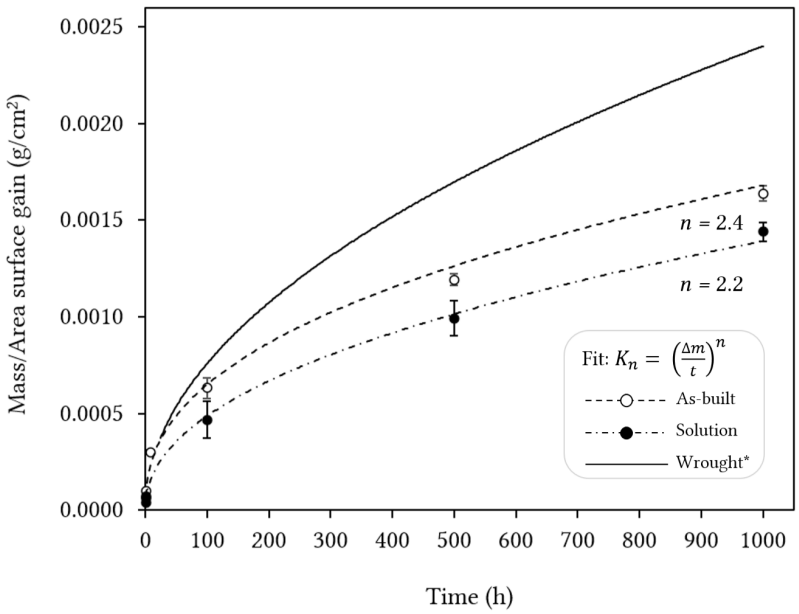


Figure 7.2: Mean mass gain/area vs time for as-built and solution-treated L-PBF IN625, exposed to 950°C for up to 1000 h, compared to wrought IN625 extrapolated from data reported by Chyrkin *et al.* (2022) with 0.25 µm starting surface finish tokens [1]. Data fit to Wagner's classical equation for oxidation. * Indicates data external to the study.

TABLE 7.2
EXPONENT, *n*, AND K_P, RATE CONSTANT FOR OXIDE GROWTH AT 950°C FOR T = 0.5 − 1000 H. WROUGHT DATA EXTRAPOLATED FROM CHYRKIN *ET AL.* [1].

Alloy condition	**K$_P$ (mg^2/cm^4/s)**	***n***
As-built	$7.37\ (\pm\ 0.55) \times 10^{-7}$	2.4
Solution	$5.72\ (\pm\ 0.06) \times 10^{-7}$	2.2
Wrought	1.61×10^{-6}	2.0

profile maps can be seen in Figure 7.4 and Figure 7.5. These collectively revealed the surface to be decorated in a thin fully covering oxide at t<1.0 h, where microstructural features in the substrate were still visible. Grain boundary enhanced oxidation can be observed for t = 0.5 − 8 h, and preferential oxidation dependent upon grain orientation particularly in the case of the solution-treated tokens following exposure for t = 0.5 h (Figure 7.5). Oxides appeared to grow thicker and coarsen with prolonged periods of oxidation.

The scan tracks resultant from the L-PBF process were still visible after 0.5 h exposure (see Figure 7.1 and Figure 7.3) and showed thicker oxide along the cell boundaries present up to 4 µm higher than the surroundings. Recrystallisation of the as-built microstructure can be observed after t > 0.5 h, with some evidence of twin boundary formation (see Figure 7.3 and Figure 7.5). Here equiaxed grains and grain boundaries appear, showing elevated islands of oxide. This effect was masked after 100 h of exposure, where both as-built and solution-treated alloy demonstrated

thicker, coarse layers of oxide. Oxide formed on the as-built alloy after 100 h appeared to be coarser and more porous than the dense scale grown upon the solution-treated condition evidenced by the larger islands of oxide demonstrated in the 3D profiles generated. Areas of the oxide appear to have spalled from the surface (see Figure 7.4 (a), Figure 7.5 (a)) leaving behind areas exposed to the gaseous environment. This was less apparent in the solution-treated case, although both tokens showed visual evidence of spalling upon removal from the tube furnace.

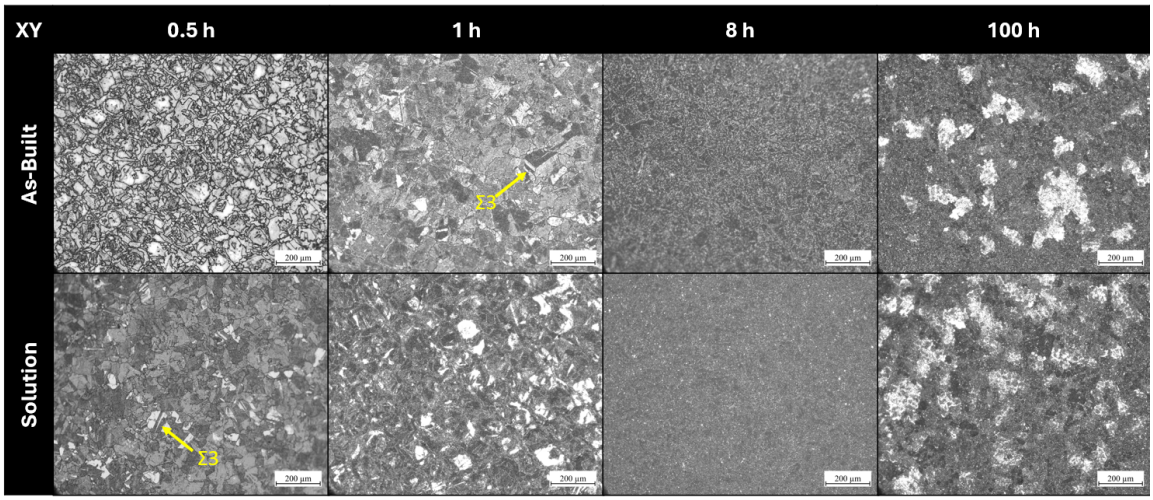


Figure 7.3: A summary of optical micrographs showing the external oxide of as-built and solution-treated L-PBF IN625 from t = 0.5 h – 100 h. Imaged perpendicular to the build direction, thicker oxides show darker contrast, compared to thinner thickness films. Note, partial recrystallisation of the microstructure was observed following 1 h of high temperature exposure evidenced by the formation of equiaxed grains and instances of twin boundaries (Σ3). Microstructural features beneath the oxide film were however obscured for t > 1 h.

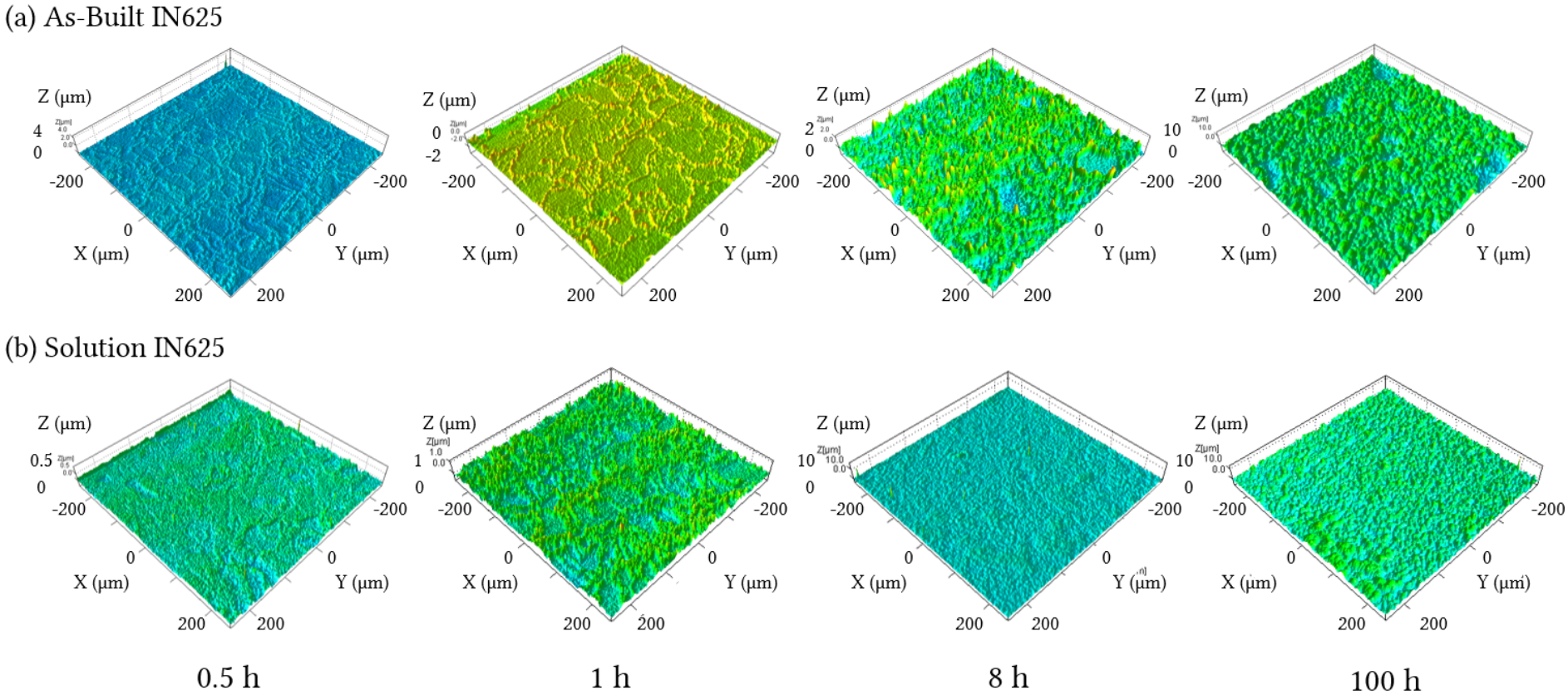


Figure 7.4: A summary of 3D profilometry maps of the surface of samples of as-built and solution-treated L-PBF IN625 held at 950˚C for 0.5 – 100 h. Note the elevated topography along scan tracks and grain boundaries at early periods of oxidation, t<1 h. A summary of 2D profilometry maps of the surface of samples of as-built and solution-treated L-PBF IN625 held at 950˚C for 0.5 – 100 h. Note the elevated topography along scan tracks and grain boundaries at early periods of oxidation, t<2 h showing enhanced oxidation in these regions compared to the bulk matrix. Evidence of oxide spallation can be seen in both sample cases, particularly following 100 h exposure. Oxide islands in the as-built 100 h case appeared visually coarser than the solution treated L-PBF IN625.

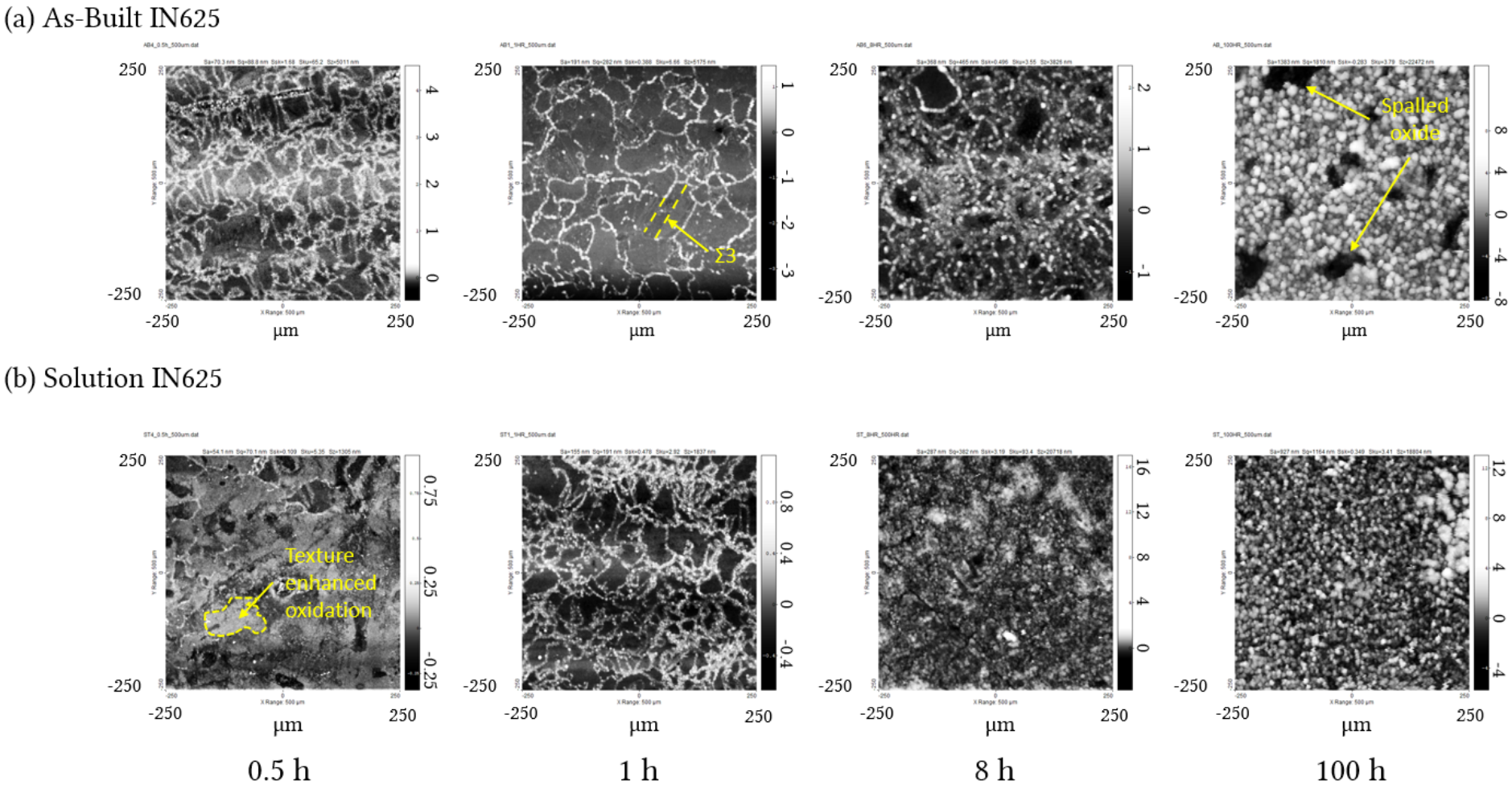


Figure 7.5: A summary of 2D profilometry maps of the surface of samples of as-built and solution-treated L-PBF IN625 held at 950˚C for 0.5 – 100 h. Note the elevated topography along scan tracks, grain boundaries and certain grain orientations at early periods of oxidation, t<2 h showing enhanced oxidation in these regions compared to the bulk matrix. Evidence of oxide spallation can be seen in both sample cases, particularly following 100 h exposure.

7.5.4 Grain boundary evolution - Oxide cross-sections

The cross-sections through the oxides formed upon as-built L-PBF IN625 are shown via EBSD IPF maps and SEM-SE micrographs in Figure 7.6 and Figure 7.7 respectively. Special grain boundary character is overlaid. EBSD and SEM examination of the scale revealed the presence of a thick chromia Cr_2O_3 external scale, with an underlying near-continuous Ni_3Nb δ-phase layer (see Figure 7.6). This correlated to results obtained with the same materials in a previous study by the authors [191] using SEM-EDS and XRD (ICSD collection codes: Chromia - 261801, δ-phase - 105175). Grain coarsening in the oxidation-affected region was observed for both sample conditions, showing coarsening of the sub-scale to give mean grain sizes of 26.0 μm (± 2.0 μm) for the as-built samples, and 29.1 μm (± 0.7 μm) for the solution-treated tokens. This further indicated partial recrystallisation of the microstructure. This was thought to be due the fact that the high exposure temperature of 950˚C was close to the solutionising temperature of the alloy (1150˚C).

Significant fractions of twin family CSL boundaries were formed during exposures up to 1000 h; a summary of these are shown in Table 7.3. The as-built material experienced recrystallisation at the high exposure temperature of T = 950 ˚C, exhibiting up to approximately 60% twin boundaries forming in the sub-scale oxidation-affected region following 1000 h (see Figure 7.6). The majority of these formed during the early stages of oxidation t ≤ 100 h (see Table 7.3). The fraction of twins in as-built material following recrystallisation were approx. 10% higher than the solution-treated material, which showed a decrease in twin boundary fraction in the sub-scale following oxidation.

Extensive internal oxide attack was observed along grain boundaries in the sub-scale after high temperature exposure (Figure 7.6 and Figure 7.7). Internal oxide was identified to be alumina Al_2O_3 via EDS mapping. Few instances of internal oxide were observed to propagate along CSL boundaries, shown using EBSD mapping. This was particularly visible in Figure 7.7, where internal oxide grew preferentially along random misorientation grain boundaries. An average of 70.2% (± 3.6%) of instances of internal oxide in the sub-scale appeared on random boundaries in the as-built material following 1000 h of isothermal oxidation. The same relationship was observed in the solution-treated alloy, where an average of 71.3% (± 1.4%) of instances of internal oxide occurred upon random boundaries. This was correlated to the internal oxide penetration depths, where depths of attack of 44.4 (±2.7) μm, and 55.8 (±3.7) μm were measured for as-built and solution-treated L-PBF IN625 exposed for 1000 h, respectively (see Table 7.3).

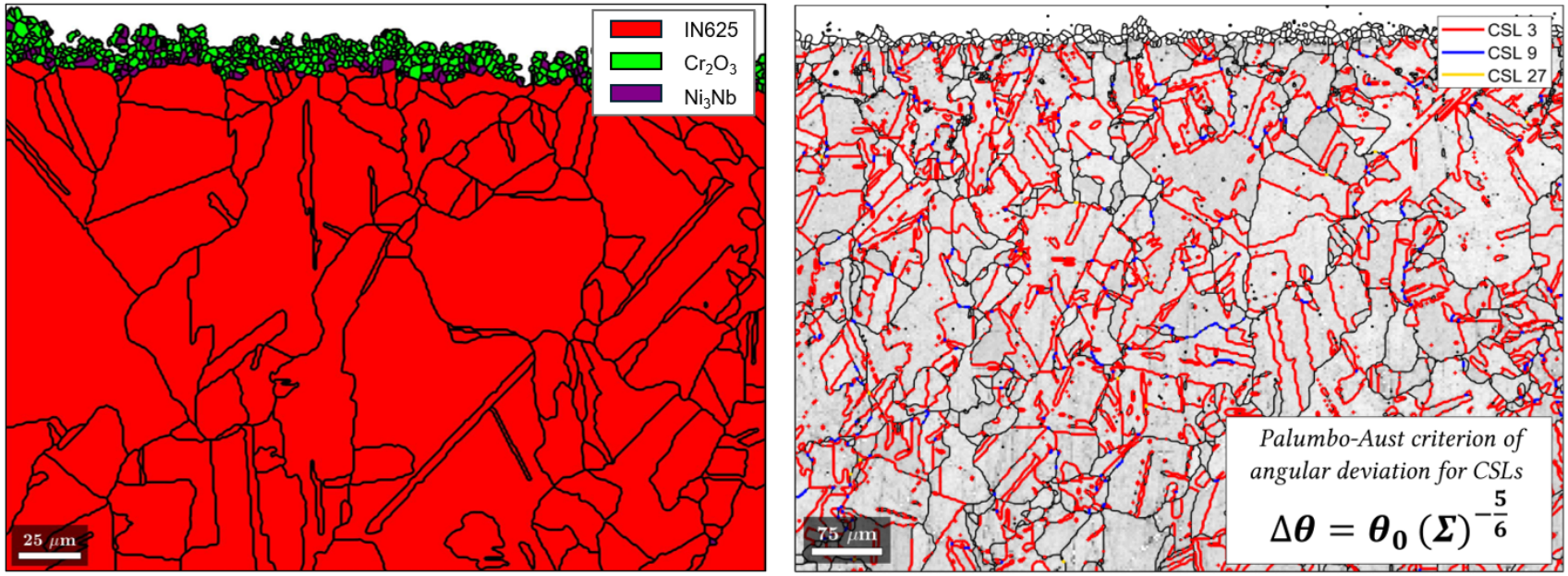


Figure 7.6: (a) EBSD phase map showing a fully indexed cross-section through as-built L-PBF IN625 exposed to 950˚C for 1000 h. Note the external chromia scale, with near-continuous δ-phase at the scale/alloy interface. (b) EBSD band contrast map showing grain boundary character, with special boundaries highlighted (Σ3 = red, Σ9 = blue, Σ27 = yellow). Palumbo-Aust criterion taken from [236].

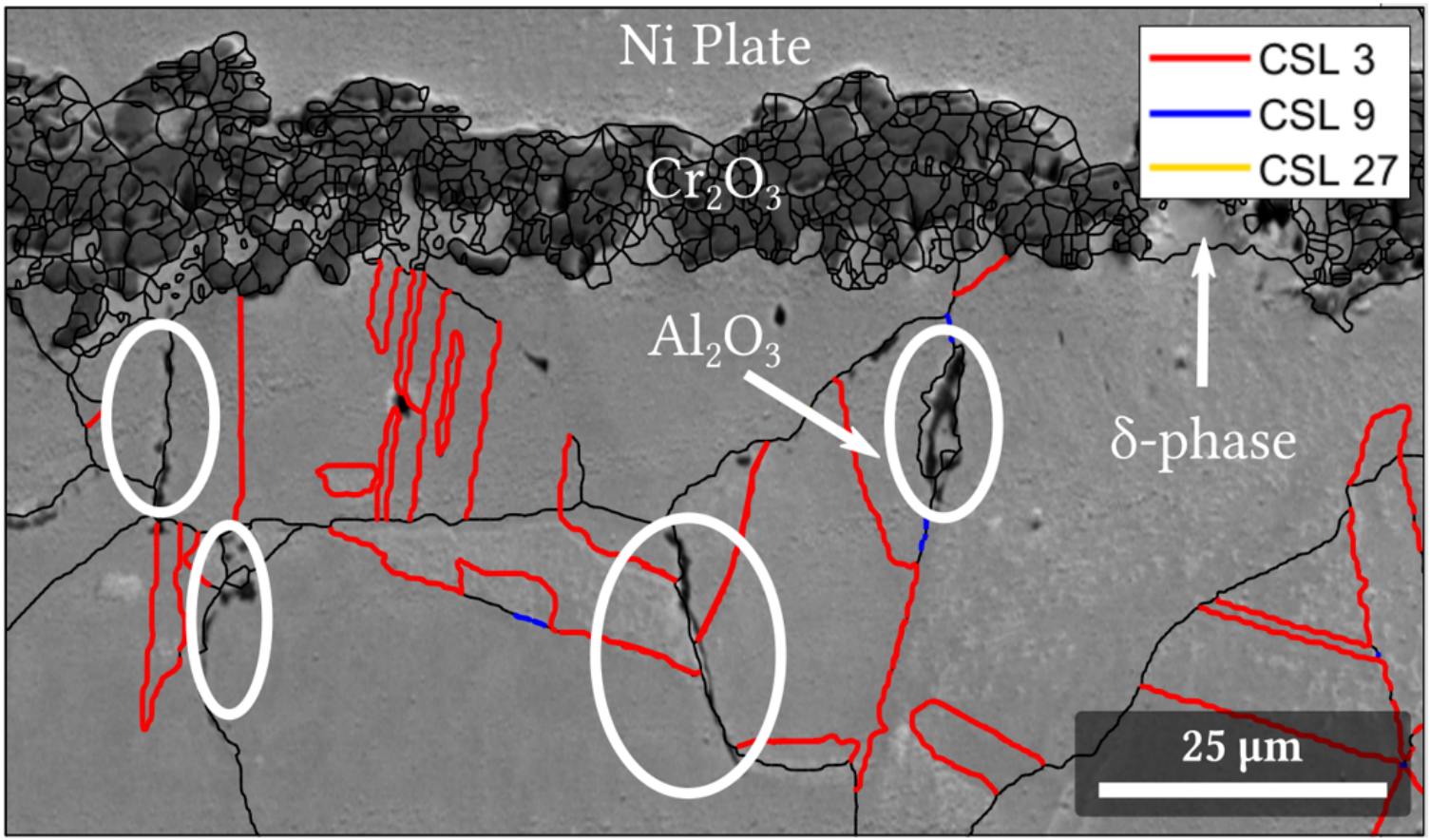


Figure 7.7: SEM-SE micrograph of a cross-section with special boundaries highlighted, through as-built L-PBF IN625 exposed at 950°C for 1000 h. Note internal oxide growing primarily along random oriented boundaries only, circled in white.

TABLE 7.3
Σ3 BOUNDARIES (%) IN L-PBF IN625 BEFORE AND AFTER OXIDATION AT T = 950°C FOR T = 100, 1000 H, RELATED TO INTERNAL OXIDE PENETRATION DEPTH.

	% CSL Boundaries (Σ3)			
Sample	**As-received**	**100 h***	**1000 h***	**Internal oxide depth (μm)***
As-built	4.5 (± 2.1)	53.0 (± 3.1)	59.7 (± 1.7)	44.4 (± 2.7)
Solution	62.0 (± 4.0)	49.7 (± 5.0)	50.1 (± 3.2)	55.8 (± 3.7)

*EBSD IPF maps obtained in the sub-scale oxidation-affected region.

7.5.5 Grain boundary evolution - External oxide

The microstructure evolution beneath the oxide scale was examined in the as-built condition following oxidation periods of 1 – 100 h, shown in Figure 7.8, Figure 7.9 and Figure 7.10, respectively. After exposures of t = 1 h, small amounts of recrystallisation were observed, with slight changes to grain texturing. Clusters of twin boundaries tended to form in fine-grained areas of the microstructure with high grain boundary density (Figure 7.8 (b)), with some instances of twin family Σ9 boundaries beginning to form. Figure 7.8 (c) shows small islands of un-indexed phase on grain boundaries, identified to be alumina using EDS mapping. Note, no internal oxide formed upon Σ3 boundaries, nucleating preferentially upon random misorientation boundaries and Σ9 CSLs. Recrystallisation became more apparent following exposure for 100 h, small grains grew inter/intragranularly, and a higher frequency of Σ3 twins were encountered of approximately 10%.

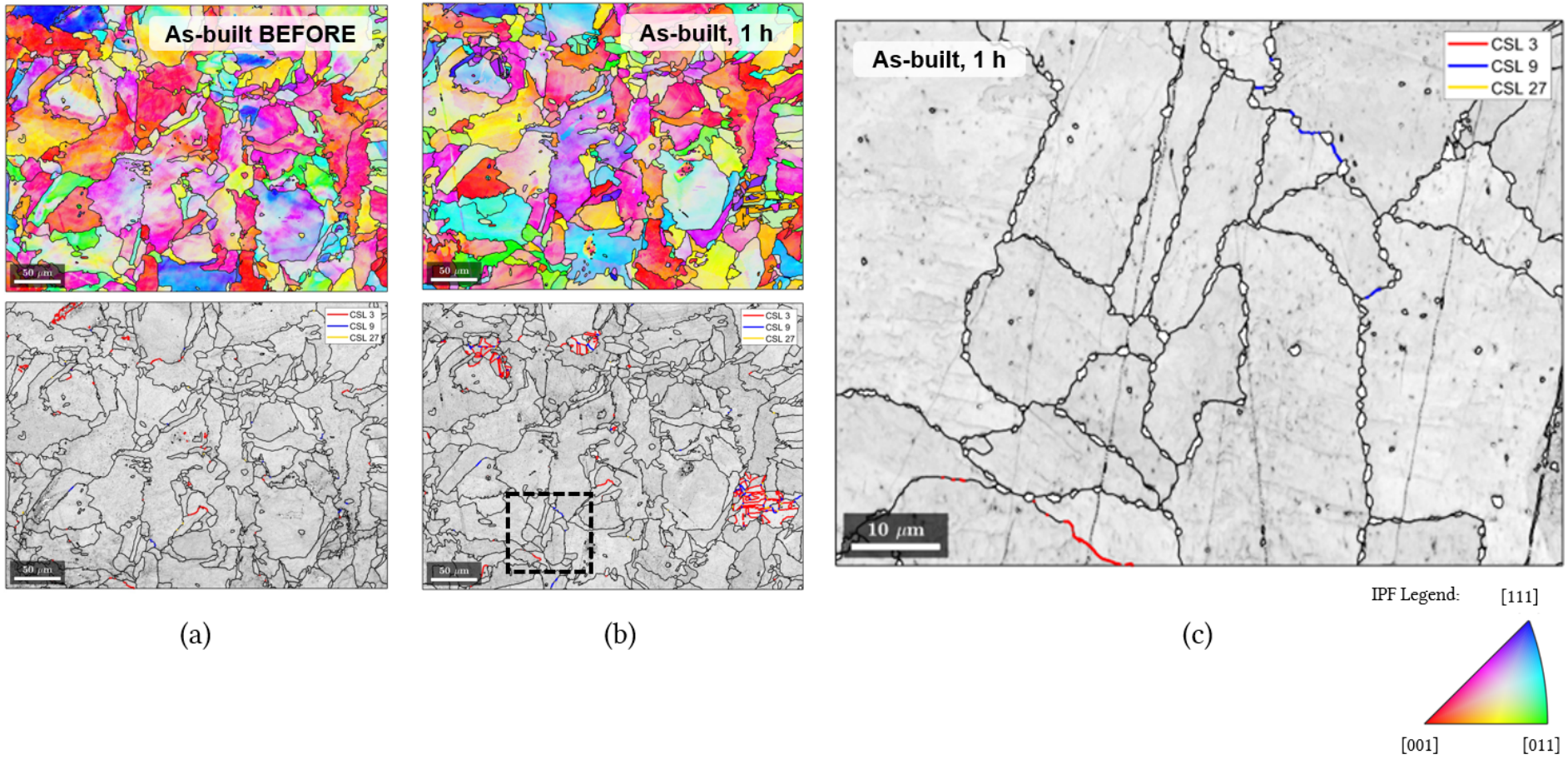


Figure 7.8: EBSD IPF maps and their corresponding band contrast maps with grain boundary character overlaid, for (a) as-built L-PBF IN625 before, and (b) after 1 h of isothermal oxidation at 950˚C. (c) A magnified EBSD band contrast image, highlighted in (b). Note the un-indexed phase decorating grain boundaries, identified to be internal oxide via EBSD. Evidence of partial recrystallisation can be viewed in areas with fine grains, evidenced by formation of clusters of twin grain boundaries (CSL 3).

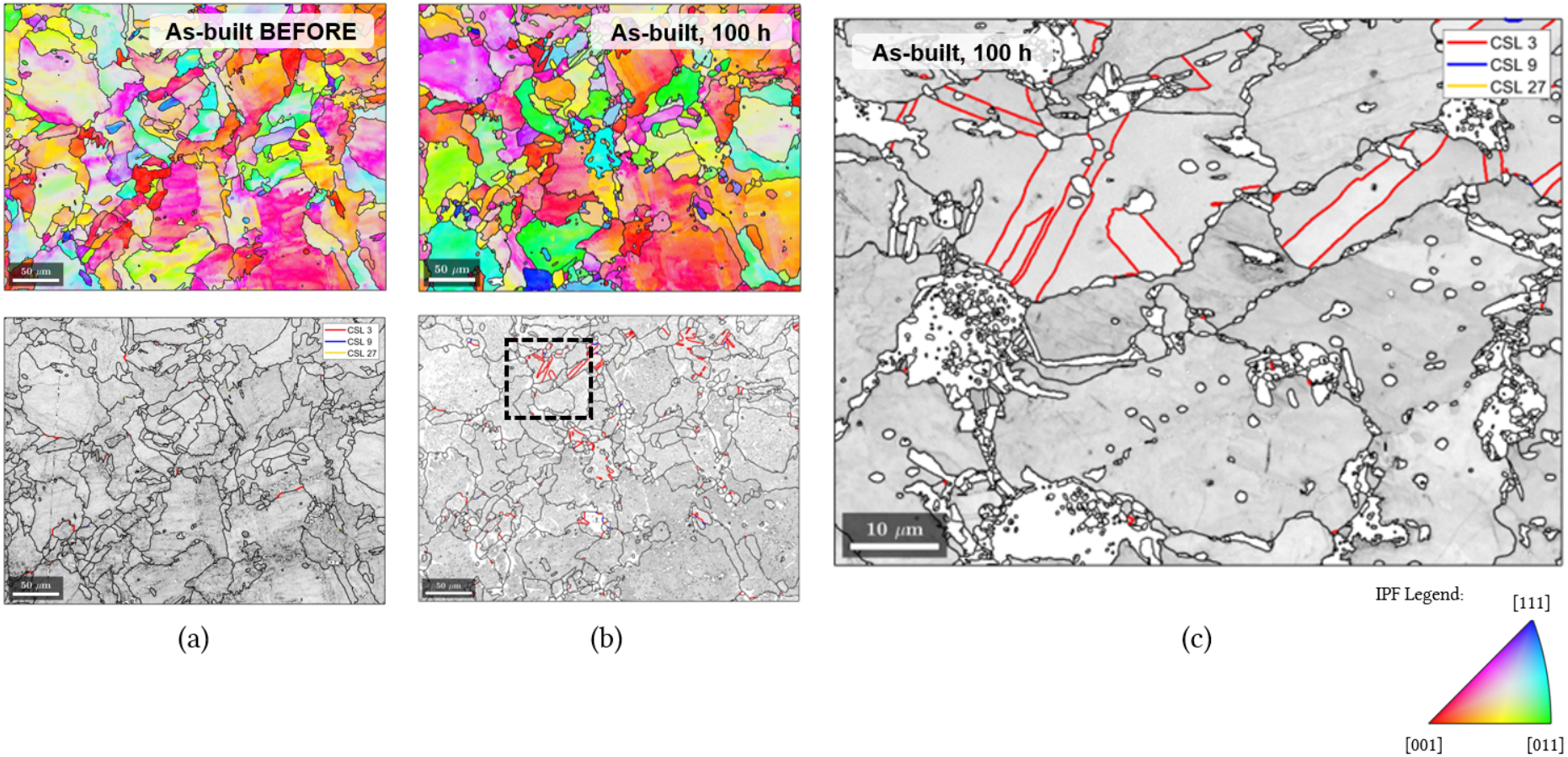


Figure 7.9: EBSD IPF maps and their corresponding band contrast maps with grain boundary character overlaid, for as-built L-PBF IN625 before (a), and after 100 h (b) of isothermal oxidation at 950˚C. (c) A magnified band contrast image, highlighted in (b). Note the un-indexed phase decorating grain boundaries, identified to be a mixture of internal oxide and external oxide via EBSD. Full recrystallisation was shown to occur following exposure for t = 100 h, evidenced by formation of equiaxed grains and higher fractions of twin boundaries.

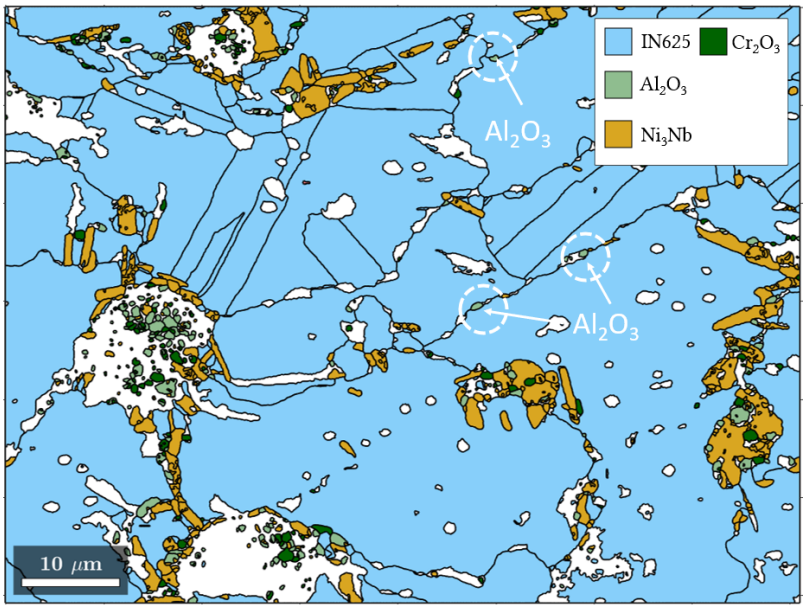


Figure 7.10: Phase map of the site shown in Figure 7.9, showing the elemental distribution across the sample surface following partial oxide removal via vibropolishing. Note Cr_2O_3 and Al_2O_3 presence along instances of Ni_3Nb δ-phase. White clustered phase is un-indexed partially removed oxide.

Figure 7.10 shows a phase EBSD IPF map for the 100 h sample following partial oxide removal. Phase mapping showed the presence of chromia Cr_2O_3 and alumina Al_2O_3 within the external oxide scale. Small presence of rutile TiO_2 was also detected on the oxide surface, though this was not clear to see from EBSD phase maps produced at this magnification. Of special interest was the presence of localised islands of chromia, alumina and rutile upon instances of Ni_3Nb δ-phase on the sample.

7.5.6 TEM - nano-sized precipitates in the sub-scale

Further examination of the oxidation-affected sub-scale using STEM-EDS was carried out via FIB and TEM with STEM-EDS. Figure 7.11 shows a High Angle Annular Dark Field (HAADF) micrograph of as-built L-PBF IN625 following 100 h exposure at 950˚C. Sub-micron globular precipitates were detected beneath the chromia and δ-phase external layer. These appeared to be a mixture of two precipitates embedded into each other. STEM-EDS mapping revealed that the finer precipitate at the centre of the globular phase to be enriched in O and Al. The larger precipitate enveloping this however appeared to be enriched in Ti and Nb. Areas enriched in precipitate were also depleted in Ni and Cr compared to the surrounding γ' matrix. No SiO_2 was detected in the oxide scale, compared to Chrykin *et al.* (2022) [196].

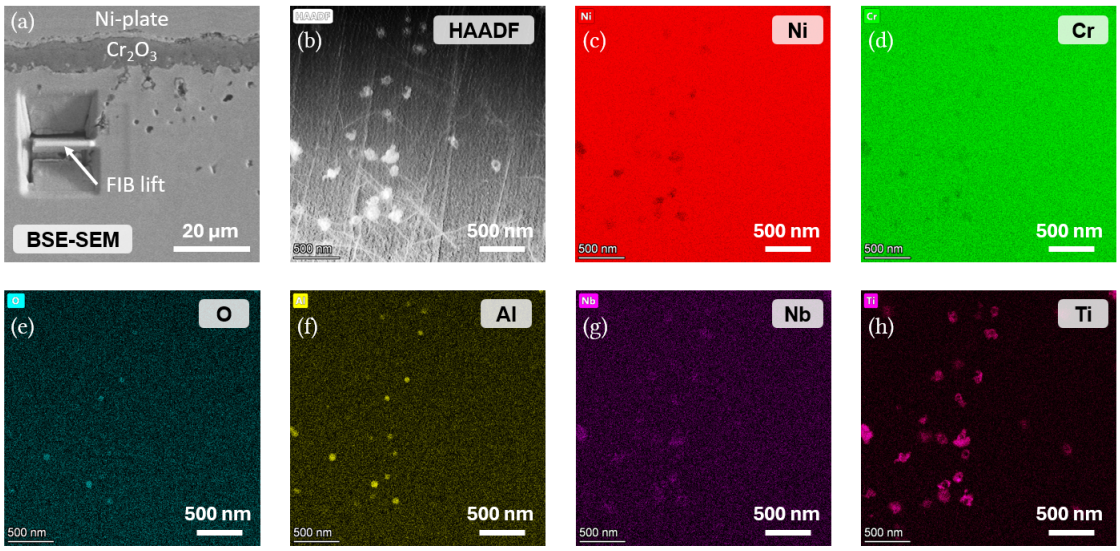


Figure 7.11: (a) BSE-SEM micrograph showing the location of the FIB lift-out performed for solution-treated L-PBF IN625 following exposure at 950˚C for 100 h. Note the FIB lift-out was performed in the oxidation affected region. (b) HAADF micrograph produced showing the sub-scale microstructure, and corresponding STEM-EDS maps (c – h) showing the elemental distribution of Ni, Cr, O, Al, Nb and Ti. Note the formation of fine Al-rich oxides, surrounded by (Nb,Ti) rich globular precipitates in the oxide sub-scale.

7.6 Discussion

7.6.1 Oxidation kinetics and external scale

Oxidation growth rate kinetics of the L-PBF material were observed to be slower than typical parabolic wrought alloys found in the literature (Table 7.2), where the solution-treated L-PBF material outperformed the as-built alloy. The oxide scale formed on the solution-treated tokens was finer and more compact, as evidenced by the surface profile maps in Figure 7.4 and Figure 7.5, showing fewer visual instances of spallation compared to the as-built alloy oxides formed after 100 h exposure. Slower rates of oxidation were attributed to a lower density of grain boundaries acting as short circuit diffusion pathways, due to the larger initial grain size of 25 µm compared to 22 µm. This is supported by findings reported by Parizia *et al.* (2020) who investigated the oxidation kinetics of both as-built and heat-treated material for t ≤ 96 h exposure at 900˚C [15]. This effect is expected to diminish over time, where the as-built alloy experienced a partial recrystallisation after t > 100 h exposure. These results showed good agreement with those presented in an additional work by the authors [191] using the same cylinders of material. These results were supported by findings by Chyrkin *et al.* (2022), who reported that grain size influenced oxidation rate, where L-PBF IN625 following hot rolling (fine-grained), and ageing treatments (coarse-grained) showed faster (7.93×10^{-7} mg/cm^2/s) and slower rates (2.19×10^{-7} mg/cm^2/s), respectively. [1].

Enhanced oxidation above grain boundaries has been widely discussed in the literature for Ni-based superalloys, producing wrinkled oxide scales [1, 9, 15, 176]. It is likely such wrinkling is produced as a result of grain boundaries acting as short-circuit diffusion pathways for ion transport from the bulk to the surface oxide. Higher supply of Cr to the grain boundary therefore results in faster growth of the oxide above these regions [290, 291].

7.6.2 Post-oxidation microstructure, Oxide sub-scale

No significant differences in chemical composition are thought to have contributed to variations in the mass gain across the as-built and solution-treated samples. However, the (Al, O) and (Ti, Nb)-enriched globular precipitates examined using TEM existed solely in the solution-treated material following t = 100 h exposure. These appeared to form intragranularly with no preference for formation on grain boundaries. Literature suggests the smaller circular precipitate enriched in Al and O to be most likely Al_2O_3 [1, 7, 14, 15, 80, 117, 187]. Ageing treatments comparable to prolonged exposures to high temperatures suggest the larger globular precipitates surrounding the alumina to be likely to be (Ti,Nb)C primary carbide [19, 38, 44, 118]. Hyer *et al.* (2022) reported the presence of globular M_6C carbide inside grains and on grain boundaries via STEM and TEM diffraction patterns following solution treatment [117]. These were enriched in $(Nb, Mo, Si, Al)_6C$, and is supported by similar findings by Inaekyan *et al.* via STEM-EDS [89, 117]. Gola *et al.* (2020) also reported presence of precipitates in the sub-scale, measured to be roughly 100 nm in size, with Ni, Nb and Mo enrichment [118]. Due to the Ti enrichment displayed by the globular precipitates in the present study however, it was concluded by the author that these were MC primary carbides [19, 292]. Due to the higher stability of Al > Ti oxides according to the Ellingham-Richardson diagram, it is believed by the authors that the alumina formed prior to the MC primary carbide [2, 66]. It is thought that carbides and oxides may act to improve the oxidation resistance of the alloy by providing pinning effects to counteract coarsening in the sub-scale, and reduce related stress effects on the protective oxide [19, 38]. Smaller carbides can contribute to improved strength and creep-life, though ductility is reduced if precipitates coarsen to sizes > 1 μm at longer periods of exposure. Al-rich oxides <100 nm in size however are reported to have negligible effects on mechanical properties [117, 292]. Hence it is thought that the aforementioned precipitates observed in the current study may produce beneficial mechanical effects in the sub-scale, though could act to decrease ductility if seen to coarsen over time.

A small presence of TiO_2 was indexed via EBSD, embedded alongside alumina Al_2O_3 in the external chromia scale. This was not observed in the previous study by the authors [191], but supports findings in literature for L-PBF and wrought IN625 and IN718 for T = 750 – 950°C [1,

2, 10, 13, 15, 54, 128, 166, 174, 181, 185, 187, 237]. TiO_2 is reported to grow as intergranular small nodules on the surface of the chromia film due to the faster diffusion and mobility of Ti compared to Cr, as well as the lower oxygen partial pressure towards the sub-scale interior [181, 185, 187]. Parizia *et al.* reported rutile presence in t<8 h after exposure to 900˚C in both as-built and solution treated L-PBF IN625. This is understood to lead to an improvement in the adherence of the oxide scale under cyclic oxidation conditions, according to Al-Hatab *et al.* [181].

7.6.3 CSL boundaries and internal oxidation

A significant increase in the CSL boundary density occurred during oxidation at 950˚C following recrystallisation. This is likely due to the fact the exposure temperature was close to the annealing and recrystallisation temperature of IN625 (980 – 1050˚C), as well as the FCC material's low stacking fault energy, where a material will act to reduce it's grain boundary energy via emission of dislocations [104]. It was noted that the fraction of twin boundaries (with 60˚ misorientation) measured in both the as-built and the solution-treated materials were significantly higher than the wrought materials (cold rolled, hot extruded, annealed, solution-treated) as well as some L-PBF IN625 heat-treated materials in the literature. L-PBF material in the present study showed up to 70% of its boundaries classified as $\Sigma \leq 29$, compared to wrought alloy showing only 36% without application of Grain Boundary Engineering (GBE), according to Trindade *et al.* [34, 131, 173, 230]. The authors highlight that the special grain boundary fractions measured were comparable to that of wrought materials that have undergone extensive GBE, such as multiple cold rolling passes and heat-treatments, as shown with IN600 by Lin *et al.* (1995) [229]. These fraction were close to the theoretical limit expected for CSLs in an FCC material of 2/3 of grain boundaries, approx. 66% [34, 131, 219, 229, 230, 233].

It is understood that the as-built alloy microstructure was likely to be highly stressed, with large residual stresses measured up to 575 MPa present following the fast solidification rates (~10^6 K/s) common to the L-PBF process [38, 104]. It is expected that the high dislocation density present (<2×10^{14} dislocations/m^2 [118]) lowered the threshold energy required for twin boundary formation, and exceeded the predicted strain level of 20 – 30 % required for a GBE effect to be produced [46]. Here a mobile twin forms by way of stacking faults on parallel planes to retain the strain accumulated in the crystal lattice due to high dislocation density at the grain boundary [131]. On heat treating, when two Σ3 boundaries meet, a Σ9 boundary will form to create a triple junction via the Σ3 regeneration mechanism and strain induced grain boundary migration [46]. This was the case following 1 h of exposure, where small instances of Σ9 boundaries began to form, as shown in Figure 7.8 (b) where small amounts of strain remained in the microstructure. Once the strain

in the microstructure was reduced, the once mobile boundaries slowed down, allowing for the increased nucleation of low-energy annealing twins. Subsequently the Σ3 proportion increases to replace the random grain boundaries and disrupt the grain boundary network [23, 237]. This was observed following oxidation for 1000 h in Figure 7.6.

Very few instances of internal oxide were observed to form on intergranular CSL grain boundaries in the sub-scale, shown by EBSD and the removal of the oxide following oxidation. Both as-built and solution-treated alloy showed that approximately 70% of internal oxide in the sub-scale occurred upon random oriented grain boundaries. This is attributed to the low grain boundary diffusivity of CSL boundaries compared to random orientation grains, inhibiting the formation of alumina in these areas [4, 173, 228, 233]. In the as-built case, a higher frequency of Σ3 boundaries were formed compared to the solution-treated material following 1000 h of exposure (~10% higher). This was correlated to the shallower internal oxide penetration depth measured and supports the concept of CLS boundaries disrupting the network of diffusion along random oriented grain boundaries [228]. It is thus believed that by altering the stress state of the as-built alloy via process parameters, scan strategy design, and post-processing heat treatments, the CSL fraction could be controlled to limit internal oxidation in L-PBF IN625 at high temperatures.

7.7 Conclusion

The effect of heat treatment on the oxidation growth rate and internal oxidation of L-PBF IN625 was investigated. As-built L-PBF IN625 formed significant amounts of CSL boundaries (up to 70%) during exposure to high temperatures, comparable to the likes of GBE Ni-based superalloy in the literature. The majority of grain boundaries showing internal oxidation in the sub-scale were revealed to be on random oriented grain boundaries. This was shown visually using vibropolishing and EBSD. Whilst less internal oxide occurred on CSL boundaries, overall oxidation rates appeared to be similar for both the as-built and solution-treated alloy, meaning internal oxidation did not drive differences in mass gain. It was proposed that further work investigating induced residual stresses in AM materials could be applied to influence the CSL fraction following heat treatment via careful parameter and scan strategy selection. This has the potential to allow for the design of components with surfaces engineered against internal oxidative attack, with the added benefit of fewer costly post-processing steps than in traditional GBE. A high CSL boundary density in the L-PBF material could act to limit the occurrence of cracking in the sub-scale region, and thus decrease the likelihood of spallation of the protective scale and subsequent oxidative damage of the substrate.

7.8 Acknowledgments

The authors are grateful for the financial support of the Manufacturing Technology Centre (MTC) for the PhD Scholarship, and for the support of Parker Aerospace (UK). The authors would like to acknowledge the University of Malta for assistance with profilometry measurements. SEM was carried out at the Centre for Electron Microscopy, University of Birmingham.

7.9 Funding

This research did not receive any specific grant from funding agencies in the public, commercial, or not-for-profit sectors.

7.10 Data availability

All raw data required to reproduce these findings can be made available on request through the University of Birmingham thesis repository.

7.11 CRediT authorship contribution statement

E. R. Lewis: Writing - original draft, Writing - review & editing, Visualisation, Data Curation, Formal Analysis, Investigation, Methodology; A. C. Cruchley: Supervision, Writing - review & editing, Resources; B. Attard: Writing - review & editing, Methodology, Resources; J. P. Magnussen: Methodology, Investigation, Writing - review & editing; Z. Gao: Methodology, Investigation, Resources; N. Cruchley: Supervision, Writing - review & editing, Methodology, Resources; M. M. Attallah: Supervision, Writing - review & editing, Methodology, Project Administration, Resources; S. Cruchley: Conceptualization, Supervision, Formal Analysis, Writing - review & editing, Methodology, Project Administration, Resources.

7.12 Declaration of Interests

No conflict of interests is known/can be identified by the authors.

Chapter 8

Effects of microstructure and surface finish on the corrosion of L-PBF IN625 in Pressurised Water Reactor hydrogenated water

8.1 Abstract

The present study aims to determine the oxidation performance of Laser Powder Bed Fused (L-PBF) Inconel 625 (IN625) Ni-based superalloy for use in Pressurised Water Reactor hydrogenated primary water designs. As-built and solution-treated tokens were investigated to assess the effect of L-PBF microstructure, alongside a series of surface finishes applicable to Additively Manufactured (AM) components. Tokens were exposed to hydrogenated PWR primary water in an autoclave at 300˚C and 10.8 MPa for periods of 500 h and 1500 h. Exposure led to the formation of a duplex oxide, composed of an outer $Ni(Fe,Cr)_2O_4$ Fe-rich oxide, and a Cr-rich inner layer which coarsened over time. Microstructural anisotropy resultant of the L-PBF process did not significantly alter the oxidation kinetics, however differences in surface topography lead to small variations in the oxide crystallite morphology. Higher surface roughness and surface residual stress lead to mass loss at early stages of oxidation t < 500 h. Electropolished surface were deemed ideal for producing oxidation behaviour similar to conventional material. Grain texture was found to influence oxidation, where an orientation relationship was established in the order of increasing oxidation rate: [001] < [101] < [111].

Authors: E. R. Lewis, N. Cruchley, J. P. Magnussen, A. Dickinson-Lomas, J. Duff, A. C. Cruchley, Y. L. Chui, F. Scenini, S. Cruchley, M. M Attallah.

Keywords: Oxidation, Ni-based superalloy, Electron backscattering diffraction (EBSD), STEM.

8.2 Highlights

- Laser Powder Bed Fused IN625 showed oxidation behaviour similar to wrought Ni-based superalloys.
- Surface finish influenced oxidation behaviour more significantly than L-PBF microstructure.
- Duplex oxide formed, comprised of a Fe-rich ($Ni(Fe,Cr)_2O_4$) outer layer, and thin Cr-rich inner layer.
- Electropolished tokens produced oxides similar to the wrought alloy in terms of size and thickness.
- A grain orientation-oxidation relationship was established for increasing diffusion: [100] < [101] < [111].

8.3 Introduction

In a drive for increased efficiency, higher operational temperatures and pressures (T > 400˚C, P > 20 MPa) are key in the design of Pressurised Water Reactors and Generation IV Supercritical Water Reactors (SCWRs) [23–25, 29, 30, 57, 293]. Smaller, more compact designs of SCWRs could potentially allow for the integration of Additively Manufactured (AM) parts. AM provides a unique design control previously unavailable with traditional subtractive methods for the fabrication of complex geometries common to the nuclear industry [33, 39, 41, 42].

Ni-based superalloys such as Inconel 625 (IN625), IN718 and IN690 are widely used in new and pre-existing Light Water Reactor designs (LWRs), and are a prime material for the manufacturing of cladding, steam generator tubing, as well as control rod components [23, 29, 55, 57, 201, 202]. This is on account of their superior corrosion resistance over common stainless steels such as 316L and 304, paired with their ability to maintain high temperature mechanical properties (high fatigue cycle and creep resistance) in corrosive environments [19, 20, 25, 27, 29]. IN625 has a notably low parabolic corrosion rate compared to the likes of IN718 and stainless steels attributed to its higher Cr alloying content ($\leq$ 27.0 wt.%) [2, 23, 25, 29, 55, 204, 214]. Was *et al.* reported corrosion rates 3× less than that of stainless steel, which was further supported by works by Fujisawa *et al.* for exposure to SCW deaerated conditions [29, 210].

Due to its high weldability and low (Al, Ti) wt.% content, IN625 is highly compatible with AM techniques like Laser Powder Bed Fusion (L-PBF), making it a key candidate material [33, 39–41, 63]. At this time, there is little research into L-PBF IN625 corrosion resistance in PWR envi-

ronments, where most work investigates high temperature conditions common to the aerospace industry. Current research has deemed L-PBF IN625 to perform to approximately the same standard as conventional wrought Ni-based superalloy in high temperature air for T = 800 – 1050°C for t < 1000 h [1, 9, 10, 12–17, 196]. Microstructural anisotropy resultant of the AM process does not appear to lead to any significant variation in performance, where rapid cooling rates of 10^6 K/s produce fine dendritic grains that extend parallel to the building direction of the component [1, 38, 104]. Grain anisotropy can be removed via standard solution heat treatment, producing equiaxed grains comparable to wrought alloy [38, 44, 83, 89].

When exposed to PWR hydrogenated primary water, wrought IN625 forms a passive duplex oxide which acts as a diffusion barrier against the ingress of oxygen [29]. Exhaustive studies have identified the outer layer of the oxide to consist of $Ni(Fe,Cr)_2O_4$ spinel distributed upon the surface as irregular hexagonal crystallites embedded into a Cr-rich layer [23, 30, 201, 204, 205, 212, 214]. This occurs via the non-selective oxidation of Ni and Fe [29, 209, 214]. The scale has been reported to be non-stoichiometric, showing slight porosity and the presence of mixed oxides such as Fe_2O_3 and Fe_3O_4 [29, 68, 204]. This is related to Fe saturation in the surrounding primary water by the gradual degradation of the PWR pressure vessel [205, 216]. The Cr-rich inner layer is comprised of dense and fine equiaxed grains, and is reported to often be too thin (<1 μm) to measure without the application of TEM [24, 25, 55, 201, 205, 209, 214, 216]. In comparison to the outer layer, this grows via the selective oxidation of Cr and grows at a much slower rate, leading to a Cr-depleted sub-scale [29, 209, 212].

The predominant mechanism of failure of IN625 in PWRs is its susceptibility to intergranular oxidation and pitting [23, 25, 29, 55, 68, 206, 216, 230]. Spallation and pitting is known to occur more readily when moving into higher temperatures common to SCWRs, driven by (Ti, Nb)-rich inclusions such as MC primary carbides, nitrides or oxides [23, 25, 206, 211, 216]. This is especially important for L-PBF IN625, where significant microsegregation of Nb and Mo occurs following fast cooling and solidification rates [12, 34, 38, 48, 116, 270, 294]. The unexpected, enhanced precipitation of deleterious phases can hence occur due to non-equilibrium compositions present [47, 48, 116]. This gives rise to environmentally enhanced crack growth (EECG), observed to occur in L-PBF IN718 due to Nb segregation and formation of Nb_2O_5 ahead of the crack tip during isothermal oxidation in air [103]. This targeted corrosion leads to galvanic coupling effects in the oxide and the formation of pits (4.3 – 12.9 μm) which grow over time due to the stochastic loss of metal cations from the surface [23, 29, 55, 68, 203, 206, 216]. PWR water chemistry combats this by additions of hydrogen (25 - 30 cm^3/kg) to absorb oxygen. This impedes oxidation rates and embrittlement at higher temperatures, and destabilises the formation of non-protective oxides such

as NiO when added in amounts of 9.16 cm^3/kg at 320°C [202, 205, 207, 210, 213, 214].

Literature reports that surface finish strongly influences the oxidation performance of wrought Ni-based superalloys and steels in PWR corrosive conditions. Additive surfaces without post-processing are generally too rough and non-uniform for application in industry ($R_a \leq 30$) [10, 132, 133, 187]. This leads to poor oxidation rates, particularly if the process parameters of the build are un-optimised [16, 17, 144, 166, 176, 187]. Chang *et al.* investigated the effects of a machined surface and demonstrated that Stress Corrosion Cracking (SCC) preferentially propagates along grooves left behind from the process [218]. The oxide formed upon the machined surface was porous and non-protective. This was compared to a set of non-stressed electropolished tokens which formed denser, more stable protective oxide. Grain boundary and grain orientation effects on the surface of the alloy also led to changes in oxidation rate, where certain grain orientations exhibited greater rates of oxide growth than others [46, 173, 195, 228, 229]. Was *et al.* expanded on this in PWR primary water and SCWR conditions, showing grain orientation enhanced oxidation with IN690 with the aid of EBSD [29].

The purpose of this study was to assess the corrosion resistance of candidate L-PBF IN625 for use in current and future generation PWR environments. The study considered the effects of additive microstructure, and a variety of surface finishes suitable for complex geometries for a clearer understanding of the applicability of AM, and an optimised route for post-processing.

8.4 Experimental procedure

8.4.1 Materials

Individual disks of L-PBF IN625 (diameter = 14 mm, thickness 2 mm) were manufactured using an EOS M280 L-PBF machine with the standard IN625 parameter set at the Manufacturing Technology Centre (MTC). Disks were fabricated using the standard IN625 performance 110 parameter set, with a powder particle size range of 15 − 45 µm and a layer height of 40 µm. Powder and to-

Table 8.1
Measured composition for L-PBF IN625 metallic powders, and consolidated tokens used in the corrosion study.

Alloy	Elements (wt.%)												
	C	Mn	Si	P	S	Cr	Co	Mo	Nb	Ti	Al	Fe	Ni
Powder	-	<0.01	0.07	<0.01	-	21.27	0.04	9.02	3.65	0.10	0.11	3.66	Bal.
L-PBF	0.026	<0.02	0.05	<0.01	-	21.51	<0.02	9.48	3.87	0.11	0.130	3.50	Bal.
Wrought	0.025	0.090	0.120	0.005	0.004	21.64	0.110	8.730	3.460	0.080	0.130	3.520	Bal.

ken chemical composition was confirmed using a combination of LECO and ICP-MS (Inductively Coupled Plasma Mass Spectroscopy) and is shown in Table 8.1. Cuboidal tokens of wrought IN625 (10 mm × 10 mm × 2 mm) were also machined for comparison to additive materials using electrical discharge machining (EDM).

In addition to the as-built condition, a set of tokens were also solution heat treated at 1177°C for 1 h and water quenched to room temperature according to AMS2774D [122]. Tokens were encapsulated in an argon back-filled quartz ampule prior to treatment. To assess the effect of microstructure, a set of as-built and solution-treated tokens were polished, and the edges chamfered using wet SiC papers to 4000-grit, and mechanically polished with OP-S colloidal silica to 0.25 μm. A variety of sample surface finishes were explored, outlined in Table 8.2. A set of tokens were kept with their as-received additive surface finish. An additional set of tokens underwent Centrifugal High Energy Finishing (CHEF) to produce a smooth mirror finish, performed using three stages: (i) cutting for 120 mins with 10 mm × 10 mm ceramic media with LQ18 chemical agent and water, (ii) smoothing for 120 mins with 6 mm × 10 mm ceramic media with LQ16 chemical agent and water, and (iii) polishing for 60 mins in dry maize. Tokens were also electropolished in a 4:1 solution of sulfuric acid and methanol at room temperature, using a 30 V power supply applied for 10 min intervals until an even finish was achieved [246]. An Alicona InfiniteFocus confocal instrument was used at 5× magnification to collect surface area roughness measurements (S_a, S_v). A Surfcorder SE1700 surface analyser was used to correlate roughness measurements, allowing for the recording of R_a, R_v and R_{max} values.

8.4.2 Microstructural characterisation, as-received condition

Metallurgical samples were prepared for as-built, solution and wrought IN625. These were hot mounted in Bakelite and mechanically polished to a 0.25 μm mirror-finish with OP-S colloidal silica. The as-received sample microstructure was imaged and analysed using a combination of BSE-SEM with EDS and EBSD. A JEOL 7000F FEG-SEM equipped with a HKL Nordlys EBSD unit was used, and a tilt of 70° was applied. An accelerating voltage of 20 kV was set for imaging with a 1.0 μm step size. Grain size and texture was measured using IPF maps generated using code taken and adapted from the MATLAB MTEX toolbox, including the Heyn Lineal Intercept method [250–254, 275].

TABLE 8.2
OVERVIEW OF MATERIALS, MICROSTRUCTURES AND SURFACE FINISHES INVESTIGATED.

Study	Condition	Surface finish			
		R_a (µm)	R_z (µm)	S_a (µm)	S_v (µm)
1 – Microstructure	As-built	0.14	0.01	-	-
	Solution	0.14	0.01	-	-
2 – Surface finish	Additive (ST)	9.10	33.80	6.80	33.50
	CHEF (ST)	0.40	2.20	0.90	15.00
	Electropolish (ST)	1.76	4.91	-	-

ST = Solution-treated (1177˚C 1h, water quench).
R_a = Arithmetical average relative to base length.
R_z = Maximum valley depth below the mean line.
S_a = Maximum valley depth of a selected area.
S_v = Arithmetical mean height of the selected area.

8.4.3 Corrosion exposures and analysis

Interrupted simulated PWR corrosion testing was conducted inside a recirculating autoclave closed loop at T = 300˚C and P = 10.8 MPa for times of 500 h and 1500 h. Water chemistry was controlled and monitored, set to contain: 2 ppm Li (added as LiOH), 3 ppm H_2 and <5 ppb O_2. The autoclave feed tank had a capacity of 2.5 L and was maintained at an alkaline pH of 10.5. Following removal from the autoclave, samples were dried and weighed. Specific weight gain due to oxidation was calculated by measuring the mass prior to and following exposure with a calibrated mass balance (±0.00001 g).

External oxides were characterised using BSE-SEM with EDS with an accelerating voltage of 20 kV at a 10 mm working distance with a Zeiss EVO-15 VP ESEM microscope with Bruker eFlash EDS. Oxide cross-sectioning was performed to determine the oxide layer morphology and thickness. Cross-sectioning was carried out using a dual-beam FEI Quanta 3D FEG-SEM applying a variation on a standard Focused Ion Beam (FIB) trenching method outlined by Cruchley *et al.* [264]. To examine sub-micron features present in the additive sample case, TEM with STEM-EDS was performed using a standard FIB lift-out technique [265]. A Thermofisher Helios G4 PFIB CXe dual beam FIB-SEM was used to produce the FIB lamellae. Imaging of the lamellae was carried out using an FEI Talos F200X fitted with Oxford Super-X Detectors STEM-EDS capability. To examine the effects of grain texture on oxidation, vibropolishing was applied to remove the oxide scale and to produce a mirror-finish for EBSD. This was achieved using a VibroMet-2 tabletop vibratory polisher with OP-S (0.25µm) for times up to 50 h.

X-ray Diffraction was carried out using a Proto AXRD Benchtop X-Ray Diffractometer with

a Cu-Kα radiation source. Indexing was performed in the 2θ range of 20 – 100˚ with a 0.02˚ step size. For correlation and to resolve overlapping peaks, Raman Spectroscopy was performed using a Renishaw InVia confocal Raman microscope with WiRE 4.2 software. Measurements were carried out with a 633 nm edge laser focused at 50× magnification and a beam power of 20 mW. Sample scanning areas of 900 μm^2 were measured with a step size of 1 μm, and dwell times of 8 – 25 s dependent on sample roughness and signal resolution. For both sets of XRD and Raman measurements, 1500 h exposed tokens were inspected. This was in an effort to maximize the signal obtained via a larger crystallite size.

8.5 Results

8.5.1 Specific weight gain

The specific weight gained for all conditions examined are summarized in Table 8.3, and bar charts for each condition at t = 500 h and 1500 h are presented in Figure 8.1. Following exposure, all conditions experience a mass gain which was seen to accelerate following a period of 500 h. The as-built IN625 showed the highest mass gain of 0.00009 g/cm^2 of the conditions, followed by the wrought IN625 tokens. Following solution-treatment, mass gained was reduced slightly, producing more comparable mass gain values to the conventional wrought IN625. For the alternative surface finishes examined, electropolishing was observed to result in approximately the same mass gain as the wrought material, showing good agreement with the more uniform polished surface finishes shown in in Figure 8.1. The additive surface tokens and CHEF conditions exclusively showed significant evidence of spallation at early periods of exposure, producing a mass loss after t = 500 h. However this was overtaken after 1500 h where an overall mass gain was experienced.

Table 8.3
Summary of oxidation data collected for L-PBF IN625 held at 300°C for 1500 h.

Condition	Oxide crystal size (μm)	Weight gain (g/cm^2)	Oxide thickness (μm)	Oxide layout (SEM,TEM)	Oxide Analysis (XRD, Raman)
As-built	1.13 (±0.02)	0.00009 ($\pm 3.00 \times 10^{-6}$)	0.39 (±0.10)	Fe-rich outer, Cr-rich inner	$Ni(Fe,Cr)_2O_4$, Fe_3O_4, Nb_2O_5,
Solution	0.97 (±0.01)	0.00006 ($\pm 5.00 \times 10^{-6}$)	0.36 (±0.10)	Fe-rich outer, Cr-rich inner	$Ni(Fe,Cr)_2O_4$, Fe_3O_4, Nb_2O_5,
Wrought	0.97 (±0.02)	0.00007 ($\pm 3.00 \times 10^{-6}$)	0.29 (±0.09)	Fe-rich outer, Cr-rich inner	$Ni(Fe,Cr)_2O_4$, Fe_3O_4, Nb_2O_5,
Additive	0.53 (±0.02)	0.00001 ($\pm 6.00 \times 10^{-6}$)	0.35 (±0.05)	(Fe, Ti)-rich outer, Cr-rich inner	$Ni(Fe,Cr)_2O_4$, Fe_3O_4, Nb_2O_5, $(Nb,Mo)_2N$
CHEF	0.91 (±0.03)	0.00001 ($\pm 6.00 \times 10^{-6}$)	0.71 (±0.16)	Fe-rich outer, Cr-rich inner	$Ni(Fe,Cr)_2O_4$, Fe_3O_4, Nb_2O_5,
Electropolish	0.89 (±0.03)	0.00007 ($\pm 8.00 \times 10^{-6}$)	0.55 (±0.12)	Fe-rich outer, Cr-rich inner	$Ni(Fe,Cr)_2O_4$, Fe_3O_4, Nb_2O_5,

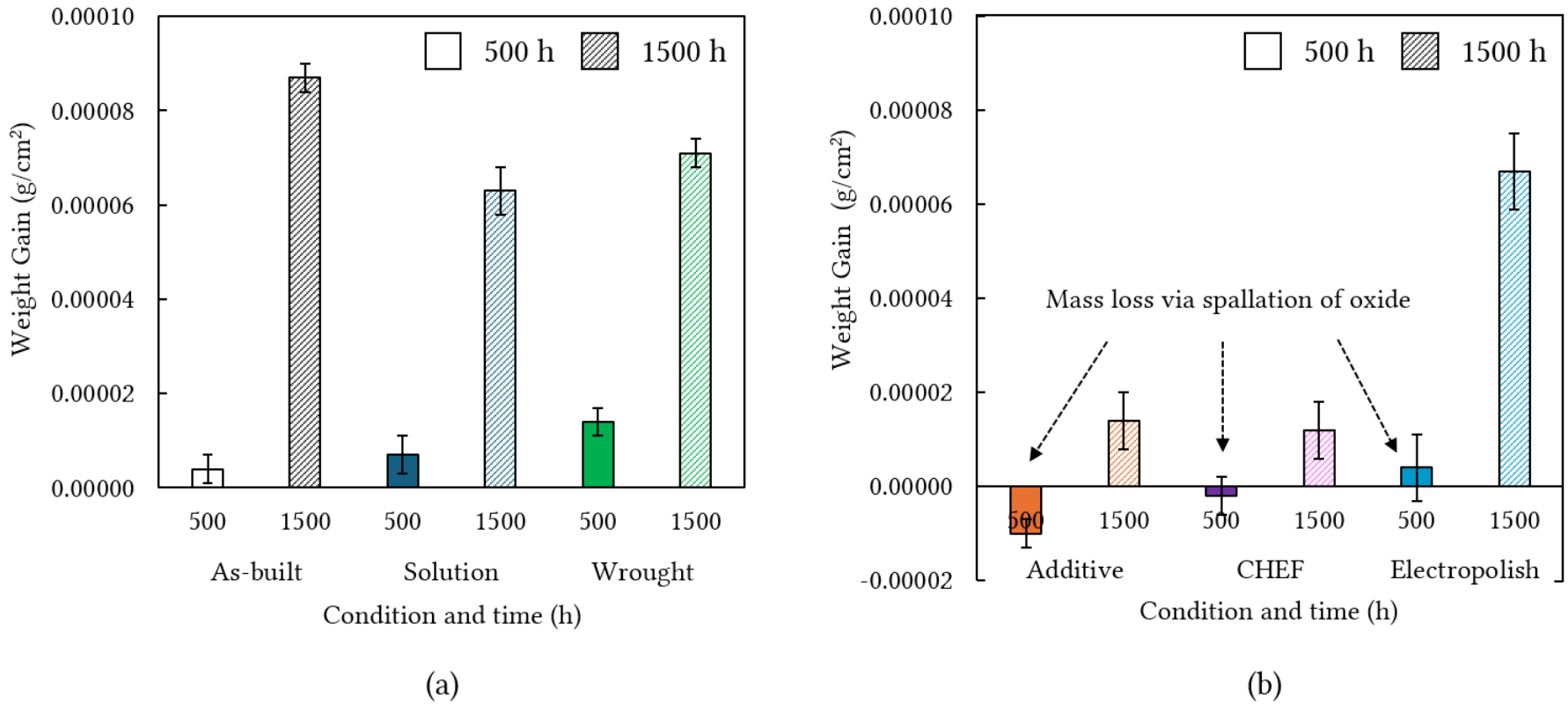


Figure 8.1: Mass gain change experienced by different conditions of L-PBF IN625 in hydrogenated PWR primary water held at 300°C for 500 h and 1500 h. (a) Microstructure study, (b) surface finish study.

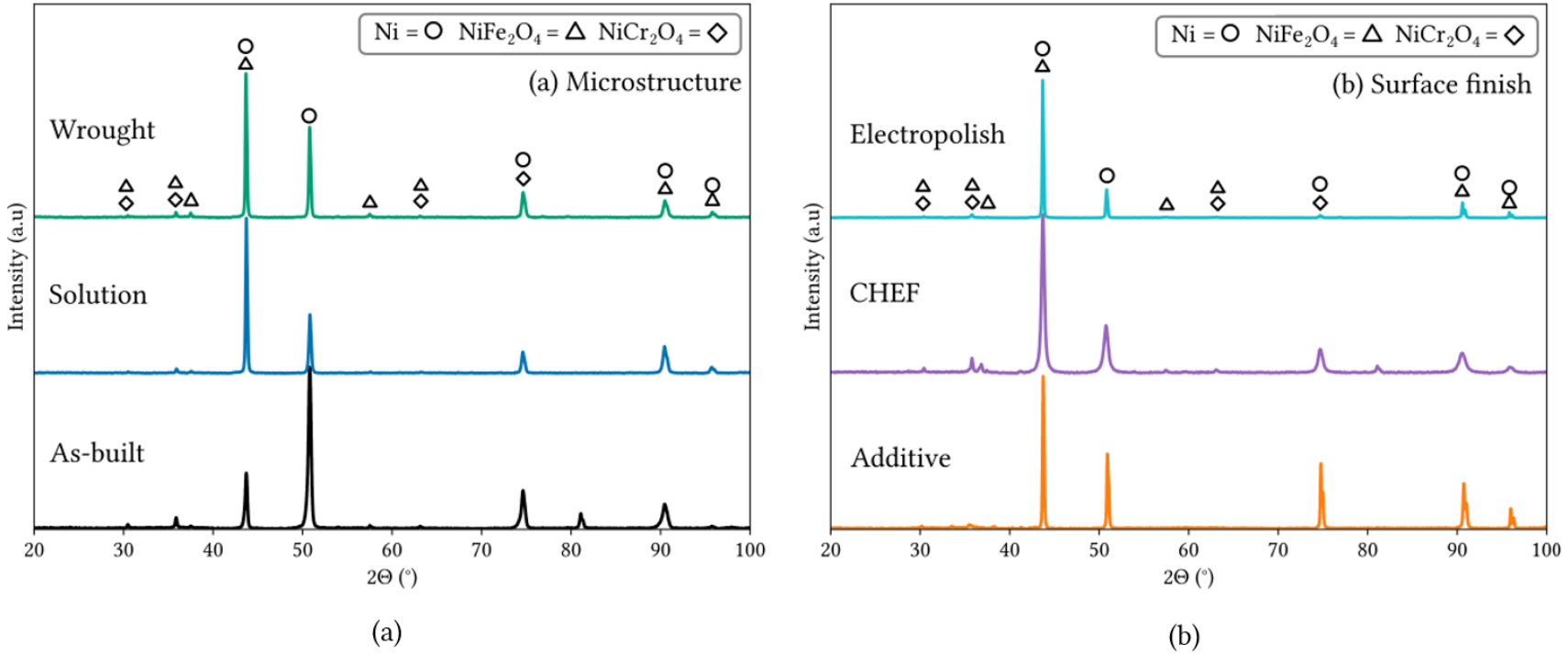


Figure 8.2: X-ray diffraction patterns from the surfaces of the corrosion tokens of different conditions of L-PBF IN625 following exposure to hydrogenated PWR primary water held at 300˚C for 1500 h. (a) Microstructure study, (b) surface finish study. ICSD collection codes: Ni - 8688, $NiFe_2O_4$ - 38999, $NiCr_2O_4$ - 84376. Note in (a) for the as-built sample case, preferential reflections can be seen for Ni ~50˚, due to the dominant [001] texture present in the additive microstructure.

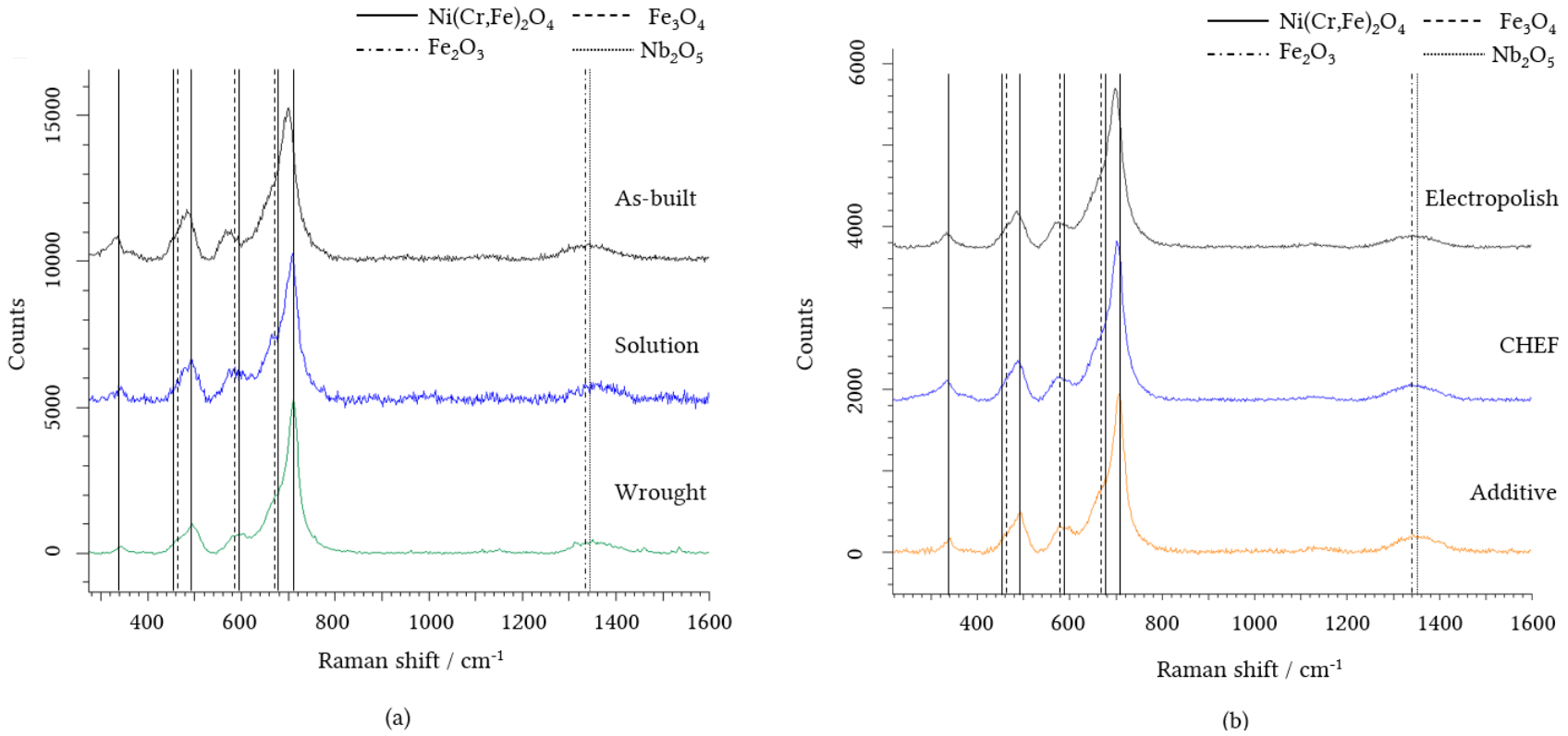


Figure 8.3: Raman spectra recorded from the surfaces of the corrosion tokens of different conditions of L-PBF IN625 following exposure to hydrogenated PWR primary water held at 300°C for 1500 h. (a) Microstructure study, (b) surface finish study. Peak shift values compared to literature and the RRUFF Project database ID: $Ni(Cr,Fe)_2O_4$ - R140860, Fe_3O_4 - R060191, Fe_2O_3 - R040024 [24, 30, 68, 212, 216, 263].

8.5.2 Analysis of the external oxide scale, microstructure

Diffraction patterns obtained via XRD of the external oxides produced can be viewed in Figure 8.2. Results demonstrated that all surface finishes produced the same external oxides, where the dominant phase was $Ni(Fe,Cr)_2O_4$. Higher Ni signal correlated to thinner oxide thickness (see Table 8.3) for the additive and wrought samples in particular. However, due to overlapping peaks the XRD results can be deemed inconclusive. To disambiguate the overlapping peaks in the XRD patters, Raman Spectroscopy analysis was performed, and the resultant spectra can be viewed in Figure 8.3. The most prominent peak in all spectra occurred at ~700 – 709 cm^{-1} corresponding to $Ni(Cr,Fe)_2O_4$, followed by a peak shift at ~491 – 503 cm^{-1} showing significant presence of $NiFe_2O_4$. A small presence of Fe_2O_3 and Fe_3O_4 was detected across all sample surfaces, alongside Nb_2O_5 for peak shift ranges of 1334 – 1356 cm^{-1}. A small peak was arguably present at the 1124 – 1141 cm^{-1} indicating some quantity of NiO, however this was deemed to be likely present from background noise, supported by the fact that hydrogen in the water chemistry exceeds the amounts required to prevent the oxides stability [213, 214]. Small amounts of peak shift was observed across the sample types investigated, particularly the as-built case, additive surface and CHEF tokens. This was assumed to be due to surface residual stresses.

Analysis of the external oxide on the token surfaces for t = 500 – 1500 h are summarized in Figure 8.4. Despite anisotropy introduced by the L-PBF processing route, similar morphology crystallites were formed on a bed of lower contrast, fine oxide across the as-built and solution-treated L-PBF material compared to conventional wrought alloy. EDS mapping shown in Figure 8.5, revealed the larger crystallites to be enriched in Fe and O and depleted in Cr and Ni. Crystallite size varied between 0.95 – 1.15 μm, where the as-built alloy showed the largest average diameter crystallites. This corresponded well to the higher mass gain experienced by the as-built alloy tokens (Table 8.3). Solution-treated alloy exhibited similar crystallite morphology and sizes to wrought alloy.

Notably, the solution-treated and wrought tokens experienced clear evidence of grain orientation enhanced oxidation (see Figure 8.5). To further investigate this and to establish a relationship between grain orientation and oxidation, selected areas upon the solution-treated tokens were marked, and the oxide removed via gentle vibratory polishing. This allowed for EBSD IPF maps to be generated and correlated to SE-SEM images taken prior to their exposure. This can be viewed in Figure 8.6. EBSD IPF mapping and analysis indicated that grains with orientation aligned to the [001] direction showed distinctly less oxide formation than grains aligned to the [101] and [111] orientations. This allowed the following grain orientation relationship to be established in order of increasing diffusion of ions through the grain orientation: [100] < [101] < [111].

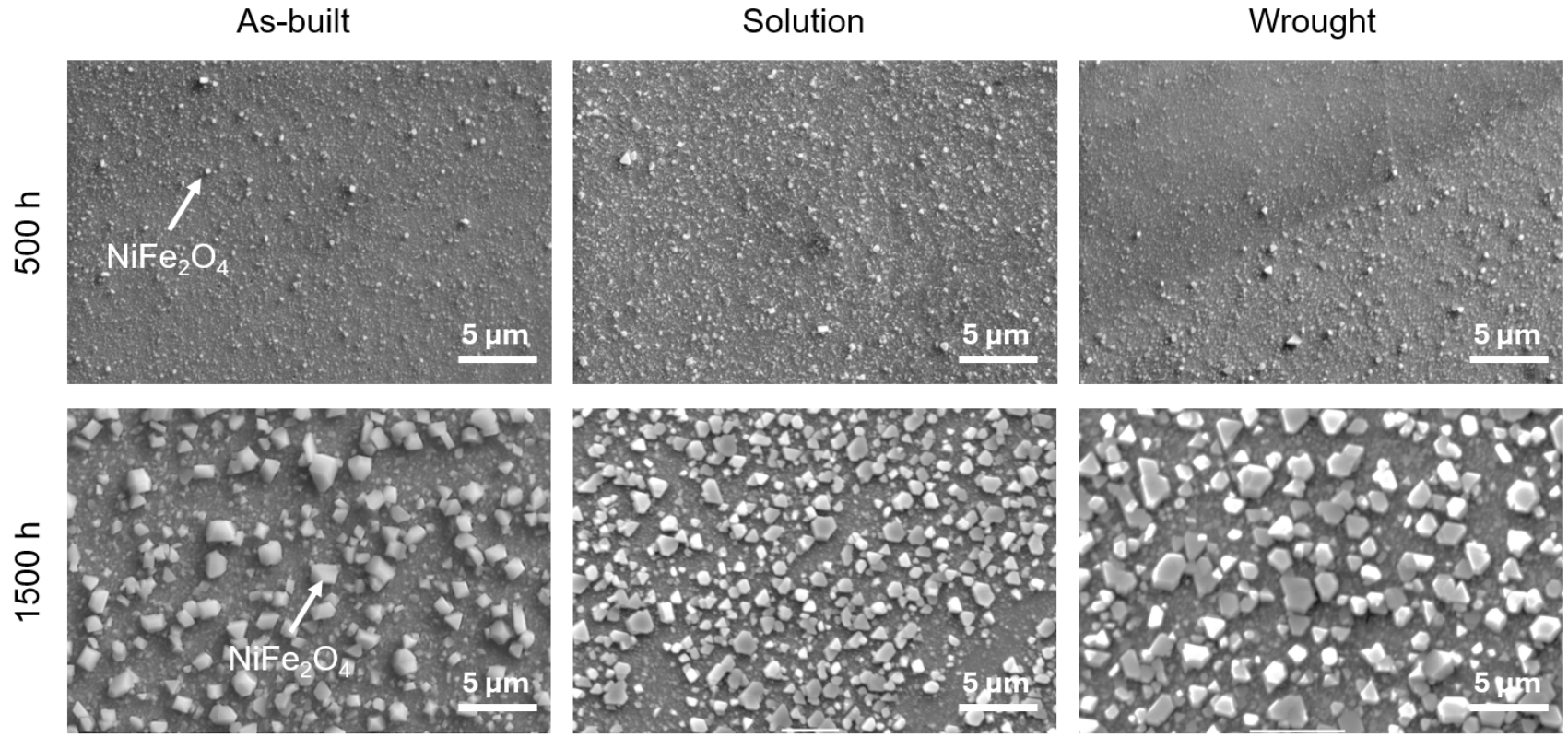
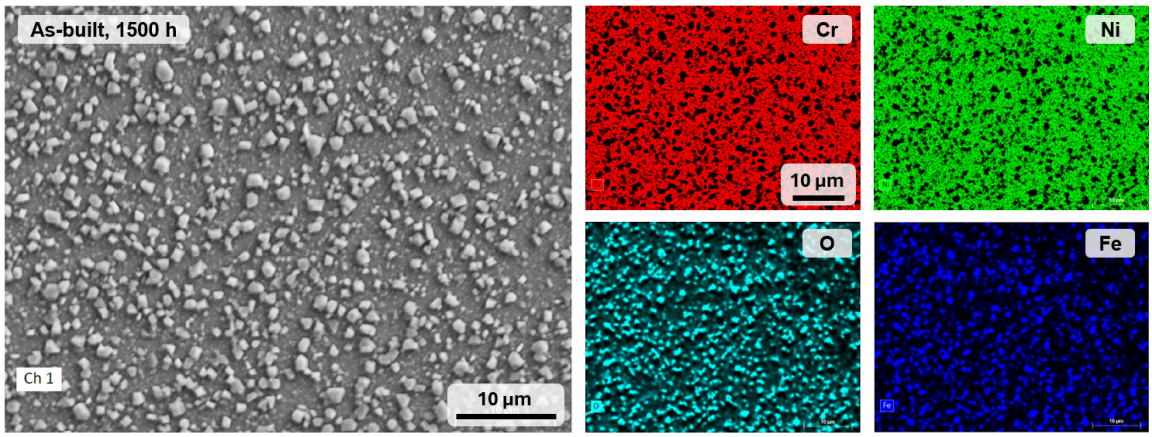
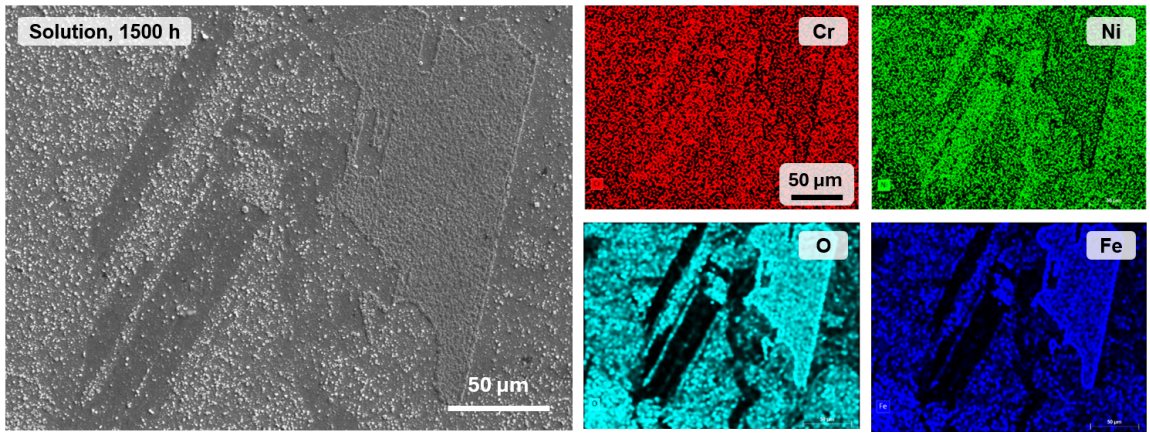


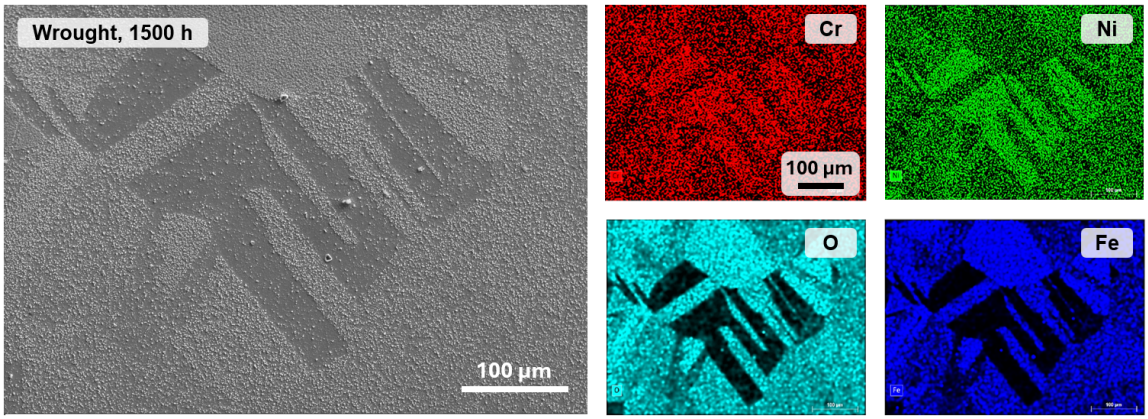
Figure 8.4: BSE-SEM micrographs of the external oxide formed upon corrosion tokens of different heat-treated conditions of L-PBF and wrought IN625 following exposure to hydrogenated PWR primary water held at 300˚C for 1500 h. Note, oxide crystallite size increased in diameter for longer periods of exposure, t. Evidence of grain orientation-related preferential oxidation can be viewed in the wrought tokens exposed for t = 500 h.



(a)



(b)



(c)

Figure 8.5: BSE-SEM micrograph and the corresponding EDS elemental maps showing the oxide crystallites formed upon (a) as-built, (b) solution-treated and (c) wrought IN625 following exposure to hydrogenated PWR primary water held at 300°C for 1500 h. Note the grain orientation enhanced oxidation visible in sample cases (b) and (c).

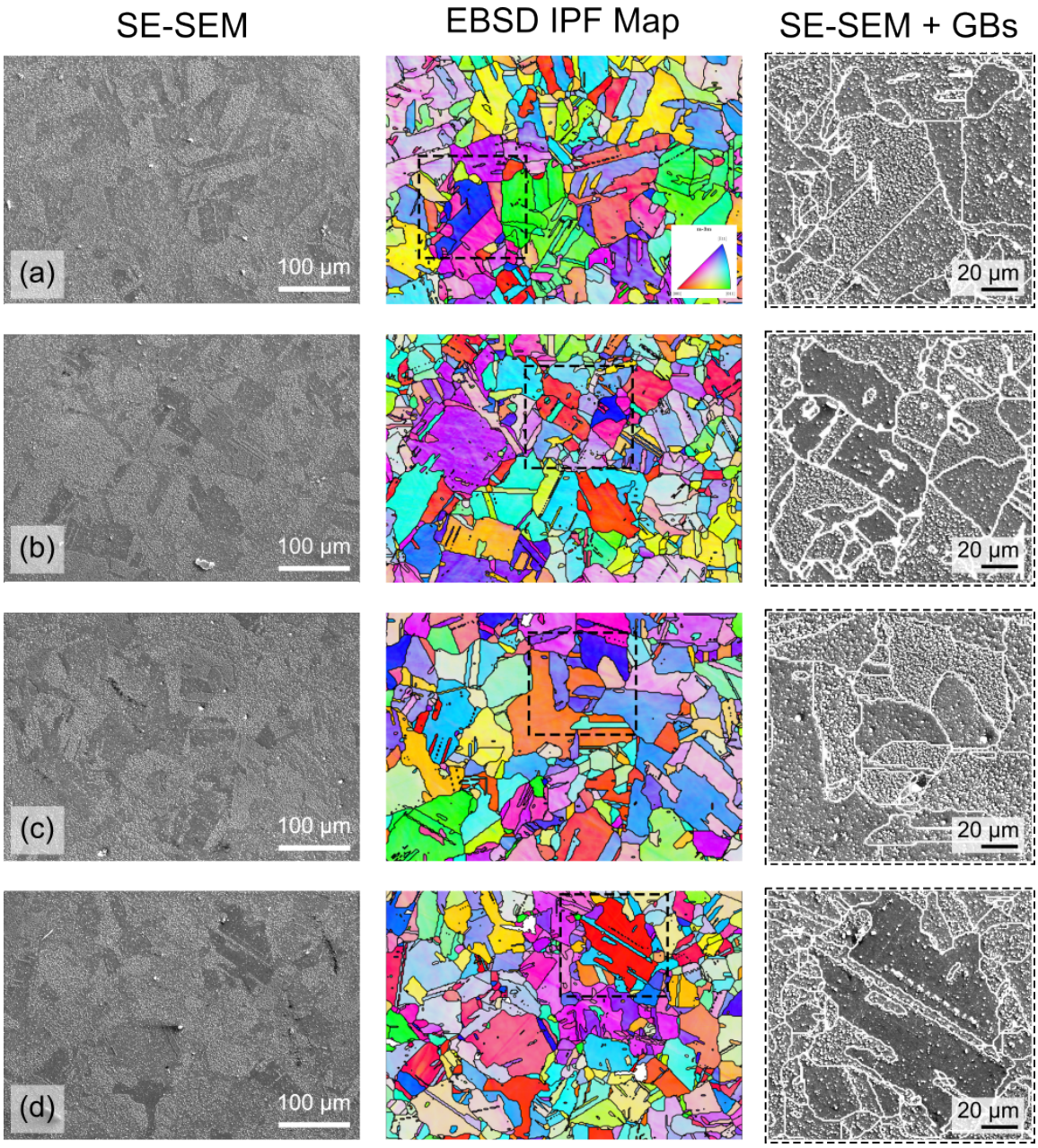


Figure 8.6: SE-SEM micrographs of selected regions of solution-treated L-PBF IN625 corrosion tokens (a,b,c,d) and their corresponding EBSD IPF maps following oxide removal after 1500 h exposure to hydrogenated PWR primary water. Note, the [001] orientated grains show less oxidation compared to [111] oriented grains, demonstrating an oxidation-grain orientation relationship.

8.5.3 Analysis of the external oxide scale, effect of surface finish

The external oxides formed upon the alternative surface finishes of the additive surface, CHEF and Electropolished tokens can be viewed in Figure 8.7. Similar to the microstructure study tokens, large higher contrast crystallites were observed to have formed upon a dense fine bed of lower contrast oxide. Crystallite sizes ranged from 0.51 – 0.94 μm. The smaller sizes here correspond to the lower mass gains observed, driven by spallation at early stages of oxidation. EDS mapping (see Figure 8.8 and Figure 8.9) revealed the larger crystallites to be enriched in Fe suggesting the expected $NiFe_2O_4$ oxide was formed, as shown via XRD and Raman spectroscopy. Additive tokens with powder particles adhered to the surface showed enhanced oxidation here, due to their higher surface area, showing greater Fe enrichment in these areas compared to the smoother regions upon the tokens. A similar relationship between sample surface area / roughness was observed in the CHEF and Electropolished cases, where enhanced oxidation and Fe-rich crystallite presence was observed in the peaks and troughs resultant of the CHEF and electropolish processes, respectfully.

EDS mapping revealed the presence of a sub-micron (Nb,Mo)-rich precipitate embedded homogeneously within the additive surface oxides, see Figure 8.9. The evolution of this precipitate was examined throughout the sample lifetime, shown in Figure 8.10 via EDS maps taken prior to solution-treatment, and following exposure to 500, and 1500 h. It appeared that the (Nb,Mo)-enriched precipitate developed primarily during the PWR exposure rather than during the heat-treatment stage.

Cross-sectional analysis of the oxides formed across all conditions of L-PBF IN625 and wrought alloy are summarized in Figure 8.11. Similar oxide morphology and thickness of 0.2 – 0.5 μm was observed, outlined in Table 8.3. Here the oxide scale appeared to be uniform, with large Fe-rich crystals discretely embedded onto the outer surface. The alternative surface finishes however showed a departure from uniformity. The CHEF sample cases showed the largest deviation in oxide thickness, with Fe-rich oxide growing preferentially inside the troughs left behind from the CHEF process. Here larger oxide thicknesses $\leq$0.87 μm were observed to form. The electropolished cross-sections however were deemed to be approximately the same as the wrought and solution-treated tokens, with similar oxide thicknesses and crystallite morphology/sizes demonstrated. This was of course with exception to areas upon the sample showing enhanced oxidation due to surface height variation following the electropolishing process, and possible grain orientation-oxidation effects.

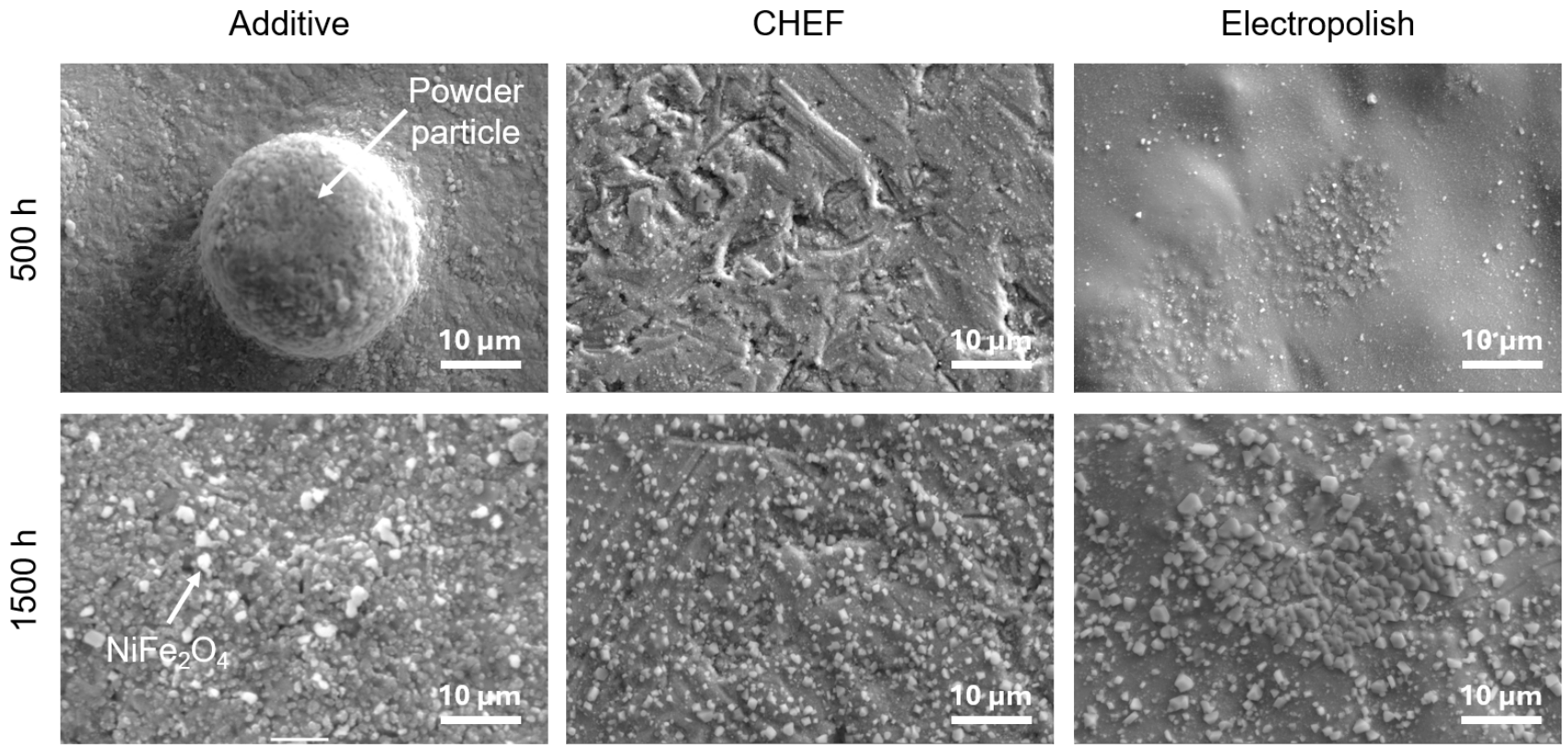


Figure 8.7: BSE-SEM micrographs of the external oxide formed upon corrosion tokens of different surface finish conditions of L-PBF IN625 following exposure to hydrogenated PWR primary water held at 300˚C for 1500 h. Note in the additive case, oxide appears to be thicker upon the powder particle compared to the flatter surroundings. For the CHEF case, troughs present from the surface finishing process appear to show enhanced oxidation. Raised areas left behind from the electropolishing process also show enhanced oxidation due to their higher surface area compared to surrounding smoother surfaces.

The additive sample case showed the thinnest oxide scales (≤0.40 μm) of the study, located in the smoother regions of the tokens in the absence of the un-melted powder particles. Extensive precipitation was also viewed beneath the scale in the oxidation-affected region. This was characterised using TEM with STEM-EDS mapping which can be viewed across maps in Figure 8.12 and Figure 8.13, and corresponding line scans through targeted areas of interest via Figure 8.14.

Figure 8.12 shows a series of HAADF (High Angle Annular Dark Field), bright-field (BF) and dark-field (DF) micrographs through the additive oxide scale following 1500 h exposure, and their corresponding EDS maps. This demonstrated the duplex nature of the scale, showing large Fe-rich oxide crystallites forming upon a thin <100 nm Cr-rich oxide layer. This was further confirmed via the STEM-EDS linescan taken through the scale shown in Figure 8.14. Mn and Ti enrichment was also viewed to be equally distributed through the protective oxide scale, with small Ti and O presence inside precipitates (≤100 nm) in the oxidation-affected sub-scale.

Figure 8.13 shows additional STEM-EDS maps generated from the additive oxide scale cross-section following 1500 h exposure. The (Nb,Mo)-rich acicular precipitate (≤600 nm) can be viewed here, showing small amounts of N enrichment, particularly along the edges of the precipitate. EDS line scanning through the acicular precipitate further demonstrated this, revealing slight N-enrichment compared to the bulk material. Small amounts of Nb and Mo enrichment also existed in the outer layer of the scale, showing the precipitate to form transversely across the protective duplex oxide. Al-rich oxide was also observed to be to be distributed throughout the (Mn,Ti)-enriched (≤100 nm) oxidation-affected sub-scale region. EDS line scanning through an instance of the precipitate (Figure 8.14) further exhibited the strong enrichment of Al, Ti and O here.

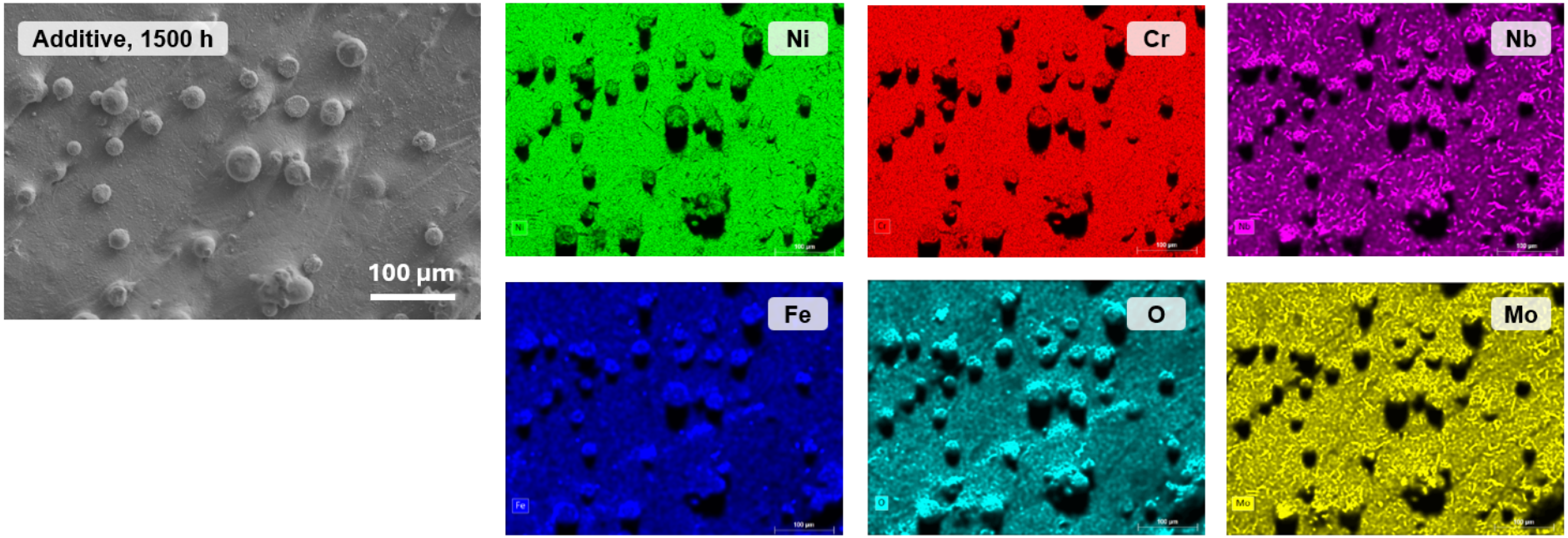


Figure 8.8: BSE-SEM micrograph and the corresponding EDS elemental maps showing the oxide crystallites formed upon additive surface L-PBF IN625 following exposure to hydrogenated PWR primary water held at 300˚C for 1500 h. Note, the (Nb,Mo)-rich precipitate forming homogeneously as acicular needles in the oxide surface. Darker areas showing lower elemental contrast adjacent to powder particles in each EDS map indicate shadowing effects due to the non-uniform surface finish of the oxide token.

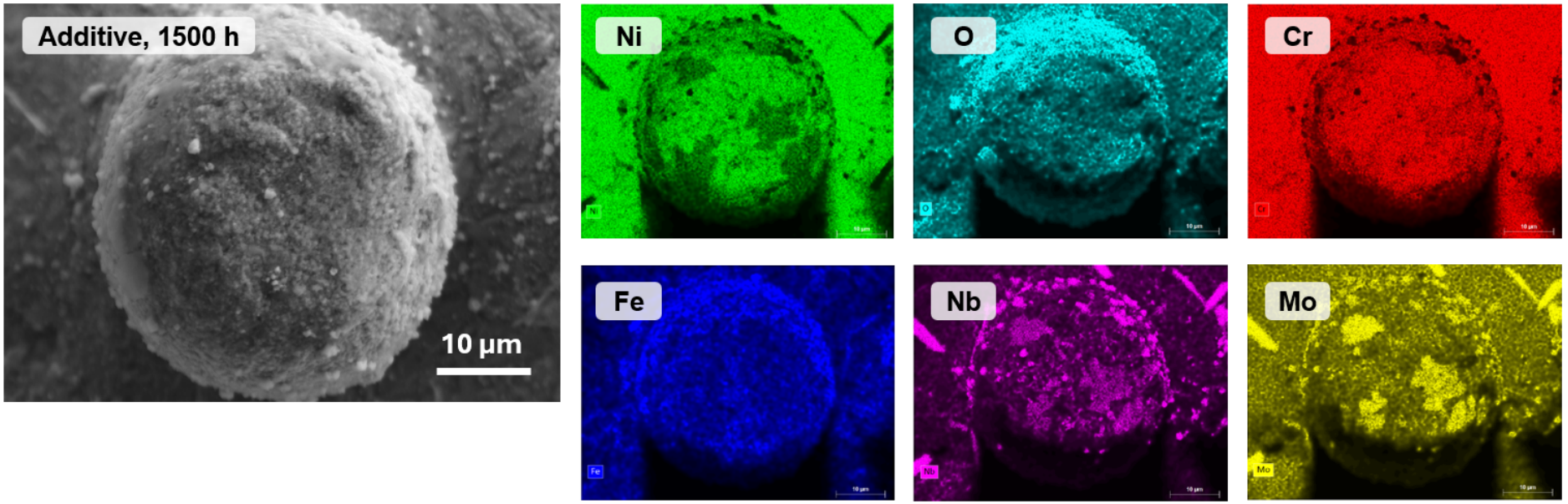


Figure 8.9: Higher magnification BSE-SEM micrograph and the corresponding EDS elemental maps showing the oxide crystallites formed upon additive surface L-PBF IN625 following exposure to hydrogenated PWR primary water. Note the acicular (Nb,Mo)-rich precipitates present, depleted in Ni.

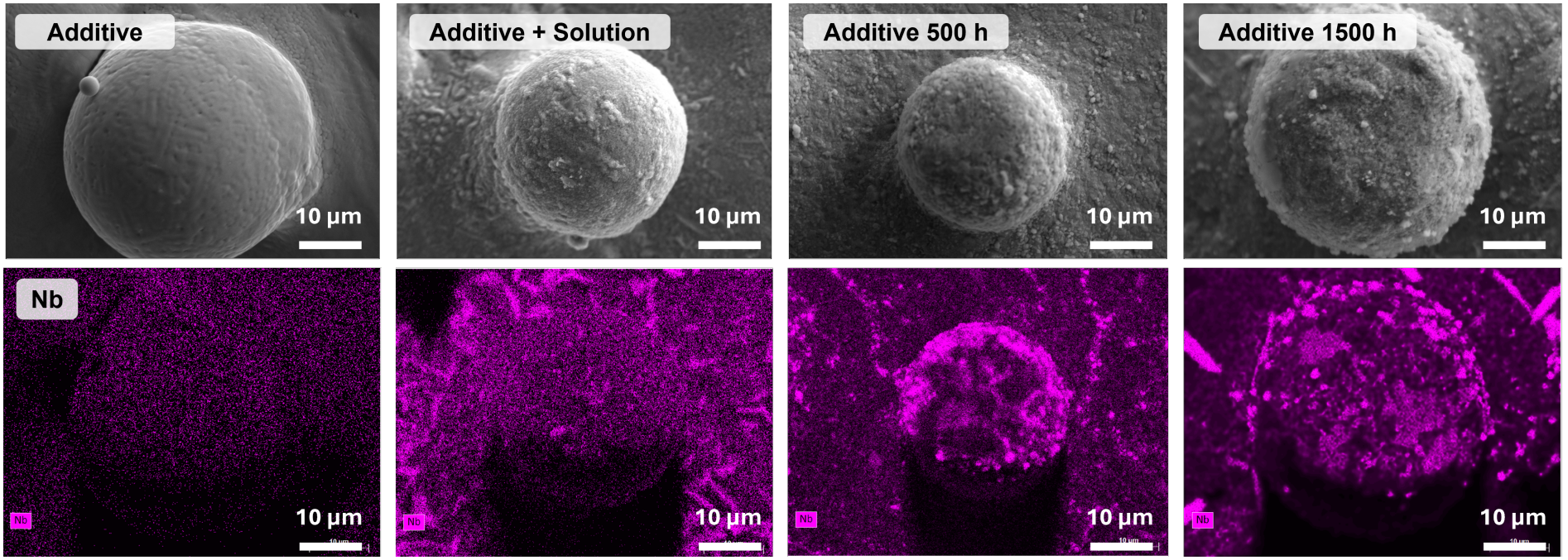


Figure 8.10: BSE-SEM micrographs and the corresponding Nb EDS elemental maps showing the evolution of the Nb-rich precipitate following solution heat-treatment (at 1177 ˚C, 1 h, water quench) and prolonged exposure to hydrogenated PWR primary water held at 300˚C for 500 and 1500 h. Following solution treatment, Nb presents itself as small needles assumed to be Ni_3Nb δ-phase. When held for 500 h in PWR simulated conditions, the Nb-rich needles dissolve and redistribute themselves to residual cell boundaries in the sample surface. After a longer holding period of 1500 h, the Nb-rich precipitate appear to reform as coarse acicular needles distributed homogeneously through the surface.

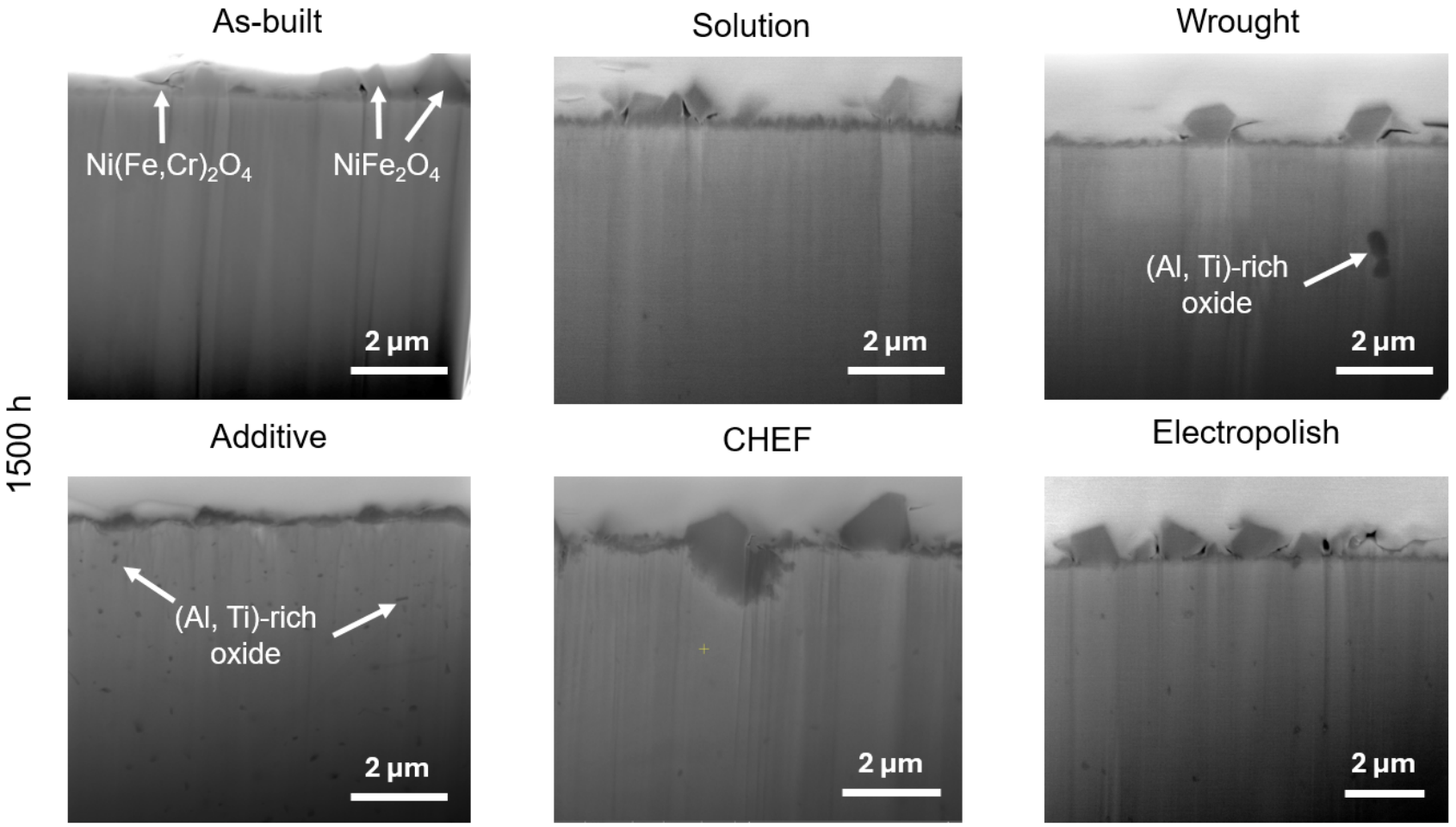


Figure 8.11: BSE-SEM micrographs showing FIB cross-sections of the oxides formed upon corrosion tokens of different heat-treated and surface finished conditions of L-PBF and wrought IN625 following exposure to hydrogenated PWR primary water held at 300˚C for 1500 h.

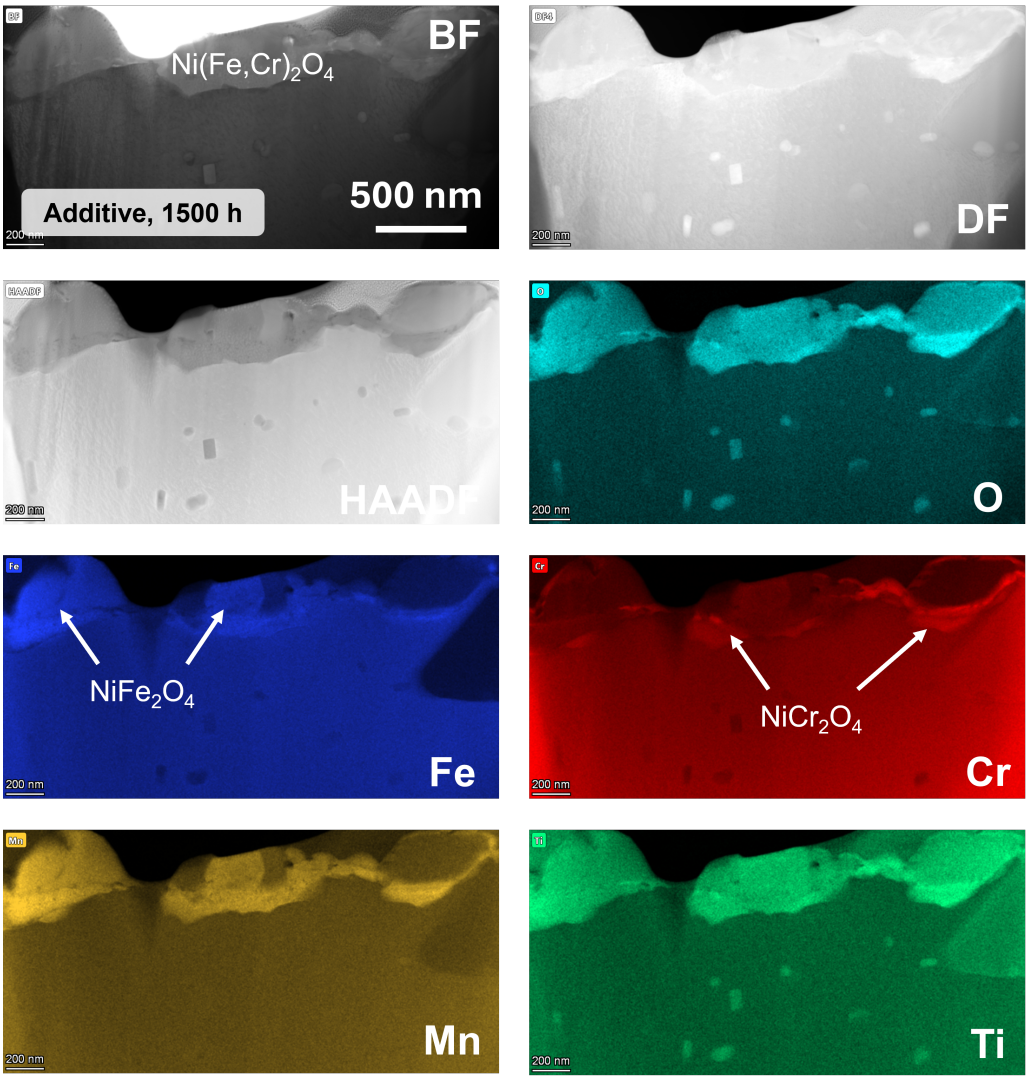


Figure 8.12: HAADF, BF and DF micrographs and corresponding STEM-EDS elemental maps showing the FIB cross-section through oxide scales formed upon additive surface L-PBF IN625 following exposure to hydrogenated PWR primary water held at 300°C for 1500 h. Note the duplex scale, with Fe-rich outer scale and Cr-rich inner scale.

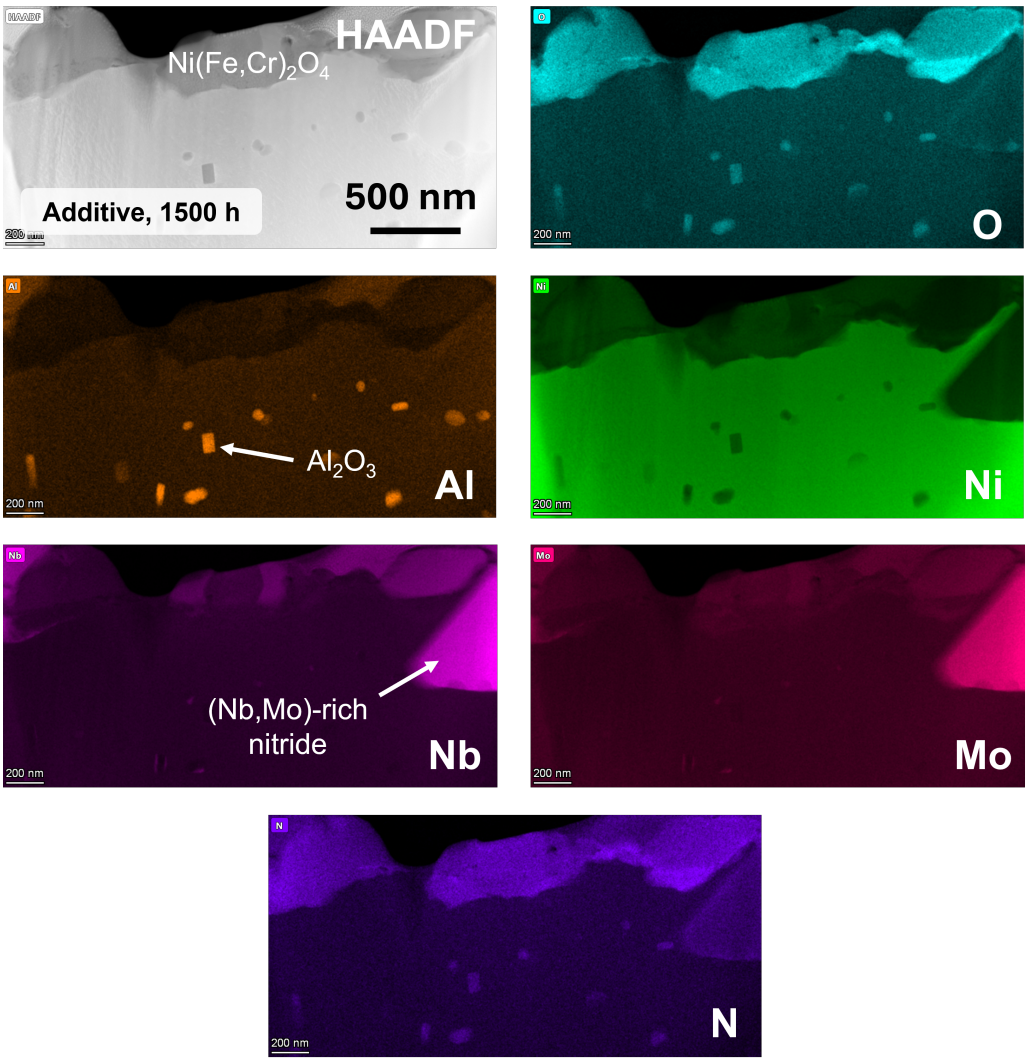


Figure 8.13: HAADF, BF and DF micrographs and corresponding STEM-EDS elemental maps showing the FIB cross-section through oxide scales formed upon additive surface L-PBF IN625 following exposure to hydrogenated PWR primary water held at 300°C for 1500 h. Note the (Nb,Mo)-rich needle-like precipitate.

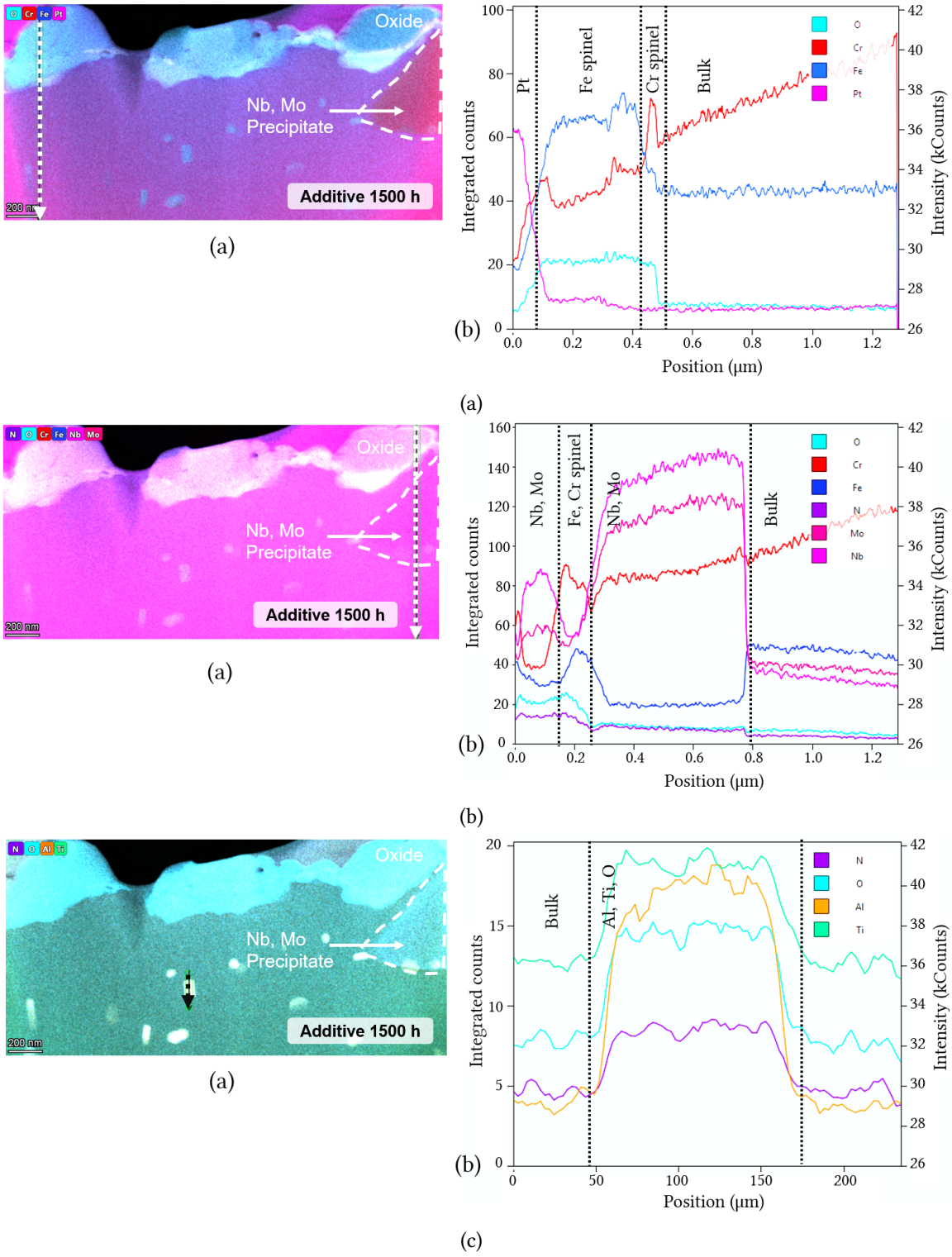


Figure 8.14: STEM-EDS elemental map and corresponding labelled STEM-EDS line scan (see white dotted line) through: (a) oxide scales, (b) Nb-rich precipitate, (c) Al-rich precipitate formed in the sub-scale region of the additive surface L-PBF IN625 following exposure to hydrogenated PWR primary water held at 300°C for 1500 h.

8.6 Discussion

8.6.1 Mass gain

The specific weight change experienced by the L-PBF IN625 tokens were within the range expected for corrosion inside a PWR environment [23, 214, 216]. Zhou *et al.* recorded similar mass gain values (~ 0.11 mg/cm^2 after 1500 h) for wrought IN625 in PWR primary water, comparable to the as-built and wrought samples examined. In contrast to Zhou *et al.* however, no pitting corrosion was observed, though this is likely due to the fact pitting effects were more dominant at earlier stages of oxidation which were not tested for (e.g. t < 100 h) in the current work [25, 68, 206, 216].

In the present study, any deviation to specific weight gain was seen to be more dependent upon the surface finish, rather than microstructural anisotropy introduced by the L-PBF process. This is clearly evidenced by the similar performance exhibited by the as-built alloy compared to both the solution and wrought tokens, and reinforces conclusions that solution treatment is successful in producing approx. the same microstructure as found in conventional material [28, 34, 44, 83, 89, 295]. It is thought that the slight increase in mass gain demonstrated by the as-built tokens is likely by consequence of the finer grain size compared to the wrought alloy, providing a higher density of short circuit diffusion pathways. It is also assumed that as-built L-PBF microstructures demonstrate higher dislocation densities ($\sim 2 \times 10^{14}$ dislocations/m^2) than those encountered in heat-treated materials [118]. An increased defect population will drive diffusion of ions and hence accelerate rates of oxidation experienced here [13]. It is also possible microsegregational effects by Nb and Mo may have contributed to faster oxidation and mass gained here, as experienced previously with L-PBF IN718 by Ramenatte *et al.* amongst other studies with AM materials [10, 109, 127, 185]

Surface finish influenced the mass gain rates significantly. This is strongly supported by the increased rates of spallation demonstrated by the additive sample case, followed by the CHEF tokens investigated, which lead to mass losses at early stages of exposure. Spallation is frequently observed for wrought IN625 investigated in the literature, though this is usually attributed to pitting corrosion effects at higher oxidation temperatures [23, 25, 29, 55, 68, 216, 230]. High surface roughness increases the surface area for oxidative attack, and has been readily observed throughout studies in the literature [16, 207, 218]. It is further understood that high residual stresses measured in the CHEF sample case can rival that of shot peening, measuring values up 550 – 800 MPa [42, 100, 134, 137]. Reynolds *et al.* investigated the effect of surface modifications on the high temperature oxidation of RR1000 in air [200]. Shot peening and high compressive stresses induced in the alloy surface led to increased buckling behaviour and accelerated oxidation. It is likely the

CHEF process produced a similar effect, with high dislocation densities providing short circuit diffusion pathways for enhanced ion transport [13, 200, 205]. Stress in the CHEF tokens can also be concluded following the peak shift demonstrated in the Raman spectra obtained for the condition compared to the polished and electropolished tokens investigated. Robertson summarized the effects of surface finish dependence upon the oxidation of stainless steels in high temperature de-oxygenated waters [209]. Here electropolished surfaces were deemed close to ideal for Ni-based superalloy in PWR environments, which supports the low rates of oxidation and similar oxide thicknesses and morphologies observed in the present study. Scalability of electropolishing for larger scale components however will remain a challenge. Common systems for electropolishing are available via bench top, wet bench or floor standing lab set ups. Large surface area parts can limit the effectiveness of the polish with regard to issues related to heat management and maintenance of the concentration of the electrolyte chemistry, leading to part size creep (longer processing times and uneven quality.)

8.6.2 Analysis of the external oxide

A duplex oxide structure (of thickness 0.20 – 0.87 μm) was consistently demonstrated across all microstructure and surface finish sample types investigated in this study, including the roughest case of the additive tokens [23–25, 30, 55, 204–206, 212, 214, 216]. The duplex oxide structure demonstrated is indicative of non-selective oxidation behaviour in the alloy, which is traditionally observed for wrought Ni-based superalloy in the literature [209, 214]. The outer layer was concluded to consist primarily of the $Ni(Fe,Cr)_2O_4$, as evidence by a combination of EDS, XRD, Raman and STEM-EDS. Formation of the discrete islands of Fe-rich spinel has been widely reported in PWR and higher temperature SCWR conditions in the literature [24, 55, 68, 201, 204–206, 214, 216]. The oxide morphology on the surface was similar in shape and size across all conditions, particularly comparable to works by Panter *et al.* with IN600 in PWR primary water [201]. It is understood that the Fe-rich spinel grows via the ingress of water along micro-pores present in the oxide. The Fe-rich spinel coarsens faster than the Cr-rich counterpart at temperature ranges common to Generation III PWR designs (T < 400˚C) due to its accelerated diffusivity in the oxide compared to Cr and other key alloying elements, $D_{Fe} > D_{Ni} > D_{Cr}$ [68, 204, 209, 214, 216]. Hence non-selective oxidation of the outer layer occurs via the diffusion of Ni^{+2} and Fe^{+2} cations to the surface along grain boundaries and vacancies, leading to the formation of a protective layer which coarsens at higher temperatures and prolonged periods [209]. Further work is required to validate the non-selective oxidation mechanism and could be determined by a comparison of the Ni:Fe:Cr ratio via extensive EDS measurement in the bulk of the alloy substrate, as demonstrated by Was *et al.* for

316L and 304 stainless steels.

It is thought that spallation of the surface oxide into the recirculating fluid may have led to enhanced Fe-cation saturation of the primary water by its dissolution [205, 209, 216]. This may pose as a solution to the significant mass gain following 500 h exposure, where an increase in Fe content would drive accelerated formation of the dominant $NiFe_2O_4$ spinel phase [214, 216]. This may also explain the presence of Fe_2O_3 and Fe_3O_4 detected via Raman spectroscopy, as observed by Yang *et al.* in the external oxide [68]. Formation of Nb_2O_5 however can be attributed to microsegregation effects, as well as relatively high Nb content in the alloys investigated [23, 24, 214, 216]. Wrought IN625 tokens demonstrated the lowest intensity peak shift for Nb_2O_5 at 1334 – 1356 cm^{-1} and can be attributed to the lower Nb compositional content measured in the bulk alloy (3.460 wt.%) compared to the L-PBF materials (3.870 wt.%) in the study. Mixed spinel formation can lead to a disruption of the protective oxide stoichiometry and uniformity, leading to accelerated rates of oxidation, and lower adherence of the scale to the substrate.

The thin, dense Cr-rich inner layer however, appeared to have a more continuous uniform interface, similar to that observed by Panter *et al.* [23, 201]. This layer demonstrated selective oxidative behaviour, with evidence of strong Cr enrichment throughout the inner oxide layer revealed using STEM-EDS, as well as Cr depletion in the sub-scale as demonstrated by Ren *et al* for alloy 625 in supercritical waters [25, 55, 68, 209, 214]. HAADF TEM micrographs further indicated a change in contrast when moving from the inside to outer oxide layer suggesting a compositional change. Raman, XRD and results from the literature allow the authors to conclude the spinel to be likely $NiCr_2O_4$, although additional thermodynamic analysis is needed to fully confirm this. Correlations between the oxygen enrichment zone and the Cr depletion depth beneath the scale could also pose as further evidence for the relationship, as stated by Panter *et al.* [201]. It is postulated that the selective oxidation of Cr will lead to the formation of vacancies which could enhanced the transport of oxygen into the substrate, promoting intergranular oxidation and SCC.

Strong Ti and Mn enrichment was shown to be distributed equally throughout the oxide film. Ti presence in the oxide scale has been associated with accelerated rates of oxidation via Ti-doping. Ti-doping of chromia Cr_2O_3 has been observed for the Ni-based superalloy RR1000 during high temperature oxidation in air. Cruchley *et al.* demonstrated that Ti ions have a greater mobility through the chromia scale to allow formation of oxide in the outermost layer [156]. For IN625 this effect is expected to diminish over time due to the low Ti content in the alloy. Mn presence has been related to improved adherence of the oxide scale by a reduction to the activity of chromia [5, 181, 188].

Sub-micron (Nb,Mo)-rich acicular precipitates were distributed across the external oxide layer

formed upon the additive surface tokens. STEM-EDS mapping and line scanning revealed the precipitate to have small amounts of N-enrichment, concentrated at the edges. These findings suggest that the precipitate is likely a (Nb,Mo)-rich nitride. Zuback *et al.* studied the formation of similar Nb-rich nitrides formed in Laser Powder Bed Fused IN625 samples of varying Fe content [130]. Following heat-treating, it was shown that high Fe, Ti and Si content (Fe: < 4.0 wt.%, Ti: 0.19 wt.%, Si: 0.0035 wt.%) lead to the enhanced formation of MN nitrides, paired with effects of Nb microsegregation in the as-built alloy. The lower content samples (Fe: 1.0 wt.%, Ti: 0.019 wt.%, Si: 0.37 wt.%) however formed Laves phase upon building which upon heat treatment experienced a partial transformation into a $(Nb,Cr,Mo)_2N$. Based on the findings posed by Zuback *et al.* and the chemical compositions in the present study, it is likely the precipitate is an MN nitride, although further quantitative STEM-EDS and diffraction patterns must be obtained to fully characterise the precipitate.

It is believed that the (Nb,Mo)-rich precipitate was exclusively present in the additive case due to the unique surface finish. Powder particles adhered to the surface lead to localised non-equilibrium chemical composition. Due to the wrinkled and convoluted surface finish, upon heat treatment there were likely fewer degrees of freedom for the diffusion of ions in the surface than within the substrate bulk. Therefore it appears likely that following post-processing microsegregational effects remained in the surface region of the sample, leading to (Nb,Mo) microsegregation and saturation, and hence the promoted nucleation of the (Nb,Mo)N.

8.6.3 Grain orientation and oxidation effects

The external oxides presented on the solution-treated L-PBF and wrought alloy tokens showed enhanced oxidation related to grain texture demonstrated on the sample surface prior to exposure. Similar research into the oxidation of Ni-based superalloys in PWR environments by Sennour *et al.* and Was *et al.* revealed that the sample oxides formed were often too thin to mask any surface features such as machining marks, or indeed grain orientation [29, 205]. Here it appeared that there was an epitaxial relationship between the between Cr-rich and Fe-rich crystallites formed on the alloy surface leading to selected raised areas showing thicker oxide formation [205]. Tan *et al.* investigated the effects of Grain Boundary Engineered Ni-based superalloy in PWR primary water. Here through control of the Coincident Site Lattice (CSL) grain boundary fraction ($\Sigma \leq 29$) a significant decrease in corrosion rate was achieved by lower diffusivity along CSLs than random misorientation boundaries [23]. A similar approach can be taken when relating the effects of grain orientation to oxidation in the present study. It is thought that the [001] orientation showed decreased rates of oxidation due to the larger interplanar spacing, and fewer nearest neighbour

atoms here compared to the likes of the [101], and [111] grain orientations. This would result in a longer pathway for the diffusion of ionic species to form oxide, hence establishing a grain orientation-oxidation relationship. The result has interesting implications for the application of, and the freedom of parameter design encountered with AM, where grain texture could potentially be controlled in order to limit oxidation in select regions of a component.

8.7 Conclusion

Oxidation of L-PBF IN625 inside simulated PWR hydrogenated water results in the formation of a duplex oxide scale. Regardless of variations in the L-PBF microstructure or surface finish, the outer layer was comprised of discrete crystallites of Fe-rich $Ni(Fe,Cr)_2O_4$ spinel, and a Cr-rich dense inner layer. It is understood that the outer layer grew by the non-selective oxidation of Fe and Ni, whereas the inner layer grew by the selective oxidation of Cr via the inward diffusion of oxygen anions to the inner layer interface. Mass gain and spallation was related to surface roughness, topography and surface residual stress, where a combination of these led to greater amounts of mass loss and formation of a less protective oxide scale. Electropolishing was deemed the more ideal surface finishing choice for L-PBF IN625, where similar oxide morphology, thicknesses and specific weight change was achieved compared to conventional wrought alloy. The oxidation of the external scale was influenced by grain orientation, where a oxidation-orientation relationship was established using SE-SEM of the oxide and correlative EBSD of the microstructure underneath. Unique metal nitrides were characterised in the additive surface oxides, shown to grow during PWR exposure. These were consistent with microsegregated L-PBF IN625 heat treated in the literature.

8.8 Acknowledgments

The authors are grateful for the financial support of the Manufacturing Technology Centre (MTC) for the PhD Scholarship. The authors would like to acknowledge the University of Manchester via the Henry Royce Institute for assistance with Pressurised Water Reactor autoclave corrosion testing. SEM was carried out at the Centre for Electron Microscopy, University of Birmingham.

8.9 Funding

This research did not receive any specific grant from funding agencies in the public, commercial, or not-for-profit sectors.

8.10 Data availability

All raw data required to reproduce these findings can be made available on request through the University of Birmingham thesis repository.

8.11 CRediT authorship contribution statement

E. R. Lewis: Writing - original draft, Writing - review & editing, Visualisation, Data Curation, Formal Analysis, Investigation, Methodology; N. Cruchley: Supervision, Writing - review & editing, Resources; J. P. Magnussen: Methodology, Investigation, Writing - review & editing; A. Dickinson-Lomas: Methodology, Investigation, Formal Analysis, Writing - review & editing, Resources; J. Duff: Methodology, Investigation, Writing - review & editing, Resources; A. C. Cruchley: Supervision, Writing - review & editing, Resources; Y. L. Chui: Methodology, Investigation, Resources; F. Scenini: Methodology, Investigation, Formal Analysis, Resources; M. M. Attallah: Supervision, Writing - review & editing, Methodology, Project Administration, Resources; S. Cruchley: Conceptualization, Supervision, Formal Analysis, Writing - review & editing, Methodology, Project Administration, Resources.

8.12 Declaration of Interests

No conflict of interests is known/can be identified by the authors.

Chapter 9

Conclusions and Future Works

9.1 Conclusions

Chapters 1 to 5 give an introduction to the oxidation and corrosion behaviour of the Ni-based superalloy IN625. Following this is original work from this project, the main conclusions of which outlined below.

Chapter 6 presents an investigation into the microstructure and oxidation properties of L-PBF IN625 following heat treatment (as-built and solution) and surface finishing (ground, additive surface roughness, and Centrifugal High Energy Finishing, CHEF), exposed to 950˚C in laboratory air and pressure for periods of 24 h – 1000 h.

Sub-parabolic to cubic oxide growth rate behaviour was demonstrated across all conditions, calculated to be slightly lower than those typically found for wrought IN625. Microstructural anisotropy introduced by the L-PBF process was not seen to influence oxidation resistance significantly compared to surface finish. Enhanced rates of oxidation and spallation in the additive roughness and CHEF tokens were attributed to having higher effective surface area for oxidative attack, and surface residual stresses increasing the defect population for diffusion of ions to the surface oxide, respectively. Overall CHEF and additive surfaces were seen to have an adverse effect on the oxidation kinetics compared to smoother ground or polished token surface finishes.

Regardless of microstructural variations or differences in the surface finishing, all conditions formed a protective external chromia scale (Cr_2O_3) alongside a near-continuous Ni_3Nb δ-phase layer at the scale/alloy interface. Significant Cr depletion was characterised beneath the scale and related to void formation, where Cr diffusion coefficients were extrapolated to inform the oxidation mechanism. Additive samples with the highest oxidation rate showed the deepest Cr depletion zone, with a corresponding high density of voids in the oxidation affected-region. Instances of internal oxidation were observed to penetrate from the oxide scale into the bulk of the substrate, identified to be alumina (Al_2O_3). Precipitates rich in (Nb,Mo,Ti) were examined in the oxidation-affected bulk, identified to be most likely a mixture of M_6C carbides and δ-phase.

Surface finish was seen to alter the precipitation of the δ-phase (Ni_3Nb) at the scale/alloy inter-

face via changes in the surface roughness morphology and the contact angle for nucleation of the phase. Surfaces with more non-uniform roughness profiles contained less δ-phase. The δ-phase coverage at scale/alloy interface was calculated to influence the theoretical temperature change for spallation (ΔT_c), where full coverage could potentially lead to a 200˚C increase in ΔT_c. This was related to physical measurements of stress in the oxide scale via XRD, where δ-phase is predicted to accommodate growth and thermal stresses generated by the chromia and substrate. This finding has important implications for the surface finish design of AM components for enhanced resistance to spallation during cooling and/or thermal cycling.

In Chapter 7, a study was presented investigating the influence of grain boundary character upon the internal oxidation of L-PBF IN625. As-built and solution treated alloy was exposed to high temperature laboratory air and pressure at 950˚C for 0.5 h – 1000 h. Solution heat treatment was applied recrystallise the microstructure and to examine Coincident Site Lattice (CSL) boundary formation resultant from the highly-stressed as-built microstructure.

Significant fractions of CSLs (up to 70%) were observed to form following heat-treatment and exposure to high temperature isothermal conditions. Whilst no notable change was seen in the oxidation growth rate with increased CSL fraction, grain boundary character was seen to influence the nucleation of internal oxides (Al_2O_3) in the sub-scale oxidation-affected region. In all cases, approximately 70% of instances of internal oxide resided upon random misorientation boundaries. High CSL fractions in the material correlated to shallower depths of internal oxide penetration, hindering possible crack propagation into the substrate. This was attributed to the lower assumed diffusivity along CSLs.

In Chapter 8, the oxidation resistance of L-PBF IN625 was explored in PWR hydrogenated water (T = 300˚C, P = 10.8 MPa) for times of 500 h, and 1500 h. This was carried out to inform possible routes of post-processing, with various heat treated (as-built, solution, wrought) and surface finish conditions (polished, additive surface, CHEF and electropolished) selected for their applicability to AM. All sample conditions produced positive mass gains after 1500 h. At early exposure times of 500 h, the additive surface tokens and CHEF materials however showed mass loss and spallation of the oxide scale. This was attributed to high amounts of surface roughness (and a higher surface area to volume ratio for oxidative attack) and residual stress (increasing the defect population for increased rates of ion transport) respectively. Despite this, mass losses were overtaken at longer periods of oxidation of t = 1500 h. No pitting corrosion was observed across all conditions investigated, despite large assumed microsegregation in the as-built samples, and high densities of (Nb,Mo)-rich nitrides in the additive surface sample case.

All samples exposed to high temperature PWR hydrogenated waters were observed to form

sub-micron duplex oxides with an Fe-rich outer layer ($Ni(Fe,Cr)_2O_4$) and a thin Cr-rich inner layer. Differences in the microstructure did not seem to alter the oxide morphology significantly, where similar sized Fe-rich crystallites were nucleated on the external layer surface across as-built and solution treated alloy. These were similar to those seen to form upon wrought alloy.

Solution treated L-PBF and wrought IN625 showed grain-orientation enhanced oxidation in the external oxide, forming raised areas across the sample surface. Oxide was removed to investigate this via EBSD mapping. Correlations made between the EBSD IPF maps and SE-SEM micrographs revealed that grains oriented in the [001] direction showed lower instances of Fe-rich spinel formation than [111] oriented grains. The following grain orientation-oxidation relationship was established, in the order of increasing rates of diffusion: [001] < [101] < [111]. This was attributed to an decreasing interplanar spacing for the diffusion of metal ions to form oxides, as well as a fewer number of nearest neighbour atoms when comparing a [001] orientation grain to a [111] grain.

The morphology of the oxide was seen to vary and was strongly dependent on the surface finish of the tokens investigated. Polished tokens showed a uniform protective scale comparable to conventional Ni-based superalloys used in industry settings. Additive surface tokens however showed enhanced oxidation of residual powder particles adhered to the surface. The convoluted surface roughness led to formation of a non-uniform oxide, with thicker regions upon powder particles compared to the surrounding more planar surfaces. Significant spallation was measured as a result. Significant precipitation was observed in the oxide surface, where (Nb,Mo)-rich nitrides were able to form due to residual microsegregational affects introduced during the L-PBF process. Electropolished tokens however showed the most comparable oxide morphology and oxide thickness compared to conventional wrought IN625 in the literature, and was thus deemed the most suitable route for post-processing.

9.2 Future work

Further testing is necessary to fully characterise the oxidation behaviour of L-PBF IN625 in both air and PWR operational environments, as well as the capabilities of AM for the tailoring of microstructure for optimized oxidation resistance. The following further work has thus been highlighted.

To continue oxidation testing for longer time periods (10,000s h) and temperature ranges (425 – 1100˚C), across multiple heat treatments and surface modifications. This will allow for extensive analysis and characterisation of the oxide scale and phase growth for further comparison to

conventional Ni-based superalloys. Multiple exposure temperatures would serve to compliment the work by allowing for the determination of the activation energy of chromia across various post-processed conditions of L-PBF IN625 via application of Arrhenius relationships. Knowledge of this would allow for their direct comparison to pure perfectly stoichiometric chromia and thus determination of the ideal route available for optimised oxidation resistance.

Detailed analysis of the long-term effects of the near-continuous δ-phase is required to fully understand the proposed mechanism for relaxation between the chromia scale and the IN625 substrate. Prolonged testing with in-situ synchrotron XRD measurements could allow for the furthered characterisation of the δ-phase growth mechanism and rate across multiple surface finish conditions. Complimentary physical measurements of stress generation in the scale upon cooling via XRD peak shift to further validate the concept. In this fashion, surface finishes could be designed to either enhance or prevent the formation of the δ-phase to alter the stress response upon cooling or thermal cycling of a component.

The effect of CSL boundaries on oxidation was studied, but only following solution-treatment. Multiple heat treatment designs could be explored to attempt to vary the CSL fraction produced, and the extent of recrystallisation. The flexibility offered by additive manufacturing could allow for the design of scan strategies aimed to produce microstructures with high dislocation densities to emulate cold working stages as seen in conventional GBE. A graded microstructure approach could then be taken to allow for the implementation of localised microstructures for optimised oxidation resistance i.e. in the surface of a component. Further work is required to ascertain if this is a scalable effect for component sizes required in industry.

Additional research is needed for further clarification of the usability of L-PBF IN625 inside corrosion simulated PWR conditions. The mechanical response of the alloy must be also characterised via in-situ corrosion tensile testing via constant extension rate tensile testing. This could be applied to assess the effect of the various surface finishing conditions upon SCC mechanisms, and for the subsequent characterisation of crack propagation and strain to failure. This will allow for a more detailed evaluation of the ideal post-processing route for L-PBF IN625 to be made compared to conventional Ni-based superalloys and stainless steels.

Further LWR environments common to Ni-based superalloys such as SCWR and Ultra-SCWRs could be explored to further investigate the effect of a reducing environment at higher temperatures and pressures. The effect of microsegregation and precipitation may also have a greater influence upon pitting here than the present study PWR conditions, due to the higher temperatures and kinetics present. TGA measurements here would also allow for continuous mass gain measurement, calculation of oxide growth rates, and a greater insight into spallation mechanisms.

The effects of corrosion in irradiated water is vital to investigate the in-service conditions experienced by IN625 in PWR and Generation IV design reactors. Irradiation will lead to changes in the sample microstructure over time, where the generation of dislocation loops will lead to a change in the defect population present in the substrate and hence diffusivity of metal ions. This will likely increase rates of oxidation and spallation. Hydrolysis effects of the water will also influence the corrosion mechanisms observed.

Further characterisation of the oxide scale and sub-scale region is desirable via TEM with STEM-EDS. Sub-micron oxides and precipitates formed required higher resolution microscopy to quantitatively analyse their composition and elemental distribution. This was especially the case in the additive sample case. Obtaining diffraction patterns for key phases and precipitates encountered such as the (Nb,Mo)-rich nitride would allow confirmation if it is MN, and for more detailed comparison to literature.

Detailed analysis is required to further characterise the level of residual stress present in the as-built tokens and CHEF cases in particular. High resolution Kernel Average Misorientation (KAM) mapping could be carried out to quantify stress and dislocation density. This could illustrate its influence upon the kinetics of the oxidation in both air and PWR primary water more strongly.

References

[1] A. Chyrkin, K. O. Gunduz, I. Fedorova, M. Sattari, A. Visibile, M. Halvarsson, J. Froitzheim, and K. Stiller, "High-temperature oxidation behavior of additively manufactured IN625: Effect of microstructure and grain size," *Corrosion Science*, vol. 205, p. 110382, Aug. 2022. [Online]. Available: https://linkinghub.elsevier.com/retrieve/pii/S0010938X22003006

[2] L. Kumar, R. Venkataramani, M. Sundararaman, P. Mukhopadhyay, and S. P. Garg, "Studies on the oxidation behavior of Inconel 625 between 873 and 1523 K," *Oxid Met*, vol. 45, no. 1-2, pp. 221–244, Feb. 1996, number: 1-2. [Online]. Available: http://link.springer.com/10.1007/BF01046827

[3] D. M. England and A. V. Virkar, "Oxidation Kinetics of Some Nickel-Based Superalloy Foils and Electronic Resistance of the Oxide Scale Formed in Air Part I," *J. Electrochem. Soc.*, vol. 146, no. 9, pp. 3196–3202, Sep. 1999, number: 9. [Online]. Available: https://iopscience.iop.org/article/10.1149/1.1392454

[4] V. Trindade, U. Krupp, P. E.-G. Wagenhuber, and H.-J. Christ, "Oxidation mechanisms of Cr-containing steels and Ni-base alloys at high-temperatures -. Part I: The different role of alloy grain boundaries," *Materials and Corrosion*, vol. 56, no. 11, pp. 785–790, Nov. 2005, number: 11. [Online]. Available: https://onlinelibrary.wiley.com/doi/10.1002/maco.200503879

[5] E. N'dah, M. P. Hierro, K. Borrero, and F. J. Pérez, "Study of the Cyclic Oxidation Resistance of Superalloy IN-625: Lifetime Predicted by COSP-Modelling Program," *Oxid Met*, vol. 68, no. 1-2, pp. 9–21, Jun. 2007, number: 1-2. [Online]. Available: http://link.springer.com/10.1007/s11085-006-9048-4

[6] J. Colas, L. Charpentier, and M. Balat-Pichelin, "Oxidation in Air at 1400 K and Optical Properties of Inconel 625, FeCrAlloy and Kanthal Super ER," *Oxid Met*, vol. 93, no. 3-4, pp. 355–370, Apr. 2020, number: 3-4. [Online]. Available: http://link.springer.com/10.1007/s11085-020-09959-6

[7] A. Chyrkin, P. Huczkowski, V. Shemet, L. Singheiser, and W. J. Quadakkers, "Sub-Scale Depletion and Enrichment Processes During High Temperature Oxidation of the Nickel Base Alloy 625 in the Temperature Range 900–1000 ℃," *Oxid Met*,

vol. 75, no. 3-4, pp. 143–166, Apr. 2011, number: 3-4. [Online]. Available: http://link.springer.com/10.1007/s11085-010-9225-3

[8] K. Staszewska and M. Scendo, "Mechanism and kinetics oxidation of Inconel 617 and 625 alloys," *Technical Issues*, vol. 1, pp. 82–89, 2016.

[9] K. Arnold, G. Tatlock, C. Kenel, A. Colella, and P. Matteazzi, "High temperature isothermal oxidation behaviour of an oxide dispersion strengthened derivative of IN625," *Materials at High Temperatures*, vol. 35, no. 1-3, pp. 141–150, May 2018, number: 1-3. [Online]. Available: https://www.tandfonline.com/doi/full/10.1080/09603409.2017.1393145

[10] N. Ramenatte, A. Vernouillet, S. Mathieu, A. Vande Put, M. Vilasi, and D. Monceau, "A comparison of the high-temperature oxidation behaviour of conventional wrought and laser beam melted Inconel 625," *Corrosion Science*, vol. 164, p. 108347, Mar. 2020. [Online]. Available: https://linkinghub.elsevier.com/retrieve/pii/S0010938X19314556

[11] A. M. de Sousa Malafaia, R. B. de Oliveira, L. Latu-Romain, Y. Wouters, and R. Baldan, "Isothermal oxidation of Inconel 625 superalloy at 800 and 1000 ℃: Microstructure and oxide layer characterization," *Materials Characterization*, vol. 161, p. 110160, Mar. 2020. [Online]. Available: https://linkinghub.elsevier.com/retrieve/pii/S1044580319327056

[12] L. Chen, Y. Sun, L. Li, and X. Ren, "Microstructural evolution and mechanical properties of selective laser melted a nickel-based superalloy after post treatment," *Materials Science and Engineering: A*, vol. 792, p. 139649, Aug. 2020. [Online]. Available: https://linkinghub.elsevier.com/retrieve/pii/S0921509320307279

[13] ——, "Improvement of high temperature oxidation resistance of additively manufactured TiC/Inconel 625 nanocomposites by laser shock peening treatment," *Additive Manufacturing*, vol. 34, p. 101276, Aug. 2020. [Online]. Available: https://linkinghub.elsevier.com/retrieve/pii/S2214860420306485

[14] M. R. Condruz, G. Matache, A. Paraschiv, T. Badea, and V. Badilita, "High Temperature Oxidation Behavior of Selective Laser Melting Manufactured IN 625," *Metals*, vol. 10, no. 5, p. 668, May 2020, number: 5. [Online]. Available: https://www.mdpi.com/2075-4701/10/5/668

[15] S. Parizia, G. Marchese, M. Rashidi, M. Lorusso, E. Hryha, D. Manfredi, and S. Biamino, "Effect of heat treatment on microstructure and oxidation properties of Inconel 625 processed by LPBF," *Journal of Alloys and Compounds*, vol. 846, p. 156418, Dec. 2020. [Online]. Available: https://linkinghub.elsevier.com/retrieve/pii/S0925838820327821

[16] Y. Sun, L. Chen, L. Li, and X. Ren, "High-temperature oxidation behavior and mechanism of Inconel 625 super-alloy fabricated by selective laser melting," *Optics & Laser Technology*, vol. 132, p. 106509, Dec. 2020. [Online]. Available: https://linkinghub.elsevier.com/retrieve/pii/S0030399220311427

[17] W. Huang, Y. Li, R. Yanjie, J. Sun, Z. Xia, L. Zhou, C. Li, J. Chen, Y. Niu, and Y. Zhao, "Effect of scanning speed on the high-temperature oxidation resistance and mechanical properties of Inconel 625 alloys fabricated by selective laser melting," *Vacuum*, vol. 206, p. 111447, Dec. 2022. [Online]. Available: https://linkinghub.elsevier.com/retrieve/pii/S0042207X22005693

[18] A. S. Khanna, "High-Temperature Oxidation," in *Handbook of Environmental Degradation of Materials*. Elsevier, 2018, pp. 117–132. [Online]. Available: https://linkinghub.elsevier.com/retrieve/pii/B978032352472800006X

[19] R. C. Reed, *The Superalloys: Fundamentals and Applications*, 1st ed. Cambridge University Press, Sep. 2006. [Online]. Available: https://www.cambridge.org/core/product/identifier/9780511541285/type/book

[20] Special Metals Corporation, "Inconel alloy 625," Tech. Rep., Aug. 2013. [Online]. Available: https://www.specialmetals.com/documents/technical-bulletins/inconel/inconel-alloy-625.pdf

[21] H. L. Eiselstein and D. J. Tillack, "The invention and definition of alloy 625," *Superalloys*, pp. 1–14, 1991. [Online]. Available: https://api.semanticscholar.org/CorpusID:56218978

[22] J. Yang, S. Wang, X. Tang, Y. Wang, and Y. Li, "Effect of low oxygen concentration on the oxidation behavior of Ni-based alloys 625 and 825 in supercritical water," *The Journal of Supercritical Fluids*, vol. 131, pp. 1–10, Jan. 2018.

[23] L. Tan, X. Ren, K. Sridharan, and T. Allen, "Corrosion behavior of Ni-base alloys for advanced high temperature water-cooled nuclear plants," *Corrosion Science*, vol. 50, no. 11, pp. 3056–3062, Nov. 2008.

[24] D. Rodriguez, A. Merwin, Z. Karmiol, and D. Chidambaram, "Surface chemistry and corrosion behavior of Inconel 625 and 718 in subcritical, supercritical, and ultrasupercritical water," *Applied Surface Science*, vol. 404, pp. 443–451, May 2017.

[25] K.-H. Chang, J.-H. Huang, C.-B. Yan, T.-K. Yeh, F.-R. Chen, and J.-J. Kai, "Corrosion behavior of Alloy 625 in supercritical water environments," *Progress in Nuclear Energy*, vol. 57, pp. 20–31, May 2012.

[26] D. M. Gorman, R. L. Higginson, H. Du, G. McColvin, A. T. Fry, and R. C. Thomson, "Microstructural Analysis of IN617 and IN625 Oxidised in the Presence of Steam for use in Ultra-Supercritical Power Plant," *Oxid Met*, vol. 79, no. 5-6, pp. 553–566, Jun. 2013.

[27] V. Shankar, K. Bhanu Sankara Rao, and S. Mannan, "Microstructure and mechanical properties of Inconel 625 superalloy," *Journal of Nuclear Materials*, vol. 288, no. 2-3, pp. 222–232, Feb. 2001.

[28] C. Li, R. White, X. Fang, M. Weaver, and Y. Guo, "Microstructure evolution characteristics of Inconel 625 alloy from selective laser melting to heat treatment," *Materials Science and Engineering: A*, vol. 705, pp. 20–31, Sep. 2017.

[29] G. Was, P. Ampornrat, G. Gupta, S. Teysseyre, E. West, T. Allen, K. Sridharan, L. Tan, Y. Chen, X. Ren, and C. Pister, "Corrosion and stress corrosion cracking in supercritical water," *Journal of Nuclear Materials*, vol. 371, no. 1, pp. 176–201, 2007, nuclear Fuels and Structural Materials 1. [Online]. Available: https://www.sciencedirect.com/science/article/pii/S0022311507007520

[30] A. Merwin, D. Rodriguez, and D. Chidambaram, "Oxidation of Superalloys in Supercritical Water," *ECS Transactions*, vol. 58, no. 41, pp. 15–24, Apr. 2014.

[31] S. Zinkle and J. Busby, "Structural materials for fission & fusion energy," *Materials Today*, vol. 12, no. 11, pp. 12–19, 2009. [Online]. Available: https://www.sciencedirect.com/science/article/pii/S1369702109702949

[32] P. Kritzer, N. Boukis, and E. Dinjus, "The corrosion of nickel-base alloy 625 in sub and supercritical aqueous solutions of oxygen: A long time study," *Journal of Materials Science Letters*, vol. 18, no. 10, pp. 771–773, 1999.

[33] M. M. Attallah, R. Jennings, X. Wang, and L. N. Carter, "Additive manufacturing of Ni-based superalloys: The outstanding issues," *MRS Bull.*, vol. 41, no. 10, pp. 758–764, Oct. 2016.

[34] G. Marchese, S. Parizia, M. Rashidi, A. Saboori, D. Manfredi, D. Ugues, M. Lombardi, E. Hryha, and S. Biamino, "The role of texturing and microstructure evolution on the tensile behavior of heat-treated Inconel 625 produced via laser powder bed fusion," *Materials Science and Engineering: A*, vol. 769, p. 138500, Jan. 2020.

[35] E. A. Lass, M. R. Stoudt, M. E. Williams, M. B. Katz, L. E. Levine, T. Q. Phan, T. H. Gnaeupel-Herold, and D. S. Ng, "Formation of the Ni3Nb δ-Phase in Stress-Relieved Inconel 625

Produced via Laser Powder-Bed Fusion Additive Manufacturing," *Metall and Mat Trans A*, vol. 48, no. 11, pp. 5547–5558, Nov. 2017.

[36] B. Dubiel and J. Sieniawski, "Precipitates in Additively Manufactured Inconel 625 Superalloy," *Materials*, vol. 12, no. 7, p. 1144, Apr. 2019.

[37] I. Choudhury and M. El-Baradie, "Machinability of nickel-base super alloys: a general review," *Journal of Materials Processing Technology*, vol. 77, no. 1-3, pp. 278–284, May 1998, number: 1-3. [Online]. Available: https://linkinghub.elsevier.com/retrieve/pii/S0924013697004299

[38] F. Zhang, L. E. Levine, A. J. Allen, M. R. Stoudt, G. Lindwall, E. A. Lass, M. E. Williams, Y. Idell, and C. E. Campbell, "Effect of heat treatment on the microstructural evolution of a nickel-based superalloy additive-manufactured by laser powder bed fusion," *Acta Materialia*, vol. 152, pp. 200–214, Jun. 2018.

[39] A. Sola and A. Nouri, "Microstructural porosity in additive manufacturing: The formation and detection of pores in metal parts fabricated by powder bed fusion," *Jnl Adv Manuf & Process*, vol. 1, no. 3, Jul. 2019, number: 3. [Online]. Available: https://onlinelibrary.wiley.com/doi/10.1002/amp2.10021

[40] L. E. Criales, Yiğit M. Arısoy, Brandon Lane, Shawn Moylan, Alkan Donmez, and Tuğrul Özel, "Laser powder bed fusion of nickel alloy 625: Experimental investigations of effects of process parameters on melt pool size and shape with spatter analysis," *International Journal of Machine Tools and Manufacture*, vol. 121, pp. 22–36, 2017.

[41] C. Y. Yap, C. K. Chua, Z. L. Dong, Z. H. Liu, D. Q. Zhang, L. E. Loh, and S. L. Sing, "Review of selective laser melting: Materials and applications," *Applied Physics Reviews*, vol. 2, no. 4, p. 041101, Dec. 2015, number: 4. [Online]. Available: http://aip.scitation.org/doi/10.1063/1.4935926

[42] S. Kalpakjian, S. R. Schmid, and K. S. V. Sekar, *Manufacturing engineering and technology*, 7th ed., ser. Always learning. Singapore: Pearson Education South Asia, 2014.

[43] C. Pleass and S. Jothi, "Influence of powder characteristics and additive manufacturing process parameters on the microstructure and mechanical behaviour of Inconel 625 fabricated by Selective Laser Melting," *Additive Manufacturing*, vol. 24, pp. 419–431, Dec. 2018. [Online]. Available: https://linkinghub.elsevier.com/retrieve/pii/S2214860418303518

[44] G. Marchese, M. Lorusso, S. Parizia, E. Bassini, J.-W. Lee, F. Calignano, D. Manfredi, M. Terner, H.-U. Hong, D. Ugues, M. Lombardi, and S. Biamino, "Influence of heat treatments on microstructure evolution and mechanical properties of Inconel 625 processed by laser powder bed fusion," *Materials Science and Engineering: A*, vol. 729, pp. 64–75, Jun. 2018.

[45] B. Attard, S. Cruchley, C. Beetz, M. Megahed, Y. Chiu, and M. Attallah, "Microstructural control during laser powder fusion to create graded microstructure Ni-superalloy components," *Additive Manufacturing*, vol. 36, p. 101432, Dec. 2020.

[46] V. Randle, "Grain boundary engineering: an overview after 25 years," *Materials Science and Technology*, vol. 26, no. 3, pp. 253–261, Mar. 2010.

[47] G. Lindwall, C. E. Campbell, E. A. Lass, F. Zhang, M. R. Stoudt, A. J. Allen, and L. E. Levine, "Simulation of TTT Curves for Additively Manufactured Inconel 625," *Metall and Mat Trans A*, vol. 50, no. 1, pp. 457–467, Jan. 2019, number: 1. [Online]. Available: http://link.springer.com/10.1007/s11661-018-4959-7

[48] M. R. Stoudt, E. A. Lass, D. S. Ng, M. E. Williams, F. Zhang, C. E. Campbell, G. Lindwall, and L. E. Levine, "The Influence of Annealing Temperature and Time on the Formation of δ-Phase in Additively-Manufactured Inconel 625," *Metall and Mat Trans A*, vol. 49, no. 7, pp. 3028–3037, Jul. 2018, number: 7. [Online]. Available: http://link.springer.com/10.1007/s11661-018-4643-y

[49] Y. Idell, L. E. Levine, A. J. Allen, F. Zhang, C. E. Campbell, G. B. Olson, J. Gong, D. R. Snyder, and H. Z. Deutchman, "Unexpected δ-Phase Formation in Additive-Manufactured Ni-Based Superalloy," *JOM*, vol. 68, no. 3, pp. 950–959, Mar. 2016, number: 3. [Online]. Available: http://link.springer.com/10.1007/s11837-015-1772-2

[50] B. Attard, A. M. A. Mohamed, and M. Attallah, "19 - new materials development," in *Fundamentals of Laser Powder Bed Fusion of Metals*, ser. Additive Manufacturing Materials and Technologies, I. Yadroitsev, I. Yadroitsava, A. du Plessis, and E. MacDonald, Eds. Elsevier, 2021, pp. 529–562.

[51] L. Shoemaker, "Alloys 625 and 725: Trends in Properties and Applications," in *Superalloys 718, 625, 706 and Various Derivatives (2005)*. TMS, 2005, pp. 409–418. [Online]. Available: http://www.tms.org/Superalloys/10.7449/2005/Superalloys_2005_409_418.pdf

[52] S. Floreen, G. Fuchs, and W. Yang, "The Metallurgy of Alloy 625," in *Superalloys 718, 625, 706 and Various Derivatives (1994)*. TMS, 1994, pp. 13–37. [Online]. Available: http://www.tms.org/Superalloys/10.7449/1994/Superalloys_1994_13_37.pdf

[53] S. Pedrazzini, D. Child, G. West, S. Doak, M. Hardy, M. Moody, and P. Bagot, "Oxidation behaviour of a next generation polycrystalline Mn containing Ni-based superalloy," *Scripta Materialia*, vol. 113, pp. 51–54, Mar. 2016. [Online]. Available: https://linkinghub.elsevier.com/retrieve/pii/S1359646215300014

[54] M. A. Khan, S. Sundarrajan, S. Natarajan, P. Parameswaran, and E. Mohandas, "Oxidation and Hot Corrosion Behavior of Nickel-Based Superalloy for Gas Turbine Applications," *Materials and Manufacturing Processes*, vol. 29, no. 7, pp. 832–839, Jul. 2014, number: 7. [Online]. Available: http://www.tandfonline.com/doi/abs/10.1080/10426914.2014.901530

[55] X. Ren, K. Sridharan, and T. R. Allen, "Corrosion Behavior of Alloys 625 and 718 in Supercritical Water," *CORROSION*, vol. 63, no. 7, pp. 603–612, Jul. 2007. [Online]. Available: http://corrosionjournal.org/doi/10.5006/1.3278410

[56] Aaltonen, P., & Hanninen, H., "Water chemistry and behavior of materials in PWRs and BWRs (IAEA-TECDOC–965)," International Atomic Energy Agency (IAEA), IAEA TECHDOC IAEA-TECDOC–965, 1997. [Online]. Available: https://inis.iaea.org/collection/NCLCollectionStore/_Public/28/075/28075997.pdf?r=1

[57] L. Garcia-Fresnillo, A. Chyrkin, C. Böhme, J. Barnikel, F. Schmitz, and W. J. Quadakkers, "Oxidation behaviour and microstructural stability of alloy 625 during long-term exposure in steam," *J Mater Sci*, vol. 49, no. 17, pp. 6127–6142, Sep. 2014, number: 17. [Online]. Available: http://link.springer.com/10.1007/s10853-014-8344-7

[58] S. Bsat and X. Huang, "Corrosion behaviour of IN625 in superheated steam at 800℃," *Corrosion Engineering, Science and Technology*, vol. 51, no. 5, pp. 321–328, Jul. 2016, number: 5. [Online]. Available: http://www.tandfonline.com/doi/full/10.1080/1478422X.2015.1104064

[59] Y. Mu, C. Wang, W. Zhou, and L. Zhou, "Effect of Nb on δ Phase Precipitation and the Tensile Properties in Cast Alloy IN625," *Metals*, vol. 8, no. 2, p. 86, Jan. 2018, number: 2. [Online]. Available: http://www.mdpi.com/2075-4701/8/2/86

[60] A. Vesel, A. Drenik, K. Elersic, M. Mozetic, J. Kovac, T. Gyergyek, J. Stockel, J. Varju, R. Panek, and M. Balat-Pichelin, "Oxidation of Inconel 625 superalloy upon treatment with oxygen or hydrogen plasma at high temperature," *Applied Surface Science*, vol. 305, pp. 674–682, Jun. 2014. [Online]. Available: https://linkinghub.elsevier.com/retrieve/pii/S0169433214007119

[61] AMS F Corrosion Heat Resistant Alloys Committee, "Heat Treatment Wrought Nickel Alloy and Cobalt Alloy Parts," SAE International, Tech. Rep. [Online]. Available: https://www.sae.org/content/ams2774

[62] M. J. Donachie and S. J. Donachie, *Superalloys: A Technical Guide*, 2nd ed. ASM International, Mar. 2002. [Online]. Available: https://dl.asminternational.org/handbooks/book/106/SuperalloysA-Technical-Guide

[63] TWI - The Welding Institute, "WELDABILITY OF MATERIALS - NICKEL AND NICKEL ALLOYS," Nov. 1996. [Online]. Available: https://www.twi-global.com/technical-knowledge/job-knowledge/weldability-of-materials-nickel-and-nickel-alloys-022

[64] "ASTM F3056-14e1, Standard Specification for Additive Manufacturing Nickel Alloy (UNS N06625) with Powder Bed Fusion„" ASTM International, West Conshohocken, PA, ASTM STANDARD, 2014. [Online]. Available: http://www.astm.org/cgi-bin/resolver.cgi?F3056-14e1

[65] R. Darolia, "Development of strong, oxidation and corrosion resistant nickel-based superalloys: critical review of challenges, progress and prospects," *International Materials Reviews*, vol. 64, no. 6, pp. 355–380, Aug. 2019, number: 6. [Online]. Available: https://www.tandfonline.com/doi/full/10.1080/09506608.2018.1516713

[66] N. Birks, G. H. Meier, and F. S. Pettit, *Introduction to the high-temperature oxidation of metals*, 2nd ed. Cambridge, UK ; New York: Cambridge University Press, 2006.

[67] D. J. Young, *High Temperature Oxidation and Corrosion of Metals*. Elsevier, 2016.

[68] Y. Yang, S. Wen, Q. Wei, W. Li, J. Liu, and Y. Shi, "Effect of scan line spacing on texture, phase and nanohardness of TiAl/TiB2 metal matrix composites fabricated by selective laser melting," *Journal of Alloys and Compounds*, vol. 728, pp. 803–814, Dec. 2017.

[69] K. Sugimoto and Y. Sawada, "The role of molybdenum additions to austenitic stainless steels in the inhibition of pitting in acid chloride solutions," *Corrosion Science*, vol. 17, no. 5, pp. 425–445, Jan. 1977. [Online]. Available: https://linkinghub.elsevier.com/retrieve/pii/0010938X77900324

[70] C. R. Clayton and Y. C. Lu, "A Bipolar Model of the Passivity of Stainless Steel: The Role of Mo Addition," *Journal of The Electrochemical Society*, vol. 133, no. 12, pp. 2465–2473, Dec. 1986. [Online]. Available: https://iopscience.iop.org/article/10.1149/1.2108451

[71] M. Ameer, A. Fekry, and F. E.-T. Heakal, "Electrochemical behaviour of passive films on molybdenum-containing austenitic stainless steels in aqueous solutions," *Electrochimica Acta*, vol. 50, no. 1, pp. 43–49, Nov. 2004. [Online]. Available: https://linkinghub.elsevier.com/retrieve/pii/S0013468604008187

[72] N. Boucherit, A. Hugot-Le Goff, and S. Joiret, "Influence of Ni, Mo, and Cr on Pitting Corrosionof Steels Studied by Raman Spectroscopy," *CORROSION*, vol. 48, no. 7, pp. 569–579, Jul. 1992. [Online]. Available: https://meridian.allenpress.com/corrosion/article/48/7/569/160201/Influence-of-Ni-Mo-and-Cr-on-Pitting-Corrosionof

[73] A. Pardo, M. Merino, A. Coy, F. Viejo, R. Arrabal, and E. Matykina, "Pitting corrosion behaviour of austenitic stainless steels – combining effects of Mn and Mo additions," *Corrosion Science*, vol. 50, no. 6, pp. 1796–1806, Jun. 2008.

[74] L. Wegrelius, F. Falkenberg, and I. Olefjord, "Passivation of Stainless Steels in Hydrochloric Acid," *Journal of The Electrochemical Society*, vol. 146, no. 4, pp. 1397–1406, Apr. 1999. [Online]. Available: https://iopscience.iop.org/article/10.1149/1.1391777

[75] W. Tobler and S. Virtanen, "Effect of Mo species on metastable pitting of Fe18Cr alloys—A current transient analysis," *Corrosion Science*, vol. 48, no. 7, pp. 1585–1607, Jul. 2006. [Online]. Available: https://linkinghub.elsevier.com/retrieve/pii/S0010938X0500185X

[76] A. Schneider, D. Kuron, S. Hofmann, and R. Kirchheim, "AES analysis of pits and passive films formed on Fe□Cr Fe□Mo and Fe□Cr□Mo alloys," *Corrosion Science*, vol. 31, pp. 191–196, Jan. 1990. [Online]. Available: https://linkinghub.elsevier.com/retrieve/pii/0010938X9090107G

[77] M. Liu, W.-j. Zheng, J.-z. Xiang, Z.-g. Song, E.-x. Pu, and H. Feng, "Grain Growth Behavior of Inconel 625 Superalloy," *J. Iron Steel Res. Int.*, vol. 23, no. 10, pp. 1111–1118, Oct. 2016, number: 10. [Online]. Available: http://link.springer.com/10.1016/S1006-706X(16)30164-9

[78] L. Ferrer, B. Pieraggi, and J. Uginet, "Microstructural Evolution During Thermomechanical Processing of Alloy 625," in *Superalloys 718, 625 and Various Derivatives (1991)*. TMS, 1991, pp. 217–228. [Online]. Available: http://www.tms.org/Superalloys/10.7449/1991/Superalloys_1991_217_228.pdf

[79] S. K. Rai, A. Kumar, V. Shankar, T. Jayakumar, K. Bhanu Sankara Rao, and B. Raj, "Characterization of microstructures in Inconel 625 using X-ray diffraction peak broadening and lattice parameter measurements," *Scripta Materialia*, vol. 51, no. 1, pp. 59–63, Jul. 2004. [Online]. Available: https://linkinghub.elsevier.com/retrieve/pii/S1359646204001642

[80] E. Lewis, "Microstructural Characterisation and Oxidation Performance of Additively Manufactured IN625," Masters Dissertation, University of Birmingham, Birmingham, UK, Mar. 2020.

[81] P. Petrzak, K. Kowalski, and M. Blicharski, "Analysis of Phase Transformations in Inconel 625 Alloy during Annealing," *Acta Phys. Pol. A*, vol. 130, no. 4, pp. 1041–1044, Oct. 2016, number: 4. [Online]. Available: http://przyrbwn.icm.edu.pl/APP/PDF/130/a130z4p65.pdf

[82] J. Singh, M. Sundararaman, P. Mukhopadhyay, and N. Prabhu, "Effect of ternary Nb additions on the stability of the D022 structure of the Ni3V phase," *Scripta Materialia*, vol. 48, no. 3, pp. 261–267, Feb. 2003.

[83] E. A. Lass, M. R. Stoudt, M. B. Katz, and M. E. Williams, "Precipitation and dissolution of δ and γ″ during heat treatment of a laser powder-bed fusion produced Ni-based superalloy," *Scripta Materialia*, vol. 154, pp. 83–86, Sep. 2018. [Online]. Available: https://linkinghub.elsevier.com/retrieve/pii/S1359646218303191

[84] D. Liu, X. Zhang, X. Qin, and Y. Ding, "High-temperature mechanical properties of Inconel-625: role of carbides and delta phase," *Materials Science and Technology*, vol. 33, no. 14, pp. 1610–1617, Sep. 2017, number: 14. [Online]. Available: https://www.tandfonline.com/doi/full/10.1080/02670836.2017.1300365

[85] J. B. Singh, A. Verma, B. Paul, and J. K. Chakravartty, "Failure of Alloy 625 tube stub ends – Effect of primary nitrides," *Engineering Failure Analysis*, vol. 32, pp. 236–247, Sep. 2013. [Online]. Available: https://linkinghub.elsevier.com/retrieve/pii/S1350630713001258

[86] F. Cortial, J. M. Corrieu, and C. Vernot-Loier, "Influence of heat treatments on microstructure, mechanical properties, and corrosion resistance of weld alloy 625," *MMTA*, vol. 26, no. 5, pp. 1273–1286, May 1995, number: 5. [Online]. Available: http://link.springer.com/10.1007/BF02670621

[87] U. Heubner and M. Kohler, "Effect of Carbon Content and Other Variables on Yield Strength, Ductility and Creep Properties of Alloy 625," in *Superalloys 718, 625, 706 and Various Derivatives (1994)*. TMS, 1994, pp. 479–488. [Online]. Available: http://www.tms.org/Superalloys/10.7449/1994/Superalloys_1994_479_488.pdf

[88] M. A. Balbaa, M. A. Elbestawi, and J. McIsaac, "An experimental investigation of surface integrity in selective laser melting of Inconel 625," *Int J Adv Manuf Technol*, vol. 104, no. 9-12, pp. 3511–3529, Oct. 2019. [Online]. Available: http://link.springer.com/10.1007/s00170-019-03949-y

[89] K. Inaekyan, A. Kreitcberg, S. Turenne, and V. Brailovski, "Microstructure and mechanical properties of laser powder bed-fused IN625 alloy," *Materials Science and Engineering: A*, vol. 768, p. 138481, Dec. 2019.

[90] A. Kreitcberg, V. Brailovski, and S. Turenne, "Elevated temperature mechanical behavior of IN625 alloy processed by laser powder-bed fusion," *Materials Science and Engineering: A*, vol. 700, pp. 540–553, Jul. 2017. [Online]. Available: https://linkinghub.elsevier.com/retrieve/pii/S0921509317308109

[91] A. Kreitcberg, K. Inaekyan, S. Turenne, and V. Brailovski, "Temperature- and Time-Dependent Mechanical Behavior of Post-Treated IN625 Alloy Processed by Laser Powder Bed Fusion," *JMMP*, vol. 3, no. 3, p. 75, Aug. 2019.

[92] S. Li, Q. Wei, Y. Shi, Z. Zhu, and D. Zhang, "Microstructure Characteristics of Inconel 625 Superalloy Manufactured by Selective Laser Melting," *Journal of Materials Science & Technology*, vol. 31, no. 9, pp. 946–952, Sep. 2015, number: 9. [Online]. Available: https://linkinghub.elsevier.com/retrieve/pii/S1005030215000663

[93] C. Li, Y. Guo, and J. Zhao, "Interfacial phenomena and characteristics between the deposited material and substrate in selective laser melting Inconel 625," *Journal of Materials Processing Technology*, vol. 243, pp. 269–281, May 2017. [Online]. Available: https://linkinghub.elsevier.com/retrieve/pii/S0924013616304769

[94] G. Marchese, X. Garmendia Colera, F. Calignano, M. Lorusso, S. Biamino, P. Minetola, and D. Manfredi, "Characterization and Comparison of Inconel 625 Processed by Selective Laser Melting and Laser Metal Deposition: Comparison of Inconel 625 processed by SLM and LMD," *Adv. Eng. Mater.*, vol. 19, no. 3, p. 1600635, Mar. 2017, number: 3. [Online]. Available: https://onlinelibrary.wiley.com/doi/10.1002/adem.201600635

[95] I. Roberts, C. Wang, R. Esterlein, M. Stanford, and D. Mynors, "A three-dimensional finite element analysis of the temperature field during laser melting of metal powders in additive layer manufacturing," *International Journal of Machine Tools and Manufacture*, vol. 49, no. 12-13, pp. 916–923, Oct. 2009.

[96] D. Wang, C. Song, Y. Yang, and Y. Bai, "Investigation of crystal growth mechanism during selective laser melting and mechanical property characterization of 316L stainless steel parts," *Materials & Design*, vol. 100, pp. 291–299, Jun. 2016.

[97] T. DebRoy, H. Wei, J. Zuback, T. Mukherjee, J. Elmer, J. Milewski, A. Beese, A. Wilson-Heid, A. De, and W. Zhang, "Additive manufacturing of metallic components – Process, structure and properties," *Progress in Materials Science*, vol. 92, pp. 112–224, Mar. 2018.

[98] C. Örnek, "Additive manufacturing – a general corrosion perspective," *Corrosion Engineering, Science and Technology*, vol. 53, no. 7, pp. 531–535, Oct. 2018, number: 7. [Online]. Available: https://www.tandfonline.com/doi/full/10.1080/1478422X.2018.1511327

[99] X. Fang, H. Li, M. Wang, C. Li, and Y. Guo, "Characterization of texture and grain boundary character distributions of selective laser melted Inconel 625 alloy," *Materials Characterization*, vol. 143, pp. 182–190, Sep. 2018. [Online]. Available: https://linkinghub.elsevier.com/retrieve/pii/S1044580317331583

[100] M. Balbaa, A. Ghasemi, E. Fereiduni, K. Al-Rubaie, and M. Elbestawi, "Improvement of fatigue performance of laser powder bed fusion fabricated IN625 and IN718 superalloys via shot peening," *Journal of Materials Processing Technology*, vol. 304, p. 117571, Jun. 2022.

[101] M. J. Anderson, J. Benson, J. W. Brooks, B. Saunders, and H. C. Basoalto, "Predicting Precipitation Kinetics During the Annealing of Additive Manufactured Inconel 625 Components," *Integr Mater Manuf Innov*, vol. 8, no. 2, pp. 154–166, Jun. 2019. [Online]. Available: http://link.springer.com/10.1007/s40192-019-00134-7

[102] S. Ghosh, M. R. Stoudt, L. E. Levine, and J. E. Guyer, "Formation of Nb-rich droplets in laser deposited Ni-matrix microstructures," *Scripta Materialia*, vol. 146, pp. 36–40, Mar. 2018. [Online]. Available: https://linkinghub.elsevier.com/retrieve/pii/S1359646217306309

[103] C. Miller, G. Simmons, and R. Wei, "Mechanism for oxygen enhanced crack growth in inconel 718," *Scripta Materialia*, vol. 44, no. 10, pp. 2405–2410, May 2001.

[104] A. Kreitcberg, V. Brailovski, and S. Turenne, "Effect of heat treatment and hot isostatic pressing on the microstructure and mechanical properties of Inconel 625 alloy processed by laser powder bed fusion," *Materials Science and Engineering: A*, vol. 689, pp. 1–10, Mar. 2017.

[105] Y. Li, H. Qi, H. Hou, and L. Lei, "Effects of Hot Isostatic Pressing on Microstructure and Mechanical Properties of Hastelloy X Samples Produced by Selective Laser Melting," in *Proceedings of the Second International Conference on Mechanics, Materials and Structural Engineering (ICMMSE 2017)*. Beijing, China: Atlantis Press, 2017. [Online]. Available: http://www.atlantis-press.com/php/paper-details.php?id=25881559

[106] Q. B. Nguyen, M. L. S. Nai, Z. Zhu, C.-N. Sun, J. Wei, and W. Zhou, "Characteristics of inconel powders for powder-bed additive manufacturing," *Engineering*, vol. 3, no. 5, pp. 695–700, 2017.

[107] L. N. Carter, C. Martin, P. J. Withers, and M. M. Attallah, "The influence of the laser scan strategy on grain structure and cracking behaviour in SLM powder-bed fabricated nickel superalloy," *Journal of Alloys and Compounds*, vol. 615, pp. 338–347, Dec. 2014. [Online]. Available: https://linkinghub.elsevier.com/retrieve/pii/S092583881401528X

[108] T. De Terris, O. Castelnau, Z. Hadjem-Hamouche, H. Haddadi, V. Michel, and P. Peyre, "Analysis of As-Built Microstructures and Recrystallization Phenomena on Inconel 625 Alloy Obtained via Laser Powder Bed Fusion (L-PBF)," *Metals*, vol. 11, no. 4, p. 619, Apr. 2021, number: 4. [Online]. Available: https://www.mdpi.com/2075-4701/11/4/619

[109] H. Xiao, S. Li, W. Xiao, Y. Li, L. Cha, J. Mazumder, and L. Song, "Effects of laser modes on Nb segregation and Laves phase formation during laser additive manufacturing of nickel-based superalloy," *Materials Letters*, vol. 188, pp. 260–262, Feb. 2017. [Online]. Available: https://linkinghub.elsevier.com/retrieve/pii/S0167577X16317323

[110] S. Cooke, K. Ahmadi, S. Willerth, and R. Herring, "Metal additive manufacturing: Technology, metallurgy and modelling," *Journal of Manufacturing Processes*, vol. 57, pp. 978–1003, Sep. 2020. [Online]. Available: https://linkinghub.elsevier.com/retrieve/pii/S1526612520304503

[111] L. N. Carter, X. Wang, N. Read, R. Khan, M. Aristizabal, K. Essa, and M. M. Attallah, "Process optimisation of selective laser melting using energy density model for nickel based superalloys," *Materials Science and Technology*, vol. 32, no. 7, pp. 657–661, May 2016. [Online]. Available: http://journals.sagepub.com/doi/10.1179/1743284715Y.0000000108

[112] K. Amato, "Comparison of Microstructures and Properties for a Ni-Base Superalloy (Alloy 625) Fabricated by Electron Beam Melting," *JMSR*, vol. 1, no. 2, p. p3, Mar. 2012. [Online]. Available: http://www.ccsenet.org/journal/index.php/jmsr/article/view/14963

[113] J. Gonzalez, J. Mireles, S. Stafford, M. Perez, C. Terrazas, and R. Wicker, "Characterization of Inconel 625 fabricated using powder-bed-based additive manufacturing technologies," *Journal of Materials Processing Technology*, vol. 264, pp. 200–210, Feb. 2019.

[114] L. Qin, C. Chen, M. Zhang, K. Yan, G. Cheng, H. Jing, and X. Wang, "The microstructure and mechanical properties of deposited-IN625 by laser additive manufacturing," *Rapid*

Prototyping Journal, vol. 23, no. 6, pp. 1119–1129, Oct. 2017. [Online]. Available: https://www.emerald.com/insight/content/doi/10.1108/RPJ-05-2016-0081/full/html

[115] L. Chen, Y. Sun, L. Li, and X. Ren, "Effect of heat treatment on the microstructure and high temperature oxidation behavior of TiC/Inconel 625 nanocomposites fabricated by selective laser melting," *Corrosion Science*, vol. 169, p. 108606, Jun. 2020. [Online]. Available: https://linkinghub.elsevier.com/retrieve/pii/S0010938X19325120

[116] F. Zhang, L. E. Levine, A. J. Allen, C. E. Campbell, E. A. Lass, S. Cheruvathur, M. R. Stoudt, M. E. Williams, and Y. Idell, "Homogenization kinetics of a nickel-based superalloy produced by powder bed fusion laser sintering," *Scripta Materialia*, vol. 131, pp. 98–102, Apr. 2017. [Online]. Available: https://linkinghub.elsevier.com/retrieve/pii/S1359646216306224

[117] H. Hyer, R. Newell, D. Matejczyk, S. Hsie, M. Anthony, L. Zhou, C. Kammerer, and Y. Sohn, "Microstructural Development in As Built and Heat Treated IN625 Component Additively Manufactured by Laser Powder Bed Fusion," *J. Phase Equilib. Diffus.*, vol. 42, no. 1, pp. 14–27, Feb. 2021, number: 1. [Online]. Available: http://link.springer.com/10.1007/s11669-020-00855-9

[118] K. Gola, B. Dubiel, and I. Kalemba-Rec, "Microstructural Changes in Inconel 625 Alloy Fabricated by Laser-Based Powder Bed Fusion Process and Subjected to High-Temperature Annealing," *J. of Materi Eng and Perform*, vol. 29, no. 3, pp. 1528–1534, Mar. 2020, number: 3. [Online]. Available: http://link.springer.com/10.1007/s11665-020-04605-3

[119] G. Marchese, G. Basile, E. Bassini, A. Aversa, M. Lombardi, D. Ugues, P. Fino, and S. Biamino, "Study of the Microstructure and Cracking Mechanisms of Hastelloy X Produced by Laser Powder Bed Fusion," *Materials*, vol. 11, no. 1, p. 106, Jan. 2018, number: 1. [Online]. Available: https://www.mdpi.com/1996-1944/11/1/106

[120] L. E. Murr, S. M. Gaytan, D. A. Ramirez, E. Martinez, J. Hernandez, K. N. Amato, P. W. Shindo, F. R. Medina, and R. B. Wicker, "Metal Fabrication by Additive Manufacturing Using Laser and Electron Beam Melting Technologies," *Journal of Materials Science & Technology*, vol. 28, no. 1, pp. 1–14, Jan. 2012.

[121] Z. Tian, C. Zhang, D. Wang, W. Liu, X. Fang, D. Wellmann, Y. Zhao, and Y. Tian, "A review on laser powder bed fusion of inconel 625 nickel-based alloy," *Applied Sciences*, vol. 10, no. 1, p. 81, 2019.

[122] "AMS2774E, Aerospace Material Specification, Heat Treatment Wrought Nickel Alloy and Cobalt Alloy Parts," Jan. 2016.

[123] G. Dey, S. Albert, D. Srivastava, M. Sundararaman, and P. Mukhopadhyay, "Microstructural studies on rapidly solidified inconel 625," *Materials Science and Engineering: A*, vol. 119, pp. 175–184, Nov. 1989. [Online]. Available: https://linkinghub.elsevier.com/retrieve/pii/0921509389905376

[124] L. Mataveli Suave, J. Cormier, P. Villechaise, A. Soula, Z. Hervier, D. Bertheau, and J. Laigo, "Microstructural evolutions during thermal aging of alloy 625: Impact of temperature and forming process," *Metallurgical and Materials Transactions A*, vol. 45, pp. 2963–2982, 02 2014.

[125] D. Zhang, W. Niu, X. Cao, and Z. Liu, "Effect of standard heat treatment on the microstructure and mechanical properties of selective laser melting manufactured Inconel 718 superalloy," *Materials Science and Engineering: A*, vol. 644, pp. 32–40, Sep. 2015. [Online]. Available: https://linkinghub.elsevier.com/retrieve/pii/S0921509315300745

[126] H. Hyer, L. Zhou, S. Park, G. Gottsfritz, G. Benson, B. Tolentino, B. McWilliams, K. Cho, and Y. Sohn, "Understanding the Laser Powder Bed Fusion of AlSi10Mg Alloy," *Metallography, Microstructure, and Analysis*, vol. 9, no. 4, pp. 484–502, Aug. 2020. [Online]. Available: https://link.springer.com/10.1007/s13632-020-00659-w

[127] X. Pang, D. Dwyer, M. Gao, P. Valerio, and R. Wei, "Surface enrichment and grain boundary segregation of niobium in inconel 718 single- and poly-crystals," *Scripta Metallurgica et Materialia*, vol. 31, no. 3, pp. 345–350, Aug. 1994, number: 3. [Online]. Available: https://linkinghub.elsevier.com/retrieve/pii/0956716X94902941

[128] Y.-J. Kang, S. Yang, Y.-K. Kim, B. AlMangour, and K.-A. Lee, "Effect of post-treatment on the microstructure and high-temperature oxidation behaviour of additively manufactured inconel 718 alloy," *Corrosion Science*, vol. 158, p. 108082, Sep. 2019. [Online]. Available: https://linkinghub.elsevier.com/retrieve/pii/S0010938X1930109X

[129] Z. Khayat and T. Palmer, "Impact of iron composition on the properties of an additively manufactured solid solution strengthened nickel base alloy," *Materials Science and Engineering: A*, vol. 718, pp. 123–134, Mar. 2018.

[130] J. Zuback, P. Moradifar, Z. Khayat, N. Alem, and T. Palmer, "Impact of chemical composition on precipitate morphology in an additively manufactured nickel base superalloy," *Journal of Alloys and Compounds*, vol. 798, pp. 446–457, Aug. 2019.

[131] Y. Gao, Y. Ding, J. Chen, J. Xu, Y. Ma, and X. Wang, "Effect of twin boundaries on the microstructure and mechanical properties of Inconel 625 alloy," *Materials*

Science and Engineering: A, vol. 767, p. 138361, Nov. 2019. [Online]. Available: https://linkinghub.elsevier.com/retrieve/pii/S0921509319311475

[132] K. Mumtaz and N. Hopkinson, "Top surface and side roughness of Inconel 625 parts processed using selective laser melting," *Rapid Prototyping Journal*, vol. 15, no. 2, pp. 96–103, Mar. 2009. [Online]. Available: https://www.emerald.com/insight/content/doi/10.1108/13552540910943397/full/html

[133] U. Ali, H. Fayazfar, F. Ahmed, and E. Toyserkani, "Internal surface roughness enhancement of parts made by laser powder-bed fusion additive manufacturing," *Vacuum*, vol. 177, p. 109314, Jul. 2020. [Online]. Available: https://linkinghub.elsevier.com/retrieve/pii/S0042207X20301512

[134] A. Diaz, J. Michaud, T. Mikulas, J. Boykin, N. Shamsaei, S. Shao, S. J. Lee, J. Pegues, T. Hall, J. Stull, T. S. Duffy, A. J. Mirabal, and P. Gradl, "Surface post-treatment of additively manufactured components," in *Additive Manufacturing of High-Performance Metallic Materials*. Elsevier, 2024, pp. 223–283.

[135] D. J. Young, "Alloy Oxidation II," in *High Temperature Oxidation and Corrosion of Metals*. Elsevier, 2016, pp. 261–333. [Online]. Available: https://linkinghub.elsevier.com/retrieve/pii/B9780081001011000066

[136] P. Edwards and M. Ramulu, "Fatigue performance evaluation of selective laser melted Ti–6Al–4V," *Materials Science and Engineering: A*, vol. 598, pp. 327–337, Mar. 2014.

[137] M. Kahlin, H. Ansell, D. Basu, A. Kerwin, L. Newton, B. Smith, and J. Moverare, "Improved fatigue strength of additively manufactured Ti6Al4V by surface post processing," *International Journal of Fatigue*, vol. 134, p. 105497, May 2020.

[138] H. Niu and I. Chang, "Liquid phase sintering of m3/2 high speed steel by selective laser sintering," *Scripta Materialia*, vol. 39, no. 1, pp. 67–72, 1998.

[139] D. Jiang, Y. Tian, Y. Zhu, and A. Huang, "Investigation of surface roughness post-processing of additively manufactured nickel-based superalloy Hastelloy X using electropolishing," *Surface and Coatings Technology*, vol. 441, p. 128529, Jul. 2022.

[140] V. Urlea and V. Brailovski, "Electropolishing and electropolishing-related allowances for powder bed selectively laser-melted Ti-6Al-4V alloy components," *Journal of Materials Processing Technology*, vol. 242, pp. 1–11, Apr. 2017.

[141] Z. Baicheng, L. Xiaohua, B. Jiaming, G. Junfeng, W. Pan, S. Chen-nan, N. Muiling, Q. Guojun, and W. Jun, "Study of selective laser melting (SLM) Inconel 718 part surface improvement by electrochemical polishing," *Materials & Design*, vol. 116, pp. 531–537, Feb. 2017.

[142] D. Caplan and G. I. Sproule, "Effect of oxide grain structure on the high-temperature oxidation of Cr," *Oxidation of Metals*, vol. 9, no. 5, pp. 459–472, Oct. 1975. [Online]. Available: http://link.springer.com/10.1007/BF00611694

[143] K. Small, D. Englehart, and T. Christman, "Guide to etching specialty alloys," *Advanced Materials and Processes*, vol. 166, pp. 32–37, 02 2008.

[144] Q. Jia and D. Gu, "Selective laser melting additive manufactured Inconel 718 superalloy parts: High-temperature oxidation property and its mechanisms," *Optics & Laser Technology*, vol. 62, pp. 161–171, Oct. 2014. [Online]. Available: https://linkinghub.elsevier.com/retrieve/pii/S0030399214000632

[145] S. Jain, M. Corliss, B. Tai, and W. N. Hung, "Electrochemical polishing of selective laser melted Inconel 718," *Procedia Manufacturing*, vol. 34, pp. 239–246, 2019.

[146] K. M. Ajmal, R. Yi, Z. Zhan, J. Ji, L. Zhang, and H. Deng, "A novel finishing approach for 3D printed inconel 718 by utilizing isotropic electrochemical etching," *Journal of Materials Processing Technology*, vol. 299, p. 117356, Jan. 2022.

[147] C. A. Huang and Y. C. Chen, "The effect of water content on the electropolishing behavior of Inconel 718 alloy in perchloric–acetic acid mixtures," *Corrosion Science*, vol. 51, no. 9, pp. 1901–1906, Sep. 2009.

[148] Mohammadian, Turenne, and Brailovski, "Electropolishing of Laser Powder Bed-Fused IN625 Components in an Ionic Electrolyte," *Journal of Manufacturing and Materials Processing*, vol. 3, no. 4, p. 86, Oct. 2019. [Online]. Available: https://www.mdpi.com/2504-4494/3/4/86

[149] S. Cruchley, "The oxidation damage of Ni-based superalloy, RR1000, with different surface modifications and the role of oxidation in fatigue crack initiation," Ph.D. dissertation, University of Birmingham, School of Metallurgy and Materials, 2015.

[150] D. A. Lesyk, V. V. Dzhemelinskyi, S. Martinez, B. N. Mordyuk, and A. Lamikiz, "Surface Shot Peening Post-processing of Inconel 718 Alloy Parts Printed by Laser Powder Bed Fusion Additive Manufacturing," *Journal of Materials Engineering and Performance*, vol. 30, no. 9, pp. 6982–6995, Sep. 2021.

[151] William W. Wellborn, "Fundamentals of Mass Finishing," *Products Finishing*, pp. 46–50, Dec. 1995. [Online]. Available: https://www.nmfrc.org/pdf/212954.pdf

[152] Clive Ponton, "Environmental Degradation of Materials - Lectures 1 - 19," School of Metallurgy and Materials University of Birmingham, 2018.

[153] D. R. Gaskell, *Introduction to the thermodynamics of materials*, 4th ed. New York: Taylor & Francis, 2003.

[154] G. Calvarin, A. Huntz, A. Hugot Le Goff, S. Joiret, and M. Bernard, "Oxide Scale Stress Determination by Raman Spectroscopy Application to the NiCr/Cr2O3 System and Influence of Yttrium," *Scripta Materialia*, vol. 38, no. 11, pp. 1649–1658, May 1998. [Online]. Available: https://linkinghub.elsevier.com/retrieve/pii/S1359646298000797

[155] A. Huntz, "Stresses in NiO, Cr2O3 and Al2O3 oxide scales," *Materials Science and Engineering: A*, vol. 201, no. 1-2, pp. 211–228, Oct. 1995. [Online]. Available: https://linkinghub.elsevier.com/retrieve/pii/092150939409747X

[156] S. Cruchley, H. Evans, M. Taylor, M. Hardy, and S. Stekovic, "Chromia layer growth on a Ni-based superalloy: Sub-parabolic kinetics and the role of titanium," *Corrosion Science*, vol. 75, pp. 58–66, Oct. 2013. [Online]. Available: https://linkinghub.elsevier.com/retrieve/pii/S0010938X13002187

[157] H. E. Evans, "Stress effects in high temperature oxidation of metals," *International Materials Reviews*, vol. 40, no. 1, pp. 1–40, Jan. 1995. [Online]. Available: http://www.tandfonline.com/doi/full/10.1179/imr.1995.40.1.1

[158] N.B. Pilling, R. E. Bedworth, "The Oxidation of Metals at High Temperatures," *J. Inst. Met*, vol. 29, pp. 529–591, 1923.

[159] H. Evans and M. Taylor, "Creep relaxation and the spallation of oxide layers," *Surface and Coatings Technology*, vol. 94-95, pp. 27–33, Oct. 1997. [Online]. Available: https://linkinghub.elsevier.com/retrieve/pii/S0257897297004714

[160] P. Hancock and R. C. Hurst, *The Mechanical Properties and Breakdown of Surface Oxide Films at Elevated Temperatures*. Boston, MA: Springer US, 1974, pp. 1–84.

[161] S. Daghigh, A. M. Huntz, and J. L. Lebrun, Ph.D. dissertation, Paris XI University, Mat. Sci. Eng., 1996.

[162] H. E. Evans, "Spallation of oxide from stainless steel AGR nuclear fuel cladding: mechanisms and consequences," *Materials Science and Technology*, vol. 4, no. 5, pp. 414–420, May 1988. [Online]. Available: http://www.tandfonline.com/doi/full/10.1179/mst.1988.4.5.414

[163] J. Brenneman, J. Wei, Z. Sun, L. Liu, G. Zou, and Y. Zhou, "Oxidation behavior of GTD111 Ni-based superalloy at 900 ℃ in air," *Corrosion Science*, vol. 100, pp. 267–274, Nov. 2015.

[164] Y. Xie, T. D. Nguyen, J. Zhang, and D. J. Young, "Corrosion behaviour of Ni-Cr alloys in wet CO2 atmosphere at 700 and 800 ℃," *Corrosion Science*, vol. 146, pp. 28–43, Jan. 2019.

[165] "High Temp Metals - Inconel 625 Technical Data," 2015. [Online]. Available: https://www.hightempmetals.com/techdata/hitempInconel625data.php#5

[166] K. Wang, D. Du, G. Liu, Z. Pu, B. Chang, and J. Ju, "High-temperature oxidation behaviour of high chromium superalloys additively manufactured by conventional or extreme high-speed laser metal deposition," *Corrosion Science*, vol. 176, p. 108922, Nov. 2020. [Online]. Available: https://linkinghub.elsevier.com/retrieve/pii/S0010938X20311641

[167] M. Guerain, J.-L. Grosseau-Poussard, G. Geandier, B. Panicaud, N. Tamura, M. Kunz, C. Dejoie, J.-S. Micha, D. Thiaudière, and P. Goudeau, "Residual stress determination in oxide layers at different length scales combining Raman spectroscopy and X-ray diffraction: Application to chromia-forming metallic alloys," *Journal of Applied Physics*, vol. 122, no. 19, p. 195105, Nov. 2017. [Online]. Available: http://aip.scitation.org/doi/10.1063/1.4990146

[168] B. Barnard, P. Liaw, R. Buchanan, and D. Klarstrom, "Affects of applied stresses on the isothermal and cyclic high-temperature oxidation behavior of superalloys," *Materials Science and Engineering: A*, vol. 527, no. 16-17, pp. 3813–3821, Jun. 2010, number: 16-17. [Online]. Available: https://linkinghub.elsevier.com/retrieve/pii/S0921509310003242

[169] J. G. Goedjen, J. H. Stout, Q. Guob, and D. A. Shores, "Evaluation of stresses in Ni□NiO and Cr□Cr2O3 during high temperature oxidation by in situ X-ray diffraction," *Materials Science and Engineering: A*, vol. 177, no. 1-2, pp. 115–124, Apr. 1994. [Online]. Available: https://linkinghub.elsevier.com/retrieve/pii/0921509394904839

[170] P. Hou and J. Stringer, "Room temperature strains in Cr2O3 scales formed at elevated temperatures on Ni-25wt%Cr and y- and Al-doped Ni-25wt%Cr," *Acta Metallurgica et Materialia*, vol. 39, no. 5, pp. 841–849, May 1991. [Online]. Available: https://linkinghub.elsevier.com/retrieve/pii/0956715191902848

[171] M. Kemdehoundja, J. Dinhut, J. Grosseau-Poussard, and M. Jeannin, "High temperature oxidation of Ni70Cr30 alloy: Determination of oxidation kinetics and stress evolution in chromia layers by Raman spectroscopy," *Materials Science and Engineering: A*, vol. 435-436, pp. 666–671, Nov. 2006. [Online]. Available: https://linkinghub.elsevier.com/retrieve/pii/S0921509306014766

[172] M. Fitzpatrick, A. Fry, P. Holdway, F. A. Kandil, J. Shackleton, and L. Suominen, "A NATIONAL MEASUREMENT GOOD PRACTICE GUIDE, No. 52, Determination of Residual Stresses by X-ray Diffraction - Issue 2." [Online]. Available: https://www.npl.co.uk/gpgs/residual-stresses-xray-diffraction

[173] V. B. Trindade and U. Krupp, "High-temperature intergranular oxidation of Ni-based alloys using EBSD," *Tecnologia em Metalurgia Materiais e Mineração*, vol. 14, no. 4, pp. 303–307, 2017, number: 4. [Online]. Available: http://tecnologiammm.com.br/doi/10.4322/2176-1523.1156

[174] R. Verma and G. Kaushal, "High temperature oxidation behavior and characterization of DMLS fabricated Ni based superalloys," *Materials Today: Proceedings*, vol. 62, pp. 7364–7372, 2022. [Online]. Available: https://linkinghub.elsevier.com/retrieve/pii/S2214785322006447

[175] M. Sharifitabar, S. Khorshahian, M. Shafiee Afarani, P. Kumar, and N. K. Jain, "High-temperature oxidation performance of Inconel 625 superalloy fabricated by wire arc additive manufacturing," *Corrosion Science*, vol. 197, p. 110087, Apr. 2022. [Online]. Available: https://linkinghub.elsevier.com/retrieve/pii/S0010938X22000051

[176] C. Juillet, A. Oudriss, J. Balmain, X. Feaugas, and F. Pedraza, "Characterization and oxidation resistance of additive manufactured and forged IN718 Ni-based superalloys," *Corrosion Science*, vol. 142, pp. 266–276, Sep. 2018. [Online]. Available: https://linkinghub.elsevier.com/retrieve/pii/S0010938X18303330

[177] H. Buscail, S. Perrier, and C. Josse, "Oxidation mechanism of the Inconel 601 alloy at high temperatures: Oxidation mechanism of Inconel 601 alloy," *Materials and Corrosion*, vol. 62, no. 5, pp. 416–422, May 2011.

[178] Eric Whitney, George Simkovich, and Jeremy Fink, "HIGH TEMPERATURE OXIDATION OF A MODIFIED ALLOY 625," in *Superalloys 718, 625, 706 and Various Derivatives*. The Minerals, Metals & Materials Society; Illustrated edition (30 Jun. 1994), 1997, pp. 695–704.

[179] Katarzyna Staszewska, "MECHANISM AND KINETICS OXIDATION OF INCONEL 617 AND 625 ALLOYS," *Technical Issues 1/2016*, pp. pp. 82–89, 2016.

[180] H. E. Evans, A. T. Donaldson, and T. C. Gilmour, "Mechanisms of Breakaway Oxidation and Application to a Chromia-Forming Steel," *Oxidation of Metals*, vol. 52, no. 5/6, pp. 379–402, 1999. [Online]. Available: http://link.springer.com/10.1023/A:1018855914737

[181] K. A. Al-Hatab, M. A. Al-Bukhaiti, U. Krupp, and M. Kantehm, "Cyclic Oxidation Behavior of IN 718 Superalloy in Air at High Temperatures," *Oxid Met*, vol. 75, no. 3-4, pp. 209–228, Apr. 2011, number: 3-4. [Online]. Available: http://link.springer.com/10.1007/s11085-010-9230-6

[182] G. A. Greene and C. C. Finfrock, "Oxidation of Inconel 718 in air at high temperatures," *Oxidation of Metals*, vol. 55, no. 5/6, pp. 505–521, 2001, number: 5/6. [Online]. Available: http://link.springer.com/10.1023/A:1010359815550

[183] M. Romedenne, R. Pillai, M. Kirka, and S. Dryepondt, "High temperature air oxidation behavior of Hastelloy X processed by Electron Beam Melting (EBM) and Selective Laser Melting (SLM)," *Corrosion Science*, vol. 171, p. 108647, Jul. 2020. [Online]. Available: https://linkinghub.elsevier.com/retrieve/pii/S0010938X20302304

[184] J. L. Evans, "Effect of Surface Roughness on the Oxidation Behavior of the Ni-Base Superalloy ME3," *J. of Materi Eng and Perform*, vol. 19, no. 7, pp. 1001–1004, Oct. 2010. [Online]. Available: http://link.springer.com/10.1007/s11665-010-9605-5

[185] F. Delaunay, C. Berthier, M. Lenglet, and J.-M. Lameille, "SEM-EDS and XPS Studies of the High Temperature Oxidation Behaviour of Inconel 718," *Mikrochim Acta*, vol. 132, no. 2-4, pp. 337–343, Apr. 2000, number: 2-4. [Online]. Available: http://link.springer.com/10.1007/s006040050027

[186] M. Lenglet, F. Delaunay, and B. Lefez, "FTIR Study of the Influence of Minor Alloying Elements on the High Temperature Oxidation of Nickel Alloys," *MSF*, vol. 251-254, pp. 267–274, Oct. 1997. [Online]. Available: https://www.scientific.net/MSF.251-254.267

[187] T. Sanviemvongsak, D. Monceau, and B. Macquaire, "High temperature oxidation of IN 718 manufactured by laser beam melting and electron beam melting: Effect of surface topography," *Corrosion Science*, vol. 141, pp. 127–145, Aug. 2018. [Online]. Available: https://linkinghub.elsevier.com/retrieve/pii/S0010938X18300702

[188] D. Kim, C. Jang, and W. S. Ryu, "Oxidation Characteristics and Oxide Layer Evolution of Alloy 617 and Haynes 230 at 900 ℃ and 1100 ℃," *Oxidation of Metals*, vol. 71, no. 5-6, pp. 271–293, Jun. 2009.

[189] F. H. Stott, F. I. Wei, and C. A. Enahoro, "The influence of manganese on the High-temperature oxidation of iron-chromium alloys," *Materials and Corrosion*, vol. 40, no. 4, pp. 198–205, Apr. 1989, number: 4. [Online]. Available: https://onlinelibrary.wiley.com/doi/10.1002/maco.19890400403

[190] W. E. Moddeman, S. M. Craven, and D. P. Kramer, "Ni3Nb alloy species in oxide surfaces of INCONEL 718," *MTA*, vol. 17, no. 2, pp. 351–355, Feb. 1986, number: 2. [Online]. Available: http://link.springer.com/10.1007/BF02643913

[191] E. Lewis, M. Taylor, B. Attard, N. Cruchley, A. Morrison, M. Attallah, and S. Cruchley, "Microstructural characterisation and high-temperature oxidation of laser powder bed fusion processed Inconel 625," *Materials Letters*, vol. 311, p. 131582, Mar. 2022. [Online]. Available: https://linkinghub.elsevier.com/retrieve/pii/S0167577X21022813

[192] W. Nowak, "Effect of Surface Roughness on Early Stage Oxidation Behavior of Ni-Base Superalloy IN 625," *ASI*, vol. 1, no. 3, p. 32, Aug. 2018, number: 3. [Online]. Available: https://www.mdpi.com/2571-5577/1/3/32

[193] P. Elliott and A. F. Hampton, "The influence of ternary additions of W, Mo, Ti, Ta, and Nb on the isothermal and cyclic oxidation of Ni-10Cr alloy," *Oxid Met*, vol. 14, no. 5, pp. 449–468, Oct. 1980. [Online]. Available: https://link.springer.com/10.1007/BF00603612

[194] C. Desgranges, F. Lequien, E. Aublant, M. Nastar, and D. Monceau, "Depletion and Voids Formation in the Substrate During High Temperature Oxidation of Ni–Cr Alloys," *Oxid Met*, vol. 79, no. 1-2, pp. 93–105, Feb. 2013, number: 1-2. [Online]. Available: http://link.springer.com/10.1007/s11085-012-9328-0

[195] V. Trindade, H.-J. Christ, and U. Krupp, "Grain-Size Effects on the High-Temperature Oxidation Behaviour of Chromium Steels," *Oxid Met*, vol. 73, no. 5-6, pp. 551–563, Jun. 2010, number: 5-6. [Online]. Available: http://link.springer.com/10.1007/s11085-010-9192-8

[196] A. Chyrkin, W. Nowak, K. Gunduz, I. Fedorova, M. Sattari, J. Froitzheim, M. Halvarsson, and K. Stiller, "Intergranular oxidation of additively manufactured Ni-base alloy 625: The role of Si," *Corrosion Science*, vol. 219, p. 111234, Jul. 2023.

[197] J. Froitzheim, G. Meier, L. Niewolak, P. Ennis, H. Hattendorf, L. Singheiser, and W. Quadakkers, "Development of high strength ferritic steel for interconnect application in SOFCs," *Journal of Power Sources*, vol. 178, no. 1, pp. 163–173, Mar. 2008.

[198] W. J. Quadakkers, "Growth mechanisms of oxide scales on ODS alloys in the temperature range 1000-1100℃," *Materials and Corrosion*, vol. 41, no. 12, pp. 659–668, Dec. 1990, number: 12. [Online]. Available: https://onlinelibrary.wiley.com/doi/10.1002/maco.19900411204

[199] A. Leon, A. Shirizly, and E. Aghion, "Corrosion Behavior of AlSi10Mg Alloy Produced by Additive Manufacturing (AM) vs. Its Counterpart Gravity Cast Alloy," *Metals*, vol. 6, no. 7, p. 148, Jun. 2016.

[200] T. D. Reynolds, M. P. Taylor, D. J. Child, and H. E. Evans, "The effect of elevated air pressure on the oxidation properties of the nickel-based superalloy, RR1000, at 650℃ with different surface modifications," *Materials at High Temperatures*, vol. 35, no. 1-3, pp. 130–140, May 2018, number: 1-3. [Online]. Available: https://www.tandfonline.com/doi/full/10.1080/09603409.2017.1389132

[201] J. Panter, B. Viguier, J.-M. Cloué, M. Foucault, P. Combrade, and E. Andrieu, "Influence of oxide films on primary water stress corrosion cracking initiation of alloy 600," *Journal of Nuclear Materials*, vol. 348, no. 1-2, pp. 213–221, Jan. 2006.

[202] T. Kim, K. J. Choi, S. C. Yoo, and J. H. Kim, "Effects of dissolved hydrogen on the crack-initiation and oxidation behavior of nickel-based alloys in high-temperature water," *Corrosion Science*, vol. 106, pp. 260–270, May 2016.

[203] T. Allen, Y. Chen, X. Ren, K. Sridharan, L. Tan, G. Was, E. West, and D. Guzonas, "Material Performance in Supercritical Water," in *Comprehensive Nuclear Materials*. Elsevier, 2012, pp. 279–326.

[204] K.-H. Chang, S.-M. Chen, T.-K. Yeh, and J.-J. Kai, "Effect of dissolved oxygen content on the oxide structure of Alloy 625 in supercritical water environments at 700℃," *Corrosion Science*, vol. 81, pp. 21–26, Apr. 2014.

[205] M. Sennour, L. Marchetti, F. Martin, S. Perrin, R. Molins, and M. Pijolat, "A detailed TEM and SEM study of Ni-base alloys oxide scales formed in primary conditions of pressurized water reactor," *Journal of Nuclear Materials*, vol. 402, no. 2-3, pp. 147–156, Jul. 2010.

[206] Y. Behnamian, A. Mostafaei, A. Kohandehghan, B. S. Amirkhiz, D. Serate, Y. Sun, S. Liu, E. Aghaie, Y. Zeng, M. Chmielus, W. Zheng, D. Guzonas, W. Chen, and J. L. Luo, "A comparative study of oxide scales grown on stainless steel and nickel-based superalloys in ultra-high temperature supercritical water at 800 ℃," *Corrosion Science*, vol. 106, pp. 188–207, May 2016.

[207] L. Chang, M. G. Burke, and F. Scenini, "Stress corrosion crack initiation in machined type 316L austenitic stainless steel in simulated pressurized water reactor primary water," *Corrosion Science*, vol. 138, pp. 54–65, Jul. 2018.

[208] J. Robertson and M. I. Manning, "Limits to adherence of oxide scales," *Materials Science and Technology*, vol. 6, no. 1, pp. 81–92, Jan. 1990. [Online]. Available: http://www.tandfonline.com/doi/full/10.1179/mst.1990.6.1.81

[209] J. Robertson, "The mechanism of high temperature aqueous corrosion of stainless steels," *Corrosion Science*, vol. 32, no. 4, pp. 443–465, Jan. 1991.

[210] R. Fujisawa, K. Nishimura, T. Nishida, M. Sakaihara, Y. Kurata, and Y. Watanabe, "Corrosion Behavior of Nickel-Based Alloys and Type 316 Stainless Steel in Slightly Oxidizing or Reducing Supercritical Water," *CORROSION*, vol. 62, no. 3, pp. 270–274, Mar. 2006.

[211] L. Volpe, M. Burke, and F. Scenini, "Oxidation behaviour of solution-annealed and thermally-treated Alloy 690 in low pressure H2-Steam," *Corrosion Science*, vol. 167, p. 108514, May 2020.

[212] M. Sun, X. Wu, Z. Zhang, and E.-H. Han, "Analyses of oxide films grown on Alloy 625 in oxidizing supercritical water," *The Journal of Supercritical Fluids*, vol. 47, no. 2, pp. 309–317, Dec. 2008.

[213] L. Volpe, M. Burke, and F. Scenini, "Correlation between Grain Boundary Migration and Stress Corrosion Cracking of Alloy 600 in Hydrogenated Steam," *Acta Materialia*, vol. 186, pp. 454–466, Mar. 2020.

[214] S. E. Ziemniak and M. Hanson, "Corrosion behavior of NiCrMo Alloy 625 in high temperature, hydrogenated water," *Corrosion Science*, vol. 45, no. 7, pp. 1595–1618, Jul. 2003. [Online]. Available: https://linkinghub.elsevier.com/retrieve/pii/S0010938X02002305

[215] International Atomic Energy Agency (IAEA), "Safety classification of structures, systems and components in nuclear power plants: Specific Safety Guide No. SSG-30," Vienna : International Atomic Energy Agency, 2014. [Online]. Available: https://www-pub.iaea.org/MTCD/publications/PDF/Pub1639_web.pdf

[216] H. Zhou, Y. Chen, Y. Sui, Y. Lv, Z. Zhu, L. Yang, Z. He, C. Li, and K. Fang, "Effect of Iron Ion on Corrosion Behavior of Inconel 625 in High-Temperature Water," *Scanning*, vol. 2020, pp. 1–8, Oct. 2020. [Online]. Available: https://www.hindawi.com/journals/scanning/2020/9130362/

[217] Association for Materials Protection and Performance (AMPP), "Corrosion Basics: Pitting Corrosion." [Online]. Available: https://www.ampp.org/technical-research/impact/corrosion-basics/group-1/pitting-corrosion#:~:text=Pitting%20corrosion%20is%20a%20localized,products%20often%20cover%20the%20pits.

[218] L. Chang, M. G. Burke, and F. Scenini, "Understanding the effect of surface finish on stress corrosion crack initiation in warm-forged stainless steel 304L in high-temperature water," *Scripta Materialia*, vol. 164, pp. 1–5, Apr. 2019.

[219] P. Davies and V. Randle, "Grain boundary engineering and the role of the interfacial plane," *Materials Science and Technology*, vol. 17, no. 6, pp. 615–626, Jun. 2001.

[220] I. Yadroitsev, P. Krakhmalev, I. Yadroitsava, S. Johansson, and I. Smurov, "Energy input effect on morphology and microstructure of selective laser melting single track from metallic powder," *Journal of Materials Processing Technology*, vol. 213, no. 4, pp. 606–613, Apr. 2013.

[221] W. J. Suder and S. W. Williams, "Investigation of the effects of basic laser material interaction parameters in laser welding," *Journal of Laser Applications*, vol. 24, no. 3, p. 032009, Aug. 2012.

[222] M. Sadowski, L. Ladani, W. Brindley, and J. Romano, "Optimizing quality of additively manufactured Inconel 718 using powder bed laser melting process," *Additive Manufacturing*, vol. 11, pp. 60–70, Jul. 2016.

[223] Z. Dong, Y. Liu, W. Wen, J. Ge, and J. Liang, "Effect of Hatch Spacing on Melt Pool and As-built Quality During Selective Laser Melting of Stainless Steel: Modeling and Experimental Approaches," *Materials*, vol. 12, no. 1, p. 50, Dec. 2018.

[224] J. Metelkova, Y. Kinds, K. Kempen, C. de Formanoir, A. Witvrouw, and B. Van Hooreweder, "On the influence of laser defocusing in Selective Laser Melting of 316L," *Additive Manufacturing*, vol. 23, pp. 161–169, Oct. 2018.

[225] V. Popovich, E. Borisov, A. Popovich, V. Sufiiarov, D. Masaylo, and L. Alzina, "Functionally graded Inconel 718 processed by additive manufacturing: Crystallographic texture, anisotropy of microstructure and mechanical properties," *Materials & Design*, vol. 114, pp. 441–449, Jan. 2017.

[226] L. Thijs, K. Kempen, J.-P. Kruth, and J. Van Humbeeck, "Fine-structured aluminium products with controllable texture by selective laser melting of pre-alloyed AlSi10Mg powder," *Acta Materialia*, vol. 61, no. 5, pp. 1809–1819, Mar. 2013.

[227] B. AlMangour, D. Grzesiak, and J.-M. Yang, "Scanning strategies for texture and anisotropy tailoring during selective laser melting of TiC/316L stainless steel nanocomposites," *Journal of Alloys and Compounds*, vol. 728, pp. 424–435, Dec. 2017. [Online]. Available: https://linkinghub.elsevier.com/retrieve/pii/S0925838817327494

[228] U. Krupp, P. E.-G. Wagenhuber, W. M. Kane, and C. J. McMahon, "Improving resistance to dynamic embrittlement and intergranular oxidation of nickel based superalloys by grain boundary engineering type processing," *Materials Science and Technology*, vol. 21, no. 11, pp. 1247–1254, Nov. 2005, number: 11. [Online]. Available: http://www.tandfonline.com/doi/full/10.1179/174328405X63935

[229] P. Lin, G. Palumbo, U. Erb, and K. Aust, "Influence of grain boundary character distribution on sensitization and intergranular corrosion of alloy 600," *Scripta Metallurgica et Materialia*, vol. 33, no. 9, pp. 1387–1392, Nov. 1995.

[230] L. Tan, K. Sridharan, T. Allen, R. Nanstad, and D. McClintock, "Microstructure tailoring for property improvements by grain boundary engineering," *Journal of Nuclear Materials*, vol. 374, no. 1-2, pp. 270–280, Feb. 2008, number: 1-2. [Online]. Available: https://linkinghub.elsevier.com/retrieve/pii/S0022311507009646

[231] T. Watanabe, "An approach to grain boundary design for strong and ductile polycrystals," *Res. Mechanica*, vol. 11, no. 1, pp. 47–84, 1984.

[232] V. Thaveeprungsriporn and G. S. Was, "The role of coincidence-site-lattice boundaries in creep of Ni-16Cr-9Fe at 360 ℃," *Metallurgical and Materials Transactions A*, vol. 28, no. 10, pp. 2101–2112, Oct. 1997.

[233] S. L. Yang, U. Krupp, H.-J. Christ, and V. Braz Trindade, "The Relationship between Grain Boundary Character and the Intergranular Oxide Distribution in IN718 Superalloy," *Adv. Eng. Mater.*, vol. 7, no. 8, pp. 723–726, Aug. 2005, number: 8. [Online]. Available: https://onlinelibrary.wiley.com/doi/10.1002/adem.200500036

[234] D. Brandon, "The structure of high-angle grain boundaries," *Acta Metallurgica*, vol. 14, no. 11, pp. 1479–1484, Nov. 1966.

[235] G. Palumbo, P. King, K. Aust, U. Erb, and P. Lichtenberger, "Grain boundary design and control for intergranular stress-corrosion resistance," *Scripta Metallurgica et Materialia*, vol. 25, no. 8, pp. 1775–1780, Aug. 1991.

[236] G. Palumbo, K. Aust, E. Lehockey, U. Erb, and P. Lin, "On a More Restrictive Geometric Criterion for "Special" CSL Grain Boundaries," *Scripta Materialia*, vol. 38, no. 11, pp. 1685–1690, May 1998. [Online]. Available: https://linkinghub.elsevier.com/retrieve/pii/S1359646298000773

[237] C. Athreya, K. Deepak, D.-I. Kim, B. de Boer, S. Mandal, and V. Subramanya Sarma, "Role of grain boundary engineered microstructure on high temperature steam oxidation behaviour of Ni based superalloy alloy 617," *Journal of Alloys and Compounds*, vol. 778, pp. 224–233, Mar. 2019. [Online]. Available: https://linkinghub.elsevier.com/retrieve/pii/S0925838818342609

[238] S. Yamaura, Y. Igarashi, S. Tsurekawa, and T. Watanabe, "Structure-dependent intergranular oxidation in Ni–Fe polycrystalline alloy," *Acta Materialia*, vol. 47, no. 4, pp. 1163–1174, Mar. 1999. [Online]. Available: https://linkinghub.elsevier.com/retrieve/pii/S1359645499000075

[239] C. A. Schuh, K. Anderson, and C. Orme, "Rapid assessment of anisotropic surface processes: experiments on the corrosion of Inconel 600," *Surface Science*, vol. 544, no. 2-3, pp. 183–192, Oct. 2003.

[240] X. Wang, J. Szpunar, and L. Zhang, "Effect of surface crystallographic orientation on the oxidation behavior of Ni-based alloy," *Applied Surface Science*, vol. 327, pp. 532–536, Feb. 2015.

[241] X. Wang, F. Fan, J. A. Szpunar, and L. Zhang, "Influence of grain orientation on the incipient oxidation behavior of Haynes 230 at 900 ℃," *Materials Characterization*, vol. 107, pp. 33–42, Sep. 2015.

[242] T. Sanviemvongsak, D. Monceau, C. Desgranges, and B. Macquaire, "Intergranular oxidation of Ni-base alloy 718 with a focus on additive manufacturing," *Corrosion Science*, vol. 170, p. 108684, Jul. 2020.

[243] F42 Committee, "Specification for Additive Manufacturing Nickel Alloy (UNS N06625) with Powder Bed Fusion," ASTM International, Tech. Rep. [Online]. Available: http://www.astm.org/cgi-bin/resolver.cgi?F3056-14R21

[244] ASTM B02 Committee, "Specification for Nickel Alloy Forgings." [Online]. Available: http://www.astm.org/cgi-bin/resolver.cgi?B564-18

[245] ActOn Additive Finishing Ltd, Normfinish Surface Treatment, "Additive Manufactured Components Polymers." [Online]. Available: https://www.normfinish.com/wp-content/uploads/AM-Polymers-brochure.pdf

[246] E04 Committee, "Guide for Electrolytic Polishing of Metallographic Specimens." [Online]. Available: http://www.astm.org/cgi-bin/resolver.cgi?E1558-09R21

[247] G01 Committee, "Practice for Preparing, Cleaning, and Evaluating Corrosion Test Specimens." [Online]. Available: http://www.astm.org/cgi-bin/resolver.cgi?G1-03R11

[248] B09 Committee, "Test Methods for Density of Compacted or Sintered Powder Metallurgy (PM) Products Using Archimedes Principle." [Online]. Available: http://www.astm.org/cgi-bin/resolver.cgi?B962-17

[249] J. Schindelin, I. Arganda-Carreras, E. Frise, V. Kaynig, M. Longair, T. Pietzsch, S. Preibisch, C. Rueden, S. Saalfeld, B. Schmid, J.-Y. Tinevez, D. J. White, V. Hartenstein, K. Eliceiri, P. Tomancak, and A. Cardona, "Fiji: an open-source platform for biological-image analysis," *Nature Methods*, vol. 9, no. 7, pp. 676–682, Jul. 2012.

[250] F. Bachmann, R. Hielscher, and H. Schaeben, "Grain detection from 2d and 3d EBSD data—Specification of the MTEX algorithm," *Ultramicroscopy*, vol. 111, no. 12, pp. 1720–1733, Dec. 2011.

[251] Bachmann, F., Hielscher, R., and Schaeben, H., "Texture analysis with MTEX – Free and Open Source Software Toolbox," *Solid State Phenomena*, vol. 160, pp. 63–68, Feb. 2010.

[252] R. Hielscher, C. B. Silbermann, E. Schmidl, and J. Ihlemann, "Denoising of crystal orientation maps," *Journal of Applied Crystallography*, vol. 52, no. 5, pp. 984–996, Oct. 2019.

[253] R. Krakow, R. J. Bennett, D. N. Johnstone, Z. Vukmanovic, Wilberth Solano-Alvarez, S. J. Lainé, J. F. Einsle, P. A. Midgley, C. M. F. Rae, and R. Hielscher, "Supplementary material from "On three-dimensional misorientation spaces"," 2017.

[254] G. Nolze and R. Hielscher, "Orientations – perfectly colored," *Journal of Applied Crystallography*, vol. 49, no. 5, pp. 1786–1802, Oct. 2016.

[255] E04 Committee, "Test Methods for Determining Average Grain Size." [Online]. Available: http://www.astm.org/cgi-bin/resolver.cgi?E112-13R21

[256] B08 Committee, "Test Method for Measurement of Metal and Oxide Coating Thickness by Microscopical Examination of Cross Section." [Online]. Available: http://www.astm.org/cgi-bin/resolver.cgi?B487

[257] J. Růžičková and B. Million, "Self-diffusion of the components in the F.C.C. phase of binary solid solutions of the Fe-Ni-Cr system," *Materials Science and Engineering*, vol. 50, no. 1, pp. 59–64, Sep. 1981. [Online]. Available: https://linkinghub.elsevier.com/retrieve/pii/0025541681900860

[258] Crystal Impact - Dr. H. Putz & Dr. K. Brandenburg GbR, "Match! - Phase Analysis using Powder Diffraction - Crystal Impact," Kreuzherrenstr. 102 D-53227 Bonn, Germany. [Online]. Available: https://www.crystalimpact.de/match

[259] CrystalMaker Software Ltd., "CrystalDiffract®: a powder diffraction program for Mac and Windows," CrystalMaker Software Ltd, Oxford, England, UK. [Online]. Available: https://crystalmaker.com/index.html

[260] I. Levin, "NIST Inorganic Crystal Structure Database (ICSD)," 2020. [Online]. Available: https://data.nist.gov/od/id/mds2-2147

[261] B. Panicaud, "Growth constraints and oxidation kinetics in layers of thermal oxides of iron and nickel: in-situ study by x-ray diffraction and modeling," Ph.D. dissertation, La Rochelle University, France, 2004. [Online]. Available: https://theses.fr/2004LAROS12z

[262] H. Sawada, "Residual electron density study of chromium sesquioxide by crystal structure and scattering factor refinement," *Materials Research Bulletin*, vol. 29, no. 3, pp. 239–245, Mar. 1994. [Online]. Available: https://linkinghub.elsevier.com/retrieve/pii/0025540894900191

[263] RRUFF™ Project, Bob Downs, Hexiong Yang, "The RRUFF™ Project, website containing an integrated database of Raman spectra, X-ray diffraction and chemistry data for minerals." [Online]. Available: https://rruff.info/

[264] S. Cruchley, J. F. Sun, M. P. Taylor, H. E. Evans, P. Bowen, J. Sumner, J. R. Nicholls, N. J. Simms, B. A. Shollock, R. J. Chater, B. J. Foss, M. C. Hardy, and S. Stekovic, "Cautionary note on use of focused ion beam sectioning as technique for characterising oxidation damage in Ni based superalloys," *Materials at High Temperatures*, vol. 31, no. 1, pp. 27–33, Jan. 2014.

[265] N. S. Rajput, K. Sloyan, D. H. Anjum, M. Chiesa, and A. A. Ghaferi, "A user-friendly FIB lift-out technique to prepare plan-view TEM sample of 2D thin film

materials," *Ultramicroscopy*, vol. 235, p. 113496, May 2022. [Online]. Available: https://linkinghub.elsevier.com/retrieve/pii/S0304399122000328

[266] S. Cruchley, M. P. Taylor, H. E. Evans, M. C. Hardy, and D. J. Child, "Characterisation of subsurface oxidation damage in Ni based superalloy, RR1000," *Materials Science and Technology*, vol. 30, no. 15, pp. 1884–1889, Dec. 2014. [Online]. Available: http://www.tandfonline.com/doi/full/10.1179/1743284714Y.0000000541

[267] S. Cruchley, H. Evans, and M. Taylor, "An overview of the oxidation of Ni-based superalloys for turbine disc applications: surface condition, applied load and mechanical performance," *Materials at High Temperatures*, vol. 33, no. 4-5, pp. 465–475, Jun. 2016, number: 4-5. [Online]. Available: http://www.tandfonline.com/doi/full/10.1080/09603409.2016.1171952

[268] S. Cruchley, H. Li, H. Evans, P. Bowen, D. Child, and M. Hardy, "The role of oxidation damage in fatigue crack initiation of an advanced Ni-based superalloy," *International Journal of Fatigue*, vol. 81, pp. 265–274, Dec. 2015. [Online]. Available: https://linkinghub.elsevier.com/retrieve/pii/S0142112315002686

[269] E. Ott, J. Groh, and H. Sizek, "Metals Affordability Initiative: Application of Allvac Alloy 718Plus® for Aircraft Engine Static Structural Components," *Superalloys 718, 625, 706, and Derivatives*, Oct. 2005. [Online]. Available: http://www.tms.org/

[270] S. Ghosh, L. Ma, N. Ofori-Opoku, and J. E. Guyer, "On the primary spacing and microsegregation of cellular dendrites in laser deposited Ni–Nb alloys," *Modelling Simul. Mater. Sci. Eng.*, vol. 25, no. 6, p. 065002, Sep. 2017, number: 6. [Online]. Available: https://iopscience.iop.org/article/10.1088/1361-651X/aa7369

[271] N. J. Harrison, I. Todd, and K. Mumtaz, "Reduction of micro-cracking in nickel superalloys processed by Selective Laser Melting: A fundamental alloy design approach," *Acta Materialia*, vol. 94, pp. 59–68, Aug. 2015. [Online]. Available: https://linkinghub.elsevier.com/retrieve/pii/S1359645415002876

[272] L. Thijs, M. L. Montero Sistiaga, R. Wauthle, Q. Xie, J.-P. Kruth, and J. Van Humbeeck, "Strong morphological and crystallographic texture and resulting yield strength anisotropy in selective laser melted tantalum," *Acta Materialia*, vol. 61, no. 12, pp. 4657–4668, Jul. 2013. [Online]. Available: https://linkinghub.elsevier.com/retrieve/pii/S1359645413003091

[273] Pinkerton, A.J, Shackleton, J., Moat, R., Li, L., Withers, P., Preuss, M., Allen, J., Hilton, P., and Folwell, R., "The effect of process parameters on residual stress within an inconel 718

part produced by the Direct Laser Deposition process," *Proceedings of the 24th International Congress on Applications of Lasers and Electro-optics (ICALEO). Laser Institute of America*, pp. 601–610, 2005.

[274] D. D. Gu, W. Meiners, K. Wissenbach, and R. Poprawe, "Laser additive manufacturing of metallic components: materials, processes and mechanisms," *International Materials Reviews*, vol. 57, no. 3, pp. 133–164, May 2012. [Online]. Available: http://www.tandfonline.com/doi/full/10.1179/1743280411Y.0000000014

[275] E04 Committee, "Test Methods for Determining Average Grain Size," ASTM International, Tech. Rep. [Online]. Available: http://www.astm.org/cgi-bin/resolver.cgi?E112-13R21

[276] I. C. Noyan and J. B. Cohen, *Residual stress: measurement by diffraction and interpretation*. Springer, 2013.

[277] F. Wang, X. H. Wu, and D. Clark, "On direct laser deposited hastelloy x: dimension, surface finish, microstructure and mechanical properties," *Materials Science and Technology*, vol. 27, no. 1, pp. 344–356, 2011. [Online]. Available: https://doi.org/10.1179/026708309X12578491814591

[278] J. Colas, L. Charpentier, and M. Balat-Pichelin, "Oxidation in Air at 1400 K and Optical Properties of Inconel 625, FeCrAlloy and Kanthal Super ER," *Oxid Met*, vol. 93, no. 3-4, pp. 355–370, Apr. 2020.

[279] G. Marchese, A. Aversa, and E. Bassini, "Microstructure and Hardness Evolution of Solution Annealed Inconel 625/TiC Composite Processed by Laser Powder Bed Fusion," *Metals*, vol. 11, no. 6, p. 929, Jun. 2021, number: 6. [Online]. Available: https://www.mdpi.com/2075-4701/11/6/929

[280] H. Buscail, R. Rolland, C. Issartel, F. Rabaste, F. Riffard, L. Aranda, and M. Vilasi, "Effects of water vapour on the oxidation of a nickel-base 625 alloy between 900 and 1,100 ℃," *J Mater Sci*, vol. 46, no. 18, pp. 5903–5915, Sep. 2011. [Online]. Available: http://link.springer.com/10.1007/s10853-011-5544-2

[281] Y. Cao, J. Zhu, Z. Nong, X. Yang, Y. Liu, and Z. Lai, "First-principles studies of the structural, elastic, electronic and thermal properties of Ni3Nb," *Computational Materials Science*, vol. 77, pp. 208–213, Sep. 2013. [Online]. Available: https://linkinghub.elsevier.com/retrieve/pii/S0927025613001948

[282] S. Dai and W. Liu, "First-principles study on the structural, mechanical and electronic properties of δ and γ″ phases in Inconel 718," *Computational Materials Science*, vol. 49, no. 2, pp. 414–418, Aug. 2010. [Online]. Available: https://linkinghub.elsevier.com/retrieve/pii/S0927025610003034

[283] N. Li, J. Xiao, N. Prud'homme, L. Li, and V. Ji, "Residual Stress Analysis on Oxide Layers Obtained by High Temperature Oxidation of Chromia-Forming Alloys," Jan. 2017, pp. 365–370. [Online]. Available: http://www.mrforum.com/product/9781945291173-62

[284] P. F. Tortorelli, "Mechanical properties of chromia scales," *J. Phys. IV France*, vol. 03, no. C9, pp. C9–943–C9–949, Dec. 1993. [Online]. Available: http://www.edpsciences.org/10.1051/jp4:1993997

[285] G. Zhou, "Nucleation thermodynamics of oxide during metal oxidation," *Applied Physics Letters*, vol. 94, no. 20, p. 201905, May 2009.

[286] D. Zhu, S. Mathur, and A. C. Society, Eds., *Advanced ceramic coatings and interfaces V: a collection of papers presented at the 34th International Conference on Advanced Ceramics and Composites, January 24 - 29, 2010, Daytona Beach, Florida ; [the Symposium on Advanced Ceramic Coatings for Structural, Environmental and Functional Applications was held at the 34th International Conference on Advanced Ceramics and Composites in Cocoa Beach, Florida …]*, ser. Ceramic engineering and science proceedings. Hoboken, NJ: Wiley, 2010, no. 31,3, meeting Name: International Conference on Advanced Ceramics and Composites.

[287] A. Chyrkin, Vladimir Shermet, L. Singheiser, and Willem J. Quadakkers, "Predicting subsurface enrichment/depletion processes during high-temperature oxidation of alloy 625 thin foils," vol. Australasian Corrosion Association, Vol. 2, Perth, Australia, Nov. 2011, p. 1556.

[288] S. Sanchez, P. Smith, Z. Xu, G. Gaspard, C. J. Hyde, W. W. Wits, I. A. Ashcroft, H. Chen, and A. T. Clare, "Powder Bed Fusion of nickel-based superalloys: A review," *International Journal of Machine Tools and Manufacture*, vol. 165, p. 103729, Jun. 2021. [Online]. Available: https://linkinghub.elsevier.com/retrieve/pii/S0890695521000390

[289] J. Pfaendtner and C. McMahon Jr, "Oxygen-induced intergranular cracking of a Ni-base alloy at elevated temperatures—an example of dynamic embrittlement," *Acta Materialia*, vol. 49, no. 16, pp. 3369–3377, Sep. 2001.

[290] L. Bataillou, L. Martinelli, C. Desgranges, S. Bosonnet, K. Ginestar, F. Miserque, Y. Wouters, L. Latu-Romain, A. Pugliara, A. Proietti, and D. Monceau, "Growth Kinetics and Character-

ization of Chromia Scales Formed on Ni–30Cr Alloy in Impure Argon at 700 ℃," *Oxidation of Metals*, vol. 93, no. 3-4, pp. 329–353, Apr. 2020.

[291] R. Peraldi, D. Monceau, and B. Pieraggi, "Correlations Between Growth Kinetics and Microstructure for Scales Formed by High-Temperature Oxidation of Pure Nickel. II. Growth Kinetics," *Oxidation of Metals*, vol. 58, no. 3/4, pp. 275–295, 2002.

[292] C. T. Sims, N. S. Stoloff, and W. C. Hagel, Eds., *Superalloys II.* New York: Wiley, 1987.

[293] P. Maziasz, I. Wright, J. Shingeldecker, T. Gibbons, and R. Romanosky, "Defining the materials issues and research for ultra-supercritical steam turbines," *Proceedings of the 4th International Conference on Advances in Materials Technology for Fossil Power Plants*, vol. 2005, 01 2005.

[294] T. Keller, G. Lindwall, S. Ghosh, L. Ma, B. M. Lane, F. Zhang, U. R. Kattner, E. A. Lass, J. C. Heigel, Y. Idell, M. E. Williams, A. J. Allen, J. E. Guyer, and L. E. Levine, "Application of finite element, phase-field, and CALPHAD-based methods to additive manufacturing of Ni-based superalloys," *Acta Materialia*, vol. 139, pp. 244–253, Oct. 2017. [Online]. Available: https://linkinghub.elsevier.com/retrieve/pii/S1359645417303804

[295] Z.-y. Zhu, Y. Sui, A.-l. Dai, Y.-f. Cai, L.-L. Xu, Z.-x. Wang, H.-m. Chen, X.-m. Shao, and W. Liu, "Effect of Aging Treatment on Intergranular Corrosion Properties of Ultra-Low Iron 625 Alloy," *International Journal of Corrosion*, vol. 2019, pp. 1–9, Jan. 2019.

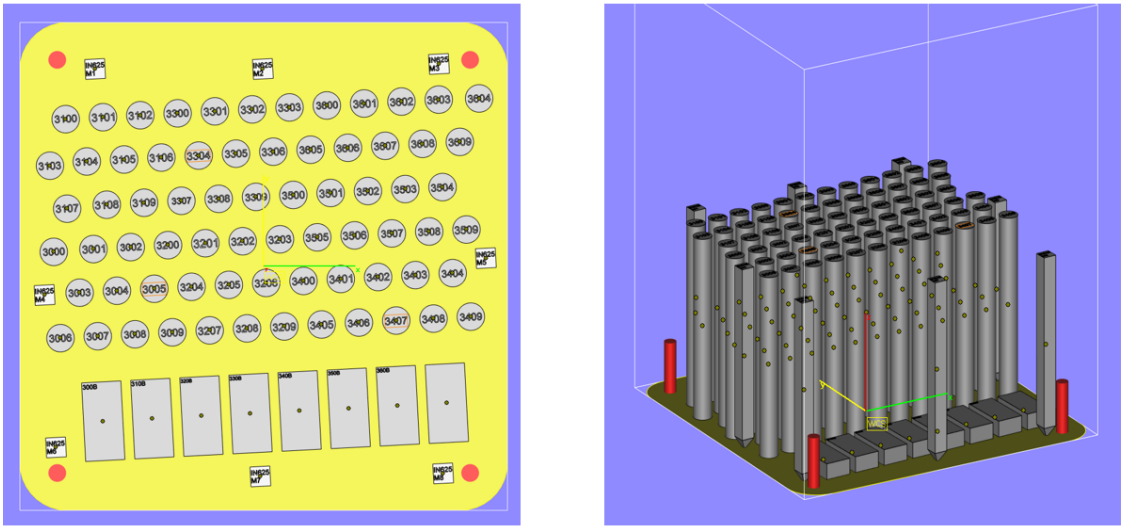
Appendix

Table 1
Summary of the oxidation performance of wrought Ni-based superalloys in literature, following isothermal oxidation testing in laboratory air and pressure [1–11].

Author	Year	Time (h)	Temperature (°C)	1/(10^4/T)	K_p ($mg^2/cm^4/s$)	Oxides
Kumar	**1996**	>3	1050	7.56	6.25E-05	Cr_2O_3
		>3	1100	7.28	1.55E-04	
		>3	1150	7.03	2.80E-04	Cr_2O_3 + Nb_2O_5 and TiO_2
		>3	1200	6.79	6.60E-04	
		>3	1050	7.56	5.58E-05	
		>3	1100	7.28	1.38E-05	
		>3	1150	7.03	2.50E-04	Cr_2O_3 + Nb_2O_5 and TiO_2
		>3	1200	6.79	4.43E-04	
England	**1999**	> 10000	800	9.32	2.81E-08	Cr_2O_3
		> 10000	850	8.90	4.81E-08	
		> 10000	900	8.53	1.54E-06	
		> 10000	950	8.18	2.97E-06	
		> 10000	1000	7.86	1.95E-05	
		> 10000	1050	7.56	6.19E-06	
		> 10000	1100	7.28	6.44E-05	
Trindade	**2005**	100	1000	7.86	1.09E-05	
N'dah	**2007**	200	900	8.53	5.56E-07	Cr_2O_3,
		200	1000	7.86	8.33E-06	Cr_2O_3, $(Mn,Cr)_2O_4$
Colas	**2020**	35	1100	7.28	2.95E-05	Cr_2O_3, NiO, NbCrO4, $MnCr_2O_4$
Chyrkin	**2011**	1000	900	8.53	2.93E-07	
Staszewska	**2016**	96	1000	7.86	9.79E-06	Cr_2O_3, Nb_2O_5, $NiCr_2O_4$
		96	1100	7.28	9.90E-06	Cr_2O_3, Nb_2O_5, $NiCr_2O_4$
		96	1200	6.79	1.00E-05	
Arnold	**2017**	1000	900	8.53	3.19E-07	Cr_2O_3, $Mn_xCr_{3-x}O_4$
Trindade	**2017**	100	850	8.90	1.53E-06	Cr_2O_3
Ramenatte	**2020**	50	900	8.53	3.50E-07	Cr_2O_3, $MnCr_2O_4$
		50	1050	7.56	8.15E-06	
Sousa Malafaia	**2020**	120	800	9.32	N/A	
		240	800	9.32	N/A	
		120	1000	7.86	N/A	Cr_2O_3, $MnCr_2O_4$
		240	1000	7.86	N/A	Cr_2O_3, $MnCr_2O_4$
Chyrkin	**2022**	300	900	8.53	4.98E-07	Cr_2O_3, $NiCr_2O_4$, TiO
			1000	7.86	5.31E-06	Cr_2O_3, $NiCr_2O_4$, TiO

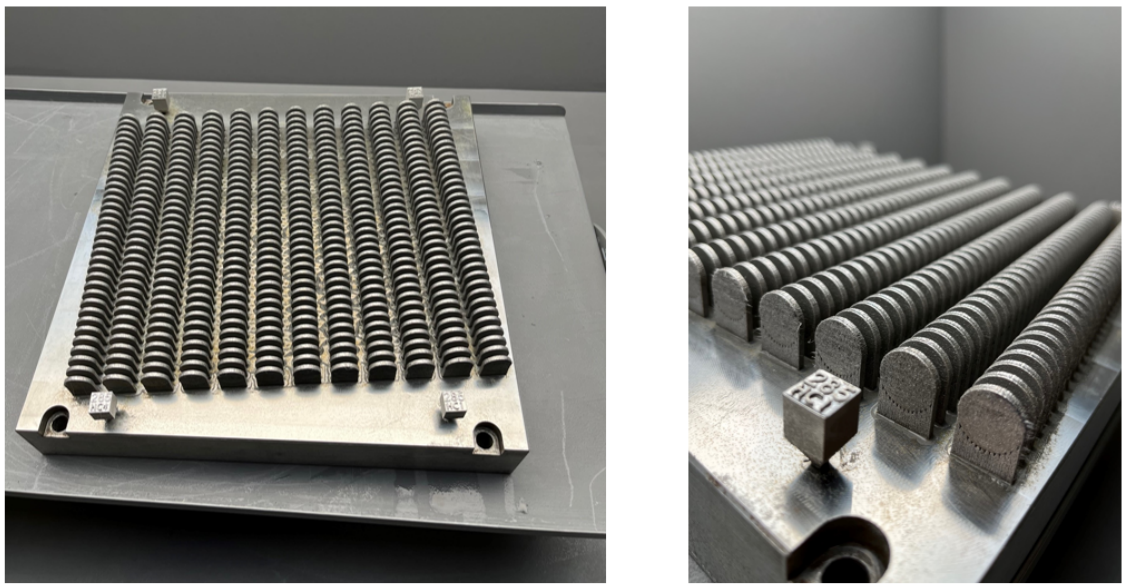
Table 2
Summary of the oxidation performance of L-PBF manufactured IN625 in literature, following isothermal oxidation testing in laboratory air and pressure [1, 9, 10, 12–17].

Author	Year	Time (h)	Temperature (°C)	1/(10^4/T)	K_p ($mg^2/cm^4/s$)	Oxides	Notes
Arnold	**2017**	1000	900	8.53	8.75E-09	Cr_2O_3	ODS alloy
Chen	**2020**	100	900	8.53	1.69E-04	Cr_2O_3, $Ni(Cr,Fe)_2O_4$	As-built TiC Nanocomposite
		100	900	8.53	1.01E-04	Cr_2O_3, $Ni(Cr,Fe)_2O_4$, NiO,	Laser shock peened (1 pass) TiC Nano
		100	900	8.53	4.50E-05	Cr_2O_3, $Ni(Cr,Fe)_2O_4$, NiO, TiO_2	Laser shock peened (2 passes) TiC
		100	900	8.53	2.37E-05	Cr_2O_3, $Ni(Cr,Fe)_2O_4$	Laser shock peened (3 passes) TiC Nano
Chen	**2020**	100	1000	7.86	2.46E-04		As-built
		100	1000	7.86	6.83E-05		As-built TiC Nanocomposite
		100	1000	7.86	1.91E-04		Solution-treated
		100	1000	7.86	2.47E-06		Heat-treated TiC Nanocomposite
Condruz	**2020**	96	900	8.53	7.23E-07	Cr_2O_3 and (Ni, Fe)Cr_2O_4	As-built
		96	1050	7.56	1.67E-05	(Ni, Fe)Cr_2O_4, Cr_2O_3	As-built
Parizia	**2020**	96	900	8.53	3.89E-07	Cr_2O_3, $NiCr_2O_4$, Nb_2O_5	As-built
		96	900	8.53	4.17E-07	Cr_2O_3, $NiCr_2O_4$, Nb_2O_5	Solution-treated
		96	900	8.53	8.06E-07	Cr_2O_3, $NiCr_2O_4$, Nb_2O_5	Solution-treated
Ramenatte	**2020**	50	900	8.53	5.25E-07	Cr_2O_3	Laser Beam Melted
		50	1050	7.56	2.66E-05		Laser Beam Melted
Sun	**2020**	100	900	8.53	2.57E-04	Cr_2O_3, $NiCr_2O_4$, $NiFe_2O_4$, NiO	VED = 76 J/mm3 As-built
		100	900	8.53	1.08E-04	Cr_2O_3, $NiCr_2O_4$, $NiFe_2O_4$, NiO	VED = 104 J/mm3 As-built
		100	900	8.53	7.42E-05	Cr_2O_3, $NiCr_2O_4$, $NiFe_2O_4$, NiO	VED = 167 J/mm3 As-built
Chyrkin	**2022**	300	900	8.53	8.78E-07	Cr_2O_3, $NiCr_2O_4$, TiO	As-built IN625 Y orientation
		300	900	8.53	9.97-07	Cr_2O_3, $NiCr_2O_4$, TiO	As-built IN625 Z orientation
		100	1000	7.86	1.24E-05	Cr_2O_3, $NiCr_2O_4$, TiO	As-built IN625 Y orientation
		100	1000	7.86	8.80E-06	Cr_2O_3, $NiCr_2O_4$, TiO	As-built IN625 Z orientation
		300	900	8.53	2.19E-07	Cr_2O_3, $NiCr_2O_4$, TiO	As-built coarse grained + annealed
		300	900	8.53	7.93E-07	Cr_2O_3, $NiCr_2O_4$, TiO	As-built + hot rolled
Huang	**2022**	40	1000	7.86	7.19E-06	Cr_2O_3, $NiCr_2O_4$,NiO	v = 600 mm/s As-built
		40	1000	7.86	2.86E-06	Cr_2O_3, $NiCr_2O_4$,NiO	v = 750 mm/s As-built
		40	1000	7.86	3.52E-06	Cr_2O_3, $NiCr_2O_4$,NiO	v = 900 mm/s As-built
		40	1000	7.86	3.18E-06	Cr_2O_3, $NiCr_2O_4$,NiO	v = 1000 mm/s As-built
		40	1000	7.86	3.05E-06	Cr_2O_3, $NiCr_2O_4$,NiO	v = 1200 mm/s As-built



(a) (b)

Figure 1: Appendix Figure 1: Laser Powder Bed Fusion (L-PBF) manufactured IN625 upon build plate, containing a total of 72 cylindrical rod samples, and 8 cuboid samples. The samples consist of cylindrical shapes with diameters of 14 mm and heights of 120 mm, and cuboids of 10 mm height, by 10mm width, by 10 mm depth. The build plate showcases a variety of sample geometries, strategically arranged for optimal space utilization and heat management during the manufacturing process.



(a) (b)

Figure 2: Appendix Figure 2: Laser Powder Bed Fusion (L-PBF) manufactured IN625 samples upon build plate, containing a total of 420 circular tokens on support struts. The samples dimensions were set to produce tokens of diameter of 14 mm and thickness of 2 mm. Four test cuboid samples were also placed in each corner (of 10 mm height, by 10 mm width, by 10 mm depth) to test for possible variations in microstructure across the build plate. The build plate showcases a variety of sample geometries, strategically arranged for optimal space utilization and heat management during the manufacturing process.